

ABSTRACT

Title of Dissertation: **OPTIMIZATION OF HIGH- β FUSION DEVICES
AGAINST LINEAR INSTABILITIES**

Rahul Gaur
Doctor of Philosophy, 2023

Dissertation Directed by: **Professor William Dorland**
Department of Physics

Magnetic confinement fusion is a technique in which a strong magnetic field is used to contain a hot plasma, which enables nuclear fusion. In terms of overall energy efficiency, the two most promising magnetic confinement concepts are tokamaks (axisymmetric devices) and stellarators (nonaxisymmetric devices). The power P produced by a magnetically confined nuclear fusion device is proportional to $V\beta^2B^4$, where V is the volume of the device, β is the plasma pressure - magnetic pressure ratio, and B is the magnetic field strength. Most tokamaks and stellarators currently in operation are low- β devices. In general, there are three ways to increase P , one may increase the operating β , the magnetic field or the volume of the device. The cost of these devices is proportional to V , making large enough devices expensive. Similarly, a large magnetic field ($>10\text{T}$) requires superconducting magnets that, even after the recent innovations in HTS (High-Temperature Superconductors), are expensive to manufacture. High- β devices are an attractive idea to efficiently produce fusion energy. However, a high- β generally also implies a large gradient in plasma pressure that can be a source of numerous instabilities. If fusion de-

vices could be optimized against such instabilities, high- β operation would become an attractive approach compared to high field or large-volume reactors. Therefore, this thesis explores the optimization of high- β tokamak and stellarator equilibrium equilibria against linear instabilities.

We will start by investigating the stability of high- β tokamaks and stellarator equilibria against the infinite- n ideal ballooning mode, an important pressure-driven MHD instability. We stabilize these equilibria against the ideal ballooning mode. To achieve this, we formulate a gradient-based adjoint technique and demonstrate its speed and effectiveness by stabilizing these equilibria. We also explain how this technique can be easily extended to low- n ideal-MHD modes in both tokamaks and stellarators.

After demonstrating the adjoint technique for stabilizing against ideal MHD modes, we first analyze the kinetic stability of a sequence of axisymmetric equilibria. We study this by numerically solving the δf gyrokinetic model, a simplified version of the Vlasov-Maxwell model. Since these kinetic instabilities are driven by temperature and density gradients, we explore them by scanning multiple values of the plasma β , temperature and density gradients, and plasma boundary shapes, discovering interesting relationships between equilibrium-dependent quantities and growth rates of these instabilities. We then repeat the same process for two recently published stellarator equilibria with quasisymmetry — a favorable hidden symmetry in stellarators. With this study, we verify that our observations from high- β tokamaks can be generalized to quasisymmetric stellarators.

From our microstability study, we find that electromagnetic effects are important for high- β devices. Hence, using the numerical tools and knowledge derived from the previous chapters we build an optimization framework that searches for stable equilibria. Due to the similarity between axisymmetry and quasisymmetry, we then use the microstability optimizer to search for ideally

and kinetically-stable, quasisymmetric, high- β stellarators.

OPTIMIZATION OF HIGH- β FUSION
DEVICES AGAINST LINEAR INSTABILITIES

by

Rahul Gaur

Dissertation submitted to the Faculty of the Graduate School of the
University of Maryland, College Park in partial fulfillment
of the requirements for the degree of
Doctor of Philosophy
2023

Advisory Committee:

Professor William Dorland, Chair/Advisor
Dr. Ian G. Abel, Co-chair
Dr. Matthew J. Landreman
Professor Alexander Philippov
Professor Thomas M. Antonsen, Jr.

© Copyright by
Rahul Gaur
2023

Dedication

To my parents Santosh and Jai, and my sister Kritika.

Acknowledgments

First, I thank my advisor Bill for including me as a Graduate Assistant in his research group. Bill's foresight, computational prowess, and strong intuition have helped me immensely on numerous occasions when I was stuck on a problem. This thesis would have been impossible without his support. I would also like to thank his family for throwing informal get-togethers that helped me take my mind off plasma physics.

Next, I thank my co-advisor Ian for his support. Most of my knowledge of gyrokinetics is due to him. He has explained these concepts to me in person hundreds of times. A lot of the new numerical and analytical techniques that I have added to my Physicist toolbox are due to him.

I thank Matt for helping me set up the VMEC equilibrium code on my system and for introducing our research group to the fascinating world of stellarator optimization. His deep insight into stellarators and the development of open source codes such as SIMSOPT has greatly helped me.

I thank all the great plasma physics professors that I had at UMD: Jim, Tom and Adil. I learned most of the basic plasma physics from their survey courses PHYS761 and 762.

I thank my collaborators Noah, David, Stefan, and Max for bouncing ideas with me on short time scales and helping me improve the presentation of my papers. Special thanks to David and Noah for fixing bugs related to sophisticated codes GS2 and GX in hours instead of days.

I thank several of my undergraduate advisors for introducing me to academic research. I thank my undergraduate thesis advisor Prof. Supreet Singh Bagha, Prof. Balaji Srinivasan, Prof.

Modak, Prof. Samanta, Prof. Kumar, and Prof. Prasad. I also would like to thank all my teachers at my high school DPS Greater Noida.

I thank many friends and co-workers during my Ph.D. at UMD. Thanks to Alessandro, Mike, Jason, Wrick, George, Rogerio, Jimmy, Elizabeth, Nathaniel, Michael, Byoungchan, Tony, Alan, John, and Siena for their encouragement and enthusiasm during physics discussion in journal clubs, group meetings, and happy hours on Friday evenings. I would like to thank my housemates Takahiro, Saad, Nguyen, Jackson, Tyler and for their help and support.

I thank my undergraduate friends for the AXLR8R Formula racing at IITD for teaching me about solving practical problems with scarce resources and limited time.

I thank my cousin Thakur, who taught me about various unsolved problems of the world, such as the availability of fossil fuels, electric vehicles, and room-temperature superconductors.

Last but not least, I thank my dissertation committee for carefully reading my thesis and making useful suggestions that significantly improved the presentation of this work.

This work was supported by the US Department of Energy, Office of Science, Office of Fusion Energy Sciences under Award Numbers DE-SC0018429 and DE-FG02-93ER54197. This research used resources of the National Energy Research Scientific Computing Center, a DOE Office of Science User Facility, and the Stellar and Traverse clusters at Princeton University.

Table of Contents

Dedication	ii
Acknowledgements	iii
Table of Contents	v
List of Tables	viii
List of Figures	x
List of Abbreviations	xvii
Chapter 1: Introduction	1
1.1 Motivation	1
1.2 Two self-consistent models of fusion plasmas	6
1.2.1 Ideal MHD	6
1.2.2 The gyrokinetic model	8
1.3 Unsolved problems in stability optimization and scope of this work	11
Chapter 2: Ideal MHD stability analysis and optimization of high-β equilibria	13
2.1 Overview	13
2.2 Ideal MHD: Equilibrium	14
2.2.1 Numerical equilibria	18
2.3 Ideal MHD: Stability	23
2.3.1 Low- n modes	28
2.3.2 The infinite- n , ideal ballooning mode	29
2.3.3 Leveraging the self-adjoint property to formulate an optimizer	34
2.3.4 Details of the optimization process	38
2.4 Results	44
2.4.1 Stabilizing the DIII-D-like equilibrium	44
2.4.2 Stabilizing the NCSX equilibrium	46
2.4.3 Stabilizing the modified Henneberg-QA equilibrium	48
2.5 Summary and Conclusions	49
Chapter 3: Kinetic microstability analysis of high-β equilibria	52
3.1 Overview	52
3.2 Microstability analysis	53

3.2.1	The gyrokinetic model	53
3.2.2	Kinetic stability analysis with <i>GS2</i>	60
3.2.3	The Greene-Chance analysis	63
3.3	High- β axisymmetric equilibria	64
3.3.1	ITG study	70
3.3.2	TEM study	79
3.3.3	Linear Electromagnetic study	86
3.4	High- β stellarator equilibria	90
3.4.1	LBD QA low- β equilibrium	91
3.4.2	LBD QH intermediate- β equilibrium	93
3.5	Relationship between ideal and kinetic ballooning modes	95
3.5.1	$\hat{s} - \alpha_{\text{MHD}}$ analysis of axisymmetric equilibria	96
3.5.2	Ideal ballooning analysis of LBD equilibria	101
3.6	Summary and Conclusions	102
Chapter 4: Towards a combined MHD and kinetic stability optimization of high-β equilibria		105
4.1	Overview	105
4.2	The MicroStOpt framework	106
4.3	Finding a high- β , KBM-stable tokamak	110
4.4	Finding a high- β , KBM-stable quasisymmetric stellarator	111
4.5	Summary and Conclusions	114
Chapter 4: Conclusions		116
Appendix A: Details of the adjoint method and ideal ballooning equation		118
A.1	The discretized ideal ballooning equation	118
A.2	Details of the adjoint ideal ballooning calculation	119
A.3	Extending our adjoint-based technique to equilibrium degrees of freedom	120
A.4	Extending our adjoint technique to low- n , ideal MHD solvers	122
A.5	Homotopy analysis method for solving the ideal ballooning equation	123
A.5.1	Using SHAM to solve the ideal ballooning equation	124
Appendix B: Local expansion of an axisymmetric equilibrium		129
B.1	The analysis of Greene and Chance	129
B.1.1	Mercier-Luc local coordinate system	130
B.1.2	Expanding the Grad-Shafranov equation locally	132
B.1.3	Variation of a local axisymmetric equilibrium	136
B.1.4	Geometric coefficients for a local analysis	136
B.2	Some tests for the geometry	137
B.2.1	$\psi_p \rightarrow -\psi_p$ invariance of the geometric coefficients	138
B.2.2	Periodicity and boundedness of physical quantities in θ_0	138
Appendix C: Hsu, Artun and Cowley's analytical ($\beta \sim 1$) tokamak equilibrium		141
C.1	Generating analytical $\beta \sim 1$ equilibria	141

C.2	Limitations of the Hsu <i>et al.</i> equilibria	143
Appendix D: Newcomb’s criterion		146
Appendix E: Extended eigenfunctions of the EM-ETG mode		148
Appendix F: GX: A robust gyrokinetic solver		149
F.1	Overview	149
F.2	Deriving the GX model equations	150
F.2.1	Fundamental identities	150
F.2.2	Intermediate derived identities	152
F.2.3	Individual terms in the gyrokinetic model	153
F.3	Linear, collisionless gyrokinetic model in Fourier-Hermite-Laguerre space	155
F.3.1	Gyrokinetic equation	156
F.3.2	Normalized gyrokinetic model	158
F.3.3	Transforming to Hermite-Laguerre space	159
F.4	Linear tests	161

List of Tables

2.1	This table shows the values of relevant physical quantities for the DIII-D like equilibrium.	21
2.2	This table shows the values of important physical quantities for the modified NCSX equilibrium.	22
2.3	This table presents values of relevant physical quantities for the modified Henneberg-QA design.	23
2.4	This table shows a comparison between relevant physical quantities of the intial and optimized DIII-D equilibrium	45
2.5	This table provides the boundary shape Dofs for the NCSX case.	46
2.6	This table presents a comparison between relevant physical quantities of the intial and optimized NCSX equilibrium	48
2.7	This table lists the boundary shape Dofs for the modified Henneberg-QA case. . .	48
2.8	This table shows a comparison between relevant physical quantities of the intial and optimized modified Henneberg-QA equilibrium	49
3.1	This table contains input parameters used for the VMEC equilibria. Throughout this study, in this table, every parameter remains fixed.	66
3.2	This table contains the Miller parameters for the outer boundary	67
3.3	This table contains the normalized β values on selected flux surfaces	68
3.4	This table contains the nominal gradient scale length values	71
3.5	This table contains the values of a/L_{Ti} at $\rho = 0.5$ for the ITG study	72
3.6	This table contains the values of a/L_{Ti} at $\rho = 0.8$ for the ITG study	72
3.7	This table contains the values of gradient scale lengths at $\rho = 0.5$ used for the TEM study	80
3.8	This table contains the values of gradient scale lengths at $\rho = 0.8$ used for the TEM study	80
3.9	This table contains the values of quantities needed for a gyrokinetic run with the LBD QA equilibrium. The gradient scale lengths are the same for both ions and electrons.	91
3.10	This table contains the values of quantities needed for a gyrokinetic run with the LBD QH equilibrium. The gradient scale lengths are the same for both ions and electrons.	94
4.1	This table shows a comparison between relevant physical quantities of the intial and optimized DIII-D equilibrium.	110
4.2	This table provides the boundary shape degrees of freedom for the QH, high- β stellarator equilibrium. The number of degrees of freedom is 46.	113

4.3	This table shows a comparison between relevant physical quantities of the initial and optimized LBD-QH-like equilibrium.	114
B.1	This table lists the complete set of geometric coefficients needed to perform an ideal ballooning or gyrokinetic analysis.	137

List of Figures

1.1	This figure shows the trajectory of a positively charged particle in a divergence free equilibrium field $B_\phi \propto 1/r$, where r is the radial distance from the center. The blue line represents a magnetic field line. The particle drifts vertically upwards and is deconfined. A negatively charged particle would drift downwards.	2
1.2	This figure shows the trajectory of a particle at two different times in a an equilibrium where magnetic field lines lie on a toroidal surface. The particles is launched from the blue-colored field line. Due to the twist of the magnetic field in the θ direction, the particle is confined to the toroidal surface.	3
1.3	This figure shows the strength of the magnetic field $ B $ on a flux surface and the cross section at various toroidal and radial locations for an axisymmetric equilibrium and two 3D equilibria. The cross sections are plotted in cylindrical coordinates (R, ϕ, Z) . The number of repeatable toroidal segments or field periods n_{fp} is 1 for DIII-D, 2 for Henneberg-QA, and 3 for NCSX.	4
1.4	This figure illustrates the “frozen-in” condition of ideal MHD. The tubes represent magnetic field lines containing plasma (colored purple). The “frozen-in” condition prohibits the tubes from passing through each other. This topological constraint allows 3D toroidal equilibria to retain their nested flux surface topology in figure 1.3. A short and intuitive derivation of the “frozen-in” condition is given in chapter 3 of Freidberg [1].	7
1.5	This figure shows the disparate range of length and time scales that exist in a typical nuclear fusion plasma. The length scales (from small to large) are: electron Debye length, electron gyroradius, ion gyroradius, reactor size and ion mean free path. The time scales (from short to long) are: inverse electron plasma frequency, inverse electron cyclotron frequency, inverse ion cyclotron frequency, inverse ion-sound frequency and the energy confinement time. The dynamics at each scale along with the interaction between different scales makes this a truly multiscale physics problem.	8
1.6	This figure illustrates the main idea of the gyrokinetic model. In (a), we have a fully kinetic model showing a charged particle rapidly gyrating about a magnetic field line. The time scale (Ω_s^{-1}) and length scale (ρ) on which the particle gyrates are much smaller that time and length scale of its motion along the field line. Due to the separation of these scales, in (b), we average over the fast gyromotion and replace the particle with a ring of charge moving along the field line.	9
1.7	This figure illustrates (a) a typical growth rate spectrum one obtains from solving the linear gyrokinetic equation and (b) the heat flux Q as a function of time for a particular wavenumber k_y . The red line marks the time averaged value of Q	10

2.1	This figure illustrates the two important coordinate systems used in this thesis — (a) shows the cylindrical coordinate system (R, ϕ, Z) and the orientation of a tokamak inside it. The center of the torus (marked with a red dot) is called the magnetic axis. In (b) we present the PEST coordinate system (ψ, θ, ϕ) at a constant- ϕ cross-section of the tokamak. The cross section shows the constant- ψ contours (in black) and open constant- θ contours (in blue).	16
2.2	This figure plots the inputs to the VMEC code for the DIII-D-like design: the pressure, rotational transform as a function of the normalized toroidal flux s , and cross-section of the boundary.	21
2.3	This figure plots the inputs to the VMEC code for the modified NCSX design: the pressure, rotational transform as a function of the normalized toroidal flux s , and cross-section of the boundary. Notice the large negative shear until $s \approx 0.85$.	22
2.4	This figure plots the inputs to the VMEC code for the modified Henneberg-QA design: the pressure, rotational transform as a function of the normalized toroidal flux s , and cross-section of the boundary. Notice the large negative shear in the inner-core region.	23
2.5	This figure illustrates the main idea of the ideal MHD energy principle. For a given equilibrium, if a perturbation ζ makes $\delta W < 0$, the equilibrium unstable to that perturbation. If ζ makes $\delta W > 0$, the equilibrium is stable to that perturbation. Finally, if $\delta W = 0$, the equilibrium is marginally stable.	26
2.6	In this figure we present (a) comparison between the gradients of eigenvalue $\widehat{\lambda}_{\alpha_t} = \partial \widehat{\lambda} / \partial \alpha_t$ and $\widehat{\lambda}_{\theta_0} = \partial \widehat{\lambda} / \partial \theta_0$ obtained using a finite difference scheme against ones obtained using an adjoint method. The quantity <i>iter</i> is the number of iterations taken by the local optimizer on a flux surface before finding $\widehat{\lambda}_{\max}$. The gradients match well for around four orders of magnitude. The discrepancy between the adjoint and finite difference $\widehat{\lambda}_{\alpha_t}$ is due to the finite resolution of the VMEC run. In figure (b), we illustrate the the different grids used to calculate the gradient of the eigenvalue $\widehat{\lambda}$ on a flux surface. A finite difference scheme requires four points whereas an adjoint method only requires one point. This gives us a four times speed-up.	38
2.7	This figure shows the typical process of finding the globally maximum eigenvalue $\widehat{\lambda}_{\max}$ on the flux surface $s = 0.77$. We start by first finding the maximum $\widehat{\lambda}$ on discrete grid of α_t and θ_0 . From the maximum discrete $\widehat{\lambda}$, we search for the global maximum eigenvalue using a local optimizer. In the inset, we show the approximate path taken by the optimizer to reach the $\widehat{\lambda}_{\max}$.	40
2.8	This figure shows the plots of $\widehat{\lambda}_{\max}$ against the normalized toroidal flux s for the three chosen equilibria. Note that the ideal ballooning growth rate $\gamma_{a_N} / v_A = \sqrt{\widehat{\lambda}}$ so $\widehat{\lambda}_{\max} = 0.008$ corresponds to the normalized growth rate $\gamma_{a_N} / v_A = 0.09$ which is not a small value.	40
2.9	This figure shows (a) the maximum eigenvalue $\widehat{\lambda}_{\max}$ of the initial and optimized DIII-D-like equilibrium. The optimized equilibrium is stable. In figure (b), we present the boundary shape of the initial and final equilibria. Note the negative triangularity of the initial equilibrium and the positive triangularity of the optimized equilibrium.	45

2.10	This figure shows (a) the maximum eigenvalue $\widehat{\lambda}_{\max}$ of the initial and optimized modified NCSX equilibrium. Similarly, in (b) we compare the rotational transform profiles of the initial and optimized equilibria. In (c), we present the boundary shape of the initial and final equilibria at three different value of the toroidal angle ϕ . The dotted curves correspond to the initial cross-sections whereas the solid curves are the final cross-sections.	47
2.11	This figure shows (a) the maximum eigenvalue $\widehat{\lambda}_{\max}$ of the initial and optimized modified Henneberg-QA equilibrium. Similarly, in (b) we compare the rotational transform profiles of the initial and optimized equilibria. In (c), we present the boundary shape of the initial and final equilibria at three different positions of the toroidal angle ϕ . The dotted curves correspond to the initial cross-sections whereas the solid curves are the final cross-sections.	49
3.1	This figure shows (a) the output from a typical electrostatic GS2 run showing the normalized frequency and growth rate spectrum with both electron-gradient- ($\omega a_N/v_{\text{th},i} < 0$) and ion-gradient-driven ($\omega a_N/v_{\text{th},i} > 0$) instabilities and (b) showing the variation along the field line of the square of the normalized electrostatic potential $ \varphi ^2$. We can see that the potential is well resolved and decays sufficiently before reaching the boundaries.	62
3.2	This figure summarizes the idea of Greene and Chance. The new pressure profile (black) with localized variation over the flux surface $\psi = \psi_0$ lies over the equilibrium profile (dashed red). Although the variation in pressure at $\psi = \psi_0$ is small, the change in pressure <i>gradient</i> can be large.	64
3.3	This figure shows the safety factor and normalized pressure profiles used for creating the equilibria. The two red lines correspond to the values of the normalized radius ρ at which the local equilibria will be analyzed for their stability.	67
3.4	This figure shows the flux surfaces for all equilibria generated using VMEC. The local equilibria that will be studied in this paper are highlighted in red. The magnetic axis in each figure is the black cross.	69
3.5	This figure shows two high- β equilibria and their corresponding best-Miller-fit. We can see that the fit for the negative triangularity is worse due to the “squareness” of the flux surface on the inboard side. The agreement between gradients of various physical quantities will be even worse.	69
3.6	This figure illustrates the definition of θ_{geo} . The coordinates of the magnetic axis, marked with a cross, are $(R_{\text{ax}}, Z_{\text{ax}})$	74
3.7	This figure explains the physical meaning of the local magnetic shear with (a) showing a typical local shear plot of negative triangularity equilibria at the nominal $\hat{s} = 0.45$ and nominal α_{MHD} values at $\rho = 0.8$ for different beta values and a low- β shifted-circle model (abbreviated SC). On the right side (b) illustrates a modified interpretation from Antonsen and Drake [2] explaining the concept of local magnetic shear. Negative local shear twists the turbulent eddies more than positive or zero local shear in the region of bad curvature, stabilizing the ITG mode.	75

3.8	This figure shows (a) the change in the local shear for $\text{fac} = 4$ (increased pressure gradient). The local shear is much more negative with an approximately linear dependence with fac on outboard side. On the other hand, (b) shows the comparison between the ITG driving term η and the pressure gradient scaling factor fac . The term η is calculated using the values given in table 3.5. We can see that η grows linearly, but with a larger pre-factor. These figures illustrate how the ITG driving term grows more rapidly than the stabilizing local shear as we increase the pressure gradient.	75
3.9	These plots show the ITG $\max(\gamma a_N/v_{\text{th},i})$ (over $k_y \rho_i \in [0.05, 2]$) vs the typical β for nominal equilibria at different radial locations.	76
3.10	This figure shows the ITG $\max(\gamma a_N/v_{\text{th},i})$ plots for positive triangularity equilibria against the temperature gradient length scale. For the high- β equilibria, ITG is stabilized at both $\rho = 0.5$ and $\rho = 0.8$. The rightmost figures in each row are the local magnetic shear vs the geometric theta θ_{geo} at the nominal $dp/d\rho$ and \hat{s} . The grey line corresponds to the local shear for a low- β shifted-circle equilibrium (abbreviated SC). The magnetic shear \hat{s} is the same for all the equilibria at every ρ	77
3.11	shows the ITG $\max(\gamma a_N/v_{\text{th},i})$ plots for negative triangularity equilibria. For the high- β equilibria, ITG is stabilized at both $\rho = 0.5$ and $\rho = 0.8$. The local shear for the high- β equilibria is negative over the whole outboard side. The grey line corresponds to the local shear for a low- β shifted-circle equilibrium (abbreviated SC).	78
3.12	This figure shows the precession drift in (a) and the corresponding magnetic field magnitude in (b) for negative triangularity equilibria at $\hat{s} = 0.45$ and nominal α_{MHD} values at $\rho = 0.8$ for different beta values. Note the atypical magnetic field for the high- β equilibria where $\min(B)$ is located at a finite θ	82
3.13	This figure shows the TEM $\gamma_{\text{TEM}}(a_N/v_{\text{th},i})$ vs the typical β plots for nominal equilibria at different radial locations.	83
3.14	This figure presents $\gamma_{\text{TEM}}(a_N/v_{\text{th},i})$ plots for positive triangularity equilibria and the electron precession drifts at the nominal pressure gradient. For the high- β equilibria, TEM is stabilized at both $\rho = 0.5$ and $\rho = 0.8$. As you can see in figures 3.14(c) and 3.14(f), the precession drift for the high- β equilibria is negative for all values of the bounce angle θ_b	84
3.15	This figure presents $\gamma_{\text{TEM}}(a_N/v_{\text{th},i})$ plots for negative triangularity equilibria. For the high- β equilibria, TEM is stabilized at both $\rho = 0.5$ and $\rho = 0.8$. The rightmost plots on each row is the electron precession drift frequency.	85
3.16	This figure shows comparison between the electrostatic (abbreviated ES) and electromagnetic (abbreviated EM) growth rates for all the nominal positive triangularity equilibria. Some of the branches have been labeled by their corresponding mode names. Notice the KBM in the intermediate and high- β equilibria in figures (3.16)(e) and (3.16)(f), respectively and the emergence of the collisionless-micro-tearing and electromagnetic-ETG modes in figure (3.16)(c) for all values of $k_y \rho_i$ and figures (3.16)(e) and (3.16)(f) for $k_y \rho_i > 1$	87

3.17	This figure shows comparison between the electrostatic (ES) electromagnetic (EM) growth rates for all the nominal negative triangularity equilibria. The sudden jump in figure (f) around $k_y \rho_i = 4.5$ is a different branch of the collisionless MTM. Note also that the growth rate around $k_y \rho_i = 0$ in figure (e) goes to fixed value of $\gamma a_N / v_{th,i} = 0.152$ since the equilibrium is unstable to the ideal ballooning mode.	88
3.18	This figure plots the inputs to the VMEC code for the LBD QA design: the pressure, rotational transform as a function of the normalized radius ρ , and cross-section of the boundary. The red lines mark the radii $\rho = 0.5$ and $\rho = 0.8$, locations at which we perform the gyrokinetic analysis.	91
3.19	This figure compares the normalized electrostatic and electromagnetic growth rates for the LBD QA equilibria. In figures 3.19(a) and (b) we plot the electrostatic and electromagnetic growth rates, respectively at $\rho = 0.5$. In figures 3.19(c) and (d), we do the same for $\rho = 0.8$. Note that due to strong shaping of stellarators, we also scan in the ballooning parameter θ_0	92
3.20	This figure plots the inputs to the VMEC code for the LBD QH design: the pressure, rotational transform as a function of the normalized radius ρ , and cross-section of the boundary. The red lines mark the radii $\rho = 0.5$ and $\rho = 0.8$, locations at which we perform the gyrokinetic analysis.	93
3.21	This figure compares the normalized electrostatic and electromagnetic growth rates for the LBD QH equilibria. In figures 3.21(a) and (b) we plot the electrostatic and electromagnetic growth rates, respectively at $\rho = 0.5$. In figures 3.21(c) and (d), we do the same for $\rho = 0.8$. Note that due to strong shaping of stellarators, we also scan in the ballooning parameter θ_0	94
3.22	This figure shows the normalized growth rate $\gamma a_N / v_{th,i}$ contours along with the curve of marginal stability (white line) for the positive triangularity equilibria. The columns correspond to the low, intermediate and high- β regimes, respectively. The nominal equilibrium value is given by the green cross. The difference between the growth rates from the low and high- β equilibria is due to our choice of normalization in (3.63).	98
3.23	This figure shows the normalized growth rate contours along with the marginal stability curve for the negative triangularity equilibria. The nominal equilibrium value is denoted by the green cross.	99
3.24	This figure shows the maximum ideal ballooning eigenvalue $\hat{\lambda}_{max}$ as a function of the radial location ρ . In figure 3.24(a) we plot $\hat{\lambda}_{max}$ for the LBD QA equilibrium and in figure 3.24(b) we plot $\hat{\lambda}_{max}$ for the LBD QH equilibrium.	101
4.1	This figure shows the flow chart explaining how the MicroStOpt framework operates. The dashed gray box denotes the flow of logic inside an optimizer. The red box indicates work in progress as we are still testing nonlinear, electromagnetic GX.	107
4.2	This figure shows the scan of the objective function \mathcal{F} with respect two boundary Fourier modes $\hat{R}_b(0, 1)$ and $\hat{R}_b(0, 2)$. In figure (a), we observe a case where the most unstable mode does not change leading to a smooth \mathcal{F} . However, noisy behaviour in figure (b) is because the mode corresponding to the maximum gamma changes as we change RBC(0, 2).	109

4.3	This figure plots the initial and optimized rotational transform and cross sections in the top row. In the bottom row, it shows the the ideal ballooning eigenvalue in figure 4.3(c) and the KBM growth rate in figure 4.3(d). Using MicroStOpt, we are able to stabilize the ideal ballooning mode and reduce the KBM growth rate by a factor of three.	111
4.4	This figure shows the initial profiles and boundary shape of a high- β stellarator equilibrium. Note that the pressure and rotational transform profiles are the same as the LBD QH equilibrium. However, the boundary is different which makes this equilibrium non-quasisymmetric.	112
4.5	This figure shows the initial and final cross-section of the high- β stellarator equilibrium in figure 4.5(a). In figures 4.5(b) and (c), we present the ideal ballooning eigenvalue and KBM growth rates of the initial and optimized equilibrium. MicroStOpt is able to stabilize the initial equilibrium.	113
A.1	This figure shows the “plateau” plot created using a homotopy analysis method. Over the plateau region, the eigenvalue $\hat{\lambda}$ changes minimally with respect to the homotopy parameter c_0 . This indicates convergence of the homotopy solution.	127
A.2	This figure shows a comparison between the initial guess of the eigenfunction \hat{X}_0 and the final converged solution to the ideal ballooning equation. For this case, we solved the homotopy equation up to the 20 th order.	127
B.1	This figure illustrates the local orthogonal coordinate system $(\tilde{\rho}, \phi, l_p)$. The radial distance $\tilde{\rho}$ is measured in the direction normal to a flux surface and poloidal arc length l_p is measured in a counter-clockwise sense from the outboard side. We choose $\nabla\psi_p$ to point in the direction opposite to $\nabla\tilde{\rho}$	131
B.2	This figure shows contours of the ballooning eigenvalue $\hat{\lambda}$ in figure (a) for the original set of coefficients, figure (b) after flipping the sign of gds21 without changing other coefficients, and in figure (c) after flipping the sign of cvdrift0 while keeping other coefficients fixed. For incorrect signs of cvdrift0 or gds21, the $\hat{\lambda}$ increases with θ_0 for every α_t , which is incorrect. This can be used as a test for the geometric coefficients in a local simulation. Note the symmetry of $\hat{\lambda}$ in figures (b) and (c) which is a consequence of the stellarator symmetry of NCSX.	139
C.1	This figure illustrates the process of creating the two regions of the $\beta \sim 1$ solution in Hsu <i>et al.</i> The bold black line is the LCFS and the red line is the flux surface contour — (a) shows the core solution (C.3) which is only a good approximation on the inboard side of the device and (b) shows the boundary layer solution (C.4) which is only valid in the boundary layer region. The inset in the right figure highlights the approximation $\xi(\hat{R}, R) = \xi(\hat{R}, R_{\text{boundary}})$ which is necessary to construction the boundary layer solution (C.4).	143
C.2	This figure shows (a) the numerical equilibrium solution and (b) a comparison between the analytical equilibrium from figure 6 in the paper by Hsu <i>et al.</i> [3] and the same equilibrium generated using VMEC. The significant deviation of the analytical solution is evident, as well as how it develops a kink near the outboard side as we approach the magnetic axis.	144

C.3	<p>In this figure (a) compares $\hat{\kappa}$ vs. θ_{geo} obtained using the analytical equilibrium (in figure 6) in Hsu <i>et al.</i> with the corresponding VMEC equilibrium for a common flux surface (shown in (b)). The inset plot in (a) shows a zoomed-in version of the same plot near the discontinuity at $\theta_{\text{geo}} = 1.46$. Figure (b) shows the difference in slopes of the tangents at the point of discontinuity, with a zoomed-in version in the inset. Notice also the deviation of $\hat{\kappa}$ in (a) for $\theta_{\text{geo}} > 1.5$. There are other issues like the small sharp feature near $\theta_{\text{geo}} = 1.3$ that we will not delve into. . . .</p>	145
E.1	<p>This figure shows the eigenfunctions at two different $k_y \rho_i$ values from figure 3.17(c). The values in each row have been normalized with $\max(\varphi)$. Notice the opposite parities of the eigenfunctions in the two rows and the extended and highly-oscillatory structure along θ. The eigenfunctions in the upper row correspond to a non-tearing-parity EM-ETG mode whereas the lower row corresponds to a tearing-parity EM-ETG mode. Classifying modes becomes harder for up-down asymmetric equilibria and virtually impossible for non-linear analyses.</p>	148
F.1	<p>This figure shows a comparison between the growth rates and real frequencies obtained from GS2 and GX for a realistic tokamak equilibrium. We have used the GS2 normalization for $v_{th,i}$. Note that with the given resolution, GX can capture the KBM but cannot capture the electron-driven mode around $k_y \rho_i = 1.5$. This should not affect our optimization results as we are only optimizing against the KBM.</p>	162

List of Abbreviations

MHD	Magnetohydrodynamics
QA	Quasiaxisymmetric
QH	Quasihelically symmetric
Dofs	Degrees of freedom
ITG	Ion Temperature Gradient
TEM	Trapped Electron Mode
ETG	Electron Temperature Gradient
KBM	Kinetic Ballooning Mode
MTM	Microtearing Mode
EM-ETG	Electromagnetic Electron Temperature Gradient
LBD	Landreman-Buller-Drevlak
ODE	Ordinary Differential Equation
SHAM	Spectral Homotopy Analysis Method
CFL	Courant-Friedrichs-Lewy
HL	Hermite-Laguerre

Chapter 1: Introduction

In this chapter, we provide a general overview of the ideas presented in this dissertation. In §1.1, we will motivate the advantages of operating in the high- β regime. In the following section, we will briefly explain a simple fluid model known as ideal magnetohydrodynamics (MHD), its properties, and how it is used to generate equilibria and evaluate their stability. In the third section, we will explain a more complex model known as gyrokinetics, a kinetic theory used to calculate the linear microstability of MHD equilibria. We will also explain why linear gyrokinetic stability is important and how it is directly related to heat and particle losses from a fusion device. In the last section, we will provide an overview of some of the open problems in high- β stability optimization and explain in detail the scope of this dissertation.

1.1 Motivation

Magnetic confinement is currently considered the most promising way [4] to achieve the United States' goal of building a pilot fusion power plant that generates net electricity before 2040 [5]. The biggest joint international project, ITER [6] also plans to demonstrate net fusion power gain using a magnetic confinement scheme. Most advanced fusion reactor designs today are based on two main designs that use magnetic confinement: tokamaks and stellarators. These devices work by using strong magnetic fields to keep a hot, dense plasma at their center. At high

plasma pressures and temperatures ($\sim 10^8 K$) the ions overcome the repulsive Coulomb force and fuse together to release energy. The fusion reaction for a Deuterium-Tritium plasma is



which combines the (charged) nuclei of deuterium and tritium and yields an alpha particle and a fast neutron. Fast neutrons are then captured by a physical barrier (known as a neutron blanket), and the resulting heat can be used to produce electricity. Fusion plasma comprises a high-temperature ionized gas of charged particles. To be able to confine these charged particles we require a specific topology of the magnetic field. For example, simply closing the field lines in a loop, as in a Z-pinch will not confine the particles, as they will drift perpendicular to the field line due to the curvature of the field line as shown in figure 1.1. It was hypothesized by Andrei

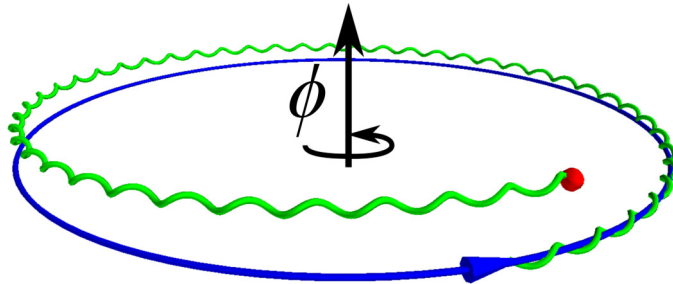


Figure 1.1: This figure shows the trajectory of a positively charged particle in a divergence free equilibrium field $B_\phi \propto 1/r$, where r is the radial distance from the center. The blue line represents a magnetic field line. The particle drifts vertically upwards and is deconfined. A negatively charged particle would drift downwards.

Sakharov [7] and Igor Tamm and independently by Lyman Spitzer Jr. [8] that to prevent particles from drifting out of the machine, magnetic field lines must twist in the form of a torus as shown in figure 1.2. Once twisted, the particles following these field lines, on average, have zero radial

displacement¹. The long way around the torus is called the toroidal direction, denoted by the

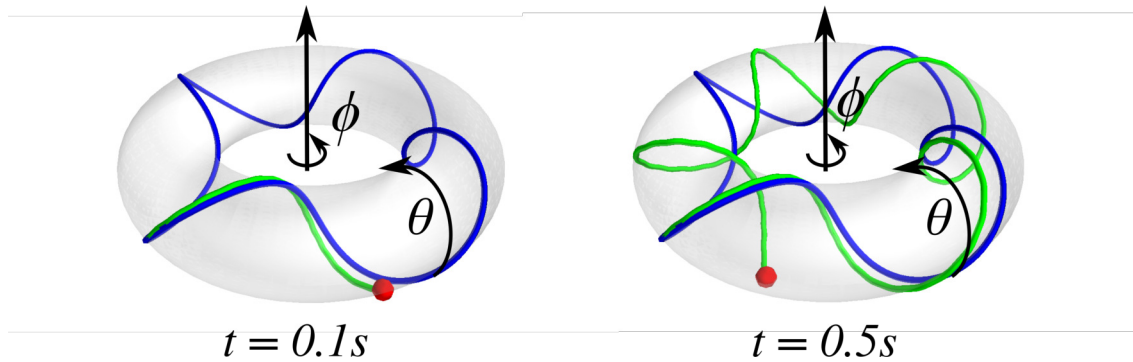
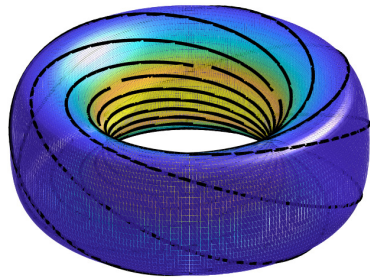


Figure 1.2: This figure shows the trajectory of a particle at two different times in an equilibrium where magnetic field lines lie on a toroidal surface. The particle is launched from the blue-colored field line. Due to the twist of the magnetic field in the θ direction, the particle is confined to the toroidal surface.

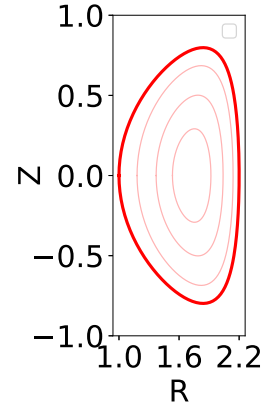
coordinate ϕ , while the short way round is called the poloidal direction, denoted by the coordinate θ . The toroidal field can be created by electromagnets. To create the poloidal field, i.e., the twist, one could induce a toroidal current throughout the plasma using a solenoid or break the symmetry of the device in the toroidal direction, shaping the walls in such a way that they cause the field lines to twist without the help of a solenoid. The former idea, conceptualized by Tamm and Sakharov [9], is called a tokamak, and the latter idea, conceptualized by Spitzer [8], is called a stellarator. The toroidal surface on which magnetic fields lie will be referred to as a flux surface.

Figure 1.3 shows the tokamak and stellarator equilibria that will be studied in chapter two of this thesis.

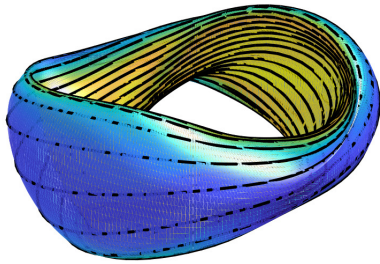
¹Note that this is only true for passing particles, i.e., particles that move fast enough along a field line to complete a full toroidal turn. Particles that are trapped between two toroidal angles are eventually deconfined in an unoptimized stellarator.



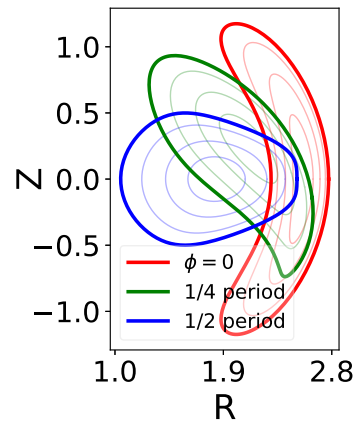
(a) DIII-D $|B|$



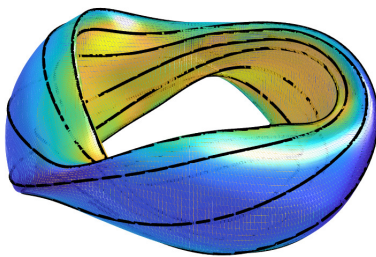
(b) DIII-D cross-section



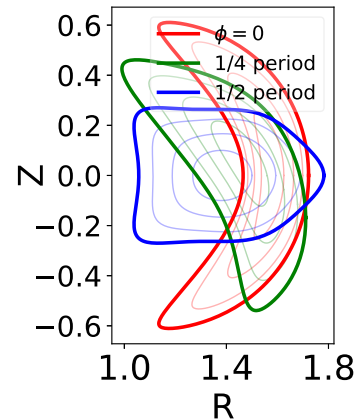
(c) Henneberg-QA $|B|$



(d) Henneberg-QA cross-section



(e) NCSX $|B|$



(f) NCSX cross-section

Figure 1.3: This figure shows the strength of the magnetic field $|B|$ on a flux surface and the cross section at various toroidal and radial locations for an axisymmetric equilibrium and two 3D equilibria. The cross sections are plotted in cylindrical coordinates (R, ϕ, Z) . The number of repeatable toroidal segments or field periods n_{fp} is 1 for DIII-D, 2 for Henneberg-QA, and 3 for NCSX.

The main difference between tokamaks and stellarators lies in their geometric shape. Tokamaks are symmetric about a fixed axis, whereas stellarators are not. The tokamak equilibria are 2D-axisymmetric, as they have a continuous symmetry in the toroidal direction, whereas stellarator equilibria are 3D. Note that, in general, stellarator equilibria have discrete symmetry in the toroidal direction since one can always divide a stellarator toroidally into multiple identical segments. The number of identical segments in a stellarator is known as the field period nfp . Moreover, all the stellarator designs analyzed in this work have stellarator up-down symmetry — at any point on the stellarator $R(\theta, \phi) = R(-\theta, -\phi)$ and $Z(\theta, \phi) = -Z(-\theta, -\phi)$, where (R, ϕ, Z) is the cylindrical coordinate system. However, if optimized, stellarators can also achieve a continuous hidden symmetry known as quasisymmetry [10, 11], where the strength of the magnetic field $|\mathbf{B}|$ does not change along the field line with respect to one of the coordinates. Quasisymmetry is a powerful favorable property because it ensures orbit confinement of both trapped and passing particles, which helps improve energetic particle confinement, a major issue in stellarators.

Since tokamaks require an internal current to twist the field lines, they are vulnerable to instabilities caused by that current. However, stellarators do not need a large internal current and are usually free of current-driven instabilities. Another important difference is the design. As tokamaks are axisymmetric, they are easier to build, whereas stellarator engineering designs are more complicated [12, 13]. In this thesis, we will use two simplified models to study physics problems that are common to both tokamaks and stellarators.

1.2 Two self-consistent models of fusion plasmas

The particle confinement model presented in the previous section to explain magnetic confinement is overly simplistic, as we assume that particles travel in a fixed magnetic field. However, in reality, there are enough charged particles in a fusion plasma ($\sim 10^{20} m^{-3}$) to create their own electromagnetic fields that can significantly alter their dynamics. To self-consistently consider the effect of the fields on the particle and vice versa, we solve mathematical models that vary in their levels of complexity and accuracy. In the following sections, we describe two such models: ideal MHD and gyrokinetics.

1.2.1 Ideal MHD

One of the simplest models used to study a plasma is ideal MHD. This model assumes that the plasma behaves like a single, perfectly-conducting, fluid. The tokamak and stellarator equilibria presented in figure 1.3 are obtained by numerically solving the steady state ideal MHD equations numerically. To assume that the plasma acts like a fluid, ideal MHD assumes that the plasma is strongly collisional. But even though ideal MHD is only valid in the limit of a highly collisional plasma, we will use it to calculate steady-state tokamak and stellarator equilibria as it will separate the non-ideal effects from our study. These non-ideal effects such as magnetic islands, neutral beam injection, wave heating etc. are important but ignored in this work. The most important property of the ideal MHD model is that plasma is perfectly confined perpendicular to a magnetic field line. This is known as the “frozen-in” condition. Figure 1.4 illustrates the “frozen-in” condition.

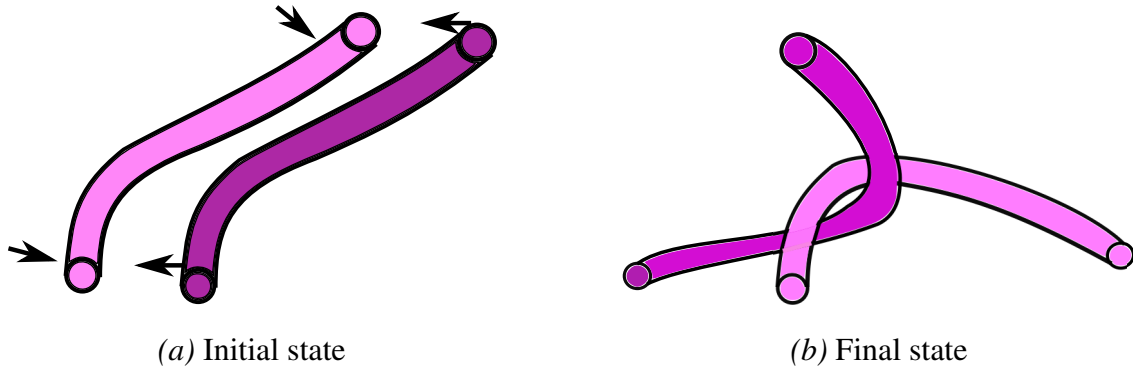


Figure 1.4: This figure illustrates the “frozen-in” condition of ideal MHD. The tubes represent magnetic field lines containing plasma (colored purple). The “frozen-in” condition prohibits the tubes from passing through each other. This topological constraint allows 3D toroidal equilibria to retain their nested flux surface topology in figure 1.3. A short and intuitive derivation of the “frozen-in” condition is given in chapter 3 of Freidberg [1].

The existence of an MHD equilibrium does not guarantee its stability. Therefore, the next step is to perform an ideal MHD stability analysis. There are multiple classes of ideal MHD instabilities driven by pressure and current [14]. In this dissertation, we focus on an important pressure-driven instability, called the infinite- n ideal ballooning mode [15, 16]. For tokamaks, the ideal ballooning mode sets a hard threshold on the plasma β . For stellarators, the stability conditions of the ideal ballooning mode are closely correlated with a type of kinetic instability called the kinetic ballooning mode (KBM). The KBM is thought to limit performance of stellarators. Therefore, stabilizing the equilibria against the ideal MHD instability is an important step before studying additional effects with more sophisticated models.

Ideal MHD is the simplest model to describe a fusion plasma. But due to its simplicity, we miss a lot of important effects, especially the effects dependent on smaller length scales. In a more general model of a fusion plasma, we must also include dynamics that occur at different length and time scales, as shown in figure 1.5.

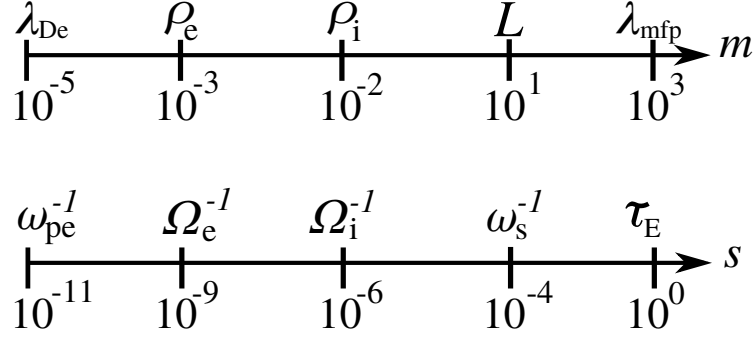


Figure 1.5: This figure shows the disparate range of length and time scales that exist in a typical nuclear fusion plasma. The length scales (from small to large) are: electron Debye length, electron gyroradius, ion gyroradius, reactor size and ion mean free path. The time scales (from short to long) are: inverse electron plasma frequency, inverse electron cyclotron frequency, inverse ion cyclotron frequency, inverse ion-sound frequency and the energy confinement time. The dynamics at each scale along with the interaction between different scales makes this a truly multiscale physics problem.

To account for the smaller-scale effects, we study kinetic models of fusion plasmas. One of the most successful kinetic models in fusion plasma physics [17] the gyrokinetic model. We will present the details of this model in the next section.

1.2.2 The gyrokinetic model

One of the most general models used to study fusion plasmas is the gyrokinetic model. This model, unlike ideal MHD, treats both ions and electrons as separate species represented by distribution functions in velocity and configuration space. The gyrokinetic model is a simplification of a fully kinetic model (6+1)D model (three configuration space dimensions, three velocity space dimensions, and time), due to the fact that particles gyrate perpendicular to a field lines much faster and on much smaller scales than the time and length scales along a field line. This allows us to average over the gyration of the charged particles leaving us with a (5+1)D model (three configuration space dimensions, two velocity space dimensions, and time). Figure 1.6 illustrates

the reason for reducing the velocity space dimension in a gyrokinetic model.

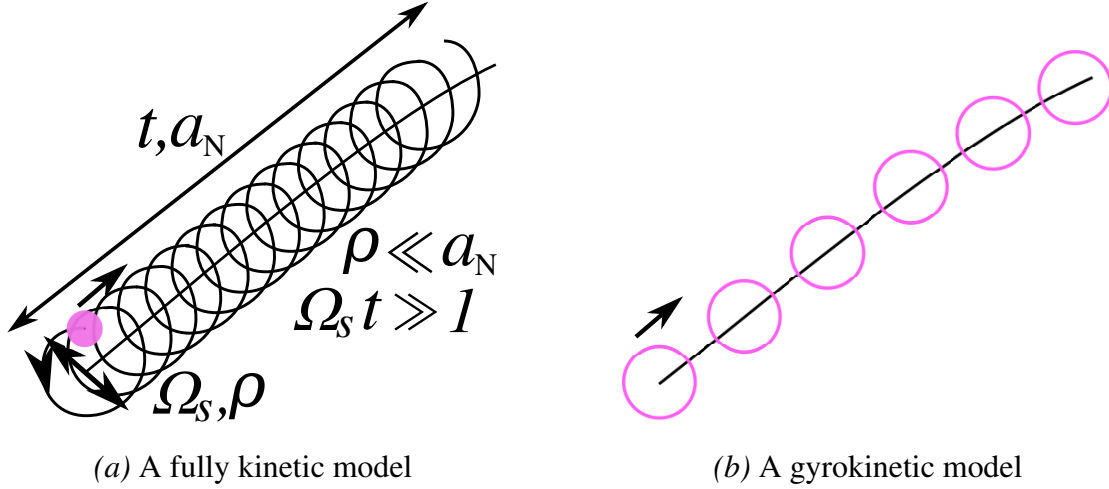


Figure 1.6: This figure illustrates the main idea of the gyrokinetic model. In (a), we have a fully kinetic model showing a charged particle rapidly gyrating about a magnetic field line. The time scale (Ω_s^{-1}) and length scale (ρ) on which the particle gyrates are much smaller than time and length scale of its motion along the field line. Due to the separation of these scales, in (b), we average over the fast gyromotion and replace the particle with a ring of charge moving along the field line.

Kinetic instabilities are not as deleterious as MHD instabilities, since they do not lead to disruptions, but are directly related to anomalous/turbulent diffusion which significantly increases the heat flux (Q) and particle flux (Γ) out of the plasma. This reduces the plasma pressure throughout the volume, reduces the output fusion energy, and reduces the device efficiency. Once an equilibrium has been optimized against MHD instabilities, the next step is usually to reduce turbulent diffusion so that a steep pressure profile can be maintained with practical heat sources. Gyrokinetics has been remarkably successful in predicting the heat and particle transport for realistic tokamaks and stellarators, especially in the core of a fusion plasma [18]. However, to calculate these transport rates, we have to numerically solve the nonlinear gyrokinetic model, which is computationally expensive and time consuming. The computational cost is even higher for a general stellarator equilibrium because of its lack of continuous symmetry.

In light of the cost of nonlinear analyses, one usually solves the linear gyrokinetic equation and analyzes the growth rate spectrum; a measure of a linear instability for different modes of perturbation of the equilibrium state. This is much faster and can be used as a proxy for nonlinear heat and particle loss. For a growth rate γ , calculated as a function of the fluctuation wavenumber k_y , a simple random walk estimate of the diffusion coefficient [19] gives

$$D \sim \frac{\gamma}{k_y^2}, \quad (1.2)$$

which means that, in general, low-wavenumber modes cause the most heat and particle transport². Figure 1.7 illustrates the typical growth rate spectrum and the heat flux time trace that one obtains from a gyrokinetic simulation. Note that the linear growth rates can be calculated with remarkable precision and accuracy, but the non-linear heat fluxes Q always have some statistical variation that depends strongly on the domain size, initial conditions, velocity and configuration space resolution and affects the precision of Q .

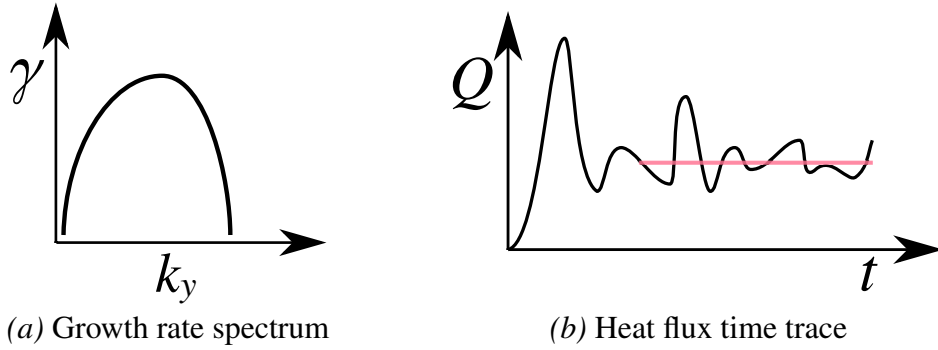


Figure 1.7: This figure illustrates (a) a typical growth rate spectrum one obtains from solving the linear gyrokinetic equation and (b) the heat flux Q as a function of time for a particular wavenumber k_y . The red line marks the time averaged value of Q .

²Note that this is a qualitative estimate of the diffusion coefficient. One must always run the complete non-linear solver to obtain the exact relationship diffusivity.

1.3 Unsolved problems in stability optimization and scope of this work

Recent advances in stellarator optimization techniques and computational capabilities have allowed physicists to find new designs that have many favorable properties such as quasisymmetry, low neoclassical transport, simpler coil shapes, reduced magnetic island widths, etc. These developments have led to an increased interest in optimizing stellarators. However, only a few recent publications have considered optimization against kinetic instabilities [20, 21, 22]. Moreover, there have been no studies that include all the kinetic effects such as self-consistent electromagnetic fluctuations, particle collisions, finite velocity shear into account. Thus, as we move towards the design of a realistic high- β stellarator, it is imperative to include a fully kinetic microstability analysis into the typical optimization loop.

Moreover, these optimization tools can be easily extended to optimize tokamaks, and even though the parameter space for tokamaks is much smaller due to axisymmetry, this could help us learn more about stability of tokamaks and derive trends, which can then be extended to stellarators. In the past, some optimization work has been performed against low- n ideal MHD modes but a freely available, general, MHD and kinetic optimizer does not exist. To that end, we will present a framework for developing a general ideal MHD and kinetic stability optimizer for tokmaks and stellarators.

In chapter 2, we will explain in detail how to use the ideal MHD model to calculate a set of 2D-axisymmetric and 3D equilibria. Next, we present a linear stability analysis, derive the ideal MHD energy principle and describe how it gives instabilities with different toroidal mode number n , i.e., low- n and high- n modes. We will solve the infinite- n ideal ballooning equation for the equilibria described in the previous sections. Using the self-adjoint property of ideal

MHD, we then construct a technique to calculate the gradient of the growth rate and demonstrate this technique by stabilizing equilibria against the infinite- n ideal ballooning mode.

In chapter 3, we will linearize the complete electromagnetic, gyrokinetic model and solve it for a set of high- β tokamak and stellarator equilibria. For the tokamak equilibria, we will self-consistently scan these equilibria in the temperature and density gradients to study the effect of high- β on their stability. We will also obtain equilibrium-dependent quantities that can be used to explain the enhanced stability of high- β equilibria against electrostatic instabilities. We present the analysis of the high- β stellarator equilibria and explain how the stability trends are similar to that of high- β tokamaks.

In chapter 4, we combine the tools used and our observations to study ideal MHD and kinetic stability in the previous two chapters to create a general finite- β optimization framework that optimizes a high- β equilibrium against various kinetic instabilities. We explain the details of the optimizer and present some tests done with an axisymmetric high- β equilibrium obtained in chapter 3.

Chapter 2: Ideal MHD stability analysis and optimization of high- β equilibria

2.1 Overview

In this chapter, we will explain in detail the ideal MHD model. We will start by deriving the steady-state ideal MHD force balance equation and show how it can be rewritten for a general toroidal geometry. We will use a numerical solver `VMEC` to solve the force balance equation for one 2D (axisymmetric) and two 3D equilibria. To infer the stability of these equilibria, we will linearize the ideal MHD model and describe the stability problem as a variational principle known as the energy principle. We will then explain useful properties of the energy principle and categorize it based on the toroidal mode number n .

To obtain the pressure gradient-driven instability known as the ideal ballooning mode, we will simplify the energy principle in the limit of infinite toroidal mode number, explain how the energy principle can be reduced to a simple ODE called the ideal ballooning equation, and argue for the importance of stabilizing this mode in tokamaks and stellarators. We proceed to solve this equation for the three equilibria described in §2.2.1. Finally, using the self-adjoint property of ideal MHD, we will explain the details of optimization of the three equilibria against the ideal ballooning mode and explain how it can be extended to modes with lower mode numbers.

2.2 Ideal MHD: Equilibrium

The simplest model that describes a hot plasma is ideal MHD. Ideal MHD assumes the plasma to behave as a isentropic, perfectly conducting fluid with a mass density ρ , pressure p , flowing with a flow velocity \mathbf{V} immersed in a magnetic field \mathbf{B} . The governing equations are

$$\frac{\partial \rho}{\partial t} + \nabla \cdot (\rho \mathbf{V}) = 0, \quad (2.1)$$

$$\rho \left(\frac{\partial \mathbf{V}}{\partial t} + \mathbf{V} \cdot \nabla \mathbf{V} \right) = -\nabla p + \frac{(\nabla \times \mathbf{B}) \times \mathbf{B}}{\mu_0}, \quad (2.2)$$

$$\frac{\partial}{\partial t} \left(\frac{p}{\rho^\gamma} \right) + \mathbf{V} \cdot \nabla \left(\frac{p}{\rho^\gamma} \right) = 0, \quad (2.3)$$

$$\frac{\partial \mathbf{B}}{\partial t} = \nabla \times (\mathbf{V} \times \mathbf{B}), \quad (2.4)$$

$$\nabla \cdot \mathbf{B} = 0, \quad (2.5)$$

where γ is the ratio of specific heat capacities. In a steady state, i.e., $\partial/\partial t = 0$, with no equilibrium flow, we can rewrite the ideal MHD model as

$$\nabla p_0 = \frac{(\nabla \times \mathbf{B}_0) \times \mathbf{B}_0}{\mu_0} = \frac{\mathbf{B}_0 \cdot \nabla \mathbf{B}_0}{\mu_0} - \nabla \left(\frac{B_0^2}{2\mu_0} \right), \quad (2.6)$$

$$\nabla \cdot \mathbf{B}_0 = 0, \quad (2.7)$$

where p_0 and \mathbf{B}_0 are the equilibrium pressure and magnetic field vector, respectively. The steady-state force balance equation (2.6) represents a balance between plasma pressure, magnetic pressure, and magnetic tension of the magnetic field lines. The divergence-free condition (2.7) is an

additional constraint that must be satisfied by the magnetic field vector throughout the plasma. For a general 3D geometry, this can be achieved by writing the magnetic field in the Clebsch form [23]

$$\mathbf{B}_0 = \nabla\alpha_t \times \nabla\psi_p. \quad (2.8)$$

The form in (2.8) is generally used for tokamak equilibria. For stellarators, we use the following equivalent representation

$$\mathbf{B}_0 = \nabla\psi \times \nabla\alpha_s. \quad (2.9)$$

We will focus on solutions whose magnetic field lines lie on closed nested toroidal surfaces, known as flux surfaces. By taking the component of (2.9) along \mathbf{B}_0 , we get $\mathbf{B}_0 \cdot \nabla p_0 = 0$ which gives $p_0 = p_0(\psi)$, i.e., each surface experiences constant plasma pressure. For tokamaks, we label the flux surfaces with their enclosed poloidal flux ψ_p whereas for stellarators, we use the enclosed toroidal flux ψ . On each flux surface, lines of constant α_t and α_s coincide with the magnetic field lines in tokamaks and stellarators, respectively. Thus, the variables α_t and α_s are known as field line labels.

To facilitate the calculation of various physical quantities from a general equilibrium solver, we use multiple coordinate systems. The first system we will use is the right-handed cylindrical coordinate system (R, ϕ, Z) where R and Z are the radial and vertical distances from the origin and ϕ is the azimuthal angle around the symmetry axis. We also define a curvilinear coordinate system called PEST [24] coordinates (ψ_p, ϕ, θ) where ψ_p is the flux surface label, ϕ is the cylindrical azimuthal angle and θ is the ‘‘straight-field-line’’ poloidal angle [23] such that $\alpha_t = \phi - q(\psi_p)(\theta - \theta_0)$. Similarly, for 3D equilibria, we use the coordinate system (ψ, ϕ, θ) and $\alpha_s = \theta - \iota(\psi)(\phi - \phi_0)$. We illustrate the cylindrical and PEST coordinate systems in figure 2.1.

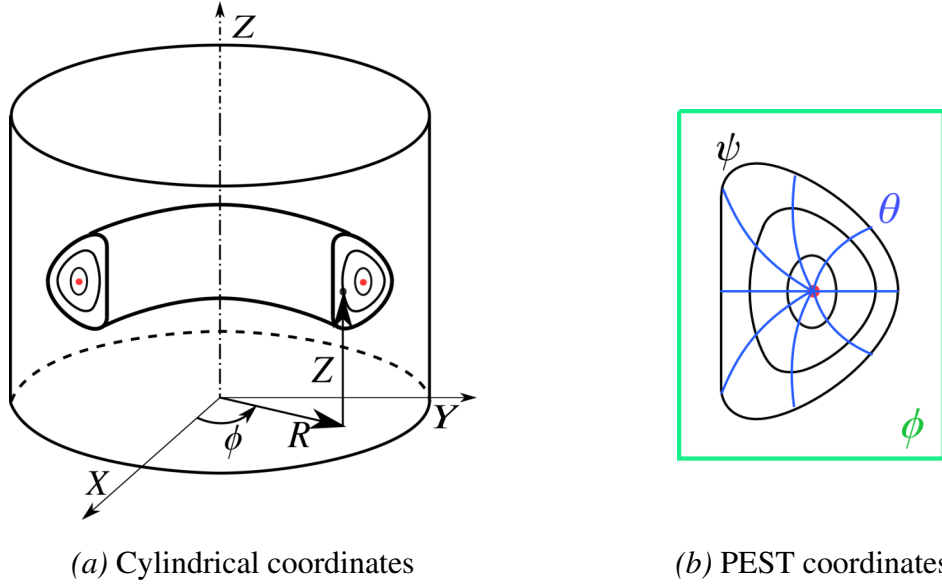


Figure 2.1: This figure illustrates the two important coordinate systems used in this thesis — (a) shows the cylindrical coordinate system (R, ϕ, Z) and the orientation of a tokamak inside it. The center of the torus (marked with a red dot) is called the magnetic axis. In (b) we present the PEST coordinate system (ψ, θ, ϕ) at a constant- ϕ cross-section of the tokamak. The cross section shows the constant- ψ contours (in black) and open constant- θ contours (in blue).

The pitch of the magnetic field line on a flux surface is described by the safety factor

$$q(\psi) = \frac{1}{\iota(\psi)} \equiv \frac{d\psi}{d\psi_p} = \frac{1}{(2\pi)^2} \oint d\phi \oint d\theta \frac{\mathbf{B}_0 \cdot \nabla \phi}{\mathbf{B}_0 \cdot \nabla \theta}, \quad (2.10)$$

where ι , the rotational transform, is the inverse of the safety factor. For axisymmetric equilibria,

$$q(\psi) = \frac{1}{(2\pi)} \oint d\theta \frac{\mathbf{B}_0 \cdot \nabla \phi}{\mathbf{B}_0 \cdot \nabla \theta}. \quad (2.11)$$

Using the Clebsch representation for (2.8) or (2.9) for the magnetic field, finding the equilibrium involves solving a single vector equation (2.6).

For axisymmetric devices, (2.6) can be further simplified. We can use the following form

of the magnetic field

$$\mathbf{B} = \nabla\phi \times \nabla\psi_p + F(\psi, \theta)\nabla\phi, \quad (2.12)$$

substitute it in the $\nabla\phi$ component of (2.6), and use the fact $\partial/\partial\phi = 0$ for all the equilibrium quantities to obtain

$$\frac{\partial F}{\partial\theta} = 0. \quad (2.13)$$

Hence, for an axisymmetric system, $F = F(\psi_p)$. Next, we take a component of (2.6) along $\nabla\psi_p$ and simplify it to obtain the Grad-Shafranov [25, 26] equation

$$\Delta^*\psi_p \equiv R^2\nabla \cdot \left(\frac{\nabla\psi_p}{R^2} \right) = -\mu_0 R^2 \frac{dp}{d\psi_p} - F \frac{dF}{d\psi_p}. \quad (2.14)$$

The Grad-Shafranov equation is a non-linear equation for the poloidal flux $\psi_p(R, Z)$ that depends on the profiles of pressure $p(\psi_p)$ and current $F(\psi_p)$. For simple profiles of p and F , (2.14) can be solved analytically.

For a general 3D system, a reduction used to obtain (2.14) cannot be performed and the two components (2.6) must be solved simultaneously. An analytical equation does not exist for a general 3D system. For stability analyses, solving (2.6) is usually the most expensive step. Therefore, throughout this work, we will use a general numerical equilibrium solver to solve (2.6) for all the ideal MHD equilibria. In the following section, we explain how we use the numerical solver VMEC¹ to obtain both 2D-axisymmetric and 3D equilibria.

¹The main ideas of this work are independent of the equilibrium solver. Our technique will work with any other equilibrium solver.

2.2.1 Numerical equilibria

We generate numerical equilibria using the 3-D equilibrium code VMEC [27]. The code works by minimizing the integral

$$W = \int \left(\frac{p}{\gamma - 1} + \frac{B^2}{2\mu_0} \right) dV, \quad (2.15)$$

Kulsrud and Kruskal [28] have shown that minimizing W , subject to various topological constraints such as existence of nested flux surfaces, constant pressure on each flux surface etc. is equivalent to solving the ideal MHD force balance equation

$$\nabla p = \mathbf{j} \times \mathbf{B}. \quad (2.16)$$

For our study, we used the fixed-boundary mode of VMEC. The fixed-boundary mode takes the shape of the boundary surface denoted by the cylindrical coordinates R_b and Z_b in terms of the Fourier-decomposed poloidal (Θ) and toroidal (ϕ) modes

$$\begin{aligned} R_b &= \sum_n \sum_m \hat{R}_b(m, n) \exp(i(m\Theta - n\phi)), \\ Z_b &= \sum_n \sum_m \hat{Z}_b(m, n) \exp(i(m\Theta - n\phi)), \end{aligned} \quad (2.17)$$

where m and n are integers. We also provide VMEC with the coefficients of the polynomials representing the global radial pressure $p(s)$ and the rotational transform $\iota(s)$ as a function of the normalized toroidal flux $s = \psi/\psi_b$, and the total toroidal flux (ψ_b) or poloidal flux ($\psi_{p,b}$) enclosed by the boundary. The poloidal angle Θ used by VMEC is related to the straight-field-line

θ by the following equation

$$\Theta = \theta + \Lambda(\Theta, \phi), \quad (2.18)$$

where Λ is a monotonic function calculated by VMEC.

For a given boundary shape, pressure, rotational transform, and enclosed toroidal flux, fixed-boundary VMEC then solves for the shapes of the flux surfaces to minimize the integral in (2.15) on each surface for fixed p and ι subject to various topological constraints imposed by the ideal MHD. In a more compact form, VMEC solves

$$\min_{R, Z, \Lambda} W[R, Z, \Lambda; p, \iota, \psi(s=1)], \quad \text{s.t. } R(s=1) = R_b, \quad Z(s=1) = Z_b. \quad (2.19)$$

After running the code, we obtain the shape of the flux surfaces, the magnetic field, and a set of important physical quantities. The characteristic physical quantities that we will use in this work are defined below:

- The total enclosed toroidal flux by the boundary $\psi_b = \int dV \mathbf{B} \cdot \nabla \phi$,
- The normalizing magnetic field $B_N = \psi_b / (\pi a_N^2)$ where $a_N = \sqrt{\mathcal{A}_b / \pi}$ is the effective minor radius and \mathcal{A}_b is the average area enclosed by the boundary, averaged over ϕ for 3D equilibria,
- The ratio of the total plasma pressure to the magnetic pressure on the magnetic axis — the flux corresponding to $s = 0$, $\beta_{ax} = 2\mu_0 p(s=0) / B_N^2$,
- The aspect ratio A and the normalized minor radius a_N of the device,
- The radius of curvature of the boundary $R_c(\theta) = \frac{d^2 R}{dZ^2} / \left(1 + \left(\frac{dR}{dZ} \right)^2 \right)^{3/2}$ where R and

Z are the cylindrical coordinates used to parametrize the boundary,

- The volume-averaged, normalized plasma pressure $\langle\beta\rangle = \int dV \beta / \int dV$ where dV is the differential volume element and $\beta = 2\mu_0 p / B^2$,
- The total enclosed toroidal current $j_\phi = |\int dV (\mathbf{j} \cdot \nabla\phi)|$,
- The volume-averaged magnetic field $\langle B\rangle = \int dV B / V$ where dV is the differential volume element, and
- The mean rotational transform $\bar{\iota} = \int ds \iota / \int ds$.

Using VMEC, we generate three equilibria: an axisymmetric equilibrium with a DIII-D-like boundary shape [29] and two 3D equilibria: modified NCSX [30] and modified Henneberg-QA [31]. In the following sections, we provide important details for each of these equilibria.

In this study, the first equilibrium that we choose is a high- β , axisymmetric, DIII-D-like equilibrium with a negative triangularity boundary — a boundary that looks like an inverted-D. Negative triangularity equilibria have previously been found to have enhanced confinement [29] while avoiding MHD-driven disruptions. Specifically, we choose a negative triangularity equilibrium from [32] where has been shown to be unstable against the ideal ballooning mode. The input pressure, the rotational transform, and the boundary shape profile for this equilibrium are shown in figure 2.2. With this equilibrium as an initial state, we run our ideal ballooning stability optimization to find a stable equilibrium.

The optimizer sometimes tends to find solutions that are ideal MHD stable in a trivial manner. For example, the optimizer may give us a large aspect ratio causing the β to decrease such that it stabilizes pressure-driven instabilities. Sometimes, it may reduce the enclosed toroidal

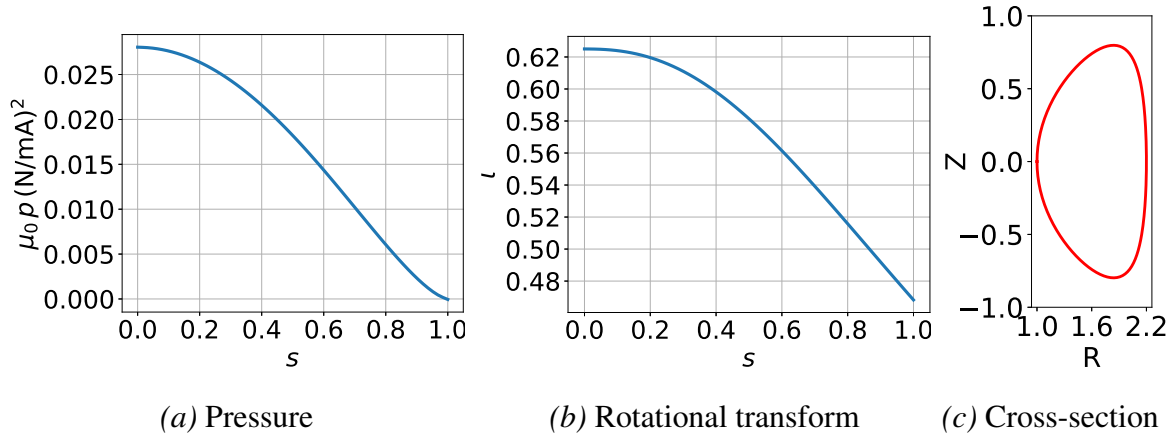


Figure 2.2: This figure plots the inputs to the VMEC code for the DIII-D-like design: the pressure, rotational transform as a function of the normalized toroidal flux s , and cross-section of the boundary.

current to eliminate current-driven instabilities. To avoid these trivial solutions, we have to impose additional constraints on important characteristic physical quantities to prevent them from changing significantly. The values of the relevant physical quantities for this equilibrium are provided in table 2.1. The second equilibrium we select is the 3D equilibrium for the NCSX

$\beta_{\text{ax}}(\%)$	$\langle\beta\rangle(\%)$	$j_\phi(\text{MA})$	$\langle B\rangle(\text{T})$	$\bar{\nu}$	A	$a_N(\text{m})$	$\psi_{\text{LCFS}}(\text{Tm}^2)$
14	7.6	0.616	0.677	0.568	2.42	0.68	1.0

Table 2.1: This table shows the values of relevant physical quantities for the DIII-D like equilibrium.

design [30, 33]. The pressure, rotational transform, and boundary shape profile for this equilibrium are shown in figure 2.3. In tokamaks, magnetic field lines are twisted through an internal toroidal plasma current j_ϕ . On the other hand, in stellarators, the fieldlines are twisted using a non-axisymmetric boundary shape instead of inducing an internal plasma current. The 3D boundary shape alleviates the need for an internal current and eliminates the typical current-driven instabilities known to cause some disruptions in tokamaks. However, because of neoclassical

effects [34, 35], stellarator equilibria can still generate toroidal current. To completely eliminate the need for external current drive (to reduce the internal current, for example), one must ensure that the neoclassically-induced “bootstrap” current [35] is self-consistent with the 3D equilibrium. Since we are not optimizing for a self-consistent bootstrap current, it is essential to ensure that the toroidal current does not have a large value ($\sim 10MA$). Therefore, we include additional constraints in our optimizer to prevent large changes in the toroidal current and other important quantities. The values of these equilibrium-dependent quantities are presented in table 2.2.

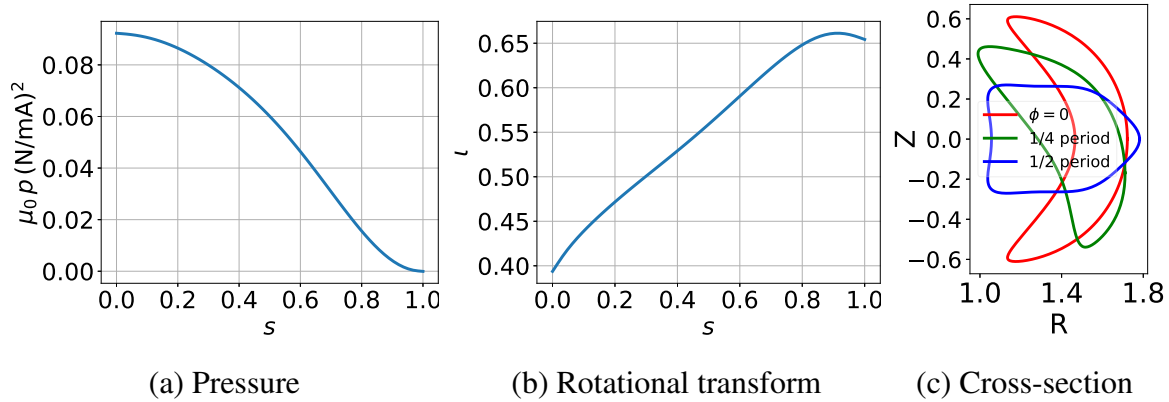


Figure 2.3: This figure plots the inputs to the VMEC code for the modified NCSX design: the pressure, rotational transform as a function of the normalized toroidal flux s , and cross-section of the boundary. Notice the large negative shear until $s \approx 0.85$.

$\beta_{\text{ax}}(\%)$	$\langle\beta\rangle(\%)$	$j_\phi(MA)$	$\langle B\rangle(T)$	$\bar{\nu}$	A	$a_N(m)$	$\psi_{\text{LCFS}}(Tm^2)$
9.38	5.14	0.174	1.59	0.55	4.36	0.32	0.514

Table 2.2: This table shows the values of important physical quantities for the modified NCSX equilibrium.

The final equilibrium we study is the modified Henneberg-QA design [31]. This equilibrium is also designed to have quasisymmetry for a wide variety of pressure profiles. The pressure, rotational transform and boundary shape profile for this equilibrium are shown in figure 2.4.

$\beta_{\text{ax}}(\%)$	$\langle\beta\rangle(\%)$	$j_\phi(\text{MA})$	$\langle B\rangle(\text{T})$	\bar{v}	A	$a_N(\text{m})$	$\psi_{\text{LCFS}}(\text{Tm}^2)$
4.5	2.4	0.235	2.5	0.263	3.37	0.60	2.67

Table 2.3: This table presents values of relevant physical quantities for the modified Henneberg-QA design.

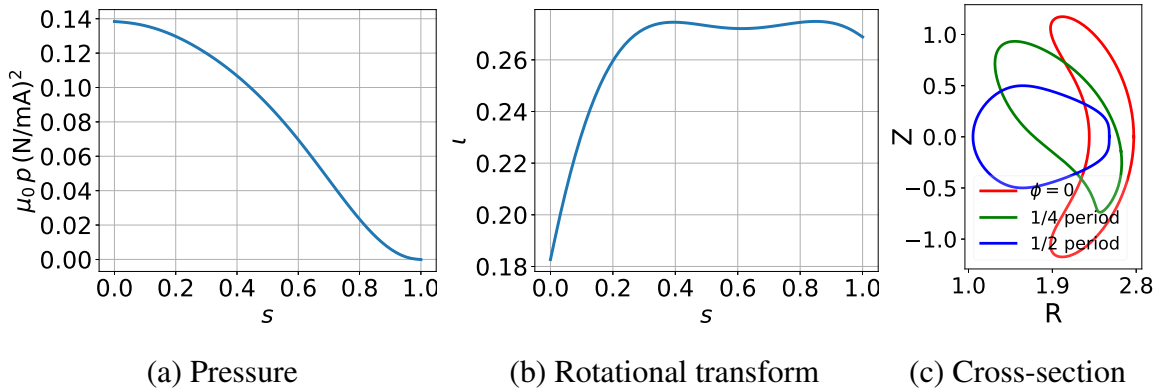


Figure 2.4: This figure plots the inputs to the VMEC code for the modified Henneberg-QA design: the pressure, rotational transform as a function of the normalized toroidal flux s , and cross-section of the boundary. Notice the large negative shear in the inner-core region.

For reasons explained in the previous section, we will impose additional constraints on some of the physical quantities. The values of these equilibrium-dependent parameters that we will use as constraints in §2.4 are presented in table 2.3.

The existence of an MHD equilibrium does not guarantee its stability. Therefore, the next natural step is to perform stability analyses of the three ideal MHD equilibria calculated in this section. We explain our approach and then present our stability analyses in the next section.

2.3 Ideal MHD: Stability

In this section, we will explain how to formulate and analyze the stability of an ideal MHD equilibrium. We will linearize the ideal MHD model about an equilibrium state, subject to an in-

finitesimal displacement of magnetic field lines. We will show that this linearized model gives us a single equation governed by a linear (force) operator and how it can be reduced to a variational principle known as the ideal MHD energy principle [14]. We will then explain how the energy principle can be simplified in the limit of radially localized modes, which gives us a pressure-driven instability, known as the ideal ballooning mode.

To derive the linearized stability equations, we will closely follow chapter 8 of Freidberg [1]. We start by using the ideal MHD equations (2.1)-(2.7), assuming no equilibrium flow $\mathbf{V}_0 = 0$ and equilibrium plasma density and pressure that only depend on the enclosed flux ψ . In steady-state equilibrium, $\partial/\partial t = 0$ which reduces the model to the force balance equation (2.6).

We subject the steady state, no-flow ideal MHD system to an infinitesimal perturbation of a magnetic field line ζ of the following form

$$\tilde{\zeta}(\mathbf{r}, t) = \sum \zeta(\mathbf{r}) e^{i\omega t} \quad (2.20)$$

summed over different frequencies ω . Upon subjecting the system to this perturbation, we obtain the perturbed physical quantities

$$\rho = \rho_0(\psi) + \rho_1, \quad (2.21)$$

$$\mathbf{V} = \mathbf{V}_1, \quad (2.22)$$

$$p = p_0(\psi) + p_1, \quad (2.23)$$

$$\mathbf{B} = \mathbf{B}_0 + \mathbf{B}_1, \quad (2.24)$$

where $\rho_1/\rho_0 \sim p_1/p_0 \sim |\mathbf{B}_1|/|\mathbf{B}_0|$. Due to the frozen-in condition of ideal MHD, the motion of

the fluid and the field line are identical. Hence, we can argue that $\tilde{\mathbf{V}} = \partial\tilde{\boldsymbol{\zeta}}/\partial t = i\omega\boldsymbol{\zeta}$. Using this fact, we can linearize and simplify the MHD equations so that we are left with a single eigenvalue equation for $\boldsymbol{\zeta}$

$$-\omega^2\rho_0\boldsymbol{\zeta} = \nabla(\boldsymbol{\zeta} \cdot \nabla p_0 + \gamma p_0(\nabla \cdot \boldsymbol{\zeta})) + \frac{[\nabla \times (\nabla \times (\boldsymbol{\zeta} \times \mathbf{B}_0))] \times \mathbf{B}_0}{\mu_0} + \frac{(\nabla \times \mathbf{B}_0) \times (\nabla \times (\boldsymbol{\zeta} \times \mathbf{B}_0))}{\mu_0}. \quad (2.25)$$

The left-hand-side of (2.25) denotes the kinetic energy of the plasma due to the perturbation $\boldsymbol{\zeta}$ whereas the right-hand-side denotes the stored potential energy. The right side of (2.25) is also known as the ideal MHD force operator $\mathbf{F}[\boldsymbol{\zeta}]$.

It is often convenient and useful to write the eigenvalue equation (2.25) in the form of a variational principle. Multiplying (2.25) by $\boldsymbol{\zeta}^*/2$ on both sides and integrating over the whole volume, we obtain

$$-\frac{1}{2} \int dV \rho\omega^2|\boldsymbol{\zeta}|^2 = \frac{1}{2} \int dV \boldsymbol{\zeta}^* \cdot \mathbf{F}[\boldsymbol{\zeta}]. \quad (2.26)$$

Assuming that the boundary is a perfectly conducting wall containing the plasma, the frozen-in condition constrains $\boldsymbol{\zeta}$ to be such that $\boldsymbol{\zeta} \cdot \hat{\mathbf{n}}|_{\text{wall}} = 0$, where $\hat{\mathbf{n}}$ is the normal unit vector of the wall. Using the perfectly conducting-wall boundary condition, integration by parts, and the self-adjoint property of $\mathbf{F}[\boldsymbol{\zeta}]$, we can show that

$$\int dV \boldsymbol{\zeta}^* \cdot \mathbf{F}[\boldsymbol{\zeta}] = \int dV \boldsymbol{\zeta} \cdot \mathbf{F}[\boldsymbol{\zeta}^*]. \quad (2.27)$$

This implies that the eigenvalue $-\omega^2$ of an ideal MHD instability must be a real number. There-

fore, the perturbation ζ , will either be purely oscillating, i.e. $\omega^2 > 0$ or purely decaying / growing, i.e. $\omega^2 < 0$. We ignore the decaying mode, since the purely growing mode typically limits the lifetime of the configuration. The right side of (2.26) can be defines a functional δW :

$$\delta W[\zeta, \zeta] \equiv -\frac{1}{2} \int dV \zeta^* \cdot \mathbf{F}[\zeta]. \quad (2.28)$$

Physically, the sign of δW , which is the same as the sign of the eigenvalue $-\omega^2$, determines whether an ideal MHD equilibrium is stable or unstable. This is known as the ideal MHD energy principle. Figure 2.5 presents an intuitive illustration of the energy principle.

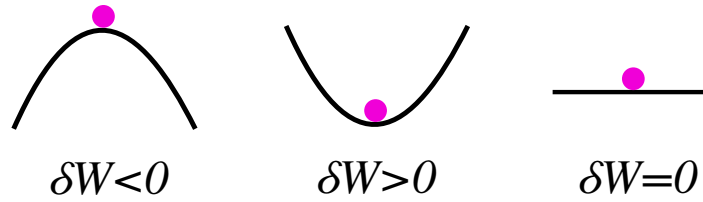


Figure 2.5: This figure illustrates the main idea of the ideal MHD energy principle. For a given equilibrium, if a perturbation ζ makes $\delta W < 0$, the equilibrium is unstable to that perturbation. If ζ makes $\delta W > 0$, the equilibrium is stable to that perturbation. Finally, if $\delta W = 0$, the equilibrium is marginally stable.

The self-adjoint property of the force operator and its variational form will be the basis for an adjoint-based method in §2.3.3. To further analyze the stability of an MHD equilibrium against a particular mode, it is useful to separate the components of the perturbation ζ in two different directions

$$\zeta(\mathbf{r}) = \zeta_{\parallel} \mathbf{b}_0 + \zeta_{\perp}. \quad (2.29)$$

In total, there are three components of ζ , i.e., three unknowns. Substituting this form of ζ

into (2.28), using the divergence theorem,

$$\int dV \nabla \cdot \mathbf{X} = \int dS \hat{\mathbf{n}} \cdot \mathbf{X} \quad (2.30)$$

and applying the perfectly conducting-wall boundary condition, we can expand the energy integral [1, 36] into a different form

$$\begin{aligned} \delta W = \frac{1}{2\mu_0} \int dV \left\{ & |[\mathbf{b}_0 \times \nabla \times (\boldsymbol{\zeta}_\perp \times \mathbf{B}_0)] \times \mathbf{b}_0|^2 + B_0^2 |\nabla \cdot \boldsymbol{\zeta}_\perp + 2\boldsymbol{\zeta}_\perp \cdot (\mathbf{b}_0 \cdot \nabla \mathbf{b}_0)|^2 \right. \\ & \mu_0 \gamma p_0 |\nabla \cdot \boldsymbol{\zeta}|^2 - 2\mu_0 (\boldsymbol{\zeta}_\perp \cdot \nabla p_0) (\boldsymbol{\zeta}_\perp^* \cdot (\mathbf{b}_0 \cdot \nabla \mathbf{b}_0)) \\ & \left. - \mu_0 (\mathbf{b}_0 \cdot (\nabla \times \mathbf{B}_0)) \boldsymbol{\zeta}_\perp^* \times \mathbf{b}_0 \cdot (\mathbf{b}_0 \times \nabla \times (\boldsymbol{\zeta}_\perp \times \mathbf{B}_0)) \times \mathbf{b}_0 \right\}. \end{aligned} \quad (2.31)$$

Next, we argue that the most virulent ideal MHD modes are incompressible. The only term that has $\nabla \cdot \boldsymbol{\zeta}$ in (2.31) is positive definite — positive definite terms can only increase δW and hence stabilize an equilibrium. To enforce incompressibility, i.e., $\nabla \cdot \boldsymbol{\zeta} = 0$, we can replace all instances of $\nabla_{\parallel} \boldsymbol{\zeta}_{\parallel}$ with $-\nabla \cdot \boldsymbol{\zeta}_\perp$ which reduces the number of unknown components of $\boldsymbol{\zeta}$ from three to two. We also note that note is that $\delta W < 0$ only due to the last two terms in (2.31). The penultimate term corresponds to pressure-induced instabilities, while the last term causes current-induced instabilities.

Furthermore, we use the periodicity of the perturbations in θ and ϕ , to write

$$\boldsymbol{\zeta}_\perp = \sum_{m,n} \boldsymbol{\zeta}_{\perp m,n}(\psi) e^{i(m\theta - n\phi)}, \quad (2.32)$$

where m is the poloidal mode number, n is the toroidal mode number and ι is the rotational transform. The perturbations can be further categorized on the basis of the toroidal mode number

n ; large scale instabilities are characterized by low- n modes whereas small scale instabilities are categorized by high- n modes. In the following section, we will briefly explain the details of a low- n solver.

2.3.1 Low- n modes

In this section, we will briefly describe the process of solving (2.25) in the limit of a small toroidal mode number n . These are large-scale modes that are predominantly destabilized by the equilibrium parallel current. To obtain the governing equation, the Fourier-transformed ζ_{\perp} is substituted into the energy integral $\delta W[\zeta_{m,n}, \zeta_{m,n}]$ to simplify the variational equation

$$-\omega^2 = \frac{\int dV \delta W[\zeta_{m,n}, \zeta_{m,n}]}{\int dV \rho |\zeta_{m,n}|^2}, \quad (2.33)$$

to an Euler-Lagrange equation to find the minimum (the least stable) eigenvalue $-\omega^2$. To avoid confusion related to the sign of the eigenvalue, we define $\hat{\lambda} = -\omega^2$ as the eigenvalue. For low- n modes, we cannot simplify the energy integral any further and have to solve the non-linear variational eigenvalue problem with quadratic nonlinearity in ζ subject to boundary conditions at $\psi = 0, \psi_b$. One usually chooses a Dirichlet boundary condition on the magnetic axis, i.e., $\zeta_{m,n}(\psi = 0) = 0$. For a conducting wall, we can also impose a Dirichlet condition at $\psi = \psi_b$.

To numerically solve (2.33), we pick a set of low- n modes² and scan multiple values of the poloidal mode number m and discretize the energy integral so that the problem takes the following form

$$\mathcal{A}X = \hat{\lambda}\mathcal{B}X, \quad (2.34)$$

²For a general 3D problem, the toroidal modes will be coupled due to the discrete nature of toroidal symmetry. The set of mode numbers will depend on the field period n_{fp} and the rotational transform ι .

where X comprises various Fourier modes of the perturbation. Note that due to the non-linear nature of the energy integral and the discrete symmetry of 3D equilibria, one has to take into account the coupling between various toroidal modes of the perturbation $\zeta_{m,n}$ and include groups of higher-order (m, n) modes before obtaining (2.34). This makes the matrix \mathcal{A} sparse but banded. However, both matrices \mathcal{A} and \mathcal{B} are real and symmetric, therefore, self-adjoint.

Currently, there are various codes such as TERPSICHOE [37] and CAS-3D [38] that analyze low- n stability for 3D equilibria and GATO [39] and ELITE [40] for 2D axisymmetric equilibria. However, performing an optimization with these codes can be computationally expensive to run. We will not analyze our equilibria for low- n stability in this paper. However, we can use the self-adjoint property of these equations to formulate a faster method to optimize against all low- n instabilities, briefly described in appendix A.4.

2.3.2 The infinite- n , ideal ballooning mode

In this section, we will investigate the stability of the equilibria generated in the previous sections to the infinite- n ideal ballooning mode. We will start by explaining the mathematical and physical details of the ballooning mode. Next, we will explain how to solve this equation numerically. Finally, we explain properties of the ballooning equation that we will use to formulate an optimizer in the next section.

2.3.2.1 Physical and mathematical description

One of the most important MHD instabilities for us to investigate is the ideal ballooning instability [41] — a field-aligned, pressure-driven Alfvén wave that grows when the destabilizing

pressure gradient in the region of “bad” curvature exceeds the stabilizing effect of field line bending. The region of “bad” curvature is that region of a flux surface where $(\mathbf{b} \cdot \nabla \mathbf{b}) \cdot \nabla p > 0$, such that the field line curvature is in the same direction as the plasma pressure gradient. For most tokamak equilibria, this region lies on the outboard side.

The equation governing the ideal ballooning mode can be obtained by minimizing the ideal MHD energy integral [14] for incompressible modes in the limit of a large toroidal mode number. Doing so gives us a differential equation that determines X , the radial displacement of the plasma. To ensure that the displacement X satisfies the periodicity condition on the surface of interest and the surrounding surfaces, one uses the ballooning transformation

$$X = \sum_{N=-\infty}^{\infty} \hat{X}(\theta - 2\pi N) e^{in(\phi - q(\theta - \theta_0 - 2\pi N))}, \quad N \in \mathbb{Z}, \quad (2.35)$$

subject to the condition

$$\lim_{\theta \rightarrow \pm\infty} \hat{X}(\theta; \psi, \theta_0) = 0, \quad (2.36)$$

and solves for \hat{X} . The variable n is the toroidal mode number, θ_0 is the ballooning parameter³ and the rest of the terms are defined in §2.2. Upon minimizing the ideal-MHD energy integral and using the ballooning transformation, one obtains the ideal ballooning equation [16, 41]

$$\frac{1}{\mathcal{J}} \frac{\partial}{\partial \theta} \left(\frac{|\nabla \alpha|^2}{\mathcal{J} B^2} \frac{\partial \hat{X}}{\partial \theta} \right) + 2\mu_0 \frac{d(\mu_0 p)}{d\psi} \left[\mathbf{B} \times \nabla \left(p + \frac{B^2}{2} \right) \cdot \nabla \alpha \right] \hat{X} = -\rho \omega^2 \frac{|\nabla \alpha|^2}{B^2} \hat{X}, \quad (2.37)$$

where ρ is the plasma mass density and $\hat{X} = \hat{X}(\theta; \psi, \theta_0)$ is the eigenfunction in ballooning space

³In the context of infinite- n ideal ballooning mode analyses, there is a value of the ballooning parameter θ_0 at which the ballooning mode is the least stable. To find this value, one treats θ_0 as a parameter and scans over its values to find the θ_0 for which ω^2 is the smallest.

and $-\omega^2$ is the eigenvalue. The ballooning equation balances the stabilizing field-line bending term and destabilizing pressure gradient with the inertia of the resulting Alfvén wave, oscillating with a frequency ω . Note that (2.37) depends on $\psi(\psi_p)$ only as a parameter and we can compute the coefficients from the on-surface equilibrium quantities and their first derivatives. Therefore, it is possible to study the ballooning stability of the local equilibria that we chose in §2.2.1.

Due to the self-adjoint nature of ideal-MHD, all the eigenvalues (ω^2) of equation (2.37) will be real numbers. Hence, ω will be either purely real, an oscillating mode or purely imaginary, a growing mode. We refer to the oscillating modes as stable, and growing modes as unstable. Before solving (2.37) numerically, we normalize and write the ballooning equation on a fieldline (fixed α_t) as

$$\frac{d}{d\theta} g \frac{d\widehat{X}}{d\theta} + c\widehat{X} = \widehat{\lambda}f\widehat{X}, \quad (2.38)$$

where

$$\begin{aligned} g &= (\mathbf{b} \cdot \nabla_N \theta) \frac{|\nabla_N \alpha_t|^2}{B/B_N}, \\ c &= \frac{2}{(\mathbf{B} \cdot \nabla_N \theta)} \frac{d(\mu_0 p / B_N^2)}{d\psi_N} \left[\mathbf{B} \times \nabla_N \left(\frac{2\mu_0 p + B^2}{2B_N^2} \right) \cdot \nabla_N \alpha_t \right], \\ f &= \frac{|\nabla_N \alpha_t|^2}{(B/B_N)^2}, \\ \widehat{\lambda} &= - \left(\frac{\omega a_N}{v_A} \right)^2, \quad v_A = \frac{B_N}{\sqrt{4\pi\rho}}, \end{aligned} \quad (2.39)$$

where v_A is the Alfvén speed. The normalizing magnetic field B_N , and the normalizing length a_N are defined in §2.2.1. The ideal ballooning equation is numerically solved subject to the boundary conditions

$$\widehat{X}(\theta = \pm\theta_b; \psi, \alpha_t, \theta_0) = 0. \quad (2.40)$$

where θ_b is a finite user-selected value that determines the extent of the eigenfunction in the

ballooning space. In the next section, we present the numerical procedure used to solve the ideal ballooning equation.

2.3.2.2 Numerical implementation and eigenvalues of the selected equilibria

In this section, we will briefly discuss the numerical technique used to solve the ballooning equation (2.38). Our numerical technique is identical to that used by Sanchez *et al.* [42] in their ballooning solver COBRAVMEC. After briefly explaining the details of our solver, we present the maximum eigenvalue as a function of the normalized toroidal flux s for the three equilibria we presented in §2.2.1.

The ideal ballooning equation is a second-order ordinary differential equation with real-valued coefficients. This eigenvalue equation is discretized using a second-order accurate, central-finite-difference scheme

$$g_{j+1/2} \frac{(\widehat{X}_{j+1} - \widehat{X}_j)}{\Delta\theta^2} - g_{j-1/2} \frac{(\widehat{X}_j - \widehat{X}_{j-1})}{\Delta\theta^2} + (c_j - \widehat{\lambda}f_j)\widehat{X}_j = 0, \quad j = 0 \dots N - 1 \quad (2.41)$$

where N is an odd number of uniformly spaced points in the ballooning space, $\theta_j \in [-\theta_b, \theta_b]$ and $\Delta\theta = \theta_{j+1} - \theta_j$. First-order derivatives are evaluated at half points $j - 1/2, j - 3/2$ instead of grid points to ensure numerical stability. The boundary conditions satisfied by the discrete equations are $\widehat{X}_0 = \widehat{X}_N = 0$. For a fixed poloidal and toroidal resolution, the time taken by our solver is proportional to θ_b . Therefore, it is important to find the right balance between speed and accuracy. Throughout this work, we chose the domain limit $\theta_b = 5\pi$ for all calculations, as we found it to be a sufficient range to capture the ballooning eigenfunction. We observed that the values $\theta_b > 5\pi$ made a relatively small difference from the value obtained of $\widehat{\lambda}$. The discrete set

of equations (2.41) is written in the form of a matrix equation

$$A\hat{X} = \hat{\lambda}\hat{X}, \quad (2.42)$$

where the exact matrix A is provided in appendix A.1. We then solve (2.42) to find the largest eigenvalue using an Arnoldi iterative scheme using the `scipy.linalg.eigs` solver in Python and refine the accuracy of the largest eigenvalue in the grid spacing $\Delta\theta$ using variational refinement where the derivative $d\hat{X}/d\theta$ is calculated using a fourth-order accurate finite difference scheme and the integral is performed using a fourth-order accurate Simpson's rule (1/3 rule) with `scipy.integrate.simps`⁴. Note that we only solve for and refine the largest eigenvalue of (2.38) and not the entire eigenvalue spectrum.

An alternate technique that can be used to speed up the eigenvalue calculation, the Homotopy Analysis method, is also described in Appendix A.5. It is a semi-analytical method that has the advantage of being free from any noise unlike the finite-difference method that we shall use in this chapter.

2.3.2.3 Properties of the ideal ballooning equation

The ideal ballooning equation (2.38) is a linear equation that can be written as

$$\mathcal{L}\hat{X} = \hat{\lambda}\hat{X}, \quad (2.43)$$

⁴Our Python code is freely available at github.com/raahulgaur104/ideal-ballooning-solver

where the linear operator

$$\mathcal{L} \equiv \frac{1}{f} \frac{d}{d\theta} g \frac{d}{d\theta} + \frac{c}{f}, \quad (2.44)$$

and the coefficients g, c, f are real-valued functions along a field line. Mathematically, the solutions of (2.43) form the basis of a Hilbert space equipped with the following inner product

$$\langle \widehat{X}_1, \widehat{X}_2 \rangle = \int_{-\infty}^{\infty} d\theta \widehat{X}_1^* \widehat{X}_2, \quad (2.45)$$

and are square integrable, i.e., $\langle \widehat{X}, \widehat{X} \rangle < \infty$. Due to the self-adjoint nature of ideal MHD [1], for solutions \widehat{X}_1 and \widehat{X}_2 of equation (2.43) the operator \mathcal{L} satisfies the following property

$$\langle \mathcal{L} \widehat{X}_1, \widehat{X}_2 \rangle = \langle \widehat{X}_1, \mathcal{L} \widehat{X}_2 \rangle, \quad (2.46)$$

where we have used the boundary condition $\lim_{\theta \rightarrow \pm\infty} \widehat{X}_1 = \lim_{\theta \rightarrow \pm\infty} \widehat{X}_2 = 0$. Using (2.46), one can show that all eigenvalues $\widehat{\lambda}$ (2.37) will be real numbers. Therefore, $\omega = \pm i \sqrt{\widehat{\lambda}}$ will be purely real, an oscillating mode, or purely imaginary, a growing mode. We refer to oscillating modes as stable and to growing modes as unstable. We will use this property in §2.3.3 to formulate an adjoint method, a technique that can speed up the calculation of the gradient of $\widehat{\lambda}_{\max}$ on each flux surface.

2.3.3 Leveraging the self-adjoint property to formulate an optimizer

In this section, we derive and explain the process of calculating the gradients of the ideal ballooning eigenvalue $\widehat{\lambda}$ on each surface that would help us find the maximum eigenvalue $\widehat{\lambda}_{\max}$ using an adjoint method. We then elucidate how it is faster than the conventional gradient-based

method and illustrate this by plotting gradients from a typical optimization run and calculating the speed-up.

To find $\widehat{\lambda}_{\max}$ on each flux surface, we need the gradient of the eigenvalue of a general function \mathcal{H} such that \mathcal{H} is maximized if and only if $\widehat{\lambda} = \widehat{\lambda}_{\max}$. Mathematically, this problem can be defined in general as

$$\max \mathcal{H}(\widehat{\lambda}, \widetilde{\mathbf{p}}, \widehat{\mathbf{p}}), \quad \text{s.t.} \quad \mathcal{G}(\widehat{\lambda}, \widehat{X}, \widetilde{\mathbf{p}}, \widehat{\mathbf{p}}) \equiv \mathcal{L}\widehat{X} - \widehat{\lambda}\widehat{X} = 0, \quad (2.47)$$

where $\widehat{\lambda}$ is the eigenvalue, \widehat{X} is the eigenfunction, $\widetilde{\mathbf{p}}$ is the state vector that contains all the equilibrium parameters such as the boundary shape and the ι profile and $\widehat{\mathbf{p}} = (\alpha_t, \theta_0)$ is a vector that contains the parameters of the ideal ballooning equation, \mathcal{H} is an objective function, and \mathcal{G} is the ideal ballooning operator. To maximize \mathcal{H} on a flux surface for a given equilibrium, i.e., for a fixed $\widetilde{\mathbf{p}}$, we need the gradient

$$\frac{d\mathcal{H}}{d\widehat{\mathbf{p}}} = \left. \frac{\partial \mathcal{H}}{\partial \widehat{\lambda}} \right|_{\widetilde{\mathbf{p}}} \frac{\partial \widehat{\lambda}}{\partial \widehat{\mathbf{p}}} + \left. \frac{\partial \mathcal{H}}{\partial \widehat{\mathbf{p}}} \right|_{\widehat{\lambda}}. \quad (2.48)$$

The most expensive term to calculate in (2.48) is the gradient of the eigenvalue λ . To obtain that, we take the derivative of the operator \mathcal{G} with respect to λ ⁵ for a fixed $\widetilde{\mathbf{p}}$

$$-\frac{\partial \mathcal{G}}{\partial \widehat{\lambda}} \frac{\partial \widehat{\lambda}}{\partial \widehat{\mathbf{p}}} = \frac{\partial \mathcal{G}}{\partial \widehat{X}} \frac{\partial \widehat{X}}{\partial \widehat{\mathbf{p}}} + \left. \frac{\partial \mathcal{G}}{\partial \widehat{\mathbf{p}}} \right|_{\widehat{X}, \widehat{\lambda}}. \quad (2.49)$$

⁵Note that the derivative of an eigenvalue is only well-defined when the eigenvalue is isolated. Optimization problems with stringent penalty terms can lead the optimizer to points with multiplicity [43].

This equation can be explicitly written with the help of (2.44)

$$\frac{\partial \hat{\lambda}}{\partial \hat{\mathbf{p}}} \hat{X} = (\mathcal{L} - \hat{\lambda}) \frac{\partial \hat{X}}{\partial \hat{\mathbf{p}}} + \frac{\partial \mathcal{L}}{\partial \hat{\mathbf{p}}} \hat{X}. \quad (2.50)$$

To simplify (2.50) further, we multiply it by the eigenfunction \hat{X}^* and integrate it throughout the domain $\theta \in [-\theta_b, \theta_b]$. Upon doing that, we use the self-adjoint property (2.46) and work through the algebra (given in appendix A.2) to obtain the adjoint relation

$$\frac{\partial \hat{\lambda}}{\partial \hat{\mathbf{p}}} = \frac{\int_{-\theta_b}^{\theta_b} d\theta \left(\frac{\partial c}{\partial \hat{\mathbf{p}}} |\hat{X}|^2 - \frac{\partial g}{\partial \hat{\mathbf{p}}} \left| \frac{d\hat{X}}{d\theta} \right|^2 - \hat{\lambda} \frac{\partial f}{\partial \hat{\mathbf{p}}} |\hat{X}|^2 \right)}{\int_{-\theta_b}^{\theta_b} d\theta f |\hat{X}|^2}. \quad (2.51)$$

To obtain $\partial \hat{\lambda} / \partial \hat{\mathbf{p}}$ using a central finite difference scheme, one has to solve the ideal ballooning equation $2n_{\hat{\mathbf{p}}} = 4$ times at each optimization step, where $n_{\hat{\mathbf{p}}}$ is the length of the vector $\hat{\mathbf{p}}$. However, using the adjoint relation (2.51), we only have to solve it once per optimization step, as long as we can calculate the gradients of geometry-related quantities g , c , and f four times. Since gradients of g , c , f can be calculated roughly two orders of magnitude faster than solving the ideal ballooning equation, we speed up the gradient calculation by approximately a factor of four. Therefore, we use the adjoint relation (2.51) to calculate the gradient of $\hat{\lambda}$. In this study, we choose

$$\mathcal{H}(\hat{\lambda}, \tilde{\mathbf{p}}, \hat{\mathbf{p}}) = \hat{\lambda}. \quad (2.52)$$

Applying this fact to (2.48) and using (2.51),

$$\frac{d\mathcal{H}}{d\widehat{\mathbf{p}}} = \frac{\partial\widehat{\lambda}}{\partial\widehat{\mathbf{p}}} = \frac{\int_{-\theta_b}^{\theta_b} d\theta \left(\frac{\partial c}{\partial\widehat{\mathbf{p}}} |\widehat{X}|^2 - \frac{\partial g}{\partial\widehat{\mathbf{p}}} \left| \frac{d\widehat{X}}{d\theta} \right|^2 - \widehat{\lambda} \frac{\partial f}{\partial\widehat{\mathbf{p}}} |\widehat{X}|^2 \right)}{\int_{-\theta_b}^{\theta_b} d\theta f |\widehat{X}|^2}. \quad (2.53)$$

This relation gives us the derivative of the ballooning objective function at any point $\widehat{\mathbf{p}} = (\alpha_t, \theta_0)$.

Note that in this work we will use (2.53) to find $\widehat{\lambda}_{\max}$ on a flux surface. However, this method is valid and, under appropriate conditions, can be extended to the equilibrium parameters $\widetilde{\mathbf{p}}$. The details of the extended adjoint method are given in appendix A.3.

In the next section, we present data and explain the advantages of adjoint methods over the regular finite-difference-based method to calculate the gradients of $\widehat{\lambda}_{\max}$.

2.3.3.1 Comparing adjoint gradients with a finite difference method

In this section, we will first compare the values of the gradients of $\widehat{\lambda}_{\max}$ from the adjoint method with their values obtained using a central-finite difference method. We take a typical optimization loop in the modified NCSX case and show a gradient comparison in figure 2.6. As you can see, the gradients obtained using an adjoint method match well with the gradients obtained with a finite-difference method.

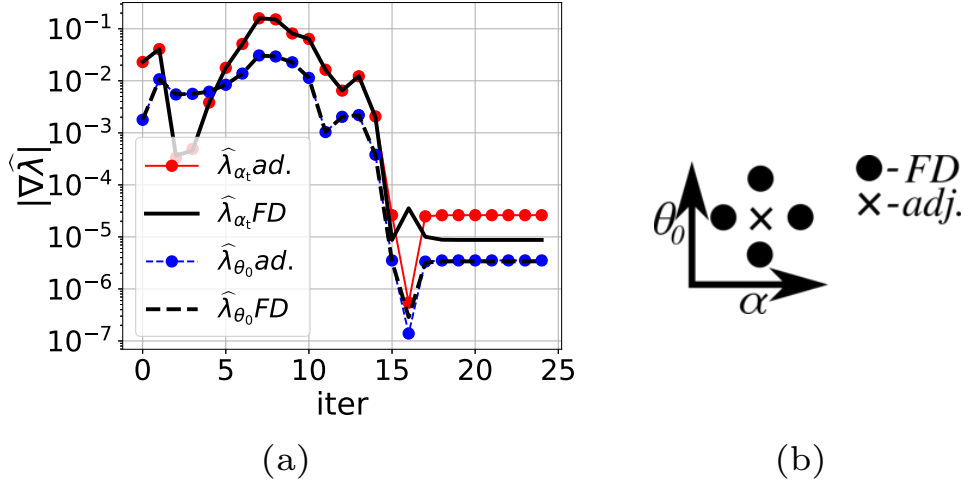


Figure 2.6: In this figure we present (a) comparison between the gradients of eigenvalue $\hat{\lambda}_{\alpha_t} = \partial\hat{\lambda}/\partial\alpha_t$ and $\hat{\lambda}_{\theta_0} = \partial\hat{\lambda}/\partial\theta_0$ obtained using a finite difference scheme against ones obtained using an adjoint method. The quantity iter is the number of iterations taken by the local optimizer on a flux surface before finding $\hat{\lambda}_{\max}$. The gradients match well for around four orders of magnitude. The discrepancy between the adjoint and finite difference $\hat{\lambda}_{\alpha_t}$ is due to the finite resolution of the VMEC run. In figure (b), we illustrate the the different grids used to calculate the gradient of the eigenvalue $\hat{\lambda}$ on a flux surface. A finite difference scheme requires four points whereas an adjoint method only requires one point. This gives us a four times speed-up.

To show the computational speedup, we also compare the time taken by an adjoint method with the regular finite-difference-based method. For the thirty iterations shown in figure 2.6(a), the adjoint method was about 4 times faster than the finite difference method. Indeed, the most expensive part of the gradient calculation is the ballooning solver. As shown in the illustration in figure 2.6(b), for a second-order accurate central-difference scheme, an adjoint method only needs a single call to the ballooning solver, whereas the finite difference solver needs four. In principle, a speed-up factor of up to 4 should be possible.

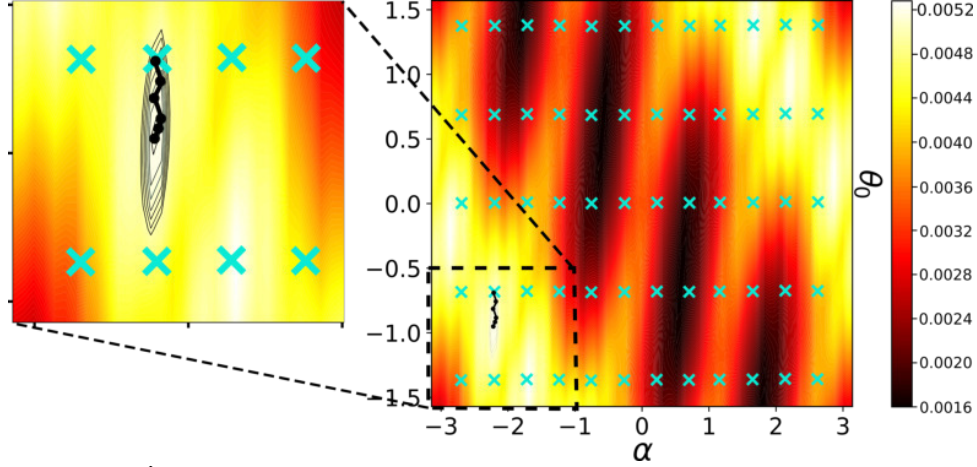
2.3.4 Details of the optimization process

In this section, we will explain the optimization process to find equilibria that are stable against the ideal ballooning mode. In §2.3.4.1, we describe the process of using an adjoint

method to find the maximum growth rate $\widehat{\lambda}_{\max}$ on each flux surface. In §2.3.4.2, we then explain how we use $\widehat{\lambda}_{\max}$ and other penalty terms to construct the overall objective function \mathcal{F} . Finally, in §2.3.4.3, we explain how we search for ballooning stable equilibria while minimizing \mathcal{F} using the SIMSOPT framework.

2.3.4.1 Finding $\widehat{\lambda}_{\max}$ on each flux surface

To calculate the ballooning objective function we find the maximum $\widehat{\lambda}$ on each flux surface. To do that, we solve (2.38) on several flux surfaces, multiple field lines on each surface, and numerous values of θ_0 on each field line. We calculate $\widehat{\lambda}_{\max}$ on $n_s = 16$ flux surfaces for each equilibrium. For the 3D equilibria, we scan $n_{\alpha_t} = 42$ field lines in the range $\alpha_t = [-\pi, \pi)$. Since all field lines are identical in a 2D axisymmetric equilibrium, we scan only one field line, i.e., $n_{\alpha} = 1$ for the 2D equilibrium. On each field line, we scan $n_{\theta_0} = 21$ values of θ_0 in the range $\theta_0 = [-\pi/2, \pi/2)$. The maximum $\widehat{\lambda}$ from a coarse grid scan gives us a value close to the global maximum. From the maximum $\widehat{\lambda}$ of the coarse grid, we launch a local gradient-based optimizer to find the global maximum eigenvalue. This process is explained using the illustration 2.7.



(a) $\hat{\lambda}$ landscape and optimizer path at $s = 0.77$

Figure 2.7: This figure shows the typical process of finding the globally maximum eigenvalue $\hat{\lambda}_{\max}$ on the flux surface $s = 0.77$. We start by first finding the maximum $\hat{\lambda}$ on discrete grid of α_t and θ_0 . From the maximum discrete $\hat{\lambda}$, we search for the global maximum eigenvalue using a local optimizer. In the inset, we show the approximate path taken by the optimizer to reach the $\hat{\lambda}_{\max}$.

Using this process, we obtain $\hat{\lambda}_{\max}$ as a function of the normalized toroidal flux s . Figure 2.8 shows the plot of $\hat{\lambda}_{\max}$ against s for the three chosen equilibria.

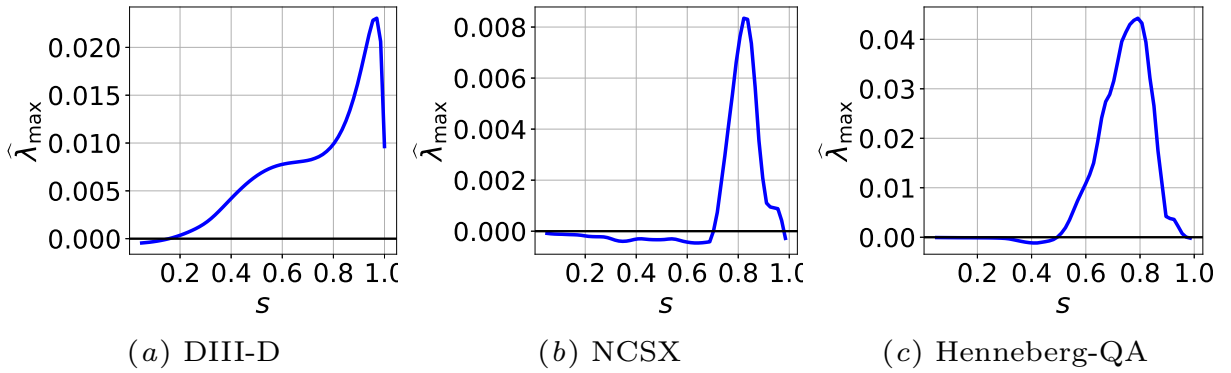


Figure 2.8: This figure shows the plots of $\hat{\lambda}_{\max}$ against the normalized toroidal flux s for the three chosen equilibria. Note that the ideal ballooning growth rate $\gamma a_N/v_A = \sqrt{\hat{\lambda}}$ so $\hat{\lambda}_{\max} = 0.008$ corresponds to the normalized growth rate $\gamma a_N/v_A = 0.09$ which is not a small value.

For each new equilibrium, on all $n_s = 16$ flux surfaces, the local optimizer takes an average of 20 iterations to find $\hat{\lambda}_{\max}$. Moreover, as described in figure 2.6(b), at each step, the use of a

finite difference method requires 4 evaluations of the eigenvalue $\hat{\lambda}$. This means that on average, we have to call the ballooning solver 1280 ($16 \times 20 \times 4$) times. This is a computationally expensive step that we speed up using our adjoint-based method.

2.3.4.2 Finding ballooning-stable equilibria

Once we have found $\hat{\lambda}_{\max}$, we seek an equilibrium stable to the ideal ballooning mode by minimizing $\hat{\lambda}_{\max}$ on each flux surface. To do so, we need to define an objective function that depends on $\hat{\lambda}_{\max}$ such that minimizing the objective function should allow us to achieve a stable equilibrium. Moreover, during optimization, once a flux surface is stabilized against the ideal ballooning mode, our objective function should ignore that particular surface. This would be useful as we do not want to penalize a stable equilibrium. To this end, we design the following ideal ballooning objective function

$$f_{\text{ball}} = \sum_{j=1}^{\text{ns}} \text{ReLU}(\hat{\lambda}_{\max,j} - \hat{\lambda}_{\text{th},j}), \quad (2.54)$$

where ns is the total number of surfaces and

$$\text{ReLU}(x) = \begin{cases} 0, & \text{if } x \leq 0 \\ x, & x > 0 \end{cases}$$

is the Rectified Linear Unit operator — an operator that sets all the non-positive values to zero and $\hat{\lambda}_{\text{th},j}$ is the threshold below which we declare a surface ideal ballooning-stable. The value $\hat{\lambda}_j = 0$ on the j^{th} surface implies marginal stability but we choose $\hat{\lambda}_{\text{th},j} = 0.0001$ to ensure that

all the surfaces are slightly away from marginal ideal ballooning stability. An equilibrium is ideal ballooning stable if $f_{\text{ball}} = 0$.

It is also important to prevent the optimizer from minimizing f_{ball} in a trivial manner. For example, for 2D equilibria, going to a larger aspect ratio value stabilizes the ideal ballooning mode. For 3D equilibria, the optimizer can sometimes reduce the minor radius, which, for a fixed toroidal flux, causes the magnetic field to increase. This lowers the overall β and consequently the unstable curvature drive term. Similarly, if we allow rotational transforms to increase freely, the optimizer can sometimes create large gradients of ι , generating large currents which is suboptimal. To avoid achieving such trivial solutions and uninteresting equilibria, we add a combination of squares of the following penalty terms to the optimizer:

1. $f_{\text{asp}} = (A - A_0)$ to penalize any deviation from the aspect ratio of the initial equilibrium,
2. $f_{\text{minr}} = (a_N - a_{N0})$ to penalize any deviation from the minor radius of the initial equilibrium,
3. $f_{\langle B \rangle} = (\langle B \rangle - \langle B \rangle_0)$ to penalize any deviation of the volume-averaged magnetic field from its value in the initial equilibrium,
4. $f_{R_c} = \int d\theta \text{ReLU}(-R_c)$ where R_c is the radius of curvature of the boundary. This term penalizes any boundary shapes that are curved into the plasma,
5. $f_{\bar{\iota}} = (\bar{\iota} - \bar{\iota}_0)$ where $\bar{\iota}$ and $\bar{\iota}_0$ to penalize deviation of the mean rotational transform,
6. $\mathcal{G}_{\iota} = \text{ReLU}(\iota_{\text{th}} - \iota)$ where ι_{th} is some threshold value of ι , and
7. $\mathcal{G}_{j_{\zeta}} = \text{ReLU}(j_{\zeta, \text{th}} - j_{\zeta})$ where $j_{\zeta, \text{th}}$ is some threshold value of the enclosed toroidal current.

Using the ballooning objective function (2.54) and one or more of the penalty terms described above, we can get the overall objective function \mathcal{F} . Given a vector of input parameters \mathbf{p} , our goal is to solve

$$\min_{\mathbf{p}} \mathcal{F}(\mathbf{p}). \quad (2.55)$$

and select equilibria for which $f_{\text{ball}} = 0$. We achieve this with the help of the SIMSOPT [44] package. The implementation details of the optimization are described in the next subsection.

2.3.4.3 Optimization with the SIMSOPT package

In this subsection, we discuss the implementation-related details of an adjoint ballooning solver with the SIMSOPT [44] package. First, we briefly explain how an optimization problem can be solved using SIMSOPT. Next, we go into the details of how we solve the ideal ballooning optimization and how the use of an adjoint method can speed up this process.

The SIMSOPT package is a optimization framework containing a suite of codes that, along with the VMEC code, have been used to optimize 3D equilibria for various properties like energetic fast-particle confinement, quasisymmetry, simpler magnetic coil geometry, neoclassical transport, etc. The user specifies the input parameters (also referred to as Degrees of Freedom (Dofs)) and the objective function \mathcal{F} and SIMSOPT can perform a gradient-based or gradient-free nonlinear least squares optimization.

As an example, let us construct an optimization problem to stabilize an equilibrium while penalizing the change in the aspect ratio and the minor radius of the boundary

$$\mathcal{F} = f_{\text{asp}}^2 + f_{\text{minr}}^2 + f_{\text{ball}}^2. \quad (2.56)$$

To do so, we use gradient-based optimization in SIMSOPT, where one calculates $\partial\mathcal{F}/\partial\mathbf{p}$ to update the parameter vector at the i^{th} iteration, \mathbf{p}_i as

$$\mathbf{p}_{i+1} = f\left(\mathbf{p}_i, \frac{\partial\mathcal{F}}{\partial\mathbf{p}_i}\right). \quad (2.57)$$

This is done until the optimizer reaches a local minima, i.e., a region in the parameter space where $\partial\mathcal{F}/\partial\mathbf{p} = 0$ or the relative change in the gradient is small enough. Typically, one has to evaluate the gradient of \mathcal{F} hundreds of times during an optimization loop before finding a local minimum. In this study, evaluating f_{ball} is the most expensive step. Because the speed of the optimization is limited by the rate at which we can compute f_{ball} , we have used an adjoint method to calculate $\widehat{\lambda}_{\text{max}}$ which gives us f_{ball} .

2.4 Results

In this section, we present the results of our study. In §2.4.1, we compare the initial and optimized 2D axisymmetric equilibrium. In §§2.4.2 and 2.4.3, we do the same for the modified NCSX and modified Henneberg-QA equilibria, respectively. In addition, we also compare the values of relevant physical quantities in the initial and optimized equilibria.

2.4.1 Stabilizing the DIII-D-like equilibrium

For the 2D axisymmetric case, we start with a high- β equilibrium with a negative triangularity boundary. Due to axisymmetry, the 2D boundary does not depend on the toroidal angle ζ , i.e., $n = 0$ in (2.17). Therefore, the number of modes needed to specify a 2D boundary is much lower than that for a typical 3D boundary. In this problem, we pick the six largest Fourier modes

as our Dofs: $\widehat{R}_b(0, 1), \widehat{R}_b(0, 2), \widehat{R}_b(0, 3), \widehat{Z}_b(0, 1), \widehat{Z}_b(0, 3), \widehat{Z}_b(0, 5)$. The full objective function is

$$\mathcal{F} = f_{\text{asp}}^2 + f_{R_c}^2 + f_{\text{minr}}^2 + f_{\langle B \rangle}^2 + f_{\text{ball}}^2, \quad (2.58)$$

where all terms except f_{ball} are penalty terms to prevent the optimizer from producing a trivial solution. After this, we start with the negative triangularity equilibrium described in §2.2.1 and run SIMSOPT to find multiple equilibria that are stable against the ideal ballooning mode, i.e., equilibria with $f_{\text{ball}} = 0$. We present one of the optimized equilibria in figure 2.9. We also compare the values of equilibrium-dependent quantities in table 2.4.

State	$\beta_{\text{ax}}(\%)$	$\langle \beta \rangle(\%)$	$j_\phi(\text{MA})$	$\langle B \rangle(\text{T})$	\bar{t}	A	$a_N(m)$	$\psi_b(\text{Tm}^2)$
Initial	14.0	7.6	0.616	0.677	0.568	2.42	0.68	1.0
Optim.	13.7	7.3	0.728	0.686	0.568	2.42	0.68	1.0

Table 2.4: This table shows a comparison between relevant physical quantities of the intial and optimized DIII-D equilibrium

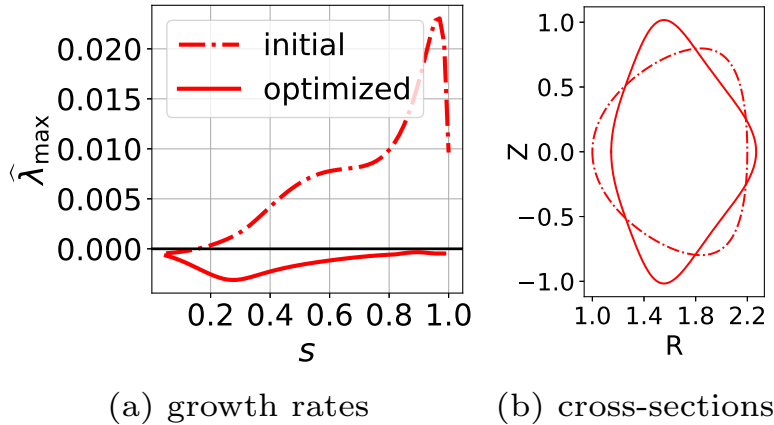


Figure 2.9: This figure shows (a) the maximum eigenvalue $\widehat{\lambda}_{\text{max}}$ of the intial and optimized DIII-D-like equilibrium. The optimized equilibrium is stable. In figure (b), we present the boundary shape of the initial and final equilibria. Note the negative triangularity of the initial equilibrium and the positive triangularity of the optimized equilibrium.

We observe that the optimizer is moving toward a positive triangularity equilibrium, indicating that, for the similar values of the relevant parameters (given in table 2.4) positive triangularity high- β equilibria are more stable than their negative triangularity counterparts. Our findings are consistent with recent observations by [45] and [46] that negative triangularity equilibria are more unstable against the ideal ballooning mode compared to positive triangularity ones. This behavior prevents the formation of a steep pressure gradient, which may limit operational beta value of negative triangularity equilibria.

2.4.2 Stabilizing the NCSX equilibrium

The first 3D equilibrium we optimize is an unstable NCSX equilibrium. Since the boundary has a 3D shape, we have to use both toroidal and poloidal modes to change its shape. For this demonstration, we choose the 72 boundary modes listed in table 2.5 as Dofs: where $[i, j]$ denotes

$\widehat{R}_b(n, m)$	$\widehat{Z}_b(n, m)$
$([1, 4], 0)$	$([1, 4], 0)$
$([-3, 3], 1)$	$([-3, 3], 1)$
$([-3, 3], 2)$	$([-3, 3], 2)$
$([-2, 2], 3)$	$([-2, 2], 3)$
$([-2, 2], 4)$	$([-2, 2], 4)$
$([-2, 2], 5)$	$([-2, 2], 5)$
$([-1, 1], 6)$	$([-1, 1], 6)$

Table 2.5: This table provides the boundary shape Dofs for the NCSX case.

all integers between i and j (including i and j). Additionally, we also provide the optimizer with the coefficients of the rotational transform profile $\iota(s)$. For this study, we have 6 Dofs that determine the rotational transform profile. Therefore, we have a total of 78 Dofs, much larger

than the axisymmetric case. After choosing the Dofs, we choose the following general objective function

$$\mathcal{F} = 0.5f_{\text{asp}}^2 + 0.5f_{\text{minr}}^2 + f_{(B)}^2 + f_t^2 + (70f_{\text{ball}})^2. \quad (2.59)$$

Note that the weights of different penalty terms in the objective function are chosen based on the relative size of different terms. There are no well-defined rules and finding the right objective function occasionally requires trial-and-error by the user. We run SIMSOPT with this configuration to obtain multiple equilibria with $f_{\text{ball}} = 0$. We have plotted a comparison of one of these equilibria with the initial equilibrium in 2.10.

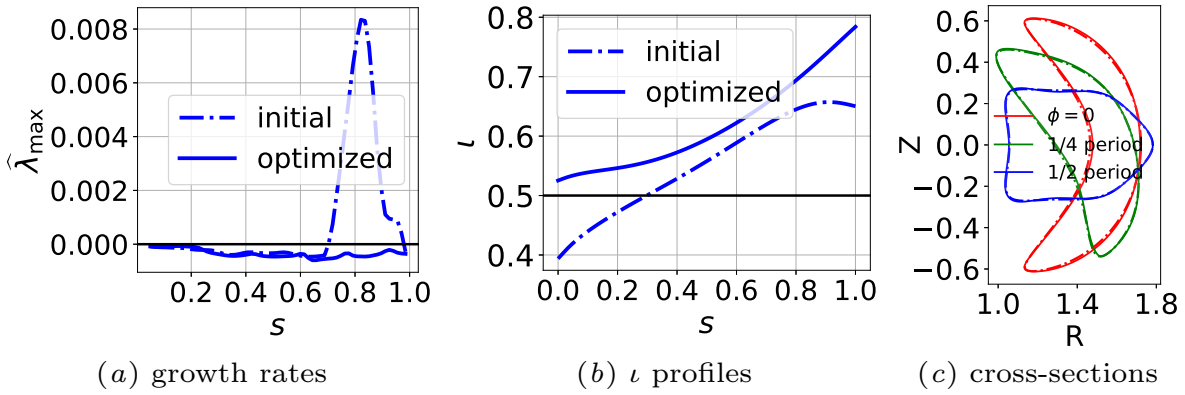


Figure 2.10: This figure shows (a) the maximum eigenvalue $\hat{\lambda}_{\text{max}}$ of the initial and optimized modified NCSX equilibrium. Similarly, in (b) we compare the rotational transform profiles of the initial and optimized equilibria. In (c), we present the boundary shape of the initial and final equilibria at three different value of the toroidal angle ϕ . The dotted curves correspond to the initial cross-sections whereas the solid curves are the final cross-sections.

The optimizer stabilizes the equilibrium mostly through negative global magnetic shear $\hat{s} = -2(s/\nu)(d\nu/ds)$. There is minimal change in the shape of the boundary. We also present a comparison of the important equilibrium-dependent quantities for the initial and optimized equilibria in table 2.6.

State	$\beta_{\text{ax}}(\%)$	$\langle\beta\rangle(\%)$	$j_\phi(\text{MA})$	$\langle B\rangle(\text{T})$	\bar{t}	A	$a_{\text{N}}(m)$	$\psi_{\text{b}}(Tm^2)$
Initial	9.3	5.1	0.174	1.596	0.48	4.36	0.325	0.514
Optim.	8.2	4.5	0.215	1.694	0.59	4.48	0.316	0.514

Table 2.6: This table presents a comparison between relevant physical quantities of the initial and optimized NCSX equilibrium

2.4.3 Stabilizing the modified Henneberg-QA equilibrium

As a final example, we present a modified modified Henneberg-QA equilibrium. In this example, we allow the boundary coefficients given in table 2.7 to change freely.

$\widehat{R}_{\text{b}}(n, m)$	$\widehat{Z}_{\text{b}}(n, m)$
$([1, 5], 0)$	$([1, 5], 0)$
$([-3, 3], 1)$	$([-3, 3], 1)$
$([-3, 3], 2)$	$([-3, 3], 2)$
$([-2, 2], 3)$	$([-2, 2], 3)$
$([-2, 2], 4)$	$([-2, 2], 4)$
$([-2, 2], 5)$	$([-2, 2], 5)$
$([-1, 1], 6)$	$([-1, 1], 6)$

Table 2.7: This table lists the boundary shape Dofs for the modified Henneberg-QA case.

We also have seven coefficients that determine the rotational transform profile, giving us a total of 83 Dofs. For this problem, we choose the following objective function

$$\mathcal{F} = 0.1f_{\text{asp}}^2 + 0.1f_{\text{minr}}^2 + f_{\langle B\rangle}^2 + 10^{-8}\mathcal{G}_{j_\zeta} + 5\mathcal{G}_l^2 + 10f_{\text{ball}}^2, \quad (2.60)$$

After choosing the Dofs and the objective function, we run SIMSOPT and obtain multiple sta-

ble equilibria. We compare one of the stable equilibria with the initial, unstable equilibrium in figure 2.11 and the equilibrium-dependent quantities in table 2.8.

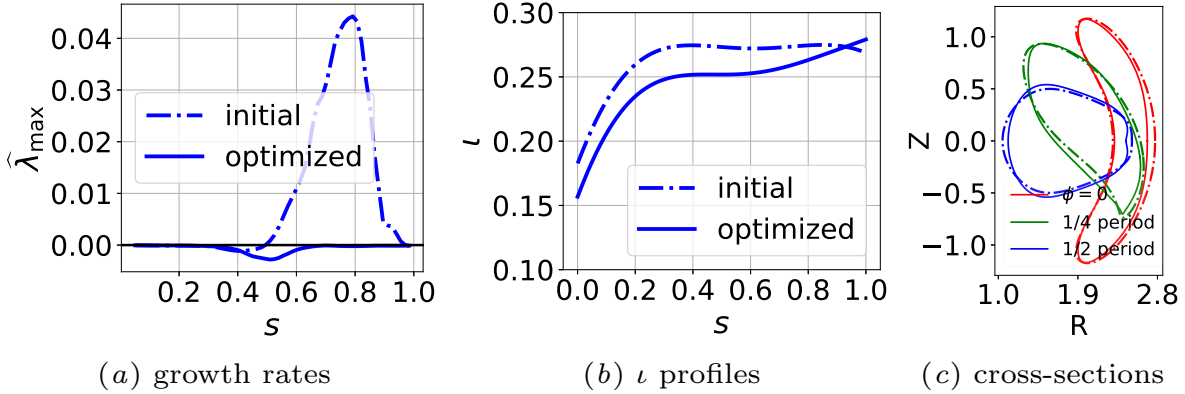


Figure 2.11: This figure shows (a) the maximum eigenvalue $\hat{\lambda}_{\max}$ of the initial and optimized modified Henneberg-QA equilibrium. Similarly, in (b) we compare the rotational transform profiles of the initial and optimized equilibria. In (c), we present the boundary shape of the initial and final equilibria at three different positions of the toroidal angle ϕ . The dotted curves correspond to the initial cross-sections whereas the solid curves are the final cross-sections.

State	$\beta_{\text{ax}}(\%)$	$\langle\beta\rangle(\%)$	$j_{\phi}(\text{MA})$	$\langle B\rangle(\text{T})$	$\bar{\tau}$	A	$a_{\text{N}}(\text{m})$	$\psi_{\text{b}}(\text{Tm}^2)$
Initial	4.9	2.65	0.235	2.501	0.263	3.374	0.601	2.677
Optim.	4.5	2.47	0.002	2.588	0.245	3.381	0.592	2.677

Table 2.8: This table shows a comparison between relevant physical quantities of the initial and optimized modified Henneberg-QA equilibrium

We find that the equilibrium is stabilized by a combination of boundary shaping and rotational transform. The rotation transform creates negative magnetic shear in the outer core, whereas the boundary shape reduces the curvature in the “bad”-curvature region.

2.5 Summary and Conclusions

We began this chapter by briefly explaining the ideal MHD model and various coordinate systems that we used to fully define a general 3D ideal MHD equilibrium. In §2.2.1, we gen-

erated three different equilibria: one axisymmetric 2D and two 3D, and described the important associated physical quantities that could be used to penalize large deviations or trivial solutions generated by the optimizer. In the following section, we briefly explain the linear stability analysis in ideal MHD and the two important limits classified according to the toroidal mode number n : low- n and the infinite- n modes.

In §2.3.2, we provided a physical description and explained the numerical methods used to calculate the eigenvalues. We also described the self-adjoint property of the ideal ballooning mode and using this property developed an adjoint method in §2.3.3 and used it to speed up the calculation of the maximum ballooning eigenvalue λ_{\max} on each surface for the three chosen equilibria. To demonstrate the efficiency and accuracy of the adjoint method, we also presented a comparison of gradients between an adjoint method and a finite difference scheme. We found that the adjoint method is up to four times faster than the finite-difference scheme.

In §2.3.4, we describe the details of the overall optimization process and how we do it using the SIMSOPT code. After implementing the optimization, we presented the results in §2.4. We presented the specific details of the objective function and the degrees of freedom (Dofs) for each equilibrium and stabilized the initial, ideal ballooning unstable equilibria. We briefly described the physical mechanism of the optimized equilibria that stabilize the ideal ballooning mode.

This work presents many avenues for future research. A key step forward is to extend our technique to include all equilibrium-dependent parameters \tilde{p} as explained in the appendix A.3. One could also use the exact same method to optimize stellarators and tokamaks against low- n , unstable ideal MHD modes, as explained in the appendix A.4. Since solving for low- n ideal MHD codes is much more computationally expensive, the advantage of using an adjoint method would be even greater. Another possible direction would be to use an adjoint method to get

derivatives of the ballooning growth rate with respect to the plasma shape. Finally, one could use the ideal balloon optimizer as a tool that could help optimize an equilibrium against Kinetic Ballooning Modes (KBM).

In context of ideal MHD stability, there has been a significant progress by Glasser [47, 48] in developing the DCON3D code, which is based on Newcomb's criterion (briefly explained in appendix D) to determine the stability of ideal MHD equilibria. This method determines the stability without calculating the maximum eigenvalue. Hence, DCON3D has the potential to determine stability much faster than our solver. However, it is not clear how to do gradient-based analysis or if we can apply our adjoint method to DCON3D. Therefore, in our quest to accelerate ideal MHD stability optimization, it would be crucial to compare our solver with DCON3D in the future.

Chapter 3: Kinetic microstability analysis of high- β equilibria

3.1 Overview

In this chapter, we will present a detailed kinetic microstability analysis of finite- β equilibria with a focus on high- β tokamaks and stellarators. We will start by introducing the δf gyrokinetic model. We will then linearize, Fourier-transform, and simplify the model and explain the origin and importance of drift waves. Next, we will use the numerical δf solver GS2 to solve the gyrokinetic model, first for six tokamak and then for two stellarator equilibria. It is important to point out that for all of this thesis, we will only investigate modes that have small wavelengths perpendicular to the field line, i.e., modes that are localized to a flux surface, henceforth referring to our study as a local stability analysis and the equilibria as local equilibria. The behavior of the most unstable mode could be different on different flux surfaces. Hence, we will study multiple flux surfaces for each equilibrium. For axisymmetric equilibria, we will vary the local equilibria using a semi-analytical technique and observe interesting behavior for the high- β equilibria — stabilization of the ITG and TEMs through two distinct mechanisms: large negative local shear and reversal of electron precession drift. Finally, we will solve the full linear electromagnetic gyrokinetic model for all the tokamak and stellarator equilibria at nominal values of the temperature and density gradients.

Using the results from the gyrokinetic analyses, we explore an important link between

the ideal and the Kinetic Ballooning Mode (KBM) [49], an electromagnetic mode observed in tokamaks and stellarators. To further understand this relationship, we analyze the equilibria against the infinite- n ideal ballooning mode and explain the connection between the ideal and kinetic ballooning modes.

3.2 Microstability analysis

This section contains the general theoretical and numerical details of our microstability analysis. In §3.2.1, we will explain the physical basis and theoretical details of the gyrokinetic model. In the next section, we will explain how the model is implemented numerically using the GS2 code and provide the general details of our numerical study.

3.2.1 The gyrokinetic model

The electromagnetic gyrokinetic model is a simplification of the 6D Vlasov-Maxwell system of equations that predict the self-consistent evolution of a distribution of charged particles and the resulting electromagnetic fields

$$\frac{\partial f_s}{\partial t} + \mathbf{w} \cdot \nabla f_s + \frac{d\mathbf{w}}{dt} \cdot \frac{\partial f_s}{\partial \mathbf{w}} = \sum_{s'} C_{s,s'}[f_s, f_{s'}], \quad (3.1)$$

$$-\nabla^2 \varphi = \sum_s Z_s e \int d^3 \mathbf{w} f_s, \quad (3.2)$$

$$-\nabla \mathbf{A} = \mu_0 \sum_s Z_s e \int d^3 \mathbf{w} \mathbf{w} f_s, \quad (3.3)$$

where $f_s(\mathbf{r}, \mathbf{w}, t)$ is the plasma distribution function for species s , $C_{s,s'}$ is the Coulomb collision operator, $\varphi(\mathbf{r}, t)$ is electrostatic potential such that the electric field is given by

$$\mathbf{E} = -\nabla\varphi - \frac{1}{c} \frac{\partial \mathbf{A}}{\partial t}, \quad (3.4)$$

and $\mathbf{A}(\mathbf{r}, t)$ is the magnetic vector potential such that the magnetic field,

$$\mathbf{B} = \nabla \times \mathbf{A}. \quad (3.5)$$

In this chapter, we work with Coulomb gauge, i.e., $\nabla \cdot \mathbf{A} = 0$. The general 6D Vlasov-Maxwell model has six independent variables (not including time t): three configuration space \mathbf{r} dimensions and three velocity-space dimensions \mathbf{w} . To reduce this to a 5D model, we first divide the distribution and the fields into an equilibrium component and a superimposed fluctuation

$$\begin{aligned} f_s &= F_{0s} + \delta f_s, & F_{0s} &= \frac{n_{0s} m_s^{3/2}}{(2\pi T_{0s})^{3/2}} \exp(-w^2/w_{\text{th},s}^2) \\ \mathbf{E} &= \mathbf{E}_0 + \delta \mathbf{E}, \\ \mathbf{B} &= \mathbf{B}_0 + \delta \mathbf{B}, \end{aligned} \quad (3.6)$$

where the equilibrium components have a subscript 0, $n_{0s}(\psi)$ is the equilibrium plasma density, $T_{0s}(\psi)$ is the equilibrium plasma temperature, $w_{\text{th},s} = \sqrt{2T_s/m_s}$ is the thermal speed and the perturbed fields

$$\delta \mathbf{E} = -\nabla \delta \varphi - \frac{\partial \delta \mathbf{A}}{\partial t}, \quad (3.7)$$

$$\delta \mathbf{B} = \nabla \times \nabla \delta \mathbf{A}. \quad (3.8)$$

The fluctuations δf_s , $\delta \mathbf{E}$, and $\delta \mathbf{B}$ are defined such that they vanish when averaged over length and time scales much larger than the length and times scales, ρ_s and $1/\omega$, respectively. This assumption is motivated by the importance of low-frequency, small-scale fluctuations in context of fusion plasmas [50].

Next, we choose a set of asymptotic orderings to further simplify the model. We define the small parameter

$$\tilde{\epsilon} \equiv \frac{\omega}{\Omega_s} \sim \frac{\rho_s}{a_N} \sim \frac{k_{\parallel}}{k_{\perp}} \sim \frac{\delta f_s}{F_{0s}} \sim \frac{Z_s e \varphi}{T_s} \sim \frac{|\delta \mathbf{B}|}{|\mathbf{B}_0|} \ll 1, \quad (3.9)$$

where $\Omega_s = (Z_s e B)/(m_s c)$ is the cyclotron frequency. The particle gyroradius ρ_s , given by

$$\rho_s \equiv \frac{w_{\text{th},s}}{\Omega_s}, \quad (3.10)$$

is the perpendicular length scale of the turbulent fluctuations. The length scale a_N is the effective minor radius, defined in §2.2.1. The wavenumbers of the mode perpendicular and parallel to the equilibrium magnetic field are denoted by k_{\perp} and k_{\parallel} , respectively. These orderings imply that the charges particles gyrate much faster than the time scales of interest. Therefore, we can average the Vlasov-Maxwell equations (3.1)-(3.3) over the fast gyromotion to obtain the gyrokinetic model.

In the small $\tilde{\epsilon}$ limit, one can reduce the dimensionality of the problem from 6D $(\mathbf{r}, w_{\perp}, w_{\parallel}, \vartheta)$ to 5D $(\mathbf{r}, w_{\perp}, w_{\parallel})$ by averaging the Vlasov-Maxwell system over the gyrophase ϑ . We mostly use the velocity coordinate system $(w_{\perp}, w_{\parallel}, \vartheta)$ instead of the Cartesian components (w_x, w_y, w_z) due to the cylindrical symmetry of the motion of charged particles around the field lines. For the new 5D coordinate system, we will transform back and forth between two different coordinates, the particle position and velocity coordinates $(\mathbf{r}, w_{\perp}, w_{\parallel}, t)$ and the guiding center coordinates

$(\mathbf{R}_s, E_s, \mu_s, t)$ where

$$E_s = \frac{1}{2}m_s w^2, \quad (3.11)$$

$$\mu_s = \frac{m_s w_\perp^2}{2B}, \quad (3.12)$$

are the total kinetic energy and the magnetic moment of the particle. The guiding center is given in terms of the particle position by the Catto transformation [51]

$$\mathbf{R}_s = \mathbf{r} - \frac{\mathbf{b} \times \mathbf{w}_\perp}{\Omega_s}, \quad (3.13)$$

where $\mathbf{w}_\perp = w_\perp(\cos(\vartheta)\hat{x} + \sin(\vartheta)\hat{y})$. The gyroaveraging operators $\langle \rangle_{\mathbf{R}_s}$ and $\langle \rangle_{\mathbf{r}}$

$$\langle X \rangle_{\mathbf{R}_s} = \frac{1}{2\pi} \int_0^{2\pi} X(\mathbf{r}) d\vartheta, \quad (3.14)$$

$$\langle X \rangle_{\mathbf{r}} = \frac{1}{2\pi} \int_0^{2\pi} X(\mathbf{R}_s) d\vartheta, \quad (3.15)$$

denote the average of X over a gyration period at fixed guiding center \mathbf{R}_s and at fixed position \mathbf{r} , respectively. It is also convenient to define the gyrokinetic model in terms of the parallel component δA_\parallel of the magnetic vector potential, the magnetic field strength fluctuation δB_\parallel

$$\delta B_\parallel = \mathbf{b} \cdot (\nabla \times \delta \mathbf{A}_\perp), \quad (3.16)$$

and the gyrokinetic distribution function in the guiding-center coordinate system $(\mathbf{R}_s, E_s, \mu_s, t)$

$$h_s(\mathbf{R}_s, E_s, \mu_s, t) = \frac{Z_s e \varphi(\mathbf{r}, t) F_{0s}}{T_s} + \delta f_s(\mathbf{R}_s, E_s, \mu_s, t). \quad (3.17)$$

Using these new fields and applying the gyroaveraging operator to (3.1)-(3.3), we can now introduce the δf gyrokinetic theory that was first derived for the linear electromagnetic case by Antonsen and Lane [52] and the nonlinear case by Frieman and Chen [53]. For a linearized model, following the notation of Abel *et al.* [54], we get the governing equations

$$\frac{\partial h_s}{\partial t} + (w_{\parallel} \mathbf{b} + \mathbf{v}_{Ds}) \cdot \frac{\partial h_s}{\partial \mathbf{R}_s} = \frac{Z_s e F_{0s}}{T_s} \frac{\partial \langle \varphi - \mathbf{w} \cdot \delta \mathbf{A} / c \rangle_{\mathbf{R}_s}}{\partial t} - \mathbf{V}_E \cdot \nabla F_{0s} + \langle C_s[h_s] \rangle_{\mathbf{R}_s}, \quad (3.18)$$

$$\sum_s \frac{(Z_s e)^2 \varphi}{T_s} = \sum_s Z_s e \int d^3 \mathbf{w} \langle h_s \rangle_{\mathbf{r}}, \quad \tau = \frac{T_e}{T_i}, \quad (3.19)$$

$$-\nabla_{\perp}^2 \delta A_{\parallel} = \frac{4\pi}{c} \sum_s Z_s e \int d^3 \mathbf{w} w_{\parallel} \langle h_s \rangle_{\mathbf{r}}, \quad (3.20)$$

$$\nabla_{\perp}^2 \frac{\delta B_{\parallel} B}{4\pi} = -\nabla_{\perp} \nabla_{\perp} : \sum_s \int d^3 \mathbf{w} \langle m_s \mathbf{w}_{\perp} \mathbf{w}_{\perp} h_s \rangle_{\mathbf{r}}, \quad (3.21)$$

where the velocity integrals in (3.19) are taken at fixed \mathbf{r} . The velocities \mathbf{V}_E and \mathbf{v}_{Ds} are the $\mathbf{E} \times \mathbf{B}$ and the magnetic drift velocities, respectively:

$$\mathbf{V}_E = \frac{c}{B} \mathbf{b} \times \langle \nabla \varphi \rangle_{\mathbf{R}_s} - \frac{1}{B} \mathbf{b} \times \langle \nabla (\mathbf{w} \cdot \delta \mathbf{A}) \rangle_{\mathbf{R}_s}, \quad (3.22)$$

$$\mathbf{v}_{Ds} = \frac{w_{\parallel}^2}{\Omega_s} \mathbf{b} \times (\mathbf{b} \cdot \nabla \mathbf{b}) + \frac{w_{\perp}^2}{2\Omega_s} \frac{\mathbf{b} \times \nabla B}{B}. \quad (3.23)$$

Throughout this study, we use the linearized Coulomb operator obtained by Abel *et al.* [55] instead of the full nonlinear collision operator.

We have now fully defined the linear gyrokinetic system. The gyrokinetic model is a good approximation for the core region of a tokamak plasma in which our study is being carried out [17, 18]. We solve the gyrokinetic model in a 3-D flux tube, a tube with a rhombus-shaped cross section following the field line. The appropriate length of the flux tube and the boundary conditions at the ends are determined using the ideas developed by Beer *et al.* [56]. All the fluctuating quantities are assumed to be periodic perpendicular to the field line. This allows us to further simplify (3.18) by writing the fluctuating quantities as Fourier series

$$\begin{aligned}
h_s &= \sum_k h_{k_\perp, s}(\theta, E, \mu, t) \exp(i\mathbf{k}_\perp \cdot \mathbf{R}_s), \\
\varphi &= \sum_k \varphi_{k_\perp}(\theta, t) \exp(i\mathbf{k}_\perp \cdot \mathbf{r}), \\
\delta A_\parallel &= \sum_k \delta A_{\parallel, k_\perp}(\theta, t) \exp(i\mathbf{k}_\perp \cdot \mathbf{r}), \\
\delta B_\parallel &= \sum_k \delta B_{\parallel, k_\perp}(\theta, t) \exp(i\mathbf{k}_\perp \cdot \mathbf{r}).
\end{aligned} \tag{3.24}$$

Applying this ansatz to (3.18) and using the identities given below

$$\mathbf{w}_\perp = w_\perp \left(-\cos(\vartheta) \frac{\mathbf{b} \times \mathbf{k}_\perp}{k_\perp} + \sin(\vartheta) \frac{\mathbf{k}_\perp}{k_\perp} \right), \tag{3.25}$$

$$\int_0^{2\pi} d\vartheta \exp\left(\mp \frac{ik_\perp v_\perp \cos(\vartheta)}{\Omega_s}\right) = J_{0s} \left(\frac{k_\perp v_\perp}{\Omega_s} \right), \tag{3.26}$$

$$\int_0^{2\pi} d\vartheta \cos(\vartheta) \exp\left(-\frac{ik_\perp w_\perp \cos(\vartheta)}{\Omega_s}\right) = -iJ_1 \left(\frac{k_\perp w_\perp}{\Omega_s} \right), \tag{3.27}$$

$$\int_0^{2\pi} d\vartheta \cos^2(\vartheta) \exp\left(-\frac{ik_\perp w_\perp \cos(\vartheta)}{\Omega_s}\right) = \frac{\Omega_s}{k_\perp w_\perp} J_1, \tag{3.28}$$

$$\int_0^{2\pi} d\vartheta \sin(2\vartheta) \exp\left(-\frac{ik_\perp w_\perp \cos(\vartheta)}{\Omega_s}\right) = 0. \tag{3.29}$$

Using these identities, we obtain the linearized, Fourier-transformed gyrokinetic model

$$\begin{aligned} \left(\frac{\partial}{\partial t} - i\omega_{Ds} \right) h_{k_{\perp},s} + (\mathbf{b} \cdot \nabla \theta) w_{\parallel} \frac{\partial h_{k_{\perp},s}}{\partial \theta} = & \left\{ \frac{\partial}{\partial t} - i\omega_{*,s} \left[1 + \eta_s \left(\frac{E_s}{T_s} - \frac{3}{2} \right) \right] \right\} \times \\ & \left[J_0 \left(\frac{k_{\perp} w_{\perp}}{\Omega_s} \right) \left(\varphi_{k_{\perp}} - \frac{w_{\parallel} \delta A_{\parallel}}{c} \right) + J_1 \left(\frac{k_{\perp} w_{\perp}}{\Omega_s} \right) \frac{w_{\perp} \delta B_{\parallel}}{k_{\perp} c} \right] F_{0s} \\ & + \left\langle e^{-i(\mathbf{k} \cdot \frac{\mathbf{b} \times \mathbf{w}_{\perp}}{\Omega_s})} C \left[e^{i(\mathbf{k} \cdot \frac{\mathbf{b} \times \mathbf{w}_{\perp}}{\Omega_s})} h_{k_{\perp},s} \right] \right\rangle_{\mathbf{R}_s}, \end{aligned} \quad (3.30)$$

$$\sum_s \frac{q_s^2 N_s \delta \varphi_{k_{\perp}}}{T_s} = \sum_s q_s \int d^3 \mathbf{v} J_0 h_{s,k_{\perp}}, \quad (3.31)$$

$$k_{\perp}^2 A_{\parallel,k_{\perp}} = \sum_s \frac{4\pi q_s}{c} \int d^3 \mathbf{v} v_{\parallel} J_0 h_{s,k_{\perp}}, \quad (3.32)$$

$$\frac{B}{4\pi} \delta B_{\parallel,k_{\perp}} = - \sum_s \int d^3 \mathbf{v} v_{\perp}^2 \frac{M_s J_1 \Omega_s}{k_{\perp} v_{\perp}} h_{s,k_{\perp}}. \quad (3.33)$$

Here,

$$\omega_{Ds} = \mathbf{k}_{\perp} \cdot \mathbf{v}_{Ds}, \quad (3.34)$$

is the magnetic drift frequency, and $J_0(k_{\perp} \rho_s)$ and $J_1(k_{\perp} \rho_s)$ are the zeroth- and first-order cylindrical Bessel functions, respectively,

$$\frac{a_N}{L_{Ts}} = - \frac{d \log(T_s)}{d\rho}, \quad \frac{a_N}{L_{ns}} = - \frac{d \log(n_s)}{d\rho}, \quad \eta_s = \frac{L_{ns}}{L_{Ts}}, \quad (3.35)$$

and $\rho = \sqrt{s} = \sqrt{\psi/\psi_b}$

$$\omega_{*,s} = \frac{T_s}{Z_s e B} [(\mathbf{b} \times \mathbf{k}_{\perp}) \cdot \nabla \log n_s]. \quad (3.36)$$

For this study, we choose a Hydrogen plasma, i.e., $Z_i = 1, Z_e = -1$. The variables L_{ns} and L_{Ts} are the density and temperature gradient scale lengths. The quantity $\omega_{*,s}$, the diamagnetic

drift frequency, is the typical frequency of a drift wave — waves caused due to gradients in temperature or density. For these modes

$$\frac{\partial}{\partial t} \sim \omega \sim \frac{v_{\text{th},s}}{a_N} \sim \omega_{*,s}. \quad (3.37)$$

All the different instabilities we study using the gyrokinetic model are a result of destabilized drift waves. Instabilities are characterized by the degree to which charged species and electromagnetic fields contribute to a drift wave.

In this chapter, we will first investigate collisionless electrostatic instabilities such as the Temperature Gradient (ITG) mode and the Trapped Electron Mode (TEM). For purely electrostatic modes, we solve equations (3.18)-(3.19) only and assume the magnetic fluctuations, δA_{\parallel} and δB_{\parallel} to be absent. After an electrostatic stability analysis, we investigate the effect of magnetic fluctuations by solving the full set of equations (3.18)-(3.21). To ensure that our observations can be generalized to stellarator equilibria, we will then solve the full linear, collisionless gyrokinetic model for various high- β , quasisymmetric stellarator equilibria. The procedure for numerically solving the gyrokinetic model is explained in the following section.

3.2.2 Kinetic stability analysis with GS2

GS2¹ [57, 58, 59, 60] is a parallel code that solves the gyrokinetic model as an initial-value problem. It solves equations (3.18)-(3.21) numerically by calculating the evolution of an initial perturbation inside a flux tube.

Before each run, one has to specify the value of the gradient scale lengths $a_N/L_{n,s}$, $a_N/L_{T,s}$,

¹The GS2 version used for this study is freely available at <https://zenodo.org/record/4461680>.

the range of normalized wavenumbers $k_{\perp}\rho_i$ and various geometric coefficients as a function of θ . The values of these inputs are specific to the linear mode under consideration and will be provided in the following sections. Since we are only studying stability against fluctuations that vary on a small perpendicular scale $k_{\perp}\rho_i \sim 1$, we can get the geometric coefficients from the equilibria in a manner similar to the ideal ballooning stability analysis performed in the previous chapter.²

The perpendicular structure of different fluctuations is defined by defining the wavevector \mathbf{k}_{\perp} that can be written as

$$\mathbf{k}_{\perp} = k_y \nabla y + k_x \nabla x. \quad (3.38)$$

where x and y are normalized forms of the coordinates ψ and α , respectively. For microstability analysis of axisymmetric equilibria, we assume $k_x = 0$, i.e., modes with no variation in the radial direction at $\theta_0 = 0$.³ We choose around 15 – 25 values of $k_y\rho_i$ in the range $k_y\rho_i = 0.05 - 6$. All of our simulations are well resolved in θ and well converged as can be seen in figure 3.1. For this study, $\theta \in [-19\pi, 19\pi]$ and more than 450 points along the θ grid for tokamak equilibria and $\theta \in [-5\pi, 5\pi]$ and more than 400 points for stellarators, unless otherwise noted.

For the velocity space structure GS2 uses an (E, λ) grid instead of the $(w_{\parallel}, w_{\perp})$ grid. The pitch angle as

$$\lambda = \frac{\mu}{E}, \quad (3.39)$$

For trapped particles $\lambda = \lambda(\theta_b)$ where θ_b is the bounce angle — the value of θ at which a trapped

²Our VMEC to GS2 interface for calculating the geometric coefficients is freely available at <https://github.com/rahulgaur104/VMEC2GK>.

³This is equivalent to choosing $\theta_0 = 0$ in the ideal ballooning study. The parameter $\theta_0 \sim k_x/k_y$ denotes the tilt of a turbulent eddy with respect to the $\nabla\psi$ direction. In axisymmetric, up-down symmetric equilibria, the most unstable modes almost always lie at $\theta_0 = 0$.

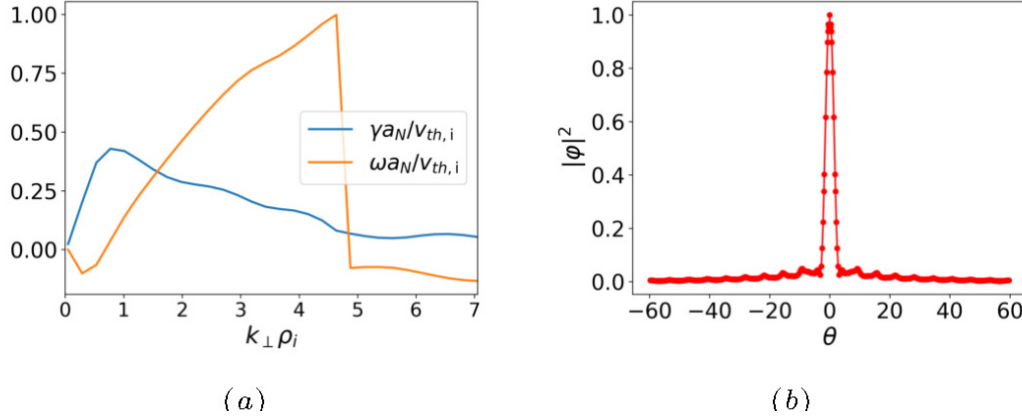


Figure 3.1: This figure shows (a) the output from a typical electrostatic GS2 run showing the normalized frequency and growth rate spectrum with both electron-gradient- ($\omega a_N/v_{th,i} < 0$) and ion-gradient-driven ($\omega a_N/v_{th,i} > 0$) instabilities and (b) showing the variation along the field line of the square of the normalized electrostatic potential $|\varphi|^2$. We can see that the potential is well resolved and decays sufficiently before reaching the boundaries.

particle with a pitch angle λ reflects back from a region of high magnetic field. For a given trapped pitch angle λ , the bounce angle is defined such that $B(\theta_b) = 1/\lambda$. In GS2, resolution of the passing particle distribution in the coordinate λ is set by the variable `nlambda`. We set `nlambda` = 12. For the trapped particle distribution, we choose 11 bounce points. Similarly, for energy-space resolution, we set the value of the GS2 variable `negrid` = 10.⁴ We choose 27 points along the flux tube for tokamaks and 40 for stellarators, for every 2π interval to ensure sufficient resolution along the field line. This completely defines the resolution in GS2.

In figure 3.1, we show the results from a typical GS2 run. After each run, one obtains the normalized growth rate $\gamma a_N/v_{th,i}$, the wave frequency $\omega a_N/v_{th,i}$, the electrostatic potential eigenfunction $\varphi(\theta, t)$ for electrostatic runs and $\varphi(\theta, t)$, $\delta A_{\parallel}(\theta, t)$, and $\delta B_{\parallel}(\theta, t)$ for electromag-

⁴For the sake of brevity, we have avoided explaining the details of the velocity grid. These details and resolution requirements can be found in Highcock [60].

netic runs. We also obtain the quasilinear particle and heat fluxes for each mode

$$\Gamma_{s,k_y} = \int \frac{d\theta}{\mathbf{B} \cdot \nabla \theta} \int d^3\mathbf{w} (\mathbf{V}_{E,k_y} \cdot \nabla \psi) h_{s,k_y}, \quad (3.40)$$

$$Q_{s,k_y} = \int \frac{d\theta}{\mathbf{B} \cdot \nabla \theta} \int d^3\mathbf{w} (\mathbf{V}_{E,k_y} \cdot \nabla \psi) E_s h_{s,k_y}, \quad (3.41)$$

where the subscript k_y denotes the mode k_y in the Fourier space. These quantities can be used to extract information about an unstable mode [61]. Since this is a linear study, the absolute values of the fluxes do not contain useful information, but their ratio $\Gamma_{s,k_y}/Q_{s,k_y}$ can still be used to characterize the type of instability. We will use this ratio for the TEM study in §3.3.2.

3.2.3 The Greene-Chance analysis

To better understand the stability of a local axisymmetric equilibrium, we use the ability to vary that equilibrium. For axisymmetric equilibria, this can be done by changing the magnetic shear and pressure gradient radially locally, independently about their nominal values — equivalent to varying the gradients of both the local current and plasma pressure — quantities that determine the solution to (2.14). This gives us the ability to generate multiple local equilibria satisfying the Grad-Shafranov equation and do a stability analysis without recalculating the global equilibrium. We define

$$\hat{s} = \frac{\rho}{q} \frac{dq}{d\rho}, \quad (3.42)$$

$$\alpha_{\text{MHD}} = -\frac{2\mu_0\rho q^2}{\epsilon B_N^2} \frac{dp}{d\rho} \quad (3.43)$$

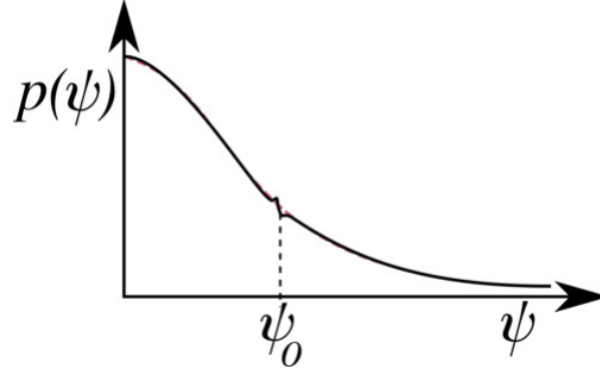


Figure 3.2: This figure summarizes the idea of Greene and Chance. The new pressure profile (black) with localized variation over the flux surface $\psi = \psi_0$ lies over the equilibrium profile (dashed red). Although the variation in pressure at $\psi = \psi_0$ is small, the change in pressure *gradient* can be large.

as the magnetic shear and pressure gradient, respectively. This method of varying a local equilibrium through \hat{s} and α_{MHD} is known as an $\hat{s} - \alpha_{\text{MHD}}$ analysis. This technique was developed by Greene and Chance [62] and has been used extensively to study local stability of different axisymmetric equilibria [15, 41, 63, 64]. Figure 3.2 illustrates the main point — we can change the gradient of the pressure and the safety factor locally by a finite amount without significantly changing their respective values. We will use this idea again in §3.3.1 and §3.3.2 to vary the pressure gradient at the nominal magnetic shear when we examine the microstability of different equilibria and later in §3.5 to analyze the ideal ballooning stability of all the axisymmetric equilibria. Details explaining the Greene-Chance analysis are given in appendix B.

3.3 High- β axisymmetric equilibria

As mentioned in the abstract, for a fixed magnetic field strength, the power density of a tokamak P scales as β^2 . Present day tokamaks are low- β devices. The achievable β is typically limited by plasma instabilities. These can lead to disruptions or large turbulent transport. The

higher β is, the higher the pressure and current are and therefore the larger the free energy available to drive these instabilities is. If these problems could be overcome, high- β operation could be an attractive choice for future high-power density [65] devices.

The high-beta, $\beta \sim 1$, regime has previously been explored in the context of asymptotic magnetohydrodynamic (MHD) equilibria by solving the Grad-Shafranov equation in the limit $\epsilon/(\beta q^2) \ll 1$ [3]. There have also been experimental explorations [66, 67] of high- β operation of the MAST and START tokamaks. There have only been a few studies [68, 69] that investigated the process of accessing these states while maintaining ideal-MHD stability; even fewer studies that study the microstability properties of $\beta \sim 1$ equilibria in detail [70]. Therefore, a detailed numerical analysis of these types of equilibria is required.

To this end, in this section, we generate a set of high- β equilibria and study their susceptibility to local gyrokinetic and ideal MHD instabilities. First, we perform linear gyrokinetic analyses against various electrostatic and electromagnetic modes of instability in these equilibria. These modes are known to cause significant heat and particle transport in existing devices [17, 18]. To understand the electromagnetic modes, specifically their susceptibility to the Kinetic Ballooning Mode (KBM), we also study the stability of these equilibria against the infinite- n , ideal ballooning mode.

To create high- β equilibria, one may start with analytical solutions of the Grad-Shafranov equation. The most general analytical solution in the $\beta \sim 1$ limit was obtained by Hsu, Artun, and Cowley [3]. However, these analytical $\beta \sim 1$ equilibria are unfit for our study, as the geometric quantities required for a local stability analysis can be discontinuous and deviate significantly from the exact numerical solution. We briefly explain the analytical procedure used to calculate such equilibria and their limitations in appendix C. To avoid these issues, we will use the

$n_0(m^{-3})$	ν_n	$T_0(eV)$	ν_T	q_0	ν_q	$\psi_{\text{LCFS}}(Tm^2)$
5×10^{20}	0.4	10	1.1	1.6	1.2	1.0

Table 3.1: This table contains input parameters used for the VMEC equilibria. Throughout this study, in this table, every parameter remains fixed.

equilibrium solver VMEC to generate high- β , axisymmetric equilibria.

We produce high-radial-resolution equilibria using the fixed-boundary solver in VMEC after providing it with an L-mode-like pressure profile $p = p(s)$ — a profile that does not have a sudden drop in pressure over a short radial distance, a monotonic safety factor $q = q(s)$ profile as a function of the normalized toroidal flux $s = \psi/\psi_{\text{LCFS}}$, and the LCFS shape. We choose a simple form for the profiles $p = p(s)$ and $q = q(s)$ given by

$$\begin{aligned}
p &= nT, & p_0 &= \tilde{p}_0 n_0 T_0 \\
n(s) &= n_0(1 + \nu_n)(1 - s^2)^{\nu_n}, & T(s) &= T_0(1 + \nu_T)(1 - s^2)^{\nu_T} \\
q &= q_0(1 + s^{2\nu_q})^{1/(2\nu_q)}.
\end{aligned} \tag{3.44}$$

The different parameters are given in the table 3.1. The parameter $\tilde{p}_0 \in [1, 10, 70]$ for the low, intermediate, and high-beta equilibria, respectively. For each triangularity value, we choose a different LCFS shape described by a Miller parameterization [63]

$$\begin{aligned}
R &= R_0 + a \cos(t + (\sin^{-1} \delta) \sin t), \\
Z &= a\kappa \sin(t).
\end{aligned} \tag{3.45}$$

The parameter t varies from $[-\pi, \pi)$. The values of the rest of the parameters in (3.45) are given in table 3.2. The radial coordinate that we will use for all the stability analyses is $\rho = \sqrt{s} =$

$R_0(m)$	$a(m)$	δ	κ
1.6	0.6	± 0.4	1.3

Table 3.2: This table contains the Miller parameters for the outer boundary

$\sqrt{\psi/\psi_{\text{LCFS}}}$ since it is a better measure of the radial distance from the magnetic axis than the normalized poloidal flux ψ/ψ_{LCFS} . The safety factor and pressure profiles as a function of ρ are given in figure 3.3.

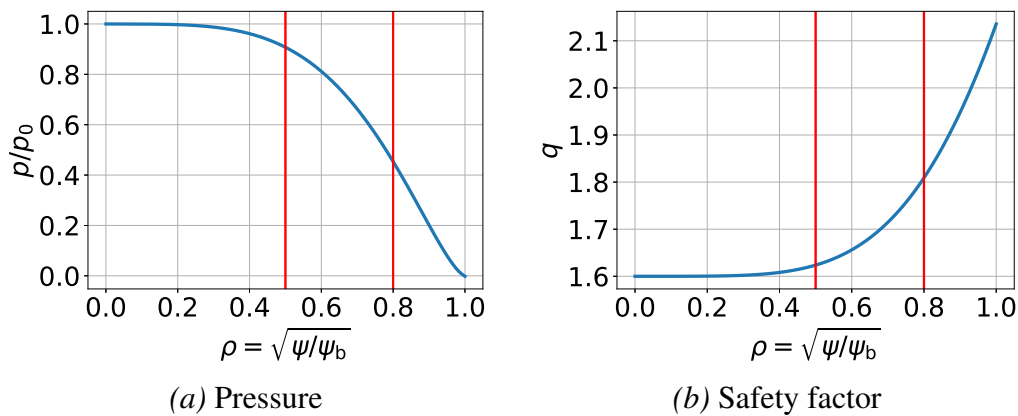


Figure 3.3: This figure shows the safety factor and normalized pressure profiles used for creating the equilibria. The two red lines correspond to the values of the normalized radius ρ at which the local equilibria will be analyzed for their stability.

For all our studies, we use the same safety factor q and the normalized pressure profile p with different values of \tilde{p}_0 . In this way, we are able to create three different pressure profiles with on-axis $\beta \sim 0.01, 0.1, 1$ corresponding to $\tilde{p}_0 = 1, 10, 70$, respectively. Henceforth, we shall refer to the equilibria with $\tilde{p}_0 = 1, 10, 70$ as low, intermediate and high- β or $\beta \sim 0.01, \beta \sim 0.1$ and $\beta \sim 1$, respectively. We need to pick flux surfaces for our local stability analyses. In this study, we choose surfaces at normalized radii $\rho = 0.5$ and 0.8 . In total, there are twelve local equilibria in our study: 3β values $\times 2$ boundary shapes $\times 2 \rho$ values. Because β varies over a flux surface, it will be convenient to introduce a reference magnetic field for each global equilibrium

and redefine

$$\beta(\rho) = 2\mu_0 p(\rho)/B_N^2, \quad (3.46)$$

$$B_N = \psi_{\text{LCFS}}/(\pi a_N^2), \quad (3.47)$$

where B_N is a reference magnetic field and a_N is the effective minor radius such that πa_N^2 is equal to the area enclosed by the boundary and ψ_{LCFS} is the toroidal flux enclosed by the LCFS. For this study, $a_N = 0.684 \text{ m}$, $B_N = 0.681 \text{ T}$. The values of β obtained from VMEC are given in table 3.3.

δ	ρ	Low- β	Intermediate- β	High- β
0.4	0.5	0.011	0.11	0.77
0.4	0.8	0.006	0.064	0.45
-0.4	0.5	0.011	0.11	0.77
-0.4	0.8	0.006	0.064	0.45

Table 3.3: This table contains the normalized β values on selected flux surfaces

Each equilibrium has 512 surfaces with each surface represented by 40 poloidal modes. We found that the equilibria converged with this choice of resolution. All the equilibria that we investigate in this study are up-down symmetric which is why we only show the upper half. The flux surface contours for the twelve equilibria are shown in figure 3.4.

The numerical high- β equilibria show qualitative features like the vertical “core” on the inboard side and thin boundary layer on the outboard side as shown by Hsu *et al.* It is interesting to see that the negative triangularity equilibria high- β equilibria are more strongly shaped than the positive triangularity ones — the vertical inboard solution causes the flux surface to develop

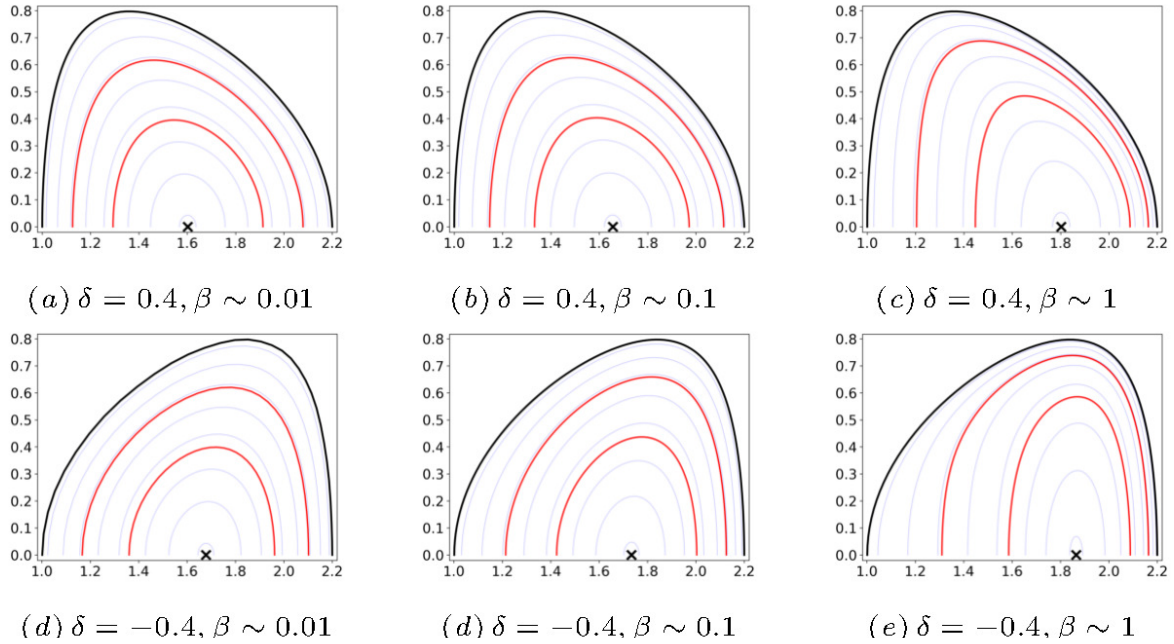


Figure 3.4: This figure shows the flux surfaces for all equilibria generated using VMEC. The local equilibria that will be studied in this paper are highlighted in red. The magnetic axis in each figure is the black cross.

a “squareness”. We illustrate the “squareness” in figure 3.5⁵.

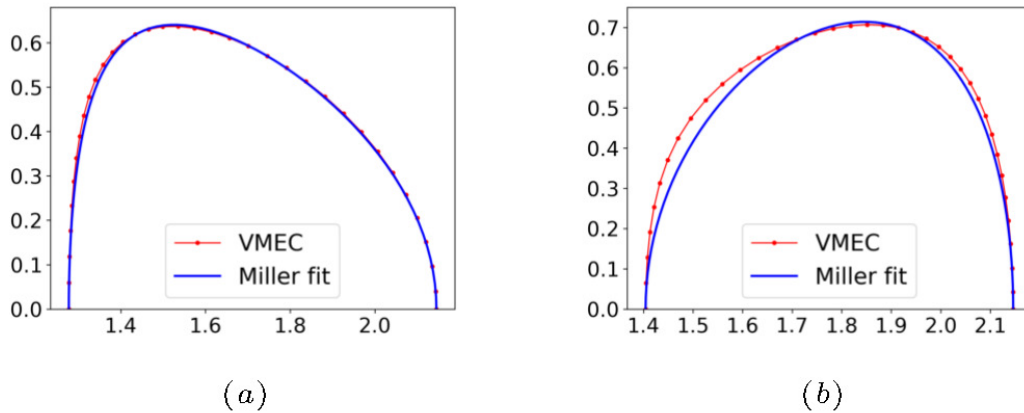


Figure 3.5: This figure shows two high- β equilibria and their corresponding best-Miller-fit. We can see that the fit for the negative triangularity is worse due to the “squareness” of the flux surface on the inboard side. The agreement between gradients of various physical quantities will be even worse.

⁵Note that we use Miller fit in figure 3.5 to demonstrate the strong shaping of high- β equilibria. We do not use Miller parametrization to calculate geometric coefficients in this thesis.

Most importantly, these numerical equilibria do not suffer from any of the issues observed in analytical high- β equilibria (discussed in appendix C) such as the ones obtained by Hsu et al [3]. Therefore, all the resulting geometric coefficients are smooth, which allows for the local stability analyses in the following sections.

3.3.1 ITG study

This section contains the results and analysis of the ITG study of the equilibria that we obtained in §3.3. In §3.3.1.1, we will present the specific details, including the values of different parameters used for the simulation and the reasoning behind our choices. In §3.3.1.2, we will introduce the local magnetic shear, a quantity that characterizes the stability of an equilibrium to the ITG mode. In the final section, we will plot and compare the results of all the different local equilibria and explain the stability of the high- β equilibria.

3.3.1.1 Details of the study

The most important form of electrostatic instability that arises at low wavenumbers, the ITG [71], occurs when a drift wave becomes unstable due to a large ion temperature gradient, i.e., large a_N/L_{T_i} . Therefore, our objective is to understand this mode by doing a scan in the temperature gradient scale length, a_N/L_{T_i} . Using the definition of the pressure $p_s = n_s T_s$, we can write

$$\frac{a_N}{L_{p_s}} \equiv -\frac{d \log(p)}{d\rho} = -\frac{d \log(T_s)}{d\rho} - \frac{d \log(n_s)}{d\rho} = a_N \left(\frac{1}{L_{n_s}} + \frac{1}{L_{T_s}} \right). \quad (3.48)$$

Using the equation above along with (3.43), we can write

$$\alpha_{\text{MHD}} = \frac{\beta}{2} \sum_s \frac{a_N}{L_{p_s}} \frac{\rho q^2}{2\mu_0 \epsilon}. \quad (3.49)$$

Furthermore, recall that we can vary the normalized pressure gradient α_{MHD} for a local equilibrium using the idea of Greene and Chance without recalculating the global equilibrium. This gives us the ability to self-consistently vary the temperature and density gradient scale lengths for a fixed β as long as we recalculate the local equilibrium for the resulting value of α_{MHD} .⁶

Table 3.3 contains the nominal density, temperature and pressure gradient scale lengths, denoted $a_N/L_{n_i}^{\text{nom}}$, $a_N/L_{T_i}^{\text{nom}}$ and $a_N/L_{p_i}^{\text{nom}}$, respectively.

ρ	$a_N/L_{T_i}^{\text{nom}}$	$a_N/L_{n_i}^{\text{nom}}$	$a_N/L_{p_i}^{\text{nom}}$	$a_N/L_{T_e}^{\text{nom}}$	$a_N/L_{n_e}^{\text{nom}}$	$a_N/L_{p_e}^{\text{nom}}$
0.5	0.59	0.21	0.80	0.59	0.21	0.80
0.8	3.00	1.09	4.09	3.09	1.09	4.09

Table 3.4: This table contains the nominal gradient scale length values

These are the values obtained from the original local equilibrium generated by VMEC and are exactly the same for all the different beta and triangularity values. For the ITG mode study, we define

$$\text{fac} = \frac{dP}{d\rho} / \left(\frac{dP}{d\rho} \right)_{\text{nom}}, \quad (3.50)$$

as the ratio of actual pressure to the nominal pressure. We choose $\text{fac} = (0.5, 1, 2, 4, 8)$ times the nominal pressure gradient for $\rho = 0.5$ and $\text{fac} = (0.5, 1, 2, 4)$ times the nominal pressure gradient for $\rho = 0.8$. For each pressure gradient, we choose two density gradient scale lengths —

⁶Maintaining self-consistency is crucial to all local analyses. Violating (3.48) can lead to specious, nonphysical instabilities [72].

the nominal and half of the nominal value from the local VMEC equilibrium while varying the temperature gradient scale length consistently for each gradient scale length. Tables 3.5 and 3.6 contain the resulting values.

a_N/L_{n_i}	a_N/L_{T_i}				
0.21	0.19	0.59	1.39	2.98	6.19
0.10	0.29	0.69	1.49	3.08	6.29

Table 3.5: This table contains the values of a/L_{T_i} at $\rho = 0.5$ for the ITG study

a_N/L_{n_i}	a_N/L_{T_i}			
1.09	0.95	3.00	7.10	15.27
0.54	1.50	3.55	7.64	15.82

Table 3.6: This table contains the values of a/L_{T_i} at $\rho = 0.8$ for the ITG study

These 18 values of various scale lengths are exactly the same for all triangularities as well as for all the different beta values due to the way we have defined ρ . From previous observations and studies, we know that the typical peak ITG growth rate lies around $k_y \rho_i = 1$. To capture the maximum growth rate, we calculate the growth rates in the range $k_y \rho_i \in [0.05, 2]$. For ITG, we have made the common assumption of adiabatic electrons to exclude the effect of kinetic electrons on the ITG mode and avoid other modes such as the TEM. Mathematically, this means that one assumes $h_{e,k_y} = 0$ when solving equation (3.30) for the electrons.

With the values given in tables 3.5 and 3.6, we run GS2 in the electrostatic limit ($\delta A_{\parallel} = 0, \delta B_{\parallel} = 0$) and obtain the maximum normalized growth rate $\gamma a_N/v_{th,i}$ for each of the 108 cases, 18 for each beta and each triangularity value. The results showing the comparison between different beta values, boundary shapes and normalized radii will be shown in §3.3.1.3. We expect the equilibria to become more stable to the ITG mode as we increase β . This behavior is well

known [73, 74] in the literature for low and intermediate- β equilibria. To try and explain this trend, in the next section, we look at the local shear as a characteristic quantity that explains the stabilization of the ITG mode with increasing β .

3.3.1.2 Characterizing stability to the ITG mode

In this section, we define and plot an important quantity, the local magnetic shear [62], which will help us understand the response of a local equilibrium to the ITG mode. We use the local shear since negative global shear \hat{s} is known to stabilize ITG [75]. In the following section, we will plot the local shear as a function of θ_{geo} at the nominal \hat{s} and α_{MHD} for the high- β equilibria and compare it with the low, intermediate and a low- β shifted-circle equilibrium (abbreviated as SC in the plots). We will show that the behavior of ITG is directly related to the local shear and argue that a large negative local shear over a wide range along the field lines stabilizes the ITG mode. Mathematically, the local shear ν is given by [16, 62]

$$\nu = -\mathbf{B} \cdot \nabla_{\text{N}} \left(\frac{\nabla_{\text{N}}\alpha \cdot \nabla_{\text{N}}\psi}{|\nabla_{\text{N}}\psi|^2} \right), \quad (3.51)$$

where $\nabla_{\text{N}} = a_{\text{N}}\nabla$ is used to non-dimensionalize ν . We will plot the local shear as a function of the geometric poloidal angle defined in the figure 3.6. The coordinate θ_{geo} is advantageous as it, unlike θ , is a physically intuitive poloidal angle. Mathematically, θ_{geo} is a monotonic function of θ — $\nu(\theta)$ can always be transformed to $\nu(\theta_{\text{geo}})$ and vice versa. To plot ν with respect to θ_{geo} , we further simplify (3.51)

$$\nu = -\frac{F}{qR^2} \left[\left(\frac{qF'}{F} + F'F \frac{q}{(R_s B_{\text{ps}})^2} \right) + \frac{qp'}{B_{\text{ps}}^2} + \frac{2q}{R_s B_{\text{ps}}} \left(\frac{\sin(u)}{R_s} - \frac{1}{R_c} \right) \right]. \quad (3.52)$$

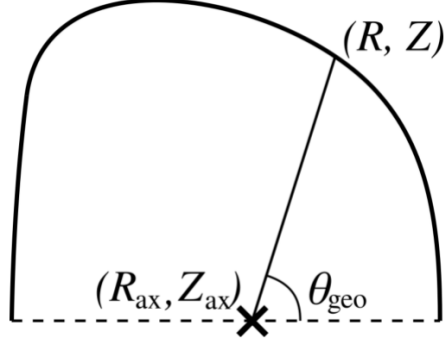


Figure 3.6: This figure illustrates the definition of θ_{geo} . The coordinates of the magnetic axis, marked with a cross, are $(R_{\text{ax}}, Z_{\text{ax}})$.

The symbols used and the formalism needed to derive (3.52) is given in appendix B. It is important to note that

$$\hat{s} = \frac{\rho |\nabla_{\text{N}} \psi|}{2\pi q a_{\text{N}}^2} \int_0^{2\pi} \frac{d\theta}{\mathbf{B} \cdot \nabla_{\text{N}} \theta} \nu. \quad (3.53)$$

Thus, the appropriately-weighted average of the local shear over a flux surface gives us the global magnetic shear \hat{s} . The global shear is held fixed for all the local equilibria at a given ρ . This relation implies that the local shear can be negative for a given range in θ for a positive global shear \hat{s} . Finally, we plot local shear at nominal \hat{s} and α_{MHD} in figure 3.7 for different beta values.

The local shear depends on the pressure gradient α_{MHD} which further depends on β as well as the gradient scale lengths L_{n} and L_{T} . The beta value increases the local negative shear through the Shafranov shift. The gradient scale length does so by increasing the poloidal current gradient $dF/d\rho$ required to balance the pressure gradient which consequently increases the toroidal magnetic field. A plot showing the effect of pressure gradient on local shear is shown in figure 13(a). Note that in our scans decreasing the pressure gradient scale length increases the driving term $\eta = L_{\text{n}}/L_{\text{T}}$. In fact, in this study, for a given β , η increases faster than $a_{\text{N}}/L_{\text{p}}$. A plot of η versus

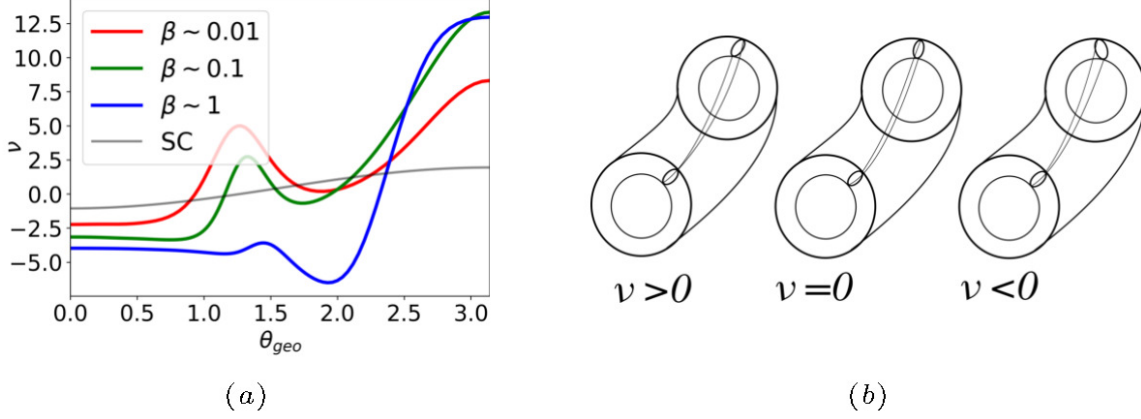


Figure 3.7: This figure explains the physical meaning of the local magnetic shear with (a) showing a typical local shear plot of negative triangularity equilibria at the nominal $\hat{s} = 0.45$ and nominal α_{MHD} values at $\rho = 0.8$ for different beta values and a low- β shifted-circle model (abbreviated SC). On the right side (b) illustrates a modified interpretation from Antonsen and Drake [2] explaining the concept of local magnetic shear. Negative local shear twists the turbulent eddies more than positive or zero local shear in the region of bad curvature, stabilizing the ITG mode.

the pressure gradient scaling factor is shown in figure 3.8.

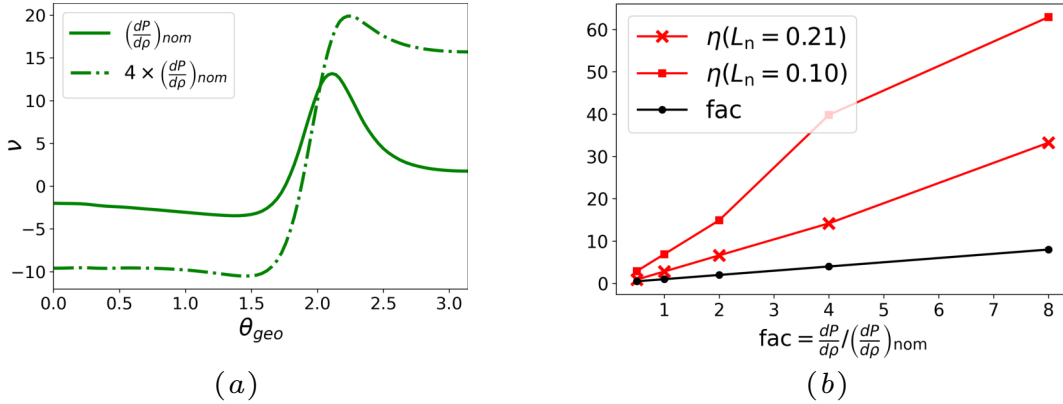


Figure 3.8: This figure shows (a) the change in the local shear for $fac = 4$ (increased pressure gradient). The local shear is much more negative with an approximately linear dependence with fac on outboard side. On the other hand, (b) shows the comparison between the ITG driving term η and the pressure gradient scaling factor fac . The term η is calculated using the values given in table 3.5. We can see that η grows linearly, but with a larger pre-factor. These figures illustrate how the ITG driving term grows more rapidly than the stabilizing local shear as we increase the pressure gradient.

The dominant mechanism for generating negative local shear is the β -induced Shafranov

shift. The local shear may also depend on the shaping, especially for negative triangularities. However, we find that shaping does not have a significant effect on the ITG stability of the high- β equilibria.

3.3.1.3 ITG results

Since GS2 is an initial value code, resolving a growth rate $\gamma \leq \gamma_{\text{thresh}}$ would require us to run the simulation for at least $t \sim 1/\gamma_{\text{thresh}}$. For large wavenumbers and a semi-implicit-time-stepping scheme, it leads to a relatively high runtime cost. Hence, we define a small positive “threshold” growth rate γ_{thresh} which we will use to separate stable and unstable modes. If the maximum ITG growth $\max(\gamma a_N/v_{th,i}) < \gamma_{\text{thresh}}$, we classify it as stable. For this study, we choose $\gamma_{\text{thresh}} = 0.005$.

We find that all the nominal equilibria stabilize as we increase β as first noted by [76] — the high- β equilibria are stable to the ITG mode, as shown in figure 3.9 below.

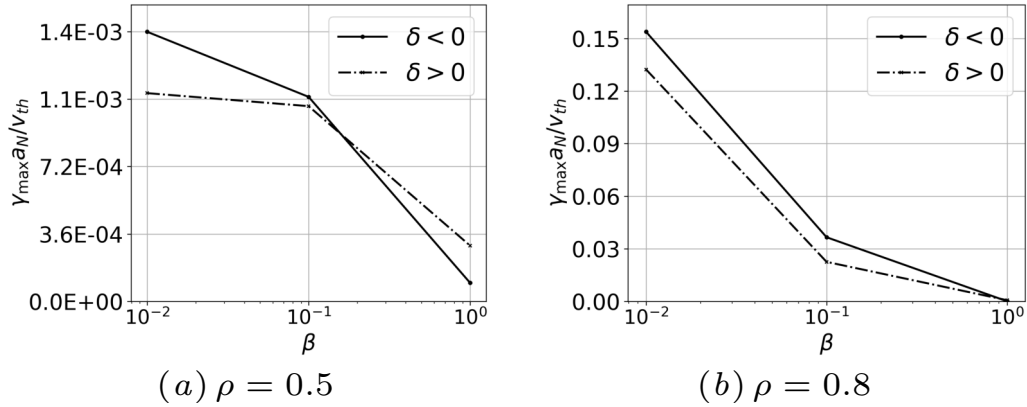


Figure 3.9: These plots show the ITG $\max(\gamma a_N/v_{th,i})$ (over $k_y \rho_i \in [0.05, 2]$) vs the typical β for nominal equilibria at different radial locations.

To better understand what causes this effect, we scan the gradient scale length values given in tables 3.5 and 3.6. Each group of plots contains maximum growth rate for a range of a/L_{T_i} at a

fixed a/L_{ni} for the three beta values. The plots are grouped by the triangularity of the equilibria. For each group, there are subgroups based on the normalized radius ρ . The results corresponding to the positive triangularity boundary shape are shown in figure 3.10.

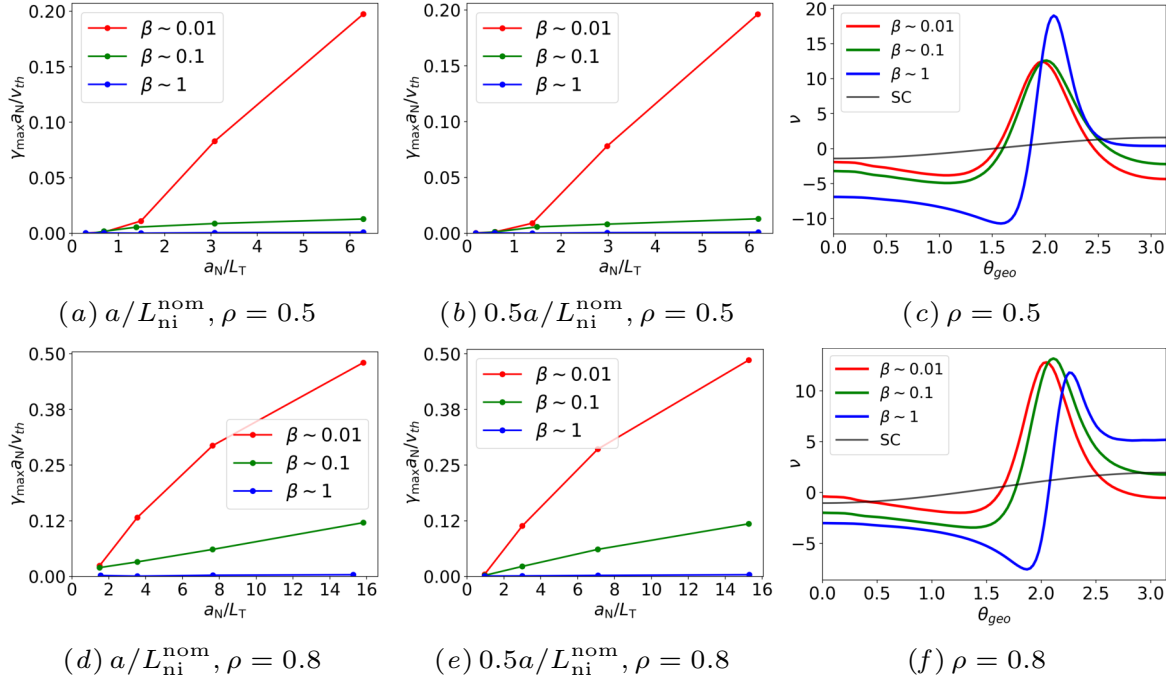


Figure 3.10: This figure shows the ITG $\max(\gamma a_N/v_{th,i})$ plots for positive triangularity equilibria against the temperature gradient length scale. For the high- β equilibria, ITG is stabilized at both $\rho = 0.5$ and $\rho = 0.8$. The rightmost figures in each row are the local magnetic shear vs the geometric theta θ_{geo} at the nominal $dp/d\rho$ and \hat{s} . The grey line corresponds to the local shear for a low- β shifted-circle equilibrium (abbreviated SC). The magnetic shear \hat{s} is the same for all the equilibria at every ρ .

In figure 3.9, one observes that for the high- β cases, the ITG mode is stable (that is, $\gamma < \gamma_{thresh}$). For the intermediate and low- β cases, figure 3.10 shows destabilization with increasing temperature gradient. We believe that the stabilization of high- β equilibria is a result of large local negative shear (rightmost panels) that spans a wide range in θ . The local shear becomes positive only after $\theta_{geo} > \pi/2$ — the whole outboard side has a large local negative shear. These large negative values are predominantly due to a large Shafranov shift but could

have subdominant effects resulting from strong shaping, especially for the negative triangularity high- β equilibria. For the shifted-circle equilibria, the local shear is small as compared with the rest of the equilibria even though it is negative over the outboard side. This is because the low- β shifted circle equilibria are neither strongly shaped nor have a large beta. The trend remains the same even for the equilibria with half-nominal density gradients. Next, we plot results for negative triangularity equilibria in figure 3.11.

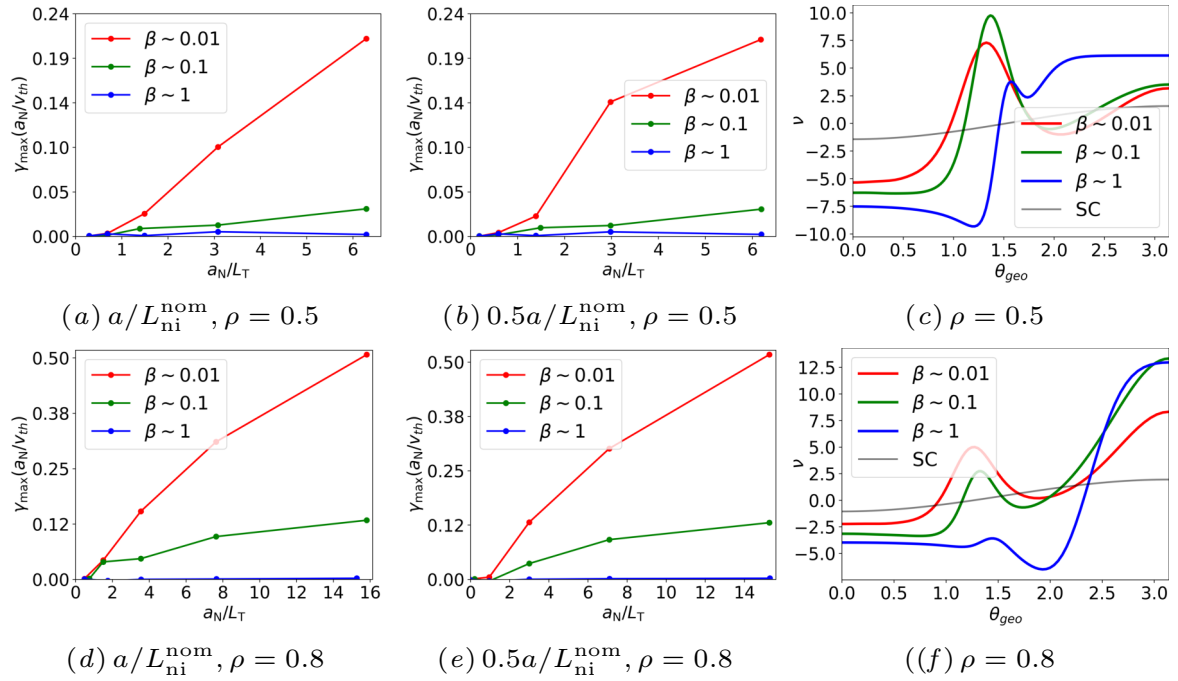


Figure 3.11: shows the ITG $\max(\gamma a_N/v_{th,i})$ plots for negative triangularity equilibria. For the high- β equilibria, ITG is stabilized at both $\rho = 0.5$ and $\rho = 0.8$. The local shear for the high- β equilibria is negative over the whole outboard side. The grey line corresponds to the local shear for a low- β shifted-circle equilibrium (abbreviated SC).

We see that the high- β equilibria with a negative triangularity boundary shape are stabilized as well. The local magnetic shear shows the same trend with beta but is even more negative and spans an even wider range in θ_{geo} as compared to the positive triangularity equilibria. We believe that this extended range in negative local shear is due to the “squareness” of the high- β profiles,

which is a stronger shaping than the positive triangularity cases. Since all the high- β equilibria are stabilized and the growth rates are small, it is hard to find a clear difference in growth rates based on triangularity.

In the next section, we will study the stability of different equilibria to an electron-driven electrostatic mode, the Trapped Electron Mode (TEM).

3.3.2 TEM study

In this section, we will present our analysis of the TEM instability. In §3.3.2.1, we explain the TEM and tabulate the parameters for which we perform our study. After that, we define the maximum TEM growth rate. In §3.3.2.2, we present the electron precession drift as a characteristic of TEM stability of a local equilibrium. In the final section, we plot the results in a fashion similar to the previous section.

3.3.2.1 Details of the study

The second type of electrostatic instability that we investigate, the collisionless TEM, becomes unstable when drift waves resonate with the precession of the electrons. This can cause significant transport loss through the electron channel that degrades plasma confinement [77]. For the TEM, we choose five pressure gradient values, corresponding to $\text{fac} = (0.5, 1, 2, 4, 8)$ for $\rho = 0.5$ and five values corresponding to $\text{fac} = (0.5, 0.75, 1, 2, 4)$ for $\rho = 0.8$. For each pressure gradient, we choose two temperature gradient scale lengths — nominal and 30% of the nominal, while scanning the growth rates in the density gradient scale lengths. We do this since TEM, unlike ITG, is primarily a density gradient-driven instability. The tables 3.7 and 3.8 contain the

values for which we solved the gyrokinetic model. Note that the temperature and density scale lengths are the same for the ions and electrons.

$a_N/L_{T_e} = a_N/L_{T_i}$	$a_N/L_{n_e} = a_N/L_{n_i}$				
0.186	0.21	0.61	1.41	3.01	6.22
0.296	0.10	0.51	1.31	2.91	6.11

Table 3.7: This table contains the values of gradient scale lengths at $\rho = 0.5$ used for the TEM study

$a_N/L_{T_e} = a_N/L_{T_i}$	$a_N/L_{n_e} = a_N/L_{n_i}$				
0.95	1.09	2.11	3.13	7.22	15.45
1.50	0.54	1.57	2.59	6.68	14.86

Table 3.8: This table contains the values of gradient scale lengths at at $\rho = 0.8$ used for the TEM study

These 20 values of gradients are the same for ions and electrons as well as both positive and negative triangularity equilibria at all the different beta values. Unlike the ITG study, we turn on the kinetic effects of electrons since TEM is an electron driven instability. The TEM growth rate peak occurs over a wide range $k_y \rho_i \in [0.5, 6]$. Since there is an overlap with the ITG and the Electron-Temperature Gradient (ETG) mode, having two species makes it difficult to separate modes with purely ITG and ETG-related effects from modes with purely TEM-related effects. Therefore, to calculate the TEM growth rate, we choose the growth rate corresponding to the wavenumber $k_y \rho_i$ at which the ratio of the quasilinear electron flux to electron heat flux is the maximum, i.e.,

$$\gamma_{\text{TEM}}(k_y \rho_i) = \gamma \Big|_{\max(\Gamma_e, k_y / Q_{e, k_y})}, \quad (3.54)$$

where the definition of quasilinear fluxes is given in equations (3.40) and (3.41).

We run GS2 for the wavenumbers in the range $k_y \rho_i \in [0.2, 6.5]$. Just like the ITG study, we run GS2 and obtain the maximum growth rate $\gamma_{a_N/v_{th,i}}$ for each of the 120 cases: 10 values of $(a_N/L_T, a_N/L_n) \times 2$ surfaces $\times 3$ β values $\times 2$ boundary shapes. The results showing the comparison between different beta values, triangularities, and normalized radius will be shown in §3.3.2.3.

Curvature-driven TEMs are associated with the precession of trapped electrons in a flux surface. To that end, we elucidate the definition and role of the electron precession drift frequency in the next section and how it characterizes the stability of an equilibrium to the TEM.

3.3.2.2 Characterizing stability against the TEM

The collisionless curvature-driven TEM is a drift wave that becomes unstable when it resonates with the bounce precession of trapped electrons. The precession of electrons is characterized by their precession frequency

$$\langle \omega_{De} \rangle = \left(\int_{-\theta_b}^{\theta_b} \frac{d\theta}{w_{\parallel}} \frac{B}{(\mathbf{B} \cdot \nabla \theta)} \right)^{-1} \int_{-\theta_b}^{\theta_b} \frac{d\theta}{w_{\parallel}} \frac{B}{(\mathbf{B} \cdot \nabla \theta)} \omega_{De}, \quad (3.55)$$

where the integral operator is the bounce-average operator. The precession frequency is a function of the bounce angle θ_b . Depending on the convention, one usually takes $\text{sign}(\omega) = \text{sign}(\omega_{*,e})$ for trapped electron modes since the TEM is a drift wave. Therefore, if

$$\text{sign}(\langle \omega_{De} \rangle) \text{sign}(\omega_{*,e}) < 0, \quad (3.56)$$

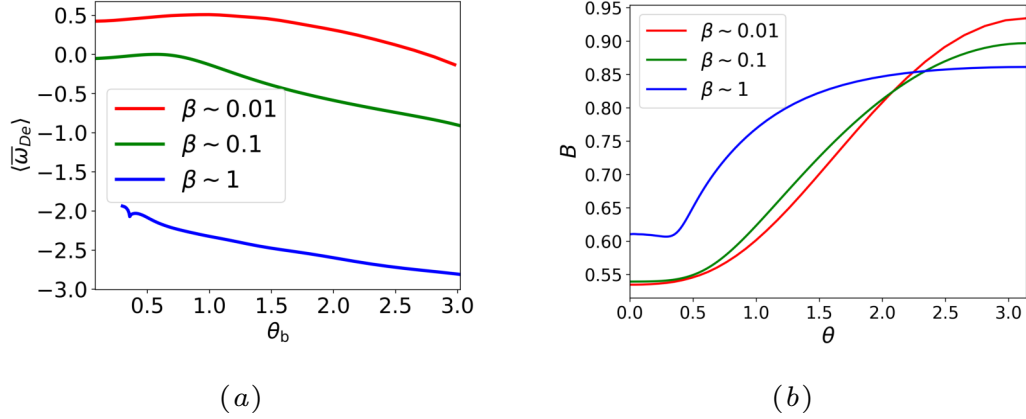


Figure 3.12: This figure shows the precession drift in (a) and the corresponding magnetic field magnitude in (b) for negative triangularity equilibria at $\hat{s} = 0.45$ and nominal α_{MHD} values at $\rho = 0.8$ for different beta values. Note the atypical magnetic field for the high- β equilibria where $\min(B)$ is located at a finite θ .

the drift wave will not be able to resonate with the precession of electrons. If the precession drift satisfies (3.56) at all the different pitch angles, the curvature-driven TEM will be stabilized [78, 79]. The expression for ω_{D} , given by (3.34) can be alternatively written as

$$\omega_{\text{De}} = \frac{k_y \rho_e}{2} \frac{v_{\text{th},e}}{a_{\text{N}}} E_e [2(1 - \lambda B) \text{cvdrift} + \lambda B \text{gbdrift}] \quad (3.57)$$

where cvdrift and gbdrift are geometric factors independent of the electron energy E_e and the pitch angle λ . A semi-analytical formula for calculating cvdrift and gbdrift is given in appendix B. As a characteristic of TEM stability, we define the quantity

$$\langle \bar{\omega}_{\text{De}} \rangle = \langle \omega_{\text{De}} \rangle \text{sign}(\omega_{*,e}) / E_e, \quad (3.58)$$

as the precession drift per energy in the electron-diamagnetic direction. A typical plot of the $\langle \bar{\omega}_{\text{De}} \rangle$ is shown at nominal \hat{s} and α_{MHD} for different β values in figure 3.12. We see that the

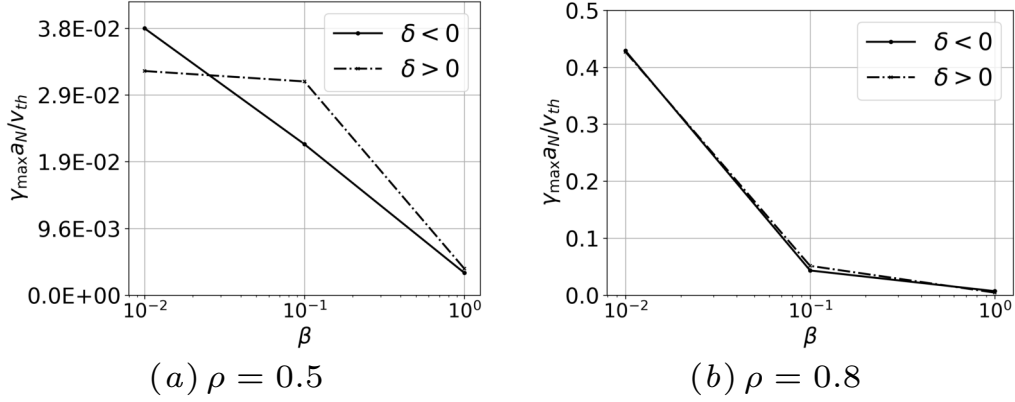


Figure 3.13: This figure shows the TEM $\gamma_{\text{TEM}}(a_N/v_{\text{th},i})$ vs the typical β plots for nominal equilibria at different radial locations.

precession drift is negative everywhere only for high- β case. This will form the basis for our understanding of the growth rate trends in the following section.

3.3.2.3 TEM results

Just like the ITG study, we choose a value of a growth rate γ_{thresh} such that if $\gamma_{\text{TEM}}(a_N/v_{\text{th},i}) < \gamma_{\text{thresh}}$, we classify an equilibrium as stable. The reasoning behind setting a threshold is described in the first paragraph of §3.3.1.3. For this study, we choose $\gamma_{\text{thresh}} = 0.005$. First, we plot the maximum TEM growth rates for the nominal equilibria in figure 3.13. We find that increasing beta stabilizes the TEM and the high- β equilibria are stable to the TEM.

To further understand this effect, we plot the result from scans in the density gradients in two groups, each group containing the maximum TEM growth rate for a range of a/L_n at a fixed a/L_T , given in tables 3.7 and 3.8 for different equilibria. Just like the ITG study, we group the plots by triangularity and arrange them in rows based on the normalized radius ρ . For positive triangularity equilibria, the results are shown in figure 3.14

We observe that the TEM is completely suppressed for the high- β , positive triangularity

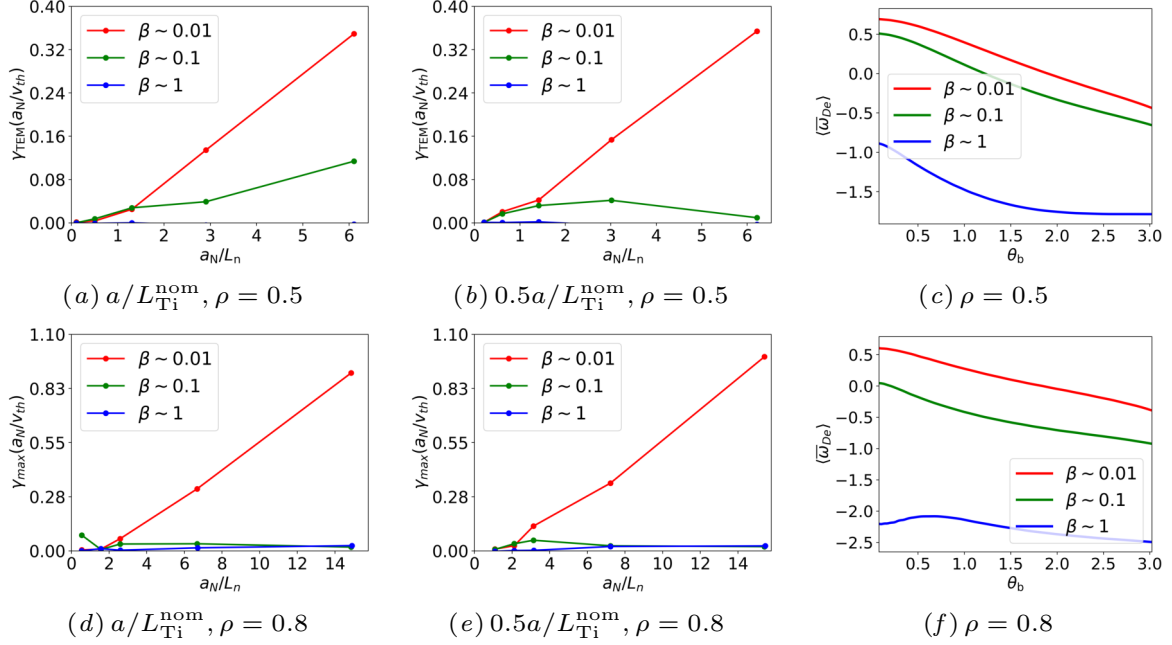


Figure 3.14: This figure presents $\gamma_{TEM}(a_N/v_{th,i})$ plots for positive triangularity equilibria and the electron precession drifts at the nominal pressure gradient. For the high- β equilibria, TEM is stabilized at both $\rho = 0.5$ and $\rho = 0.8$. As you can see in figures 3.14(c) and 3.14(f), the precession drift for the high- β equilibria is negative for all values of the bounce angle θ_b .

equilibria. The frequency $\langle \bar{\omega}_{De} \rangle$ is negative everywhere which means that all the trapped electrons precess in a direction opposite to the electron diamagnetic direction. They cannot destabilize the drift wave by exchanging energy with them.

The TEMs we seek are curvature-driven. A large pressure gradient causes the electron precession drift to become negative for all pitch angles [79]. This suppresses the curvature-driven mode and causes the slab-like branch of the TEM called the universal mode to appear. However, for high- β equilibria, the universal mode is suppressed as well since the large local shear

$$L_\nu = \frac{a_N}{\nu}, \quad (3.59)$$

combined with strong shaping reduces the shearing length scale [80] which makes it harder for

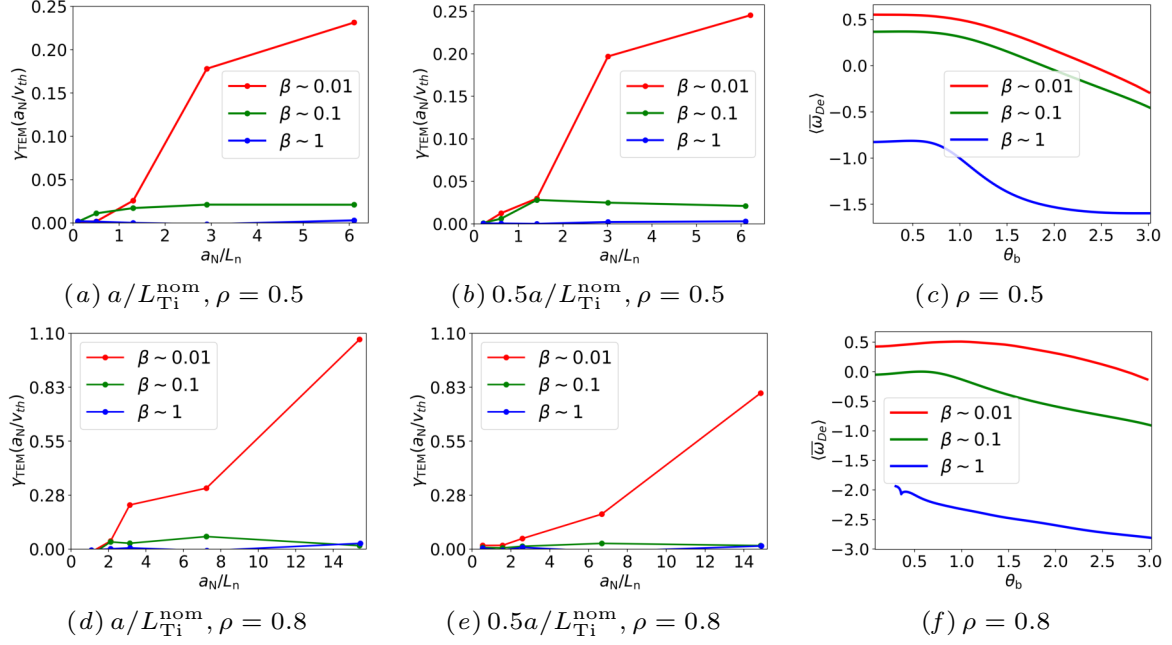


Figure 3.15: This figure presents $\gamma_{\text{TEM}}(a_N/v_{\text{th},i})$ plots for negative triangularity equilibria. For the high- β equilibria, TEM is stabilized at both $\rho = 0.5$ and $\rho = 0.8$. The rightmost plots on each row is the electron precession drift frequency.

fluctuations to grow and persist along the field line.

Next, now look at the TEM growth rate trends for the negative triangularity equilibria, shown in figure 3.15. The negative triangularity TEM growth rates follow the same trend as the positive triangularity ones. The TEM is suppressed for the high-beta equilibria due to the negative precession drift. The intermediate and low beta are more unstable for the negative triangularity equilibria at $\rho = 0.5$ and as unstable as positive triangularity ones at $\rho = 0.8$.

The result of our local analyses are only strictly valid for perturbations localized to a field-line on a flux surface. Alternatively, one can say for all fluctuations the toroidal mode number $n \gg 1$. Therefore, we must ensure that all modes in this study meet the local approximation in order to ensure that they are self-consistent. In both §3.3.1 and §3.3.2, the lowest wavenumber in our analyses is $k_y \rho_i = 0.05$. The largest ion gyroradius arises in the outer-core high- β equilibria

where $\rho_i \approx 0.005 m$. This corresponds to a wavelength $\lambda = 0.628 m$. Assuming an $n = 1$ mode has a wavelength equal to the normalized minor radius $a_N = 0.68 m$, $k_y \rho_i = 0.05$ corresponds to $n \approx 1$ — the longest modes are not localized. Hence, to accurately capture these modes at low wavenumbers, we must include nonlocal effects. However, for all the electrostatic studies, the growth rates $\gamma a_N / v_{th,i} \rightarrow 0$ as $k_y \rho_i \rightarrow 0$ and the most unstable modes always arise at $k_{y,peak} \rho_i \geq 0.5$ which corresponds to $n \geq 10$ implying that the local approximation is a fair assumption since we are only concerned with peak growth rates in §3.3.1 and §3.3.2.

We have demonstrated the stability of high- β equilibria against two main sources of electrostatic instability. However, when $\beta \sim 1$, magnetic fluctuations may play an important role in deciding the stability of an equilibrium. Therefore, in the next section, we study the effect of electromagnetic modes on the high- β equilibria.

3.3.3 Linear Electromagnetic study

To see if the stability trend seen in the electrostatic study holds when we include electromagnetic effects, we perform an electromagnetic microstability analysis for all the nominal local equilibria. This analysis is similar to the work done by [81], albeit we are testing $\beta \sim 1$ equilibria using an initial-value solver. We solve the linear, collisionless, gyrokinetic model allowing for non-zero magnetic field perturbations δA_{\parallel} and δB_{\parallel} using the GS2 code. We use the nominal gradient scale lengths for this study (given in table 3.4). First, we plot the growth rate spectrum with $k_y \rho_i$ for the positive triangularity cases in figure 3.16.

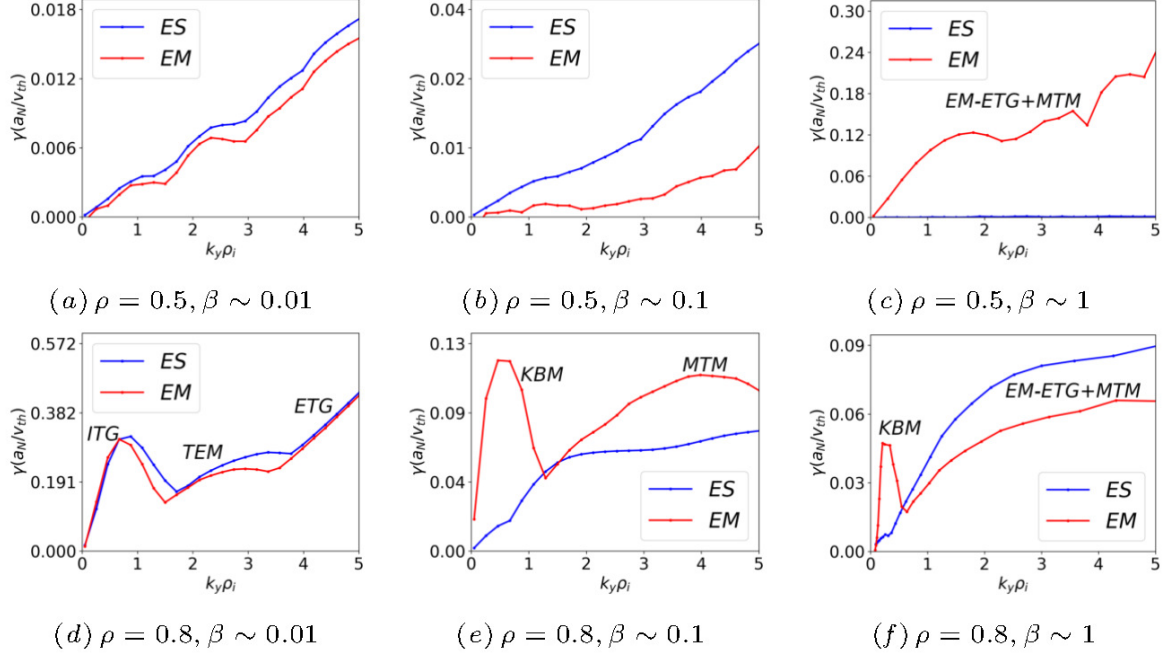


Figure 3.16: This figure shows comparison between the electrostatic (abbreviated ES) and electromagnetic (abbreviated EM) growth rates for all the nominal positive triangularity equilibria. Some of the branches have been labeled by their corresponding mode names. Notice the KBM in the intermediate and high- β equilibria in figures (3.16)(e) and (3.16)(f), respectively and the emergence of the collisionless-micro-tearing and electromagnetic-ETG modes in figure (3.16)(c) for all values of $k_y \rho_i$ and figures (3.16)(e) and (3.16)(f) for $k_y \rho_i > 1$

Since GS2 only calculates the maximum growth rate, in the inner core, we observe the finite- β stabilization of ITG [82] until the emergence of collisionless-microtearing (MTM) [83, 84, 85] and electromagnetic-ETG (EM-ETG) modes [86, 87] in figure 3.16(c)⁷. These modes arise on small scales radially ($O(\rho_e)$) and are extended in the ballooning angle θ . To accurately capture the extended eigenfunctions corresponding to these modes, we have to choose a wide range in the field-line-following coordinate ($\theta \in [-119\pi, 119\pi]$) with 21 points over a 2π interval. The eigenfunctions for two values of $k_y \rho_i$ in figure 3.17(c) are shown in appendix E.

In the outer core, we observe finite- β stabilization only for the low- β equilibrium. For the

⁷Note that the purpose of this work is to look for the most unstable modes destabilizing a local equilibrium. The distinction and correct classification of the type of mode is orthogonal to our objectives.

intermediate and high- β cases, the electrostatic modes are replaced by KBMs at low wavenumbers and collisionless-MTM and electromagnetic-ETG at high wavenumbers. Overall, positive triangularity high- β equilibria are more unstable than the low or intermediate ones in the inner core due to the collisionless-MTM and the EM-ETG mode. As we move towards the outer core, high- β equilibria become much more stable — exactly the opposite trend compared to the inner core. This means that the outer core is more stable for the high- β equilibria.

Next, we plot the growth rates for the negative triangularity equilibria in figure 3.17.

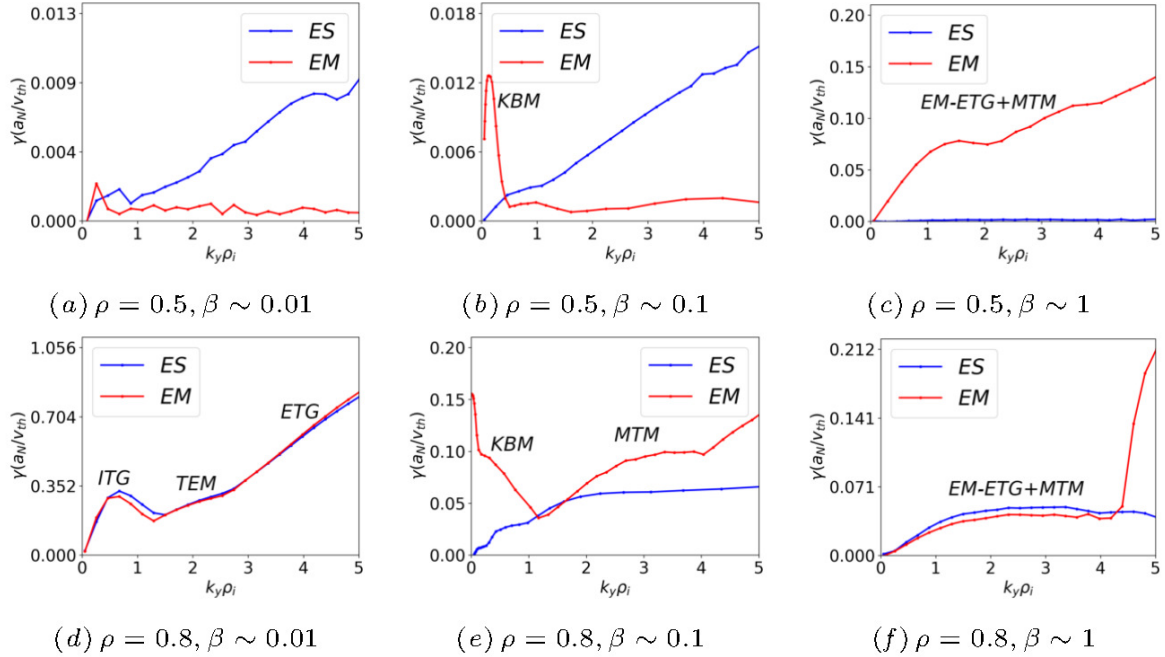


Figure 3.17: This figure shows comparison between the electrostatic (ES) electromagnetic (EM) growth rates for all the nominal negative triangularity equilibria. The sudden jump in figure (f) around $k_y \rho_i = 4.5$ is a different branch of the collisionless MTM. Note also that the growth rate around $k_y \rho_i = 0$ in figure (e) goes to fixed value of $\gamma a_N / v_{th,i} = 0.152$ since the equilibrium is unstable to the ideal ballooning mode.

The negative triangularity, inner-core equilibria are also stabilized due to finite- β effects. This effect is also visible for the intermediate- β case for $k_y \rho_i > 0.5$ but absent for the high- β cases as the ITG and TEM are superseded by electromagnetic modes: collisionless MTM

and the EM-ETG mode. For the outer-core cases, we see the exact same pattern as the inner core — finite- β stabilization for the low- β , KBM and collisionless-MTMs for the intermediate- β and collisionless-MTMs and EM-ETG modes for the high- β . Note that unlike the positive triangularity case, we do not observe the KBM in the negative triangularity, high- β equilibria. Moreover, the growth rates are also lower than positive triangularity cases for a wide range of wavenumbers ($k_y \rho_i \in [0.01, 4.5]$). Since turbulence is most likely to peak at lower wavenumbers, the growth rate characteristics of negative triangularity, high- β are the most favorable.⁸

In summary, we find that turning on the electromagnetic effects destabilizes the high- β equilibria. Figures 3.16(c), 3.17(c) and 3.17(f) show the emergence of collisionless-MTMs and EM-ETG modes whereas figure 3.17(c) also shows instability to the KBM in the range $k_y \rho_i \in [0.01, 0.5]$. These equilibria are much more unstable than the low- β ones in the inner core but they are much more stable as we move towards the outer core, with negative triangularity high- β equilibria showing the best characteristics. We believe that the outer-core stability is due to a large Shafranov shift and strong shaping. We also argue that negative triangularity has better characteristics than positive triangularity due to stronger shaping, i.e., “squareness” that we discussed in figure 3.5. Since outer-core or edge transport is usually a limiting factor in experimental low- β equilibria, these equilibria may be a novel alternative to realize higher-power devices.

In this section, the lowest wavenumber that we have scanned is $k_y \rho_i = 0.01$. Using the same analyses as presented at the end of §3.3.2, the longest wavelength $\lambda \approx 3.1 m$. Assuming

⁸Some of the $\beta \sim 1$ equilibria have small but finite TEM growth rates which are larger than the growth rates from our electrostatic TEM study. This is consistent with the electrostatic study since we chose the TEM growth rate at a value of $k_y \rho_i$ for which the ratio of Γ_e/Q was maximized. This almost always happens at a low $k_y \rho_i$ — TEM growth rates are small at low $k_y \rho_i$ values for $\beta \sim 1$. Furthermore, the lengths of the gradient scale lengths (tables 3.7 and 3.8) were different for the electrostatic study.

$n = 1$ corresponds to $\lambda = a_N = 0.68 m$, the longest mode would require $n < 1$. Modes with such long wavelengths violate the local assumption of flux tube codes. However, the growth rates go to zero at low wavenumbers (with the exception of figure 19(e)) and peak at $k_{y,\text{peak}}\rho_i \gg 0.01$. Calculating the value of n at the wavenumber $k_{\text{peak}}\rho_i$, we obtain the lowest n in figures 19(e) and 18(f) as $n = 0$ and $n = 5$, respectively. Therefore, the reader must take the low-wavenumber results shown in figures 19(e) and 18(f) with a grain of salt.

Note that this is a collisionless electromagnetic analysis. It is possible that in the presence of collisions, more modes like collisional-MTMs [88, 89], collisional EM-ETG etc. arise and supersede their collisionless variants [85] as the most dominant mode. On the other hand, it is also possible to achieve lower growth rates if we include the stabilizing effect of velocity shear [89].

3.4 High- β stellarator equilibria

To test our observations about high- β equilibria from previous sections and verify that they hold for stellarator equilibria, we scan two recent quasisymmetric 3D equilibria obtained by Landreman *et al.* [90]. The Landreman-Buller-Drevlak (LBD) quasisymmetric (QA) design is a low- β equilibrium ($\beta_{\text{ax}} \approx 5\%$) whereas the LBD quasihelically symmetric (QH) design is an intermediate- β equilibrium ($\beta_{\text{ax}} \approx 11\%$). In this section, we will perform gyrokinetic analysis of the two equilibria.

3.4.1 LBD QA low- β equilibrium

In this section, we will perform both electrostatic and fully electromagnetic gyrokinetic analysis of the two field period LBD QA equilibrium at nominal values of density and temperature gradients on a single field line. To do that we provide VMEC with the pressure, rotational transform, and cross section shown in figure 3.18.

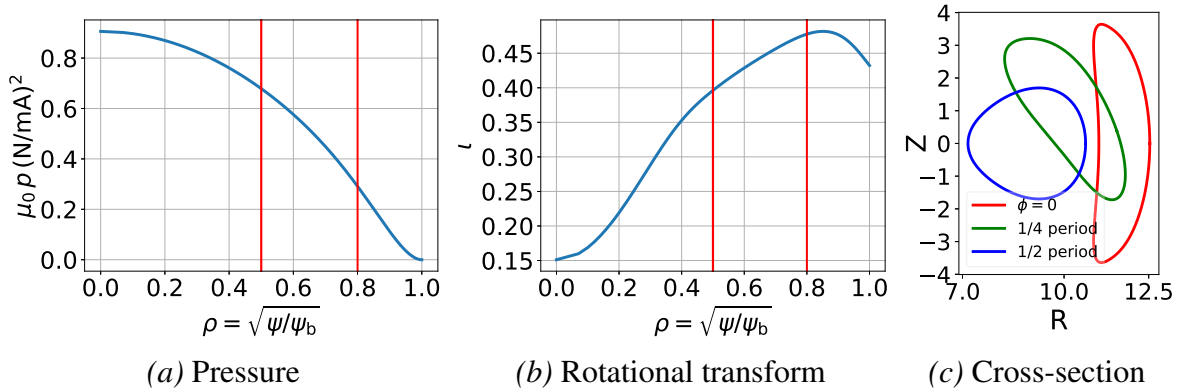


Figure 3.18: This figure plots the inputs to the VMEC code for the LBD QA design: the pressure, rotational transform as a function of the normalized radius ρ , and cross-section of the boundary. The red lines mark the radii $\rho = 0.5$ and $\rho = 0.8$, locations at which we perform the gyrokinetic analysis.

For a gyrokinetic analysis, we need the β values on the two flux surfaces and the nominal values of the density and temperature gradient scale lengths. These values are provided in the table 3.9

ρ	β_N	a_N/L_n	a_N/L_T	$k_y \rho_i$	θ_0
0.5	4.2	0.98	0.45	[0.05, 6]	[-1.5, 1.5]
0.8	1.8	3.96	1.98	[0.05, 6]	[-1.5, 1.5]

Table 3.9: This table contains the values of quantities needed for a gyrokinetic run with the LBD QA equilibrium. The gradient scale lengths are the same for both ions and electrons.

Using these values, we solve the linear electrostatic and the fully electromagnetic gy-

rokinetic model using GS2 on the field line $\alpha_t = 0$ and plot the normalized growth rate in figure 3.19.

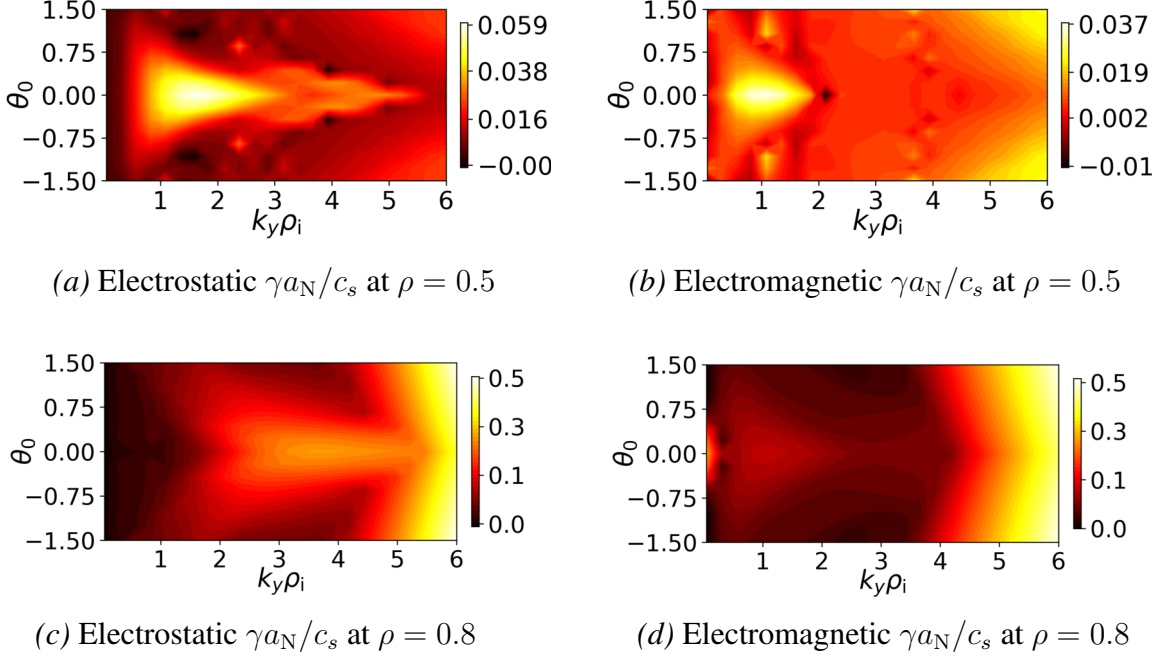


Figure 3.19: This figure compares the normalized electrostatic and electromagnetic growth rates for the LBD QA equilibria. In figures 3.19(a) and (b) we plot the electrostatic and electromagnetic growth rates, respectively at $\rho = 0.5$. In figures 3.19(c) and (d), we do the same for $\rho = 0.8$. Note that due to strong shaping of stellarators, we also scan in the ballooning parameter θ_0 .

We see the same behavior as the axisymmetric cases; finite- β stabilization of the ITG mode and emergence of KBM and EM-ETG modes. Note also that both equilibria have a finite growth rate at $k_y \rho_i = 0.05$ value. This fact will be important in §3.5. Since EM-ETG is an electron-scale mode, it does not peak in the $k_y \rho_i$ range that we have chosen. To capture the peak EM-ETG growth rate, we would have to go $k_y \rho_i \sim (m_i/m_e)^{1/2}$.

It is important to note that unlike tokamaks all field lines are not identical in stellarators even with quasisymmetry. In other words, the geometric coefficients used in a gyrokinetic calculation will vary with the field line label α_t . Hence, it is possible that the most unstable mode lies

on a different field line for a different equilibrium. However, we do not explore it further and only scan $\alpha_t = 0$ in this thesis. To understand how the microstability behavior of a stellarator changes with β , we analyze a stellarator equilibrium with a higher β in the next section.

3.4.2 LBD QH intermediate- β equilibrium

After studying a low- β stellarator equilibrium in the previous section, we look at an intermediate- β ($\langle\beta\rangle \approx 5\%$), four field period, LBD QH equilibrium at nominal density and temperature gradients on a single field line. The input pressure, rotational transform, and boundary cross-section is shown in figure 3.20.

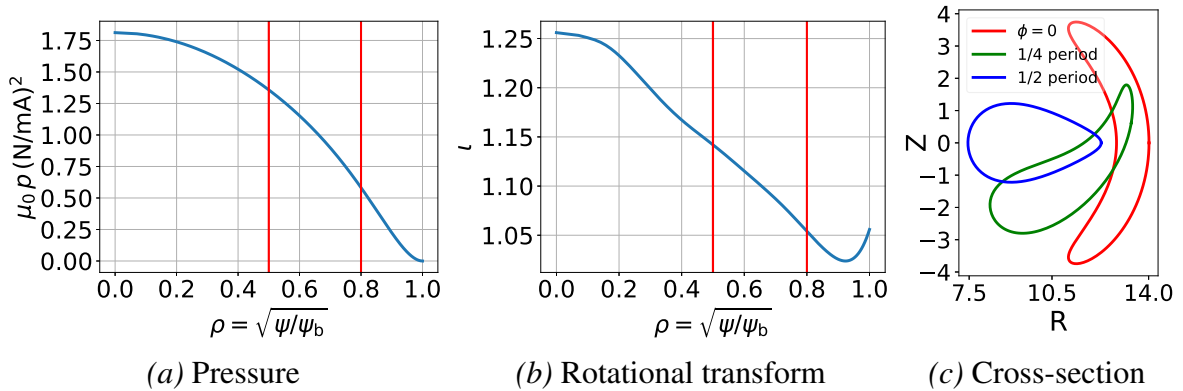


Figure 3.20: This figure plots the inputs to the VMEC code for the LBD QH design: the pressure, rotational transform as a function of the normalized radius ρ , and cross-section of the boundary. The red lines mark the radii $\rho = 0.5$ and $\rho = 0.8$, locations at which we perform the gyrokinetic analysis.

With the output equilibria, we use the information needed for a gyrokinetic run given in table 3.10. Using these values, we solve the linear electrostatic and the fully electromagnetic gyrokinetic model with GS2 on the field line $\alpha_t = 0$ and plot the normalized growth rate in figure 3.21.

ρ	β_N	a_N/L_n	a_N/L_T	$k_y\rho_i$	θ_0
0.5	10.8	0.90	0.45	[0.05, 6]	[-1.5, 1.5]
0.8	4.6	3.96	1.98	[0.05, 6]	[-1.5, 1.5]

Table 3.10: This table contains the values of quantities needed for a gyrokinetic run with the LBD QH equilibrium. The gradient scale lengths are the same for both ions and electrons.

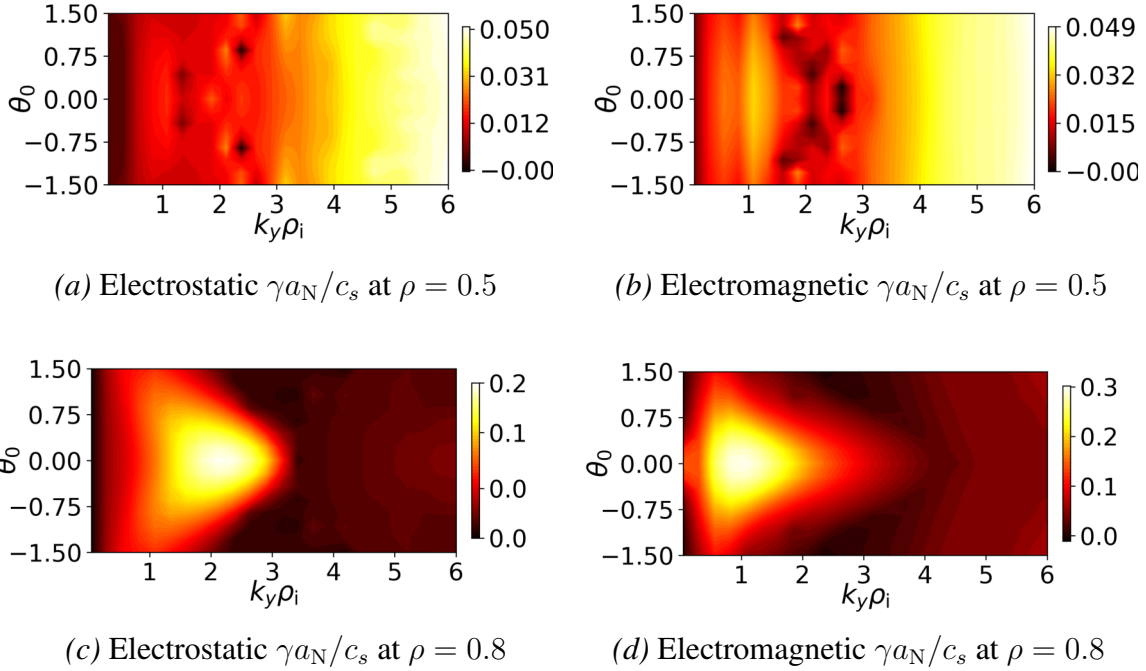


Figure 3.21: This figure compares the normalized electrostatic and electromagnetic growth rates for the LBD QH equilibria. In figures 3.21(a) and (b) we plot the electrostatic and electromagnetic growth rates, respectively at $\rho = 0.5$. In figures 3.21(c) and (d), we do the same for $\rho = 0.8$. Note that due to strong shaping of stellarators, we also scan in the ballooning parameter θ_0 .

For the intermediate- β equilibrium, we see the same effects as the axisymmetric and the 3D equilibria we studied before. As expected, due to a larger- β , the finite- β stabilization of ITG is even greater. The stabilization occurs due to the negative local shear even though the global shear is small compared to tokmaks. Due to the larger β , we also see emergence of the KBM in figures 3.21(b) and 3.21(d) in both the inner and outer core around $k_y\rho_i \approx 1$. Similar to the previous equilibrium, the electromagnetic growth rate goes to a finite non-zero value at

$$k_y \rho_i = 0.05.$$

Unlike the tokamak microstability study, we cannot do a Greene-Chance analysis for these stellarator equilibria as they are not described by an explicit, scalar, force-balance equation like the Grad-Shafranov equation. Self-consistently performing these gradient scans would either require generating multiple new equilibria using VMEC or imposing additional constraints on the type of equilibrium [91, 92]. Both of these methods are non-trivial to implement and will not be explored further in this thesis.

Some of the tokamak cases and all the stellarator cases that we studied are unstable to KBMs. Moreover, for some of these cases the growth rate approaches a finite value at $k_y \rho_i = 0.05$ instead of approaching zero. This behavior is linked to the ideal ballooning stability of these equilibria. We will explore this effect in more detail in the next section.

3.5 Relationship between ideal and kinetic ballooning modes

In this section, we will demonstrate similarities and differences between the ideal and kinetic ballooning modes. First, we will briefly explain the limit in which the linear gyrokinetic model reduces to the ideal ballooning equation. Next, we will perform an $\hat{s} - \alpha_{\text{MHD}}$ analysis of axisymmetric equilibria using the Greene-Chance method explained in §3.2.3 and calculate the maximum ballooning eigenvalue $\hat{\lambda}$ for the 3D equilibria. We will explain the correlation between the distance from marginality of the ideal ballooning mode and the KBM.

To elucidate the similarities between the ideal and the kinetic ballooning mode, we take the intermediate frequency, long wavelength, large aspect ratio limit of the gyrokinetic model (3.30)-

(3.33). In this limit

$$\frac{v_{\text{th},i}}{a_N} \ll \omega \ll \frac{v_{\text{th},e}}{a_N}, \quad k_{\perp}\rho_i \ll 1, \quad \beta \ll 1, \quad \epsilon \ll 1, \quad (3.60)$$

where $\epsilon = 1/A$ is the inverse aspect ratio of the device. Tang *et al.* [49] and Aleynikova and Zocco [93] have shown that the linear electromagnetic gyrokinetic model can be reduced to

$$\frac{1}{\mathcal{J}} \frac{\partial}{\partial \theta} \left(\frac{|\nabla\alpha|^2}{\mathcal{J} B^2} \frac{\partial \hat{X}}{\partial \theta} \right) + \frac{d(\mu_0 p)}{d\psi} [\mathbf{B} \times \nabla (2\mu_0 p + B^2) \cdot \nabla \alpha] \hat{X} = (\omega_{*,i} - \omega) \omega \rho \frac{|\nabla\alpha|^2}{B^2} \hat{X}, \quad (3.61)$$

where $\hat{X} = \delta\varphi$ is the electrostatic potential fluctuation. This equation is nearly identical to the ideal ballooning equation, except for the diamagnetic corrections from the $\omega_{*,i} = k_y \rho_i v_{\text{th},i} / L_{ni}$ term. In fact, in the long-wavelength limit $k_y \rho_i \rightarrow 0$, (3.61) reduces to the ideal ballooning equation (2.37).

To better understand this connection, we solve the ideal ballooning equation for all the equilibria discussed in this chapter. For axisymmetric equilibria, we also leverage the Greene-Chance technique to self-consistently change \hat{s} and α_{MHD} for all the twelve local equilibria.

3.5.1 $\hat{s} - \alpha_{\text{MHD}}$ analysis of axisymmetric equilibria

In this section, we will calculate the growth rate $\gamma a_N / c_s$ for all the axisymmetric cases studied in §3.3. To obtain useful maximum growth rate scans, it is computationally advantageous to know where the equilibrium transitions from being stable to unstable, i.e., the region of marginal stability. This is because stable modes are extended and require many more points and a wider range in θ than unstable modes, leading to a longer computation time. To that end, we

first integrate the marginally stable ballooning equation

$$\frac{1}{\mathcal{J}} \frac{\partial}{\partial \theta} \left(\frac{|\nabla \alpha|^2}{\mathcal{J} B^2} \frac{\partial \hat{X}}{\partial \theta} \right) + 2\mu_0 \frac{dp}{d\psi} \left[\mathbf{B} \times \nabla \left(\mu_0 p + \frac{B^2}{2} \right) \cdot \nabla \alpha \right] \hat{X} = 0, \quad (3.62)$$

along the field and count the zeros of the function $\hat{X}(\theta)$ — if \hat{X} has at least one zero, the mode is unstable; otherwise it is stable. This criterion was originally developed in [94] by Newcomb, for a screw pinch. Newcomb used it as a method to assess the stability of a screw pinch without explicitly finding the growth rates or the eigenfunctions. It is briefly explained in appendix D. Using this criterion, one can obtain the sign of $\hat{\lambda} \propto \gamma^2$ and infer the stability significantly more rapidly than by exactly solving (2.37). Coupling Newcomb’s criterion with the Greene-Chance analysis gives us the ability to scan the $\hat{s} - \alpha_{\text{MHD}}$ space and plot the marginal stability contour ($\gamma = 0$) cheaply. For axisymmetric equilibria, the marginal stability contour is a single continuous line. Upon obtaining the contour, we choose a region around it where we solve (2.37).

To solve (2.37) we use the procedure described by Sanchez *et al.* [42]. Our two-part code first finds the contour of marginal stability, then takes a region around the contour in the $\hat{s} - \alpha_{\text{MHD}}$ space and implements the algorithm given in [42]. It outputs the maximum eigenvalue and the corresponding eigenfunction for each value of \hat{s} and α_{MHD} . The plots of the maximum eigenvalue along with the curve of marginal stability are shown in the next section.⁹

This section contains the results of the $\hat{s} - \alpha_{\text{MHD}}$ analyses of the twelve local equilibria that

⁹All the calculations for axisymmetric equilibria in this chapter are done with $\theta_0 = 0$. A more complete picture would require one to scan over multiple values of θ_0 and take the union of the resulting marginal stability curves and growth rate plots.

we chose in §3.3. We plot a 2D contour plot of the magnitude of the growth rate defined as

$$\gamma = -i\sqrt{\frac{2\hat{\lambda}}{\beta_N}} \quad (3.63)$$

where the definition of $\hat{\lambda}$ is taken from (2.39). We begin by discussing the positive triangularity equilibria in figure 3.22.

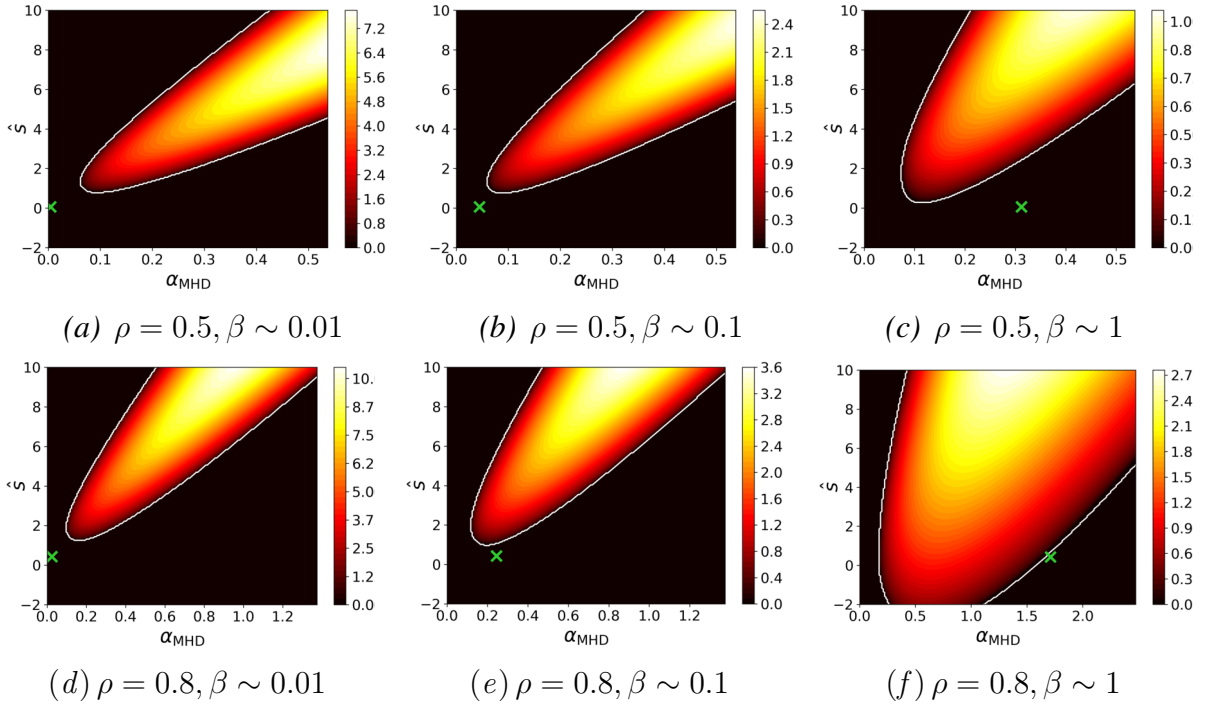


Figure 3.22: This figure shows the normalized growth rate $\gamma a_N/v_{th,i}$ contours along with the curve of marginal stability (white line) for the positive triangularity equilibria. The columns correspond to the low, intermediate and high- β regimes, respectively. The nominal equilibrium value is given by the green cross. The difference between the growth rates from the low and high- β equilibria is due to our choice of normalization in (3.63).

All the positive triangularity equilibria studied here are stable at their nominal values. The low- β equilibria lie below the marginal stability contour whereas the high- β equilibria lie above it. For low- β equilibria the ballooning threshold is well-known to be $\alpha_{MHD} \sim 1$ but for the high- β equilibria, using (3.43), $\alpha_{MHD} \sim 1/\delta_{HSU}^2 \gg 1$ which pushes these equilibria into the

region of “second” stability, first discovered by Coppi [95] and later explored by Greene and Chance [62]. Note that the high- β equilibrium in figure 3.22(f) is close to marginally stable. Also, since ballooning modes are Alfvén waves and we use ion thermal speed to normalize the ballooning eigenvalue $\hat{\lambda}$, we see that the maximum growth rate decreases as $v_{\text{th},i}/v_A = \sqrt{\beta/2}$ — high- β equilibria having the smallest maximum growth rates. The non-conventional choice of normalization used in this section helps us quantitatively compare ideal ballooning growth rates with the ones obtained from various microstability studies in §3.3.1, §3.3.2, and §3.3.3. In the next paragraph, we discuss the results from ideal ballooning scans of the negative triangularity equilibria.

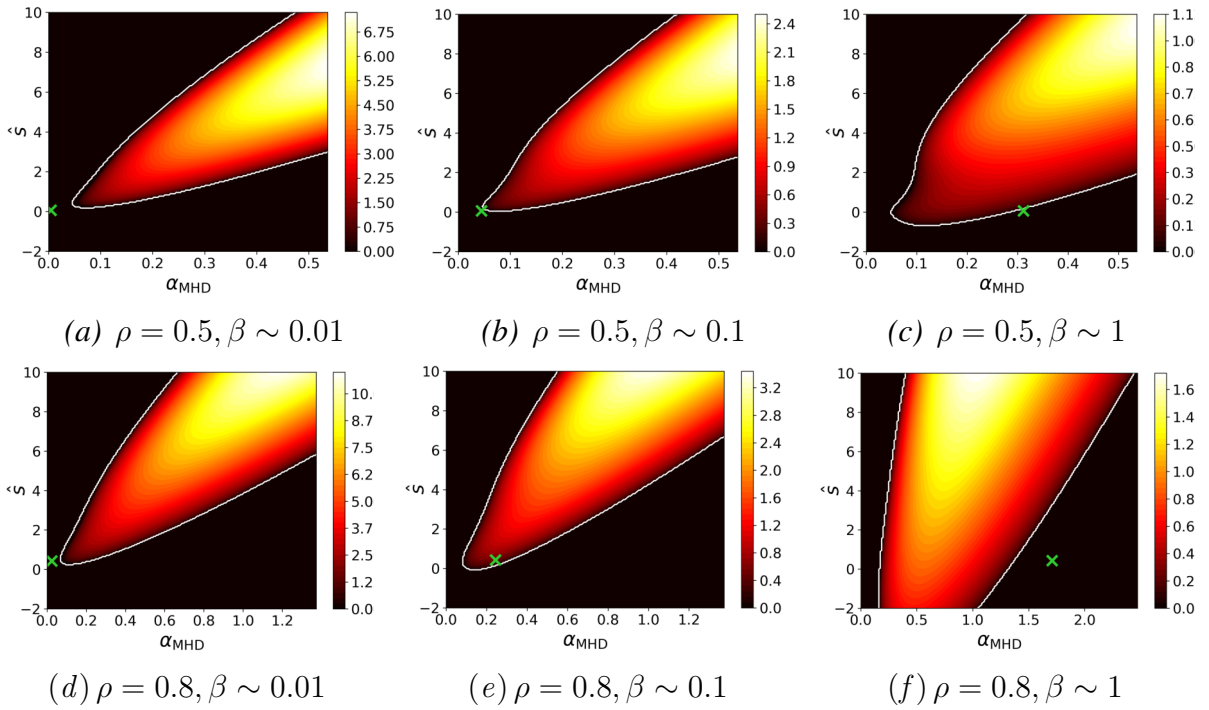


Figure 3.23: This figure shows the normalized growth rate contours along with the marginal stability curve for the negative triangularity equilibria. The nominal equilibrium value is denoted by the green cross.

In figure 3.23, we can see that the nominal equilibria for negative triangularity are stable for all cases except figure 3.23(e). The trends follow those of the positive triangularity equilibria.

ria with one important exception. Unlike positive triangularity equilibria, the high- β negative triangularity equilibria move closer to the marginal stability boundary in the inner core region as seen in figure 3.22(c). This is different from the usual result — ballooning-stable equilibria with peaked pressure profiles approach marginal stability as we move towards the boundary and pressure gradient gets steeper (as seen in figure 3.22, 3.22(a), 3.22(b), 3.22(d), and 3.22(e)) — indicating that negative triangularity, high- β equilibria have enhanced ballooning stability in the outer core. We observed a similar trend when we presented results from the electromagnetic microstability analyses in §3.3.3.

Recently, Davies *et al.* [45] have published a study investigating access to high- β spherical tokamak equilibria where they find that high- β , negative triangularity equilibria are more unstable and less accessible than their positive triangularity counterparts. At first, this may seem to contradict our results. However, looking at the plasma β values in Davies *et al.*, we realize that their high- β equilibria correspond to intermediate- β in our work. Indeed, the negative triangularity intermediate- β equilibrium in figure 3.22(e) is ballooning unstable whereas the positive triangularity equilibrium in figure 3.22(e) is ballooning stable. Furthermore, Davies *et al.* define accessibility as the ability to reach the nominal α_{MHD} from $\alpha_{\text{MHD}} = 0$ at the nominal \hat{s} — a straight line in $\hat{s} - \alpha_{\text{MHD}}$ space — the actual path of an equilibrium from startup to a steady-state operation in the $\hat{s} - \alpha_{\text{MHD}}$ space is a 2-D curve, similar to figures 2(a), 2(b) in [69]. Therefore, our results corroborate, rather than contradict, the findings of Davies *et al.*

The first important takeaway from this study is that all low- and high- β equilibria are stable to the ideal ballooning mode. This indicates that it might be possible to generate high- β axisym-

metric equilibria that are ballooning stable.¹⁰ Even though one of the intermediate- β equilibria is unstable, we will use it in our study as it will help us understand the behavior of microstability with changing β .

The second important takeaway is that equilibria that are ideal ballooning unstable are also unstable to the KBM. Moreover, there is a correlation between the distance from marginality and ideal ballooning stability, especially for intermediate- β equilibria — equilibria that are closer to the marginal stability boundary are unstable to the KBM. This will be explored further in the next chapter. In the next section, we will calculate the maximum ballooning eigenvalue $\hat{\lambda}$ for the stellarator equilibria.

3.5.2 Ideal ballooning analysis of LBD equilibria

To check if our observations for tokamaks can be extended to stellarators, we calculate the maximum eigenvalue $\hat{\lambda}_{\max}$ for both the LBD equilibria.

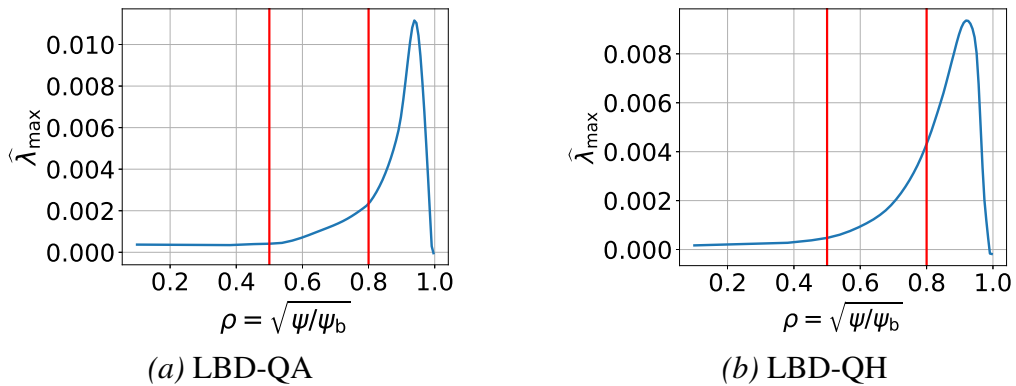


Figure 3.24: This figure shows the maximum ideal ballooning eigenvalue $\hat{\lambda}_{\max}$ as a function of the radial location ρ . In figure 3.24(a) we plot $\hat{\lambda}_{\max}$ for the LBD QA equilibrium and in figure 3.24(b) we plot $\hat{\lambda}_{\max}$ for the LBD QH equilibrium.

¹⁰Note that we do not prove the experimental accessibility of these high- β equilibria. We show that if these equilibria were to exist, they will be stable to the ideal ballooning mode. The problem of accessibility in the context of ideal ballooning stability was studied by [69].

We observe that both the LBD QA and QH equilibria are unstable to the ideal ballooning mode. Similarly, both the ideal ballooning and gyrokinetic growth rates are also larger at $\rho = 0.8$ than at $\rho = 0.5$ for both equilibria. We also see from figures 3.19(b), (d) and figures 3.21(b), (d) that the KBM growth rate is a finite positive value as $k_y \rho_i \rightarrow 0$. This serves as additional evidence to our hypothesis that ideal ballooning unstable equilibria are also unstable to KBMs.

Even though ideal ballooning modes may not necessarily lead to disruptions in stellarators, they can still deteriorate the heat and particle transport via the KBM channel. For high- β tokamaks and stellarators, the lowest wavenumber modes are KBMs. Since low-wavenumber modes are usually the most dangerous, ensuring the KBM stability of high- β devices is of paramount importance for improved plasma confinement.

3.6 Summary and Conclusions

We began this chapter by explaining the linear, collisionless, gyrokinetic model and how to solve it numerically using the GS2 code in §3.2. We also explained Greene-Chance analysis, a technique used to locally change the pressure gradient and shear of axisymmetric equilibria.

In §3.3, we studied the stability of all the axisymmetric local equilibria to the two most virulent electrostatic modes of turbulence: ITG and TEM. We found a clear inverse relationship between the beta value and the growth rates — increasing the beta value stabilized both the ITG mode and the TEM. Using a Greene-Chance analysis, we also scanned the maximum ITG, TEM growth rates vs the temperature and density gradient scale lengths, respectively. This was important to ensure that these equilibria are not “stiff”, i.e., the growth rates do not increase sharply as the gradients exceed some threshold. In §3.3.1.2, we explained how a large negative

local shear resulting from a large Shafranov shift stabilizes the ITG mode and in §3.3.2.2 we showed how the reversal of the precession of the trapped electrons stabilizes the TEM throughout the whole range of gradient scale lengths.

The effect of electromagnetic fluctuations can be important for all equilibria, especially the intermediate and high- β ones. To that end, in §3.3.3 we performed an electromagnetic study of all the nominal axisymmetric equilibria. We found that the stability trend seen for the electrostatic case did not hold after turning on electromagnetic effects. However, even though the high- β equilibria were more unstable than the low- β ones due to collisionless-MTMs and EM-ETGs in the inner core, they were much more stable than low- β in the outer core. We found that negative triangularity, high- β equilibria were stable to the KBM. We believe that this is due to the strong shaping (“squareness”) of the negative triangularity high- β equilibria. This indicates that turbulent transport may flatten the pressure gradient in the core but may not significantly affect the pressure gradient toward the edge for high- β equilibria.

To ensure that the trends obtained from the high- β tokamak study are applicable to stellarators with a high- β , in §3.4 we examined both the electrostatic and electromagnetic the microstability of two recent quasisymmetric stellarator equilibria obtained by Landreman *et al.* [90]. Similar to tokamaks, we also observed effects like finite- β stabiliztion of the ITG and emergence of KBMs and EM-ETG in both the LBD equilibria. Moreover, all the LBD equilibria that we analyzed were unstable to the KBMs.

To further explore the relationship between the ideal and kinetic ballooning modes, in §3.5, we then analyzed the ideal ballooning stability for both the tokamak and stellarator equilibria. We also performed an $\hat{s} - \alpha_{\text{MHD}}$ for the axisymmetric equilibria to visualize the distance of the nominal equilibria from the curve of ideal ballooning marginal stability. We find that all the ideal

ballooning unstable equilibria are also KBM unstable. Furthermore, equilibria that are close to marginality are also unstable to KBMs.

To explore the relationship between distance from ideal ballooning marginality and KBMs, in the next chapter, we integrate microstability analysis with the adjoint ballooning stability framework from chapter 2 and search for axisymmetric and 3D quasisymmetric equilibria that are stable against the KBM.

Chapter 4: Towards a combined MHD and kinetic stability optimization of high- β equilibria

4.1 Overview

In the previous two chapters, we have analyzed the ideal MHD and kinetic stability of high- β tokamak and stellarator equilibria. Since the overall stability of a fusion device is crucial, it would be advantageous to have a single optimizer that optimizes against both types of instabilities.

In this chapter, we combine all the ideas and tools from the previous chapters to develop a stability optimization framework called MicroStOpt. With this framework, we calculate, test, and present some results. Finally, we use this to search for axisymmetric and quasisymmetric equilibria that are stable against the ideal and Kinetic Ballooning Modes (KBM). Kinetic stability calculations are typically much more expensive than ideal MHD stability calculations. Consequently, there is a great interest in finding proxies that reliably correlate with kinetic stability. Using our optimizer, we can also test different equilibrium-dependent proxies. Using the knowledge derived from the previous chapter, we also test whether the ideal ballooning distance-from-marginality is a useful proxy for KBM stability.

4.2 The MicroStOpt framework

MicroStOpt is an optimization framework written in Python that can generate and optimize tokamak and stellarator equilibria against ideal and kinetic instabilities. We use the SIMSOPT framework to generate equilibria, our solver from chapter 2 to calculate the infinite- n ideal ballooning stability, GS2 to evaluate linear microstability, and the recent nonlinear gyrokinetic code, GX [96, 97] to calculate nonlinear heat and particle fluxes. A detailed explanation and reasoning for using GX is provided in appendix F. A flowchart that broadly explains the working of MicroStOpt is shown in figure 4.1.

MicroStOpt is a program manager that couples the three different codes. The equilibrium parameters such as the boundary Fourier coefficients, rotational transform, *etc.*, are contained in the state vector \boldsymbol{x}_0 . The general idea is to reduce the transport by stabilizing the linear mode(mode)s causing the largest transport. The algorithm follows the following steps.

1. From a non-linear GX run, we find the mode causing the most heat and particle transport and the range of wavenumbers (k_x, k_y) corresponding to that mode
2. Using GS2, our objective becomes to find a new state vector \boldsymbol{x}_0 such that the linear growth rate of the mode corresponding to the largest Q and Γ is lower than its previous value.
3. If the optimization requires a gradient, we spawn multiple instances of the optimizer. We change one element of \boldsymbol{x}_0 per instance by a small value and recalculate the objective function \mathcal{F} concurrently to find the derivative $\partial\mathcal{F}/\partial\boldsymbol{x}|_{\boldsymbol{x}_0}$.
4. After every ten iterations, we take the relatively more stable equilibria and run GX again to check how much the fluxes Q and Γ have decreased.

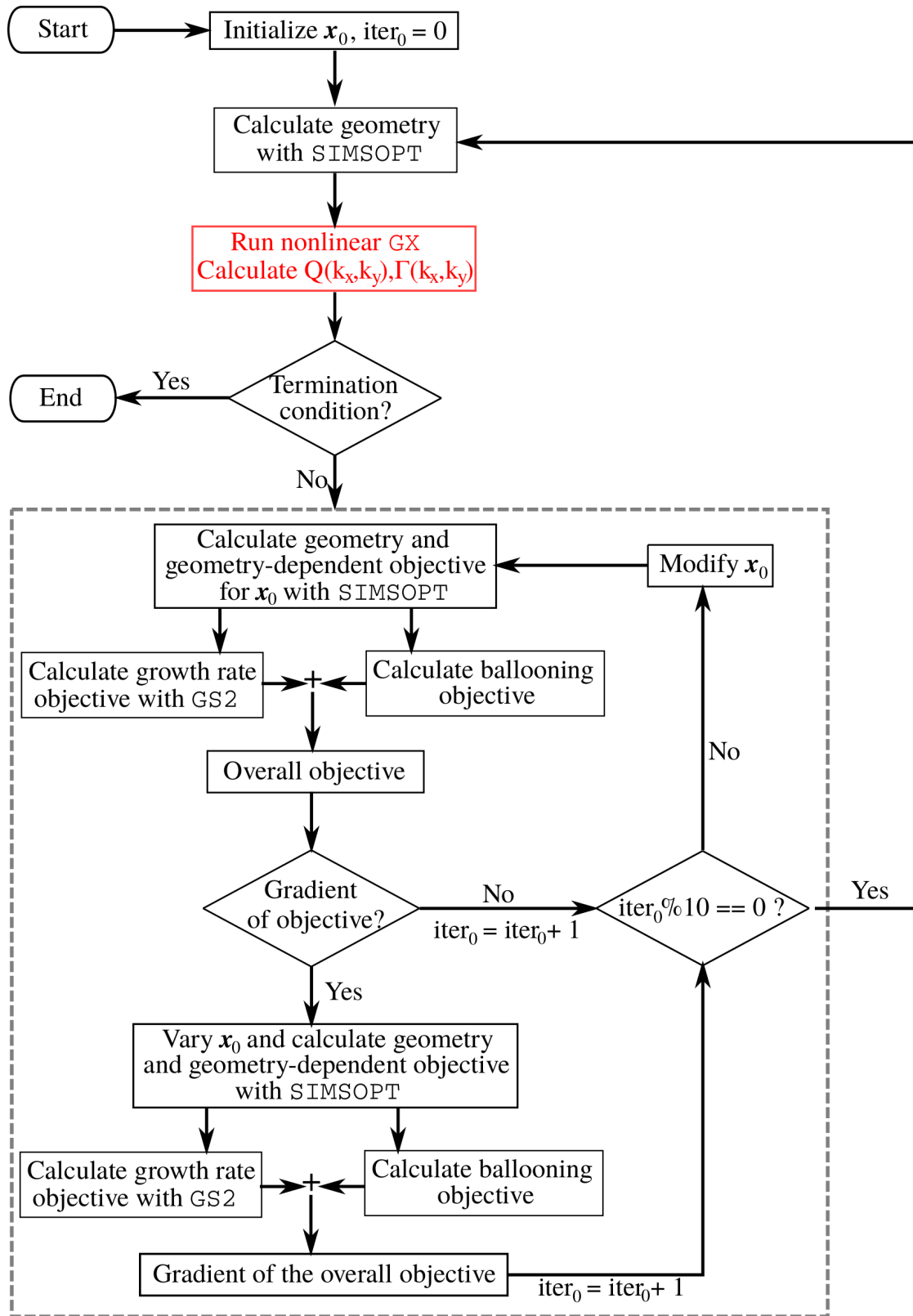


Figure 4.1: This figure shows the flow chart explaining how the MicroStOpt framework operates. The dashed gray box denotes the flow of logic inside an optimizer. The red box indicates work in progress as we are still testing nonlinear, electromagnetic GX.

Like SIMSOPT, the gradient of the objective function is calculated concurrently. We can use gradient-based or gradient-free, local or global optimizers; all of which available in Python.

Apart from wrapping these codes in an optimizer, we also implement load balancing over multiple CPUs by storing the status of each job. In this way, we can keep track of the total number of processors and reassign the processors used for a subprocess to another subprocess without using MPI from within an MPI program. Since finding the globally maximum growth rate on a (k_x, k_y) for different state vectors \mathbf{x}_0 is a highly parallel job and each GS2 run takes a different amount of time to converge, load-balancing helps us speed up the maximum growth rate calculation.

Using this framework, we first perform a few simple tests with the ideal ballooning stable, intermediate- β axisymmetric equilibrium from §2.4.1. Note that the weights of different penalty terms in the objective function \mathcal{F} are chosen based on the relative size of different objectives. There are no well-defined rules, and finding the right objective function occasionally requires trial-and-error by the user. The first two tests scan the objective function

$$\mathcal{F} = \mathcal{F}_{\text{minor}}^2 + \mathcal{F}_{\langle B \rangle}^2 + \mathcal{F}_{\text{aspect}}^2 + 4\mathcal{F}_{R_c}^2 + 2.5\mathcal{F}_{\text{micro}}^2, \quad (4.1)$$

with respect to the boundary Fourier coefficients in VMEC $\widehat{R}_b(0, 1)$ and $\widehat{R}_b(0, 2)$. All the terms except the last one are defined in §2.3.4.2. The last term,

$$\mathcal{F}_{\text{micro}} = \sum_{j=1}^{\text{ns}} \text{ReLU}(\gamma - \gamma_{\text{thresh}}), \quad (4.2)$$

sums over the maximum growth rate γ greater than γ_{thresh} in the chosen range of (k_x, k_y) on each

of ns flux surfaces indexed by j . For our study, we choose $\gamma_{\text{thresh}} = 0.02$, $k_x \in [0, 1.5]$, $k_y \in [0.05, 6.0]$, $ns = 12$ with $s \in [0.05, 0.875]$. The plot of \mathcal{F} with respect to $\widehat{R}_b(0, 1)$ and $\widehat{R}_b(0, 2)$ is given in figure 4.2.

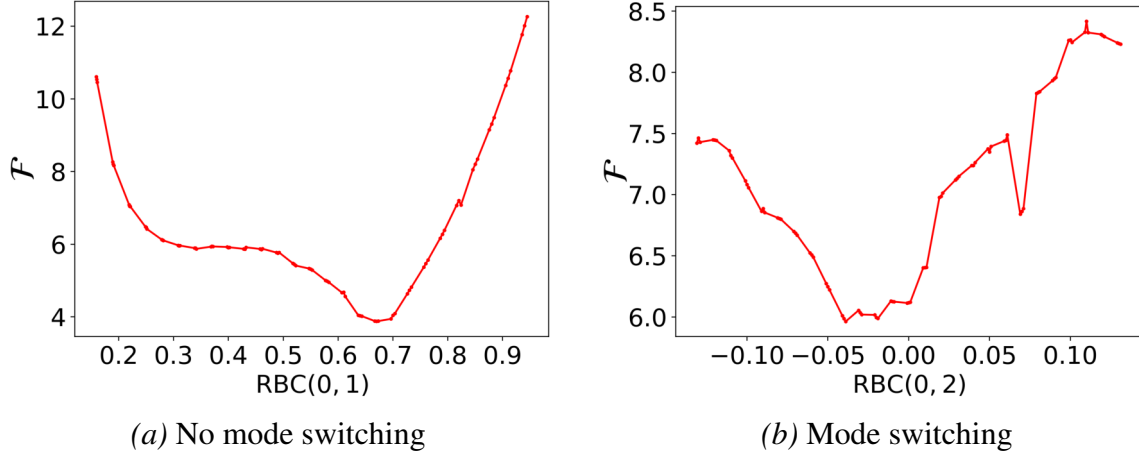


Figure 4.2: This figure shows the scan of the objective function \mathcal{F} with respect two boundary Fourier modes $\widehat{R}_b(0, 1)$ and $\widehat{R}_b(0, 2)$. In figure (a), we observe a case where the most unstable mode does not change leading to a smooth \mathcal{F} . However, noisy behaviour in figure (b) is because the mode corresponding to the maximum gamma changes as we change $\text{RBC}(0, 2)$.

The objective function is smooth in figure 4.2 (a) but non-smooth in figure 4.2 (b) because maximally growing modes switch from a KBM to an EM-ETG. The jumps occur because the maximum EM-ETG growth rate does not lie inside the chosen (k_x, k_y) domain. To capture both electromagnetic ion- and electron-driven modes, such as EM-ETGs and MTMs, we would require $k_y \sim \sqrt{m_i/m_e}$ which would make a straightforward linear calculation more expensive. A more efficient method is to isolate a single mode and reduce its growth rate. If we do that, we can use gradient-based optimization, which is much faster than gradient-free algorithms.

For the sake of simplicity, as a part of the preliminary tests, and to test our hypothesis about the connection between the ideal and kinetic ballooning modes, we will only perform stability optimization of equilibria against the KBM. We start by testing the hypothesis from chapter 3 in

State	$\beta_{\text{ax}}(\%)$	$\langle\beta\rangle(\%)$	$j_\phi(\text{MA})$	$\langle B\rangle(\text{T})$	\bar{t}	A	$a_N(m)$	$\psi_b(\text{Tm}^2)$
Initial	14.0	7.8	0.616	0.677	0.568	2.42	0.68	1.0
Optim.	12.8	7.1	0.475	0.749	0.301	2.59	0.647	1.0

Table 4.1: This table shows a comparison between relevant physical quantities of the initial and optimized DIII-D equilibrium.

the next section.

4.3 Finding a high- β , KBM-stable tokamak

In this section, we use the MicroStOpt framework to find a high- β tokamak design that is stable against both the ideal and kinetic ballooning modes. We start with the axisymmetric equilibrium used in §2.2.1. The degrees of freedom for this study are: $\widehat{R}_b(0, 1)$, $\widehat{R}_b(0, 2)$, $\widehat{R}_b(0, 3)$, $\widehat{R}_b(0, 4)$, $\widehat{Z}_b(0, 1)$, $\widehat{Z}_b(0, 3)$, $\widehat{Z}_b(0, 4)$, $\widehat{Z}_b(0, 5)$. We also vary the zeroth, third, and fifth coefficients of the rotational transform profile. Overall, we have eleven degrees of freedom. The iota and cross-section profiles of the initial and final equilibria are given in figure 4.3. A comparison between the values of important physical quantities for the initial and final equilibria is presented in table 4.2. We were able to stabilize the equilibrium against the ideal ballooning mode and reduce the KBM growth rate using MicroStOpt. Note also that after an equilibrium becomes stable against the ideal ballooning mode, there is no definitive correlation between the distance from ideal ballooning marginality and the KBM growth rate. In the next section, we test MicroStOpt for stellarator equilibria by searching for a quasisymmetric, high- β stellarator.

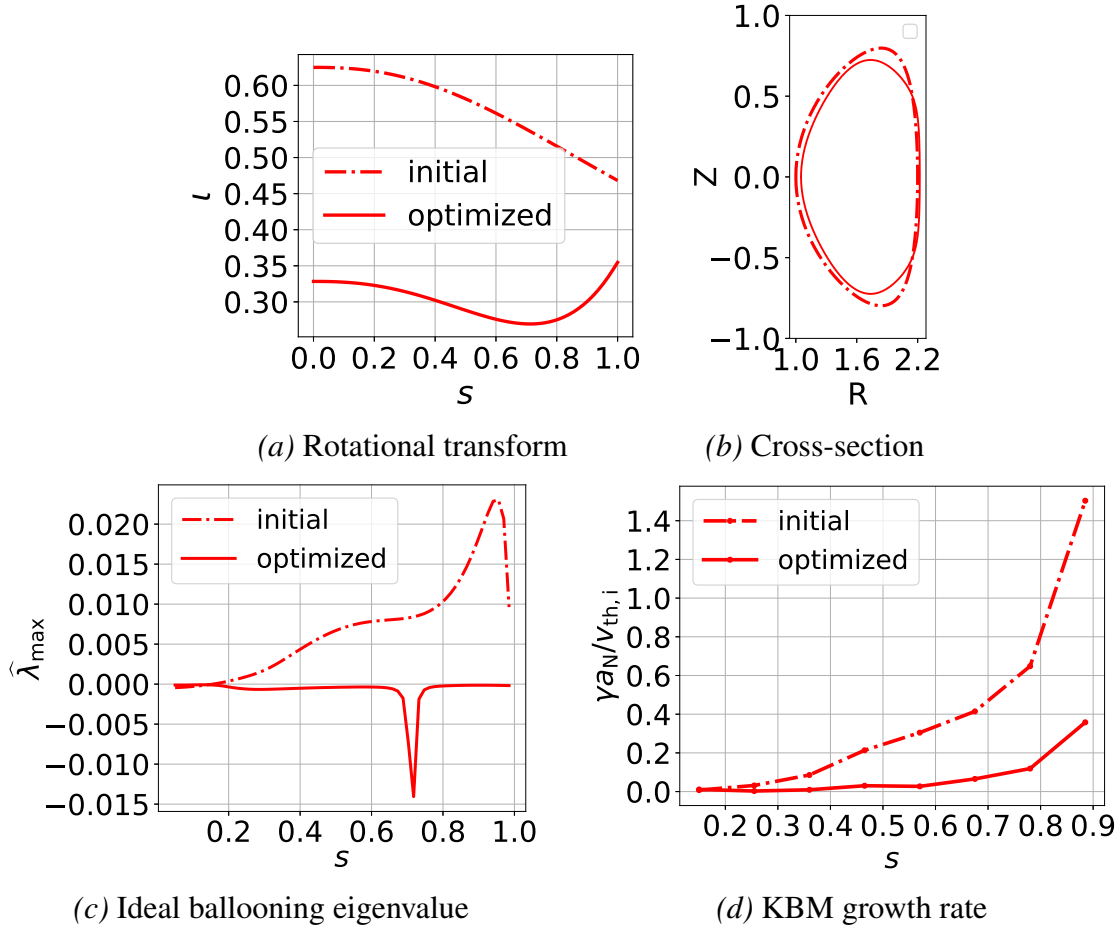


Figure 4.3: This figure plots the initial and optimized rotational transform and cross sections in the top row. In the bottom row, it shows the the ideal ballooning eigenvalue in figure 4.3(c) and the KBM growth rate in figure 4.3(d). Using MicroStOpt, we are able to stabilize the ideal ballooning mode and reduce the KBM growth rate by a factor of three.

4.4 Finding a high- β , KBM-stable quasisymmetric stellarator

In this section, we use the MicroStOpt framework to find a high- β , quasihelically symmetric stellarator equilibrium. We start with a Landreman-Buller-Drevlak (LBD) QH-like equilibrium. To obtain this equilibrium, we take the original LBD QH equilibrium and remove all the higher-order Fourier modes that define the boundary shape. Next, we vary the boundary shape coefficients of the LBD QH-like equilibrium to stabilize the ideal and kinetic ballooning modes

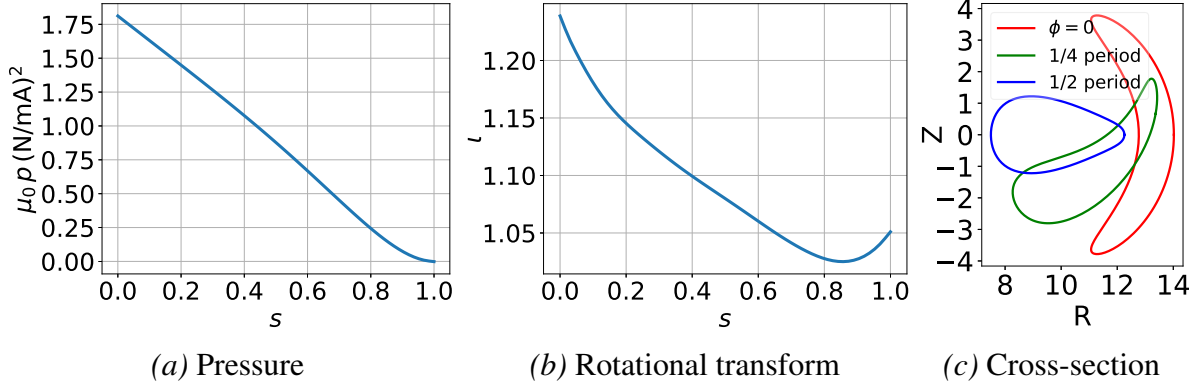


Figure 4.4: This figure shows the initial profiles and boundary shape of a high- β stellarator equilibrium. Note that the pressure and rotational transform profiles are the same as the LBD QH equilibrium. However, the boundary is different which makes this equilibrium non-quasisymmetric.

while recovering quasisymmetry. Mathematically, an equilibrium is quasisymmetric when the residual

$$f_{QS} = \sum_{s_j} \left\langle \left(\frac{1}{B^3} [(N - \iota M) \mathbf{B} \times \nabla B \cdot \nabla \psi - (MG + NI) \mathbf{B} \cdot \nabla B] \right) \right\rangle, \quad (4.3)$$

vanishes. In (4.3) N and M are the desired toroidal and poloidal mode numbers of the magnetic field, $2\pi\psi$ is the total enclosed toroidal flux, $2\pi/\mu_0 G(\psi)$ is the total poloidal current outside a flux surface and inside the boundary, and $2\pi/\mu_0 I(\psi)$ the total enclosed toroidal current. For this case, we search for quasihelically symmetric (QH) equilibria that correspond to $N = 1$ and $M = -1$.

Figure 4.4 shows the initial pressure, and rotational transform profiles, and the boundary shape profile of the initial stellarator equilibrium. We choose only the boundary coefficients as degrees of freedom. The list of coefficients is provided in table 4.2.

$\widehat{R}_b(n, m)$	$\widehat{Z}_b(n, m)$
$([1, 3], 0)$	$([1, 3], 0)$
$([-3, 3], 1)$	$([-3, 3], 1)$
$([-2, 2], 2)$	$([-2, 2], 2)$
$([-2, 2], 3)$	$([-2, 2], 3)$
$([-1, 1], 4)$	$([-1, 1], 4)$

Table 4.2: This table provides the boundary shape degrees of freedom for the QH, high- β stellarator equilibrium. The number of degrees of freedom is 46.

Using these degrees of freedom, we use MicroStOpt to find an ideal ballooning stable equilibrium that also has a lower KBM growth rate. The comparison of various growth rates is shown in figure 4.5.

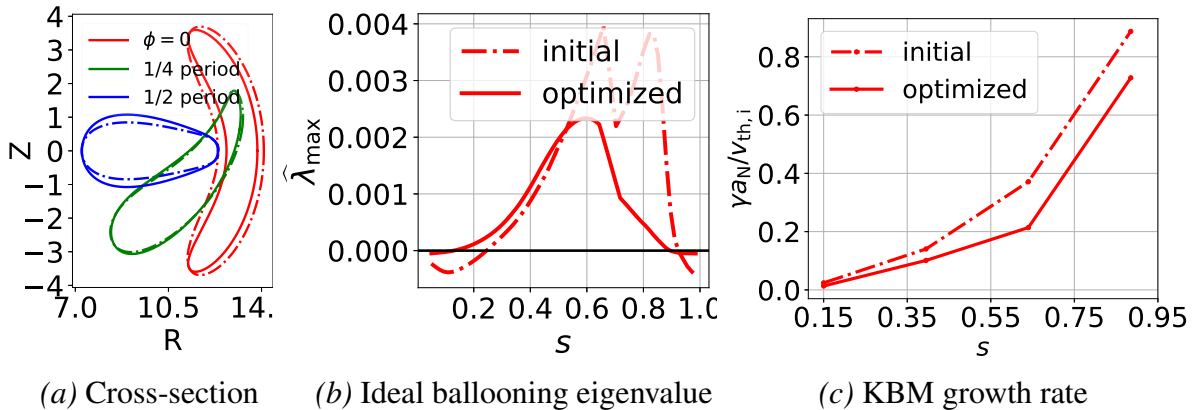


Figure 4.5: This figure shows the initial and final cross-section of the high- β stellarator equilibrium in figure 4.5(a). In figures 4.5(b) and (c), we present the ideal ballooning eigenvalue and KBM growth rates of the initial and optimized equilibrium. MicroStOpt is able to stabilize the initial equilibrium.

We observe that MicroStOpt is able to find an equilibrium that is relatively more stable to both the ideal and kinetic ballooning modes than the initial equilibrium. The maximum ideal ballooning growth rate is reduced approximately by half, and the maximum KBM growth rate is reduced by 20%. We also see a significant improvement in quasisymmetry, evident by the reduc-

State	$\beta_{\text{ax}}(\%)$	$\langle\beta\rangle(\%)$	$j_\phi(\text{MA})$	$\langle B\rangle(\text{T})$	\bar{v}	A	$a_{\text{N}}(m)$	f_{QS}	$\psi_{\text{b}}(Tm^2)$
Initial	12.6	5.7	2.15	5.54	1.12	6.50	1.74	9.0	45.6
Optim.	10.9	4.9	2.15	5.92	1.10	6.54	1.68	0.076	45.6

Table 4.3: This table shows a comparison between relevant physical quantities of the initial and optimized LBD-QH-like equilibrium.

tion of the quasisymmetry residual. This exercise serves as a proof-of-concept for MicroStOpt as a tool for finding high- β stellarator equilibria with favorable stability properties. Note that the original LBD QH equilibrium was also optimized for a self-consistent bootstrap current. Since we did not include the self-consistent bootstrap current in the penalty, the bootstrap current in this equilibrium is not self-consistent.

4.5 Summary and Conclusions

In this chapter, we described the details of a new ideal ballooning and kinetic stability optimization framework MicroStOpt. We presented some tests by scanning the kinetic instability objective function with respect to various boundary shape parameters. We followed that by stabilizing a high- β axisymmetric equilibrium against the ideal ballooning and kinetic ballooning mode (KBM). MicroStOpt was able to stabilize the equilibrium against the ideal ballooning mode and reduced the growth rate of the KBM by a factor of three. Finally, we used MicroStOpt to take a general high- β stellarator equilibrium and find a quasihelical (QH) 3D equilibrium with a reduced ideal ballooning and KBM growth rate throughout the volume. These studies demonstrate the ability of our optimization framework to reduce the linear instability growth rates of high- β tokamak and stellarator equilibria.

There are many more useful features that can be added to MicroStOpt. Currently, we can

only stabilize one mode at a time. To alleviate this, we plan to add the ability to perform a multi-mode analysis. Since these linear and nonlinear analyses are time-consuming, an interesting area of research is to find equilibrium-dependent proxies for the critical gradient [20] of nonlinear fluxes or the overall free energy [98] available to turbulence. Calculating equilibrium-dependent proxies is typically orders of magnitude faster than running gyrokinetic codes. Therefore, we can use MicroStOpt to find and test new proxies.

A complete optimization cycle with MicroStOpt requires hundreds of thousands of GS2 runs. The equilibrium data generated during the optimization combined with the linear growth rates and nonlinear fluxes can be used to train a machine learning model to map the space of favorable tokamak or stellarator operation or to discover new equilibrium-dependent proxies.

It would also be interesting to couple this framework with a transport solver such as Trinity [99, 100]. In this way, we could calculate the evolution of the temperature and density profiles on transport time scales and ensure that the kinetic turbulence is reduced and the device β is increased, thereby increasing the power output.

Chapter 4: Conclusions

In this thesis, we have studied optimization of high- β tokamaks and stellarators in the context of linear instabilities. To study the stability of these high- β equilibria, we used two models with different levels of complexity: ideal MHD and δf gyrokinetics.

In chapter 2, we analyzed three high- β fusion configurations against a pressure-driven instability, the infinite- n ideal ballooning. All the chosen equilibria were initially unstable against the ballooning mode. To stabilize said equilibria, we formulated an adjoint-based method to speed up the calculation of the gradient of the maximum growth rate of these equilibria. We implemented this method with the help of the SIMSOPT framework, finding stable equilibria for each of the initially unstable ones. A typical 3D optimization can have hundreds of Dofs. Since we only used the adjoint method with respect to two variables, our technique has the potential to speed up the gradient calculation even more. We plan to use this approach with low- n ideal MHD stability solvers which would speed up optimization against all types of fixed boundary, ideal MHD unstable modes.

In chapter 3, we performed an in-depth numerical study of twelve high- β tokamak and two stellarator equilibria against various types of kinetic instabilities. We used the fast parallel code GS2 to understand the stability mechanisms of two electrostatic modes of turbulence in high- β tokamaks, ITG and TEMs. To understand the effect of β , we compared these results with

low- β and intermediate- β tokamaks. Next, we observed the effect of electromagnetic fluctuations on these equilibria. In the high- β regime, the electromagnetic fluctuations caused the dominant modes to change from ITG and TEMs, to KBMs, EM-ETGs, and MTMs. To ensure that our observations for tokamaks could be generalized to stellarators, we then analyzed high- β stellarator equilibria and observed the same effects: finite- β stabilization of the ITG and the TEM, and emergence of KBMs, EM-ETGs, and MTMs. We also highlighted the similarity between the long-wavelength limit of the KBM and the ideal ballooning mode.

In chapter 4, we combined our ideal ballooning solver and the gyrokinetic solver GS2 along with the SIMSOPT framework to develop the MicroStOpt framework that can stabilize equilibria against ideal ballooning and kinetic instabilities. Long-wavelength modes usually dominate the heat and particle loss from a fusion device, and KBMs were the unstable electromagnetic modes with the longest wavelength. Moreover, both the stellarators and four tokamak equilibria that we analyzed in chapter 3 were unstable to KBMs. Therefore, we used MicroStOpt to stabilize these equilibria against ideal ballooning modes and KBMs. We were able to reduce the linear KBM growth rate by more than a factor of three for the tokamak and equilibria and around 20% for the stellarator equilibria, thereby demonstrating the utility of our optimization framework.

The ideas explored in this thesis can be extended in many directions, especially with the MicroStOpt framework. Since the heat and particle fluxes calculated with the nonlinear gyrokinetic solver GX generally depend on both ion- and electron-driven modes, extending our optimizer to include multiple modes would be beneficial. Once we have the results from the optimization, it would be useful to verify the long time evolution of the temperature and density profiles using a transport solver like Trinity.

Appendix A: Details of the adjoint method and ideal ballooning equation

A.1 The discretized ideal ballooning equation

After applying the boundary conditions $\widehat{X}_0 = \widehat{X}_N = 0$ to (2.41), we can rewrite the ballooning equation as

$$(A - \lambda \mathbb{I})\widehat{X} = 0, \quad (\text{A.1})$$

with \mathbb{I} being the identity matrix and the asymmetric tridiagonal matrix A with the following form

$$\begin{bmatrix} \frac{g_{1/2} + g_{3/2} - (\Delta\theta)^2 c_1}{(\Delta\theta)^2 f_1} & -\frac{g_{3/2}}{(\Delta\theta)^2 f_1} & 0 & 0 & \dots & 0 & 0 \\ -\frac{g_{3/2}}{(\Delta\theta)^2 f_2} & \frac{g_{3/2} + g_{5/2} - (\Delta\theta)^2 c_2}{(\Delta\theta)^2 f_2} & -\frac{g_{5/2}}{(\Delta\theta)^2 f_2} & 0 & \dots & 0 & 0 \\ & & \ddots & & & & \\ & & & \ddots & & & \\ 0 & 0 & 0 & 0 & \dots & \frac{g_{N-5/2} + g_{N-3/2} - (\Delta\theta)^2 c_{N-2}}{h^2 f_{N-2}} & -\frac{g_{N-3/2}}{(\Delta\theta)^2 f_{N-2}} \\ 0 & 0 & 0 & 0 & \dots & -\frac{g_{N-3/2}}{(\Delta\theta)^2 f_{N-1}} & \frac{g_{N-3/2} + g_{N-1/2} - (\Delta\theta)^2 c_{N-1}}{(\Delta\theta)^2 f_{N-1}} \end{bmatrix}$$

where the definitions of the terms g , c , and f are provided in (2.39) and $\Delta\theta$ is the (constant) spacing between the grid points. The matrix is solved for the maximum eigenvalue using an Arnoldi iterative scheme.

A.2 Details of the adjoint ideal ballooning calculation

In this appendix, we will derive (2.51) starting with (2.38). To do that, we will use the self-adjoint property of ideal MHD given in (2.46) as well as the Dirichlet boundary conditions satisfied by the eigenfunction,

$$\widehat{X}(\theta = \pm\theta_b) = \widehat{X}^*(\theta = \pm\theta_b) = 0. \quad (\text{A.2})$$

Defining $\mathbf{p} = (\tilde{\mathbf{p}}, \widehat{\mathbf{p}})$ as the union of all the parameters of the problem, we start by taking the derivative $\partial/\partial\mathbf{p}$ of (2.38),

$$\frac{d}{d\theta} \frac{\partial g}{\partial \mathbf{p}} \frac{d\widehat{X}}{d\theta} + \frac{d}{d\theta} g \frac{d}{d\theta} \frac{\partial \widehat{X}}{\partial \mathbf{p}} + \frac{\partial c}{\partial \mathbf{p}} \widehat{X} + c \frac{\partial \widehat{X}}{\partial \mathbf{p}} = \frac{\partial \widehat{\lambda}}{\partial \mathbf{p}} f \widehat{X} + \widehat{\lambda} f \frac{\partial \widehat{X}}{\partial \mathbf{p}} + \widehat{\lambda} \widehat{X} \frac{\partial f}{\partial \mathbf{p}}. \quad (\text{A.3})$$

Multiplying with \widehat{X}^* on both sides, integrating throughout the domain,

$$\begin{aligned} & \int_{-\theta_b}^{\theta_b} d\theta \widehat{X}^* \frac{d}{d\theta} \frac{\partial g}{\partial \mathbf{p}} \frac{d\widehat{X}}{d\theta} + \int_{-\theta_b}^{\theta_b} \widehat{X}^* \frac{d}{d\theta} g \frac{d}{d\theta} \frac{\partial \widehat{X}}{\partial \mathbf{p}} + \int_{-\theta_b}^{\theta_b} d\theta \frac{\partial c}{\partial \mathbf{p}} |\widehat{X}|^2 + \int_{-\theta_b}^{\theta_b} d\theta c \widehat{X}^* \frac{\partial \widehat{X}}{\partial \mathbf{p}} \\ & = \frac{\partial \widehat{\lambda}}{\partial \mathbf{p}} \int_{-\theta_b}^{\theta_b} d\theta f |\widehat{X}|^2 + \widehat{\lambda} \int_{-\theta_b}^{\theta_b} d\theta \frac{\partial f}{\partial \mathbf{p}} |\widehat{X}|^2 + \widehat{\lambda} \int_{-\theta_b}^{\theta_b} d\theta f \widehat{X}^* \frac{\partial \widehat{X}}{\partial \mathbf{p}}. \end{aligned} \quad (\text{A.4})$$

Using integration by parts, (A.2) and rearranging (A.4), we can write

$$\begin{aligned} & \int_{-\theta_b}^{\theta_b} d\theta \left(\frac{\partial c}{\partial \mathbf{p}} |\widehat{X}|^2 - \frac{\partial g}{\partial \mathbf{p}} \left| \frac{d\widehat{X}}{d\theta} \right|^2 - \widehat{\lambda} \frac{\partial f}{\partial \mathbf{p}} |\widehat{X}|^2 \right) - \frac{\partial \widehat{\lambda}}{\partial \mathbf{p}} \int_{-\theta_b}^{\theta_b} d\theta f |\widehat{X}|^2 \\ & = \int_{-\theta_b}^{\theta_b} d\theta \left(-\frac{d}{d\theta} g \frac{d\widehat{X}^*}{d\theta} - c \widehat{X}^* + \widehat{\lambda} f \widehat{X}^* \right) \frac{\partial \widehat{X}}{\partial \mathbf{p}}. \end{aligned} \quad (\text{A.5})$$

Due to the self-adjoint property of ideal MHD, the right side of (A.5) is zero. The rest of the equation can be arranged so that

$$\frac{\partial \hat{\lambda}}{\partial \mathbf{p}} = \frac{\int_{-\theta_b}^{\theta_b} d\theta \left(\frac{\partial c}{\partial \mathbf{p}} |\hat{X}|^2 - \frac{\partial g}{\partial \mathbf{p}} \left| \frac{d\hat{X}}{d\theta} \right|^2 - \hat{\lambda} \frac{\partial f}{\partial \mathbf{p}} |\hat{X}|^2 \right)}{\int_{-\theta_b}^{\theta_b} d\theta f |\hat{X}|^2}. \quad (\text{A.6})$$

Therefore, to calculate $\partial \hat{\lambda} / \partial \mathbf{p}$, we only need the gradients of the geometric coefficients g, c, f , the eigenfunction \hat{X} , and the eigenvalue $\hat{\lambda}$ of the ballooning equation; we have to solve the ideal ballooning equation only once. This speeds up the optimization loop, as it is much faster to obtain the gradient of the geometric coefficients than to solve the ballooning equation multiple times.

A.3 Extending our adjoint-based technique to equilibrium degrees of freedom

In this paper, we have used an adjoint method to find the maximum eigenvalue $\hat{\lambda}_{\max}$ with respect to the parameters $\hat{\mathbf{p}}$ of the ballooning equation. It is possible to extend our method to minimize f_{ball} to the equilibrium parameters $\tilde{\mathbf{p}}$ under the appropriate conditions. We define the problem and find the pertinent conditions in this appendix. We want to find

$$\min f_{\text{ball}}(\hat{\lambda}_{\max}, \tilde{\mathbf{p}}, \hat{\mathbf{p}}), \quad \text{s.t.} \quad \mathcal{G}(\hat{\lambda}, \hat{X}, \tilde{\mathbf{p}}, \hat{\mathbf{p}}) \equiv \mathcal{L}\hat{X} - \hat{\lambda}\hat{X} = 0. \quad (\text{A.7})$$

where all symbols are defined in §2.3.3 and the ballooning objective function f_{ball} is defined in (2.54). To minimize f_{ball} with respect to the equilibrium parameters, we need

$$\frac{df_{\text{ball}}}{d\tilde{\mathbf{p}}} = \frac{\partial f_{\text{ball}}}{\partial \hat{\lambda}_{\max}} \Big|_{\tilde{\mathbf{p}}, \hat{\mathbf{p}}} \frac{\partial \hat{\lambda}_{\max}}{\partial \tilde{\mathbf{p}}} \Big|_{\hat{\mathbf{p}}} + \frac{\partial f_{\text{ball}}}{\partial \hat{\mathbf{p}}} \Big|_{\hat{\lambda}_{\max}, \tilde{\mathbf{p}}} \frac{\partial \hat{\mathbf{p}}}{\partial \tilde{\mathbf{p}}} \Big|_{\hat{\lambda}_{\max}} + \frac{\partial f_{\text{ball}}}{\partial \tilde{\mathbf{p}}} \Big|_{\hat{\lambda}_{\max}, \hat{\mathbf{p}}}. \quad (\text{A.8})$$

The most expensive term to calculate in (A.8) is the gradient of the eigenvalue λ . To obtain that, we take the derivative of the operator \mathcal{G} with respect to λ ,

$$-\frac{\partial \mathcal{G}}{\partial \hat{\lambda}} \frac{\partial \hat{\lambda}}{\partial \tilde{\mathbf{p}}} = \frac{\partial \mathcal{G}}{\partial \hat{\lambda}} \frac{\partial \hat{\lambda}}{\partial \hat{\mathbf{p}}} + \frac{\partial \mathcal{G}}{\partial \hat{X}} \frac{\partial \hat{X}}{\partial \tilde{\mathbf{p}}} + \frac{\partial \mathcal{G}}{\partial \hat{X}} \frac{\partial \hat{X}}{\partial \hat{\mathbf{p}}} + \frac{\partial \mathcal{G}}{\partial \hat{\mathbf{p}}} + \frac{\partial \mathcal{G}}{\partial \tilde{\mathbf{p}}}. \quad (\text{A.9})$$

We also express $\hat{\lambda}$ around a point $\mathbf{p}_0 = (\tilde{\mathbf{p}}_0, \hat{\mathbf{p}}_0)$ in the state space as a Taylor series,

$$\hat{\lambda} = \hat{\lambda}(\mathbf{p}_0) + \frac{\partial \hat{\lambda}}{\partial \tilde{\mathbf{p}}} \cdot \delta \tilde{\mathbf{p}} + \frac{\partial \hat{\lambda}}{\partial \hat{\mathbf{p}}} \cdot \delta \hat{\mathbf{p}} + \frac{\partial}{\partial \tilde{\mathbf{p}}} \frac{\partial \hat{\lambda}}{\partial \tilde{\mathbf{p}}} : \delta \tilde{\mathbf{p}} \delta \tilde{\mathbf{p}} + \frac{\partial}{\partial \hat{\mathbf{p}}} \frac{\partial \hat{\lambda}}{\partial \hat{\mathbf{p}}} : \delta \hat{\mathbf{p}} \delta \hat{\mathbf{p}} + O(|\delta \mathbf{p}|^3), \quad (\text{A.10})$$

and assume that the optimizer takes a step size $|\delta \mathbf{p}|$ that is smaller than the radius of convergence of Taylor series (A.10),

$$\left| \frac{\partial}{\partial \tilde{\mathbf{p}}} \frac{\partial \hat{\lambda}}{\partial \tilde{\mathbf{p}}} : \delta \tilde{\mathbf{p}} \delta \tilde{\mathbf{p}} \right| \ll \left| \frac{\partial \hat{\lambda}}{\partial \tilde{\mathbf{p}}} \cdot \delta \tilde{\mathbf{p}} \right|, \quad \left| \frac{\partial}{\partial \hat{\mathbf{p}}} \frac{\partial \hat{\lambda}}{\partial \hat{\mathbf{p}}} : \delta \hat{\mathbf{p}} \delta \hat{\mathbf{p}} \right| \ll \left| \frac{\partial \hat{\lambda}}{\partial \hat{\mathbf{p}}} \cdot \delta \hat{\mathbf{p}} \right|. \quad (\text{A.11})$$

Using (A.10) and (A.11)

$$\frac{\partial \hat{\lambda}}{\partial \tilde{\mathbf{p}}} = \frac{\partial \hat{\lambda}}{\partial \hat{\mathbf{p}}} + \frac{\partial \hat{\lambda}}{\partial \tilde{\mathbf{p}}} \cdot \frac{\partial \tilde{\mathbf{p}}}{\partial \hat{\mathbf{p}}}. \quad (\text{A.12})$$

Next, we use the fact that $\partial \hat{\lambda} / \partial \hat{\mathbf{p}} = 0$ at $\hat{\lambda} = \hat{\lambda}_{\max}$, and that our choice of f_{ball} only explicitly depends on $\hat{\lambda}_{\max}$. Using the explicit form of the linear operator from (2.37), we multiply equation (A.9) by X^* and integrate throughout the domain, to rewrite (A.8) as

$$\frac{df_{\text{ball}}}{d\mathbf{p}} = \sum_{j=1}^{\text{ns}} \text{ReLU}'(\hat{\lambda}_{\max,j}) \frac{\int_{-\theta_b}^{\theta_b} d\theta \left(\frac{\partial c}{\partial \mathbf{p}} |\hat{X}|^2 - \frac{\partial g}{\partial \mathbf{p}} \left| \frac{d\hat{X}}{d\theta} \right|^2 - \hat{\lambda} \frac{\partial f}{\partial \mathbf{p}} |\hat{X}|^2 \right)}{\int_{-\theta_b}^{\theta_b} d\theta f |\hat{X}|^2}, \quad (\text{A.13})$$

where $\mathbf{p} = (\tilde{\mathbf{p}}, \hat{\mathbf{p}})$ is the union of all the parameters of the problem and ReLU'^1 is the derivative of the ReLU operator such that

$$\text{ReLU}'(x) = \begin{cases} 0, & \text{if } x < 0 \\ 1, & x > 0 \end{cases}$$

Calculating the derivative of the geometric coefficients g , c , and f , with respect to the equilibrium parameter vector $\tilde{\mathbf{p}}$ is not straightforward in VMEC and may lack the requisite accuracy for an adjoint method to work. However, an equilibrium solver like DESC [101, 102, 103] that is designed to calculate these gradients along with the geometric coefficients accurately may enable us to utilize the full potential of this adjoint-based method. Since the speed up obtained with an adjoint method is linearly proportional to the length of the vector $\tilde{\mathbf{p}}$, using (A.13) we can, in principle, speed up the calculation of $df_{\text{ball}}/d\tilde{\mathbf{p}}$ by an order of magnitude for 2D axisymmetric equilibria and by two orders or magnitude for 3D equilibria.

A.4 Extending our adjoint technique to low- n , ideal MHD solvers

Note that this process can be applied to any ideal MHD eigenvalue solver. For fluctuations that are not confined to a flux surface, one can simplify the energy integral subject to periodic perturbation in θ and ϕ as explained in 2.3.1 to an equation of the form

$$\mathcal{A}X = \lambda\mathcal{B}X, \tag{A.14}$$

¹The derivative of the ReLU operator is not well-defined at $x = 0$. We may have to replace it with an activation function that is continuous with a well-defined derivative. For example, we could use the logistic function $1/(1 + e^{-cx})$ with a large positive real number c .

where \mathcal{A} and \mathcal{B} are real symmetric matrices. Currently, solving such an equation using various low- n stability codes can be computationally expensive. For such a problem, we can repeat the process explained at the beginning of this appendix to obtain the gradient,

$$\frac{\partial \lambda}{\partial \mathbf{p}} = X^T \left(\frac{\partial \mathcal{A}}{\partial \mathbf{p}} - \lambda \frac{\partial \mathcal{B}}{\partial \mathbf{p}} \right) X / X^T \mathcal{B} X, \quad (\text{A.15})$$

for all modes. Equation (A.15) is similar to the Hellman-Feynman theorem [104, 105]. For axisymmetric equilibria, combining gradient information with fast equilibrium solvers such as EFIT [106] can help mitigate real-time disruption. One could also couple this adjoint approach with an optimizer to find low- n , ideal MHD stable equilibria.

A.5 Homotopy analysis method for solving the ideal ballooning equation

The Homotopy Analysis Method [107] is a powerful technique that can be used to rapidly solve complex, multi-dimension, nonlinear ODEs. In this appendix, we will use a particular flavor of the Homotopy analysis method called the Spectral Homotopy Analysis Method (SHAM) [108] to solve the infinite- n , ideal-ballooning equation (2.38).

In topology, homotopy is defined as a continuous deformation from one function to another. By extending this ability of continuous deformation to ordinary differential equations, one can solve complicated ODEs by continuously “deforming” the solution of a simpler ODE [107]. We define the homotopy function

$$\mathcal{H}(\widehat{X}; q) = q \mathcal{L}_1[\widehat{X}(\theta; q), \widehat{\lambda}(q)] + c_0(1 - q) \mathcal{L}_0[\widehat{X}(\theta; q) - \widehat{X}_0(\theta)], \quad (\text{A.16})$$

where \mathcal{L}_0 is a simple linear operator, \mathcal{L}_1 is the linear operator we seek to solve, $q \in [0, 1]$ is the homotopy parameter, c_0 is called the convergence control parameter, \widehat{X} and $\widehat{\lambda}$ are the eigenfunction and eigenvalue, respectively of homotopy function.

The equation $\mathcal{L}_1 \widehat{X} = 0$ can be solved by solving $\mathcal{H}(X; q = 1) = 0$. The homotopy method accomplishes this by writing the Taylor series expansion of $\mathcal{H}(\widehat{X}, \widehat{\lambda}; q)$, \widehat{X} , and $\widehat{\lambda}$ around $q = 0$

$$\mathcal{H}(\widehat{X}; q) = \mathcal{H}(\widehat{X}; q = 0) + \left. \frac{\partial \mathcal{H}(\widehat{X}; q)}{\partial q} \right|_{q=0} \frac{q}{1!} + \left. \frac{\partial^2 \mathcal{H}(\widehat{X}; q)}{\partial q^2} \right|_{q=0} \frac{q^2}{2!} + \dots, \quad (\text{A.17})$$

$$X(\theta; q) = \widehat{X}_0(\theta) + \left. \frac{q}{1!} \frac{\partial \widehat{X}(\theta)}{\partial q} \right|_{q=0} + \left. \frac{q^2}{2!} \frac{\partial^2 \widehat{X}(\theta)}{\partial q^2} \right|_{q=0} + \dots, \quad (\text{A.18})$$

$$\widehat{\lambda}(q) = \widehat{\lambda}_0 + \left. \frac{q}{1!} \frac{\partial \widehat{\lambda}}{\partial q} \right|_{q=0} + \left. \frac{q^2}{2!} \frac{\partial^2 \widehat{\lambda}}{\partial q^2} \right|_{q=0} + \dots, \quad (\text{A.19})$$

assuming q as a small parameter and solving \mathcal{H} order-by-order in q . To lowest order

$$\mathcal{H}(\widehat{X}; 0) = \mathcal{L}[\widehat{X}(\theta; 0) - \widehat{X}_0(\theta)] = 0, \quad (\text{A.20})$$

which can be satisfied by choosing $\widehat{X}(\theta, 0) = \widehat{X}_0$, i.e., the lowest order function \widehat{X} is equal to the starting guess \widehat{X}_0 .

A.5.1 Using SHAM to solve the ideal ballooning equation

The ideal ballooning equation

$$\frac{1}{f} \frac{d}{d\theta} \frac{d\widehat{X}}{d\theta} - \frac{c}{f} \widehat{X} - \lambda \widehat{X} = 0, \quad (\text{A.21})$$

is a second-order eigenvalue value ODE with coefficients that are functions of the independent variable θ . This equation must be solved subject to the boundary conditions

$$\widehat{X}(\theta = \pm\theta_b) = 0. \quad (\text{A.22})$$

To apply SHAM, we use the following simple linear operator

$$\mathcal{L}_0 \widehat{X} \equiv \frac{d^2 \widehat{X}}{d\theta^2} - 1 = 0, \quad \widehat{X}(\theta = \pm\theta_b) = 0. \quad (\text{A.23})$$

and rewrite the ideal ballooning operator by rescaling the eigenfunction \widehat{X} by the positive definite coefficient \sqrt{g}

$$\mathcal{L}_1 \widehat{X} \equiv \frac{d^2 \sqrt{g} \widehat{X}}{d\theta^2} + \left[\frac{1}{4} \left(\frac{g'}{g} \right)^2 - \frac{1}{2} \frac{g''}{g^2} - \lambda \frac{f}{g} \right] \sqrt{g} \widehat{X} = 0, \quad \widehat{X}(\theta = \pm\theta_b) = 0. \quad (\text{A.24})$$

Using \mathcal{L}_0 and \mathcal{L}_1 , we define the homotopy function

$$\mathcal{H}(\widehat{X}; q) = q \mathcal{L}_1 \widehat{X} + c_0 (1 - q) \mathcal{L}_0 [\widehat{X} - \widehat{X}_0], \quad (\text{A.25})$$

and write

$$X = \sum_{j=1}^n a_n T_n(\theta/\theta_b), \quad (\text{A.26})$$

where T_n is the n^{th} Chebyshev polynomial of the first kind. We also choose $X_0 = 1$. Using the solution from this order, we solve the homotopy equation for the next order

$$\mathcal{H}(X; q) = q\mathcal{L}_1 X_0 + c_0 q \mathcal{L}_0 \left[\frac{\partial X}{\partial q} \right] = q \left\{ \widehat{\lambda}_0 + c_0 \left[\frac{d^2}{d\theta^2} \left(\frac{\partial X}{\partial q} \right) - 1 \right] \right\} = 0 \quad (\text{A.27})$$

which gives us

$$\frac{\partial X}{\partial q} = \frac{(c_0 - \widehat{\lambda}_0)}{2} T_2(\theta) + a_1 T_1(\theta) + \frac{(2a_0 + c_0 - \widehat{\lambda})}{2}. \quad (\text{A.28})$$

To obtain the value of the unknown coefficients a_1 and a_0 , we impose the Dirichlet boundary conditions (A.22). To obtain $\widehat{\lambda}_0$, we have to impose an additional condition [107]. Since the amplitude of the eigenfunction of a linear ODE can be arbitrarily scaled, we utilize this freedom to set $\widehat{X}(\theta = 0) = 1$ which gives us $\widehat{\lambda}_0$. This iterative process can be automated using a computer program for each order of q until $\widehat{\lambda}$ satisfies a user-imposed convergence criterion. We then repeat the same process of calculating $\widehat{\lambda}$ for multiple values of c_0 and look for a region where $\widehat{\lambda}$ is independent of c_0 , *i.e.*, a plateau in the $\widehat{\lambda}$ - c_0 plot. The value of $\widehat{\lambda}$ in this region is an eigenvalue of the ballooning equation².

As an example, we solve the ideal ballooning equation for the low- β , negative triangularity equilibrium introduced in chapter 3.3 with a modified pressure gradient that is four times the nominal pressure gradient. We solve the equation using SHAM for 20 orders and calculate $\widehat{\lambda}$ for a range of values of c_0 . The ‘‘plateau’’ plot is shown in figure A.1.

²The ideal ballooning equation can have infinite eigenvalues but we are only considered with the largest eigenvalue. Fortunately, the SHAM converges the fastest for the largest eigenvalue, which is what we end up with.

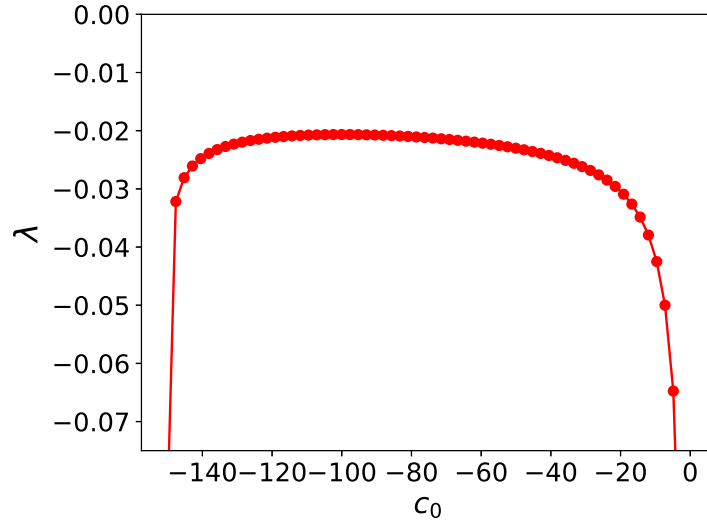


Figure A.1: This figure shows the “plateau” plot created using a homotopy analysis method. Over the plateau region, the eigenvalue λ changes minimally with respect to the homotopy parameter c_0 . This indicates convergence of the homotopy solution.

We choose the eigenfunction \hat{X} and eigenvalue $\hat{\lambda}$ for one of the values of c_0 in the plateau region which gives us the solution. The initial guess \hat{X}_0 along with the final eigenfunction \hat{X} is shown in figure A.2.

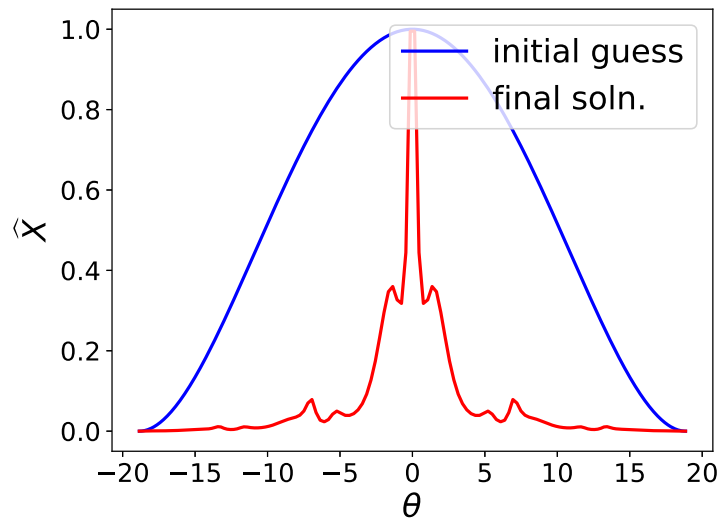


Figure A.2: This figure shows a comparison between the initial guess of the eigenfunction \hat{X}_0 and the final converged solution to the ideal ballooning equation. For this case, we solved the homotopy equation up to the 20th order.

The eigenvalue $\hat{\lambda} = 0.227$ matches the $\hat{\lambda} = -\gamma^2$ (after appropriate normalization) shown in figure 3.23(e) which was obtained by solving the discretized ideal ballooning solver.

Appendix B: Local expansion of an axisymmetric equilibrium

In this appendix, we will describe in detail how to solve the Grad-Shafranov equation locally on a flux surface. Using this method, we will write explicit analytical formulae for all the geometric coefficients needed for a local MHD or gyrokinetic simulation. In §B.1, we will explain the Greene-Chance method, introduce the local coordinate systems used for our analysis. Using the local coordinate system, we will then expand the Grad-Shafranov equation near a flux surface and explain how one can generate an arbitrary number of local equilibria using this technique.

In §B.2 we will demonstrate analytically that by appropriately choosing the signs of equilibrium-dependent quantities, the coefficients can be made invariant to the transformation $\psi_p \rightarrow -\psi_p$. We will also introduce some tests that a user of a local stability code can use to check the correctness of a set of geometric coefficients for both tokamaks and stellarators.

B.1 The analysis of Greene and Chance

This appendix explains the Greene-Chance method, a powerful technique that allows one to vary the pressure and current gradients locally and self-consistently within a global equilibrium. We will start by defining the local coordinate system first developed by Mercier and Luc [109]. After that, we will expand the Grad-Shafranov equation in those coordinates and use it to obtain

other important relations, namely the gradients of q , B , and α around a surface. Finally, we explain how the derived relations can be used to vary a local equilibrium. All lengths in the following calculations are normalized to a_N and the magnetic fields to B_N . In §B.1.1 and §B.1.2, we define $\tilde{\rho}$ to be the normalized radial distance from a flux surface whereas in appendix §B.1.3 $\tilde{\rho}$ is a normalized flux surface label — exactly the same quantity as used in the main body of this thesis.

B.1.1 Mercier-Luc local coordinate system

The Mercier-Luc coordinate system is a local orthogonal coordinate system $(\tilde{\rho}, \phi, l_p)$ where $\tilde{\rho}$ is the normalized perpendicular distance from a point on the flux surface, ϕ is the cylindrical azimuthal angle, and l_p is the normalized poloidal arc length. In these local coordinates, we can write the cylindrical (R, ϕ, Z) coordinates as

$$\begin{aligned} R &= R_0 + \tilde{\rho} \sin(u(l_p)) + \int_0^{l_p} \cos(u) dl'_p, \\ Z &= Z_0 + \tilde{\rho} \cos(u(l_p)) + \int_0^{l_p} \sin(u) dl'_p, \end{aligned} \tag{B.1}$$

where R_0, Z_0 are the normalized values of R, Z on the outboard mid-plane of the flux surface of interest and the angle u is defined as shown in figure B.1. We also define

$$\begin{aligned} R_s &\equiv R(\tilde{\rho} = 0, l_p) = R_0 + \int_0^{l_p} \cos(u) dl'_p, \\ Z_s &\equiv Z(\tilde{\rho} = 0, l_p) = Z_0 + \int_0^{l_p} \sin(u) dl'_p, \end{aligned} \tag{B.2}$$

as the on-surface cylindrical coordinates. The azimuthal angle ϕ is the same for the cylindrical and Mercier-Luc coordinates. Using equation (B.1) and after choosing a sign for the curvature,

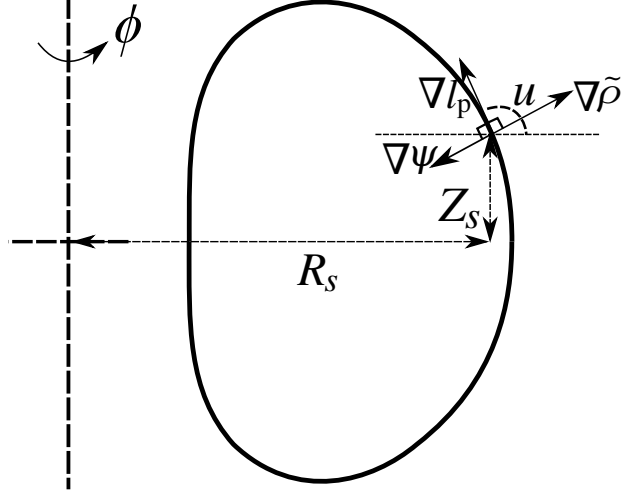


Figure B.1: This figure illustrates the local orthogonal coordinate system $(\tilde{\rho}, \phi, l_p)$. The radial distance $\tilde{\rho}$ is measured in the direction normal to a flux surface and poloidal arc length l_p is measured in a counter-clockwise sense from the outboard side. We choose $\nabla\psi_p$ to point in the direction opposite to $\nabla\tilde{\rho}$.

we can define the curvature

$$\frac{1}{R_c} = \frac{du}{dl_p}. \quad (\text{B.3})$$

where R_c is the radius of curvature. Using the coordinate transformation relation (B.1), we can

write

$$\begin{bmatrix} dR \\ d\phi \\ dZ \end{bmatrix} = \begin{bmatrix} \sin(u) & 0 & \left(1 + \frac{\tilde{\rho}}{R_c}\right) \cos(u) \\ 0 & 1 & 0 \\ -\cos(u) & 0 & \left(1 + \frac{\tilde{\rho}}{R_c}\right) \sin(u) \end{bmatrix} \begin{bmatrix} d\tilde{\rho} \\ d\phi \\ dl_p \end{bmatrix} \quad (\text{B.4})$$

This matrix can be inverted to obtain the transformation from Mercier-Luc to cylindrical coordinates. Using this transformation, we can write the transformation Jacobian

$$\tilde{J} = ((\nabla\tilde{\rho} \times \nabla\phi) \cdot \nabla l_p)^{-1} = R \left(1 + \frac{\tilde{\rho}}{R_c}\right). \quad (\text{B.5})$$

B.1.2 Expanding the Grad-Shafranov equation locally

The Grad-Shafranov equation

$$R^2 \nabla \cdot \left(\frac{\nabla \psi_p}{R^2} \right) = -R^2 \frac{dp}{d\psi_p} - F \frac{dF}{d\psi_p}, \quad F > 0, \quad (\text{B.6})$$

can be written in the Mercier-Luc coordinate system as

$$\frac{R}{(1 + \tilde{\rho}/R_c)} \left[\frac{\partial}{\partial l_p} \left(\frac{(1 + \tilde{\rho}/R_c)}{R} \frac{\partial \psi_p}{\partial l_p} \right) + \frac{\partial}{\partial \tilde{\rho}} \left(\frac{(1 + \tilde{\rho}/R_c)}{R} \frac{\partial \psi_p}{\partial \tilde{\rho}} \right) \right] = -R^2 \frac{dp}{d\psi_p} - F \frac{dF}{d\psi_p}. \quad (\text{B.7})$$

To obtain the local dependence of ψ_p on various gradients such as $dF/d\psi_p$ and $dp/d\psi_p$, we write ψ_p as an asymptotic series in terms of the normalized radial distance $\tilde{\rho}$

$$\psi_p = \psi_{p0} + \tilde{\rho} \psi_{p1}(l_p) + \tilde{\rho}^2 \psi_{p2}(l_p) + O(\tilde{\rho}^3), \quad (\text{B.8})$$

define

$$\psi_{p1} = \lim_{\tilde{\rho} \rightarrow 0} \left(\frac{\psi_p - \psi_{p0}}{\tilde{\rho}} \right) = -R_s B_{ps}, \quad \psi_{p1} < 0, \quad B_{ps} > 0. \quad (\text{B.9})$$

where B_{ps} is the poloidal magnetic field on the surface. Another way to write the above relation is to say $\nabla \psi_p|_{\tilde{\rho}=0} = \psi_{p1} \nabla \tilde{\rho}$. Using this asymptotic expansion, we can also write the following

Taylor series expansions

$$\begin{aligned}
F(\psi_p) &= F(\psi_{p0}) + \frac{\psi_p - \psi_{p0}}{1!} \left. \frac{dF}{d\psi_p} \right|_{\psi_{p0}} + \dots = F(\psi_{p0}) - \tilde{\rho} R_s B_{ps} \left. \frac{dF}{d\psi_p} \right|_{\psi_{p0}} + \dots, \\
F'(\psi_p) &= F'(\psi_{p0}) + \frac{\psi_p - \psi_{p0}}{1!} \left. \frac{dF'}{d\psi_p} \right|_{\psi_{p0}} + \dots = F'(\psi_{p0}) - \tilde{\rho} R_s B_{ps} \left. \frac{dF'}{d\psi_p} \right|_{\psi_{p0}} + \dots, \\
p(\psi_p) &= p(\psi_{p0}) + \frac{\psi_p - \psi_{p0}}{1!} \left. \frac{dp}{d\psi_p} \right|_{\psi_{p0}} + \dots = p(\psi_{p0}) - \tilde{\rho} R_s B_{ps} \left. \frac{dp}{d\psi_p} \right|_{\psi_{p0}} + \dots, \\
q(\psi_p) &= q(\psi_{p0}) + \frac{\psi_p - \psi_{p0}}{1!} \left. \frac{dq}{d\psi_p} \right|_{\psi_{p0}} + \dots = q(\psi_{p0}) - \tilde{\rho} R_s B_{ps} \left. \frac{dq}{d\psi_p} \right|_{\psi_{p0}} + \dots,
\end{aligned} \tag{B.10}$$

where the prime denotes a derivative with respect to ψ_p . After substituting the Taylor series expansions into the local Grad-Shafranov equation (B.7), we get

$$\psi_{p2} = -\frac{1}{2} \left[R_s B_{ps} \left(\frac{\sin(u)}{R_s} - \frac{1}{R_c} \right) + R_s^2 p'(\psi_{p0}) + F(\psi_{p0}) F'(\psi_{p0}) \right]. \tag{B.11}$$

Next, we write (2.11) in the Mercier-Luc coordinate system

$$q = -\frac{1}{2\pi} \oint dl_p \frac{F}{R_s^2 B_{ps}}, \tag{B.12}$$

and expand it about a flux surface to obtain

$$\begin{aligned}
\frac{dq}{d\psi_p} &= -F' \left(\oint \frac{dl_p}{R_s^2 B_{ps}} + \frac{F^2}{2\pi} \oint \frac{1}{R_s^4 B_{ps}^3} dl_p \right) + \frac{p' F}{2\pi} \oint \frac{dl_p}{R_s^2 B_{ps}^3} \\
&\quad + \frac{F}{2\pi} \oint \frac{2 d\theta}{R_s^3 B_{ps}^2} \left(\frac{\sin(u)}{R_s} - \frac{1}{R_c} \right).
\end{aligned} \tag{B.13}$$

Using the fact $dl_p/B_{ps} = d\theta/\mathbf{B} \cdot \nabla\theta$ we can write an algebraic equation in straight-field-line angle θ that defines q' in terms of F' and p'

$$\begin{aligned} \frac{1}{q} \frac{dq}{d\psi_p} &= F' \left(\frac{1}{F} + \frac{F}{2\pi} \oint d\theta \frac{1}{(R_s B_{ps})^2} \right) + \frac{p'}{2\pi} \oint \frac{d\theta}{B_{ps}^2} \\ &+ \frac{1}{2\pi} \oint \frac{2 d\theta}{R_s B_{ps}} \left(\frac{\sin(u)}{R_s} - \frac{1}{R_c} \right), \end{aligned} \quad (\text{B.14})$$

written more compactly as

$$\frac{1}{q} \frac{dq}{d\psi_p} = F' a_{s,\text{full}} + p' b_{s,\text{full}} + c_{s,\text{full}}, \quad (\text{B.15})$$

where $a_{s,\text{full}}$, $b_{s,\text{full}}$, and $c_{s,\text{full}}$ are three constants obtained by performing the respective integrals in (B.14). Next, using the Mercier-Luc coordinates, we expand the magnetic field strength around a flux surface

$$\begin{aligned} B^2 &= \frac{F^2}{R^2} + \left(\frac{1}{R} \frac{d\psi_p}{d\tilde{\rho}} \right)^2 \\ &= B_s^2 \left[1 + \frac{2\tilde{\rho}}{B_s^2} \left(-\frac{B_{ps}^2}{R_c} + R_s B_{ps} p' - \frac{F^2}{R_s^3} \sin(u) \right) \right], \end{aligned} \quad (\text{B.16})$$

which gives us the local, radial gradient of the magnetic field

$$\frac{\partial B}{\partial \tilde{\rho}} = \frac{1}{B_s} \left(-\frac{B_{ps}^2}{R_c} + R_s B_{ps} p' - \frac{F^2}{R_s^3} \sin(u) \right). \quad (\text{B.17})$$

To obtain all the geometric coefficients, we also need various gradients of the field line label α .

To that end, we can write the field line label in Mercier-Luc coordinates as

$$\alpha_t = \phi + S(\tilde{\rho}, l_p) = \phi - q\theta, \quad (\text{B.18})$$

and find $S = S(\tilde{\rho}, l_p)$ by solving the equation

$$\mathbf{B} \cdot \nabla \alpha_t = 0. \quad (\text{B.19})$$

To solve equation (B.19), we write $S(\tilde{\rho}, l_p)$ as an asymptotic series in $\tilde{\rho}$

$$S = S_0(l_p) + \tilde{\rho} S_1(l_p) + \mathcal{O}(\tilde{\rho}^2), \quad (\text{B.20})$$

and equation (B.19) becomes

$$\frac{F}{R^2} + \frac{1}{R(1 + \tilde{\rho}/R_c)} \frac{\partial \psi_p}{\partial \tilde{\rho}} \frac{\partial \alpha_t}{\partial l_p} - \frac{1}{R(1 + \tilde{\rho}/R_c)} \frac{\partial \psi_p}{\partial l_p} \frac{\partial \alpha_t}{\partial \tilde{\rho}} = 0. \quad (\text{B.21})$$

The lowest-order solution yields

$$S_0 = \int dl_p \frac{F(\psi_{p0})}{R_s^2 B_{ps}} + f(\tilde{\rho}), \quad (\text{B.22})$$

For axisymmetric equilibria, all the field lines are identical, which means we can choose $f(\tilde{\rho}) = 0$

without loss of generality. The next-order solution gives us

$$S_1 = -R_s B_{ps} \left[F' \left(\frac{q\theta}{F} + F \int_0^\theta d\theta \frac{q}{(R_s B_{ps})^2} \right) + p' \int_0^\theta d\theta \frac{q}{B_{ps}^2} + \int_0^\theta d\theta \frac{2q}{R_s B_{ps}} \left(\frac{\sin(u)}{R_s} - \frac{1}{R_c} \right) \right], \quad (\text{B.23})$$

$$\frac{\partial \alpha_t}{\partial \tilde{\rho}} = S_1 = -R_s B_{ps} \left(F' a_s + p' b_s + c_s \right). \quad (\text{B.24})$$

This completely defines the quantity $\nabla\alpha_t$. Using (B.15), (B.17), (B.24) we can calculate all the geometric coefficients¹ needed for a local stability analysis.

B.1.3 Variation of a local axisymmetric equilibrium

Using the normalized flux surface label $\rho = \sqrt{\psi/\psi_{\text{LCFS}}}$, equation (B.15) can be written as

$$\frac{\hat{s}}{\rho} \equiv \frac{1}{q} \frac{dq}{d\rho} = \frac{dF}{d\rho} a_{s,\text{full}} + \frac{dp}{d\rho} b_{s,\text{full}} + c_{s,\text{full}}, \quad (\text{B.25})$$

where $a_{s,\text{full}}$, $b_{s,\text{full}}$, and $c_{s,\text{full}}$ are constants. This equation implies that on a given surface, we can vary the pressure gradient $dp/d\rho$ and the shear \hat{s} of a local equilibrium independently by a finite amount as long as we adjust $dF/d\rho$ such that the equation (B.25) is satisfied. Using the the new values of $dp/d\rho$, $dq/d\rho$, $dF/d\rho$, we can calculate the radial gradient of α_t and B using (B.24) and (B.17), respectively. Moreover, the gradients along the field line do not change. Therefore, using this method, we can generate an arbitrary number of self-consistent local equilibria. Greene and Chance first used this idea to perform an $\hat{s} - \alpha_{\text{MHD}}$ analysis. We are going to use this for the ballooning and gyrokinetic stability analyses.

B.1.4 Geometric coefficients for a local analysis

In this section, we will present the complete set of geometric coefficients needed for a local stability analysis. Using the local expansion formulae derived in the previous sections, we simplify the complete set of coefficients to the Mercier-Luc coordinate system. The complete set of coefficients and their simplified definitions in Mercier-Luc coordinates are given table B.1.

¹For up-down asymmetric equilibria the lower limit in all the integrals should be some non-zero value θ_{low} . To include the effect of θ_0 , change the lower limit of integration in (B.24) from θ_{low} to $\theta_{\text{low}} + \theta_0$.

Geometric coefficient	Definition	Mercier-Luc expansion
gradpar	$a_N (\mathbf{b} \cdot \nabla \theta) $	$\frac{a_N}{R_s B} \psi_{p1} \frac{\partial \theta}{\partial l_p} $
bmag	$\frac{B}{B_N}$	$\frac{B}{B_N}$
gds2	$\frac{1}{(a_N B_N)^2} \left(\frac{d\psi_p}{d\rho}\right)^2 \nabla \alpha_t ^2$	$\frac{1}{(a_N B_N)^2} \left(\frac{d\psi_p}{d\rho}\right)^2 \left(\frac{1}{R_s^2} + S_1^2\right)$
gds21	$\frac{1}{(a_N B_N)^2} \frac{d\psi_p}{d\rho} \frac{dq}{d\rho} \nabla \psi_p \cdot \nabla \alpha_t$	$\frac{1}{(a_N B_N)^2} \frac{d\psi_p}{d\rho} \frac{dq}{d\rho} \psi_{p1} S_1$
gds22	$\frac{ \nabla \psi_p ^2}{(a_N B_N)^2} \left(\frac{dq}{d\rho}\right)^2$	$\frac{\psi_{p1}^2}{(a_N B_N)^2} \left(\frac{dq}{d\rho}\right)^2$
gbdrift	$\frac{2}{B^2} \frac{d\psi_p}{d\rho} \frac{dq}{d\rho} (\mathbf{b} \times \nabla B) \cdot \nabla \alpha_t$	$-\frac{1}{B^2} \frac{\partial B^2}{\partial \rho} + \frac{1}{B^3} \frac{d\psi_p}{d\rho} \frac{F}{R} S_1 \frac{\partial B}{\partial l_p}$
cvdrift	$\text{gbdrift} - \frac{1}{B^2} \frac{d(2\mu_0 p)}{d\rho}$	$-\frac{1}{B^2} \left(\frac{d(2\mu_0 p)}{d\rho} + \frac{\partial B^2}{\partial \rho}\right) + \frac{1}{B^3} \frac{d\psi_p}{d\rho} \frac{F}{R} S_1 \frac{\partial B}{\partial l_p}$
gbdrift0	$\frac{2}{B^2} \frac{dq}{d\rho} (\mathbf{b} \times \nabla B) \cdot \nabla \psi_p$	$\frac{2}{B^3} \frac{dq}{d\rho} \frac{F}{R} \frac{\partial B}{\partial l_p} \psi_{p1}$
cvdrift0	$\frac{2}{B^2} \frac{dq}{d\rho} (\mathbf{b} \times \nabla B) \cdot \nabla \psi_p$	$\frac{2}{B^3} \frac{dq}{d\rho} \frac{F}{R} \frac{\partial B}{\partial l_p} \psi_{p1}$

Table B.1: This table lists the complete set of geometric coefficients needed to perform an ideal ballooning or gyrokinetic analysis.

where ψ_{p1} is defined in (B.9) and the radial derivatives $\partial B / \partial \tilde{\rho}$ and S_1 are calculated using (B.17) and (B.24), respectively. Derivatives along the field line such as $\partial B / \partial l_p$ are calculated numerically using a finite difference scheme. Note that the quantity $\text{gbdrift0} = \text{cvdrift0}$.

B.2 Some tests for the geometry

Presently, there is a discrepancy in the geometric coefficients used by different gyrokinetic codes in the fusion community. To resolve this issue, in this section, we provide analytical and numerical tests that can be performed to ensure the correctness of the geometric coefficients. In §B.2.1, we prove the sign invariance of geometric coefficients for a simple axisymmetric case. In the next section, we present a simple numerical test based on the fact that the growth rate should be bounded in the ballooning parameter θ_0 .

B.2.1 $\psi_p \rightarrow -\psi_p$ invariance of the geometric coefficients

For this test, we change the sign of the poloidal flux ψ_b and observe how the rest of the quantities as well as the geometric coefficients change in table B.1. The table below lists the sign change of the relevant quantities when $(\psi_p, \phi, \theta) \rightarrow (-\psi_p, \phi, \theta)$.

Variable	Initial sign	Final sign
ψ_{p1}	+	-
α_{t1}	+	+
q	+	+
F	+	-

Note that α_t is not a constant on a flux surface, unlike the rest of the quantities. By the initial and final sign of α_t , we fix the sign at fixed θ . The sign-dependent coefficients are $cvdrift$, $cvdrift0 = gbdrift0$, $gbdrift$, and $gds21$. Applying the sign changes listed in table B.2.1 to these geometric coefficients, we can verify that the signs of all geometric coefficients remain unchanged. In summary, the geometric coefficients used for tokamaks are invariant to the transformation $\psi_{p1} \rightarrow -\psi_{p1}$. Since the definition of the geometric coefficients is exactly the same for 3D equilibria, we expect $\psi_p \rightarrow -\psi_p$ invariance to hold for stellarator equilibria as well.

B.2.2 Periodicity and boundedness of physical quantities in θ_0

Another test that we can use to confirm the signs of the geometric coefficients is to scan the ideal-ballooning growth rate $\widehat{\lambda}$ in the ballooning parameter θ_0 and ensure that it is periodic and bounded. When choosing a wrong set of coefficients, we observe that the growth rate increases

without limits in the $\theta_0 - \alpha_t$ plots ².

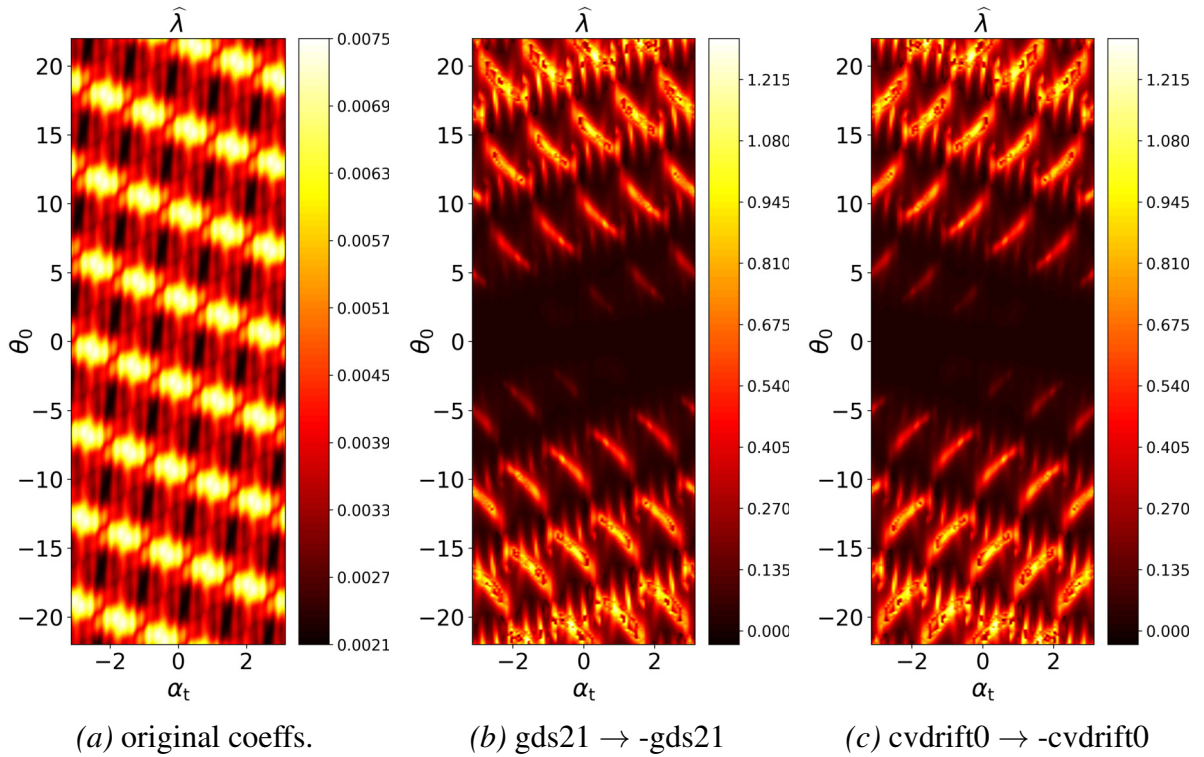


Figure B.2: This figure shows contours of the ballooning eigenvalue $\hat{\lambda}$ in figure (a) for the original set of coefficients, figure (b) after flipping the sign of $gds21$ without changing other coefficients, and in figure (c) after flipping the sign of $cvdrift0$ while keeping other coefficients fixed. For incorrect signs of $cvdrift0$ or $gds21$, the $\hat{\lambda}$ increases with θ_0 for every α_t , which is incorrect. This can be used as a test for the geometric coefficients in a local simulation. Note the symmetry of $\hat{\lambda}$ in figures (b) and (c) which is a consequence of the stellarator symmetry of NCSX.

This test helps us decide the relative signs of the quantities $cvdrift0$ and $gds21$. Note that for equilibria with stellarator symmetry, flipping the signs of both $cvdrift0$ and $gds21$ the $\hat{\lambda}$ contour plot would be a mirror image of figure B.2(a) about the vertical axis.

These tests resolve the sign issues for both up-down symmetric tokamaks and up-down stellarator symmetric stellarators. This is sufficient for all the equilibria studied in this thesis.

However, as optimization becomes more sophisticated and we explore up-down asymmetry, we

²Note that this is necessary but not sufficient condition — the coefficients may be wrong with a bounded growth rate. However, if the growth rate is unbounded, the coefficients are incorrect

may need more tests to resolve this issue fully.

Appendix C: Hsu, Artun and Cowley’s analytical ($\beta \sim 1$) tokamak equilibrium

In this appendix, we provide a brief overview of the analytical, high- β equilibrium derived by Hsu, Artun and Cowley. In §C.1, we describe the asymptotic ordering and the procedure used to analytically solve the Grad-Shafranov equation for $\beta \sim 1$. In §C.2, we discuss two major limitations of these analytical solutions in the context of local stability analyses.

C.1 Generating analytical $\beta \sim 1$ equilibria

The most general analytical theory for generating $\beta \sim 1$ equilibria was first developed by Hsu, Artun, and Cowley [3]. In that work, the Grad-Shafranov equation is solved analytically in the limit

$$\delta_{\text{Hsu}} \equiv \sqrt{\epsilon/(\beta q^2)} \ll 1, \quad (\text{C.1})$$

where $\epsilon = a/R_0$ is the aspect ratio of the flux surface — a being the minor radius of a flux surface and R_0 being the major radius. For these equilibria, it is assumed $B_t/B_p \sim q/\epsilon$ where $B_t = \mathbf{B} \cdot \nabla \phi / |\nabla \phi|$, $B_p = \mathbf{B} \cdot \nabla \theta / |\nabla \theta|$ are the toroidal and poloidal components of the magnetic field, respectively, and $\epsilon \sim \beta \sim 1$ on all surfaces of interest.

Given these assumptions, Hsu *et al.* solve the Grad-Shafranov equation to calculate the

perpendicular distance from the boundary to a point on the flux surface labeled ψ

$$\xi = \int_{R_{\min}}^{\hat{R}'} \frac{(d\psi/d\hat{R}')d\hat{R}'}{\sqrt{\int_R^{\hat{R}'} \mu_0(\hat{R}''^2 - R^2) \frac{dp}{d\hat{R}''} d\hat{R}''}}, \quad (\text{C.2})$$

where $\hat{R}(\psi)$ is the value of R on the line $Z = 0$ and p is the plasma pressure. Using ξ , they formulate the ‘‘core’’ solution, i.e., the solution on the inboard side of where the surface are nearly vertical

$$Z(\hat{R}, R) = l(R) - \frac{\xi(\hat{R}, R)}{\cos(\theta_s)}, \quad \theta_s = \arctan\left(\frac{dl}{dZ}\right), \quad (\text{C.3})$$

and the ‘‘boundary layer’’ solution, i.e., the solution in the region of closely-spaced surfaces on the outboard side

$$R_{\text{boundary}}(Z) = R(\hat{R}, Z) + \frac{\xi(\hat{R}, R_{\text{boundary}})}{\sin(\theta_s)}, \quad (\text{C.4})$$

where $l = l(R)$ in (C.3) is the value of Z on a point on the boundary. To construct a $\beta \sim 1$ equilibrium, one needs an analytical pressure, boundary shape profiles, and the value of the poloidal field at $Z = 0$. Hsu *et al.* used the following profiles:

$$\begin{aligned} p(\hat{R}(\psi)) &= p_1 \left(1 - \frac{p_2(R_{\max} - \hat{R})^2 + p_3(R_{\max} - \hat{R})^3 + p_4(R_{\max} - \hat{R})^4}{p_2(R_{\max} - R_{\min})^2 + p_3(R_{\max} - R_{\min})^3 + p_4(R_{\max} - R_{\min})^4} \right), \\ l_{\delta < 0}(\hat{R}) &= (\hat{R} - R_{\min})^{0.5} (R_{\max} - \hat{R})^{0.5} \left(\frac{a_l}{[R_{\max} - R + b_l(R_{\max} - R_{\min})]^{c_l}} \right)^{0.5}, \\ \frac{1}{\hat{R}} \frac{d\psi}{d\hat{R}} &= \frac{l(\hat{R})}{\hat{R}} [a_\psi + b_\psi(\hat{R} - R_{\min}) + c_\psi(\hat{R} - R_{\min})^2], \end{aligned} \quad (\text{C.5})$$

where $l_{\delta < 0}$ is a function used to generate boundary shapes corresponding to negative triangularity equilibria. After fixing the various input profiles, one solves (C.2) to obtain the perpendicular distance ξ as a function of \hat{R} and R . Substituting ξ in (C.3) and (C.4), one gets the core and

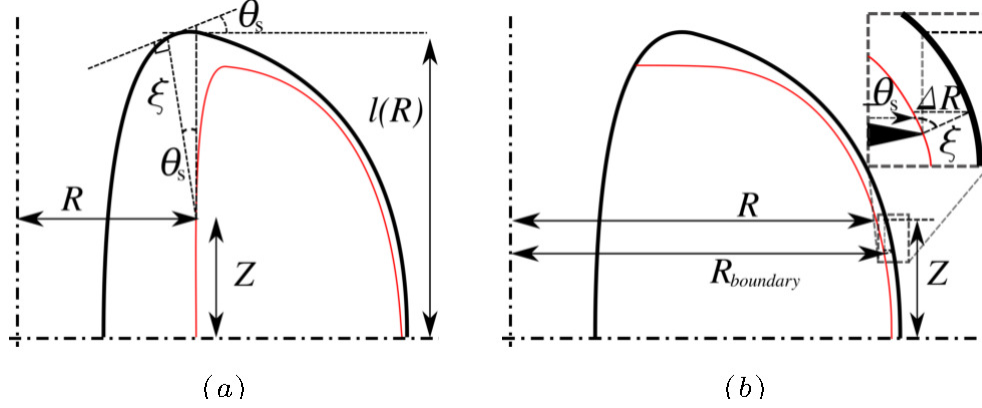


Figure C.1: This figure illustrates the process of creating the two regions of the $\beta \sim 1$ solution in Hsu *et al.* The bold black line is the LCFS and the red line is the flux surface contour — (a) shows the core solution (C.3) which is only a good approximation on the inboard side of the device and (b) shows the boundary layer solution (C.4) which is only valid in the boundary layer region. The inset in the right figure highlights the approximation $\xi(\hat{R}, R) = \xi(\hat{R}, R_{\text{boundary}})$ which is necessary to construction the boundary layer solution (C.4).

boundary layer segments, respectively. Taking union of the two segments yields the flux surface contour $\psi(R, \hat{R})$. Figure C.1 illustrates this process.

C.2 Limitations of the Hsu *et al.* equilibria

We find that the equilibria of Hsu *et al.* has two major limitations that can significantly affect the accuracy of our analyses. First, as we move closer to the magnetic axis, the accuracy of both the core and boundary layer solution degrades as the ordering $\epsilon \sim 1$ fails and $dp/d\psi$ approaches zero. We demonstrate this by plotting figure C.2 which is figure 6 in Hsu *et al.* To generate the analytical solution in figure C.2, we start with (C.5) using the following values of coefficients

$$\begin{aligned}
 (p_1, p_2, p_3, p_4) &= (0.5, 1.5, 0, 0), \\
 (a_l, b_l, c_l) &= (0.8, 0.05, 0.85), \\
 (a_\psi, b_\psi, c_\psi) &= (0.152, 0.022, 0).
 \end{aligned} \tag{C.6}$$

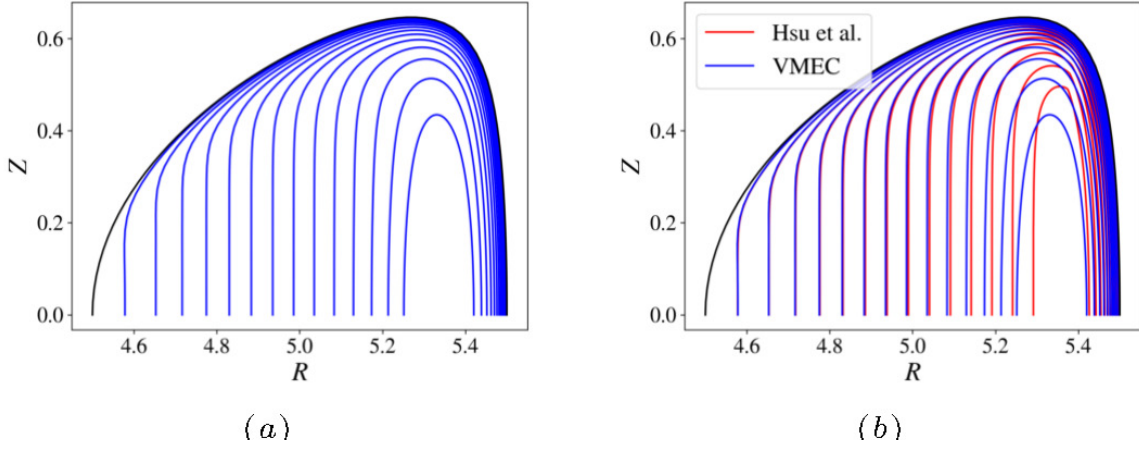


Figure C.2: This figure shows (a) the numerical equilibrium solution and (b) a comparison between the analytical equilibrium from figure 6 in the paper by Hsu *et al.* [3] and the same equilibrium generated using VMEC. The significant deviation of the analytical solution is evident, as well as how it develops a kink near the outboard side as we approach the magnetic axis.

Second, the inaccuracy and non-smoothness of flux surfaces leads to discontinuous and incorrect trends in the geometric quantities needed for a local stability analysis. To demonstrate this, we plot a physical quantity that arises in both the ballooning and gyrokinetic equation that can be seen in (2.37) and (3.23), respectively— as a curvature drive in the former and as a component of the curvature drift in the latter. We chose to plot the scalar

$$\hat{\kappa} = \frac{1}{B^3} (\mathbf{b} \times \boldsymbol{\kappa}) \cdot \nabla \alpha, \quad \boldsymbol{\kappa} = (\mathbf{b} \cdot \nabla) \mathbf{b}, \quad (\text{C.7})$$

where $\boldsymbol{\kappa}$ is the field-line curvature. To better understand the discontinuity problem, we plot $\hat{\kappa}$ as a function of θ_{geo} in figure C.3. To emphasize the importance of smoothness, we also plot the tangents on the flux surface on either side of the point at which $\hat{\kappa}$ is discontinuous.

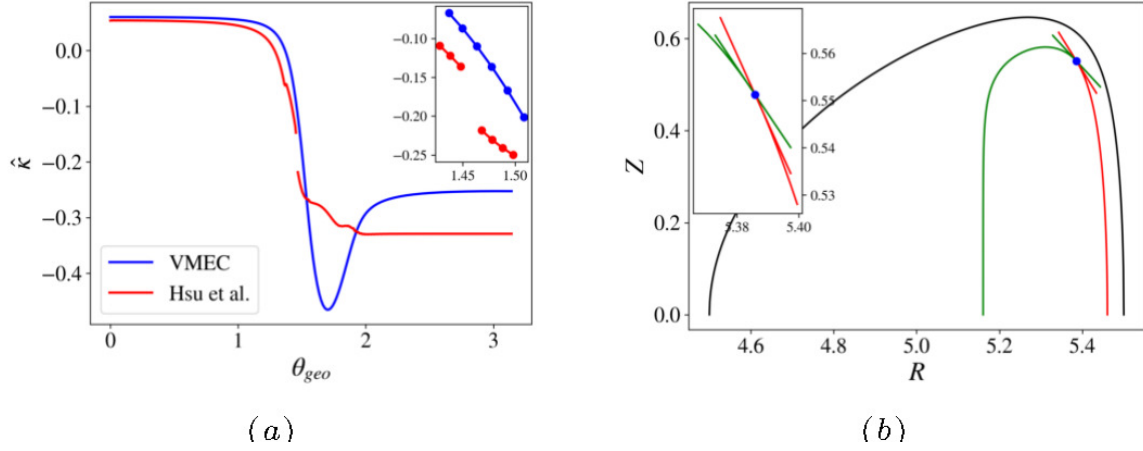


Figure C.3: In this figure (a) compares $\hat{\kappa}$ vs. θ_{geo} obtained using the analytical equilibrium (in figure 6) in Hsu *et al.* with the corresponding VMEC equilibrium for a common flux surface (shown in (b)). The inset plot in (a) shows a zoomed-in version of the same plot near the discontinuity at $\theta_{\text{geo}} = 1.46$. Figure (b) shows the difference in slopes of the tangents at the point of discontinuity, with a zoomed-in version in the inset. Notice also the deviation of $\hat{\kappa}$ in (a) for $\theta_{\text{geo}} > 1.5$. There are other issues like the small sharp feature near $\theta_{\text{geo}} = 1.3$ that we will not delve into.

The kink in ψ seen in figure 4(b) manifests itself as a discontinuity in quantities such as \mathbf{b} , $\nabla\psi$ and $\nabla\alpha$. This causes the geometric factors and hence the physical quantities needed for a local stability analysis to become discontinuous. Furthermore, in the regions where the gradients are continuous, for reasons mentioned at the beginning of this section, the distances between the surfaces deviate from the exact equilibrium, especially as $\theta_{\text{geo}} > 1.5$. To alleviate these problems, we use the numerical solver VMEC to create the equilibria used in this study.

Appendix D: Newcomb's criterion

Newcomb[94], in his analysis of a diffuse screw pinch, described a method to infer the stability of a system to incompressible ideal-MHD modes. He reduced the ideal-MHD energy principle to

$$W = \frac{\pi}{2} \int_{r_1}^{r_2} dr \left[f \left(\frac{d\xi}{dr} \right)^2 + g\xi^2 \right], \quad (\text{D.1})$$

where r is the distance from the center, $\xi(r)$ is the radial perturbation, and $f(r), g(r)$ are functions dependent on the equilibrium. One can write the kinetic energy associated with the perturbation as

$$T = \frac{\pi \omega^2}{2} \int_{r_1}^{r_2} dr \xi^2. \quad (\text{D.2})$$

Combining the potential and the kinetic energy, we can write the Lagrangian $L = T - U$ and get the Euler-Lagrange equation corresponding to $\delta L = 0$

$$(f\xi')' - g\xi = \omega^2\xi. \quad (\text{D.3})$$

This equation a self-adjoint, second-order, eigenvalue ordinary differential equation(ODE). In his paper, Newcomb explored the marginally stable ODE,

$$(f\xi')' - g\xi = 0. \quad (\text{D.4})$$

For the marginally stable equation of this form, Newcomb's theorem and the associated corollary is given below:

Theorem 1 *If r_1 and r_2 are nonsingular points of the same independent sub-interval, and if the nontrivial Euler-Lagrange solutions that vanish at r_1 also vanish at some point r_0 between r_1 and r_2 , then for any Euler-Lagrange solution $\xi_0(r)$ there exist functions $\xi(r)$ with the same boundary values and with $W(r_1, r_2; \xi) < W(r_1, r_2; \xi_0)$*

Corollary 1.1 *There exists a $\xi(r)$ that makes $W(r_1, r_2; \xi)$ negative and satisfies the boundary conditions $\xi(r_1) = \xi(r_2) = 0$*

This means that upon integrating equation (D.4) with a test function ξ , such that $\xi(r_1) = 0$, if ξ crosses the zero line at any other point, then there must exist an eigenfunction $\tilde{\xi}$ satisfying equation (D.3) such that $W < 0$, implying that $\omega^2 < 0$. In other words, the system will have a growing eigenvalue and will become unstable.

Even though Newcomb derived this theorem for an ODE that is integrated in the radial direction, the principle can be extended to any second-order, self-adjoint, eigenvalue ODE. Hence, we can use it here for the ideal-ballooning equation (3.62).

Appendix E: Extended eigenfunctions of the EM-ETG mode

In this appendix, we present two sets of eigenfunctions from the electromagnetic, negative-triangularity, inner-core, high- β growth rate spectrum shown in figure 3.17(c).

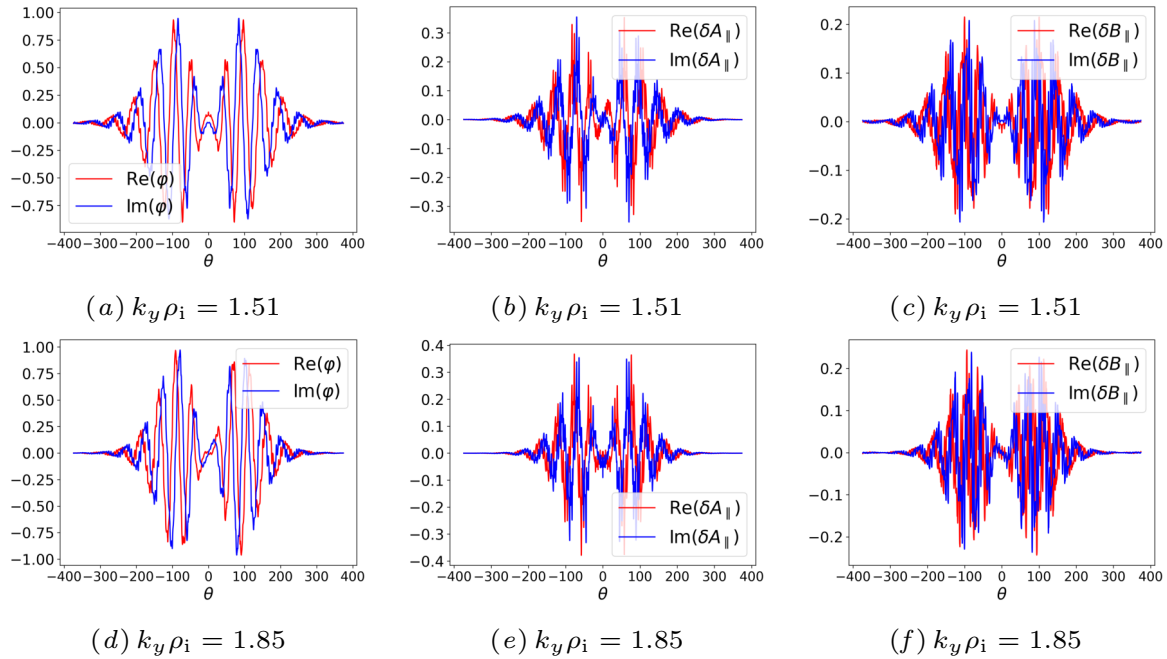


Figure E.1: This figure shows the eigenfunctions at two different $k_y \rho_i$ values from figure 3.17(c). The values in each row have been normalized with $\max(\varphi)$. Notice the opposite parities of the eigenfunctions in the two rows and the extended and highly-oscillatory structure along θ . The eigenfunctions in the upper row correspond to a non-tearing-parity EM-ETG mode whereas the lower row corresponds to a tearing-parity EM-ETG mode. Classifying modes becomes harder for up-down asymmetric equilibria and virtually impossible for non-linear analyses.

These extended eigenfunctions make it computationally expensive to calculate the accurate growth rate of an EM-ETG instability. This would directly affect the speed of an optimization where EM-ETGs or MTMs are the dominant modes.

Appendix F: GX: A robust gyrokinetic solver

F.1 Overview

For most of this work, we have used the linear gyrokinetic solver GS2 as it is the fastest linear, electromagnetic gyrokinetic solver for a general toroidal geometry. This is due to a novel implicit time-stepping algorithm [57]. This overcomes the Courant-Frederich-Levy (CFL) constraint imposed by waves and by the fast-moving electrons with explicit time stepping which makes GS2 faster than other codes by a factor of $(m_i/m_e)^{1/2}$. We can also solve the non-linear electrostatic gyrokinetic equation with GS2 for tokamak geometry. But due to the design of GS2, solving a fully electromagnetic nonlinear gyrokinetic equation has not been generally successful for tokamaks or stellarator equilibria.

The reason lies in the discretization of the velocity space of the GS2 code which uses an (E, λ) grid which makes calculating the trapped electron distribution complex. With other codes like `stella` [110] or GX, that use (w_{\parallel}, μ) discretization, the treatment of trapped particles becomes relatively easier (though less accurate at fixed resolution). Moreover, even if these problems are resolved in GS2 in the future, the ability to finely tune the velocity-scale resolution could be advantageous in terms of computational efficiency as nonlinearly solving the gyrokinetic model is computationally expensive.

To this end, Mandell and Dorland [96, 97] created the GX code. It solves the moments of

the gyrokinetic model by decomposing the gyrokinetic distribution function h_s in the Hermite-Laguerre space. In this appendix, we will derive the fully electromagnetic, linear gyrokinetic equations in the Hermite-Laguerre space and present some linear tests with fully electromagnetic effects.

F.2 Deriving the GX model equations

Before obtaining the transformed gyrokinetic equations in Fourier-Hermite-Laguerre space, we write down a set of fundamental identities related to the Hermite and Laguerre polynomials. These identities have been obtained from Mandell *et al.* [96, 97] and Abramowitz and Stegun [111].

F.2.1 Fundamental identities

$$\psi_\ell(\mu B) = (-1)^\ell L_\ell(\mu B) \tag{F.1}$$

$$\psi^\ell(\mu B) = e^{-\mu B} \psi_\ell$$

$$\begin{aligned} \phi_m(w_\parallel) &= \frac{\text{He}_m(w_\parallel)}{\sqrt{m!}} \\ \phi^m(w_\parallel) &= \frac{e^{-w_\parallel^2/2}}{\sqrt{(2\pi)^3}} \phi_m(w_\parallel) \end{aligned} \tag{F.2}$$

$$\phi_0 = 1, \phi_1 = w_\parallel, \phi_2 = \frac{w_\parallel^2 - 1}{\sqrt{2}} \tag{F.3}$$

$$\psi_0 = 1, \psi_1 = 1 - \mu B,$$

$$\int_0^\infty d(\mu B) \psi^\ell(\mu B) \psi_{\ell'}(\mu B) = \delta_{\ell\ell'} \tag{F.4}$$

$$2\pi \int_{-\infty}^{\infty} dw_{\parallel} \phi^m(w_{\parallel}) \phi_{m'}(w_{\parallel}) = \delta_{mm'} \quad (\text{F.5})$$

$$h = \sum_{\ell, m} \psi^{\ell} \phi^m H_{\ell, m} \quad (\text{F.6})$$

$$\mathcal{L}_{\ell} \mathcal{H}_m h = 2\pi \int_{-\infty}^{\infty} dw_{\parallel} \phi_m \int_0^{\infty} d(\mu B) \psi_{\ell} h = H_{\ell, m} \quad (\text{F.7})$$

$$\mu B \psi^{\ell}(\mu B) = (\ell + 1) \psi^{\ell+1}(\mu B) + (2\ell + 1) \psi^{\ell}(\mu B) + \ell \psi^{\ell-1}(\mu B) \quad (\text{F.8})$$

$$\frac{\partial \psi^{\ell}(\mu B)}{\partial \mu B} = -\frac{\ell + 1}{\mu B} [\psi^{\ell+1} + \psi^{\ell}] \quad (\text{F.9})$$

$$\frac{\partial \psi_{\ell}(\mu B)}{\partial \mu B} = \frac{\ell}{\mu B} [\psi_{\ell} + \psi_{\ell-1}] \quad (\text{F.10})$$

$$w_{\parallel} \phi^m(w_{\parallel}) = \sqrt{m+1} \phi^{m+1}(w_{\parallel}) + \sqrt{m} \phi^{m-1}(w_{\parallel}) \quad (\text{F.11})$$

$$\frac{\partial \phi^m(w_{\parallel})}{\partial w_{\parallel}} = -\sqrt{m+1} \phi^{m+1}(w_{\parallel}) \quad (\text{F.12})$$

$$\mathcal{J}_{\ell}(b) = \frac{1}{\ell!} \left(-\frac{b_s}{2} \right)^{\ell} e^{-b_s/2} \quad (\text{F.13})$$

$$J_0(\sqrt{2\mu B b}) = \sum_l \psi_{\ell} \mathcal{J}_{\ell}(b) \quad (\text{F.14})$$

$$\int_0^{2\pi} d\vartheta \exp\left(\mp \frac{ik_{\perp} w_{\perp} \cos(\vartheta)}{\Omega_s}\right) = J_{0s}\left(\frac{k_{\perp} w_{\perp}}{\Omega_s}\right) \quad (\text{F.15})$$

$$\int_0^{2\pi} d\vartheta \cos(\vartheta) \exp\left(-\frac{ik_{\perp} w_{\perp} \cos(\vartheta)}{\Omega_s}\right) = -iJ_1\left(\frac{k_{\perp} w_{\perp}}{\Omega_s}\right) \quad (\text{F.16})$$

$$\int_0^{2\pi} d\vartheta \cos^2(\vartheta) \exp\left(-\frac{ik_{\perp} w_{\perp} \cos(\vartheta)}{\Omega_s}\right) = \frac{1}{2} \left[J_0\left(\frac{k_{\perp} w_{\perp}}{\Omega_s}\right) + J_2\left(\frac{k_{\perp} w_{\perp}}{\Omega_s}\right) \right] = \frac{\Omega_s}{k_{\perp} w_{\perp}} J_1 \quad (\text{F.17})$$

$$\int_0^{2\pi} d\vartheta \sin(2\vartheta) \exp\left(-\frac{ik_{\perp} w_{\perp} \cos(\vartheta)}{\Omega_s}\right) = 0 \quad (\text{F.18})$$

F.2.2 Intermediate derived identities

In this section, we use the identities of the previous section to obtain more complex identities that are directly applicable to the terms of the gyrokinetic model in F.3.3.

Using (F.3),

$$\frac{w_{\parallel}^2 + w_{\perp}^2}{2} - \frac{3}{2} = \frac{1}{\sqrt{2}}\phi_2(w_{\parallel}) + (\mu B - 1) \quad (\text{F.19})$$

Using (F.3) and (F.11)

$$w_{\parallel} \left(\frac{w_{\parallel}^2 + w_{\perp}^2}{2} - \frac{3}{2} \right) = \sqrt{\frac{3}{2}}\phi_3(w_{\parallel}) + \phi_1(w_{\parallel}) + w_{\parallel}(\mu B - 1) = \sqrt{\frac{3}{2}}\phi_3(w_{\parallel}) + \mu B\phi_1(w_{\parallel}) \quad (\text{F.20})$$

Using (F.6) and (F.8)

$$\begin{aligned} \left. \frac{\partial h}{\partial \mathbf{R}_s} \right|_{\mathbf{R}_s, w_{\parallel}, \mu, t} &= \sum_{\ell', m'} \frac{\partial \psi^{\ell'}(\mu B)}{\partial(\mu B)} \phi^{m'} \mu B \nabla(\log(B)) H_{\ell', m'} + \sum_{\ell', m'} \psi^{\ell'} \phi^{m'} \frac{\partial H_{\ell', m'}}{\partial \mathbf{R}_s} \\ &= -\nabla(\log(B)) \sum_{\ell', m'} (\ell' + 1)(\psi^{\ell'+1} + \psi^{\ell'}) \phi^{m'} H_{\ell', m'} + \sum_{\ell', m'} \psi^{\ell'} \phi^{m'} \frac{\partial H_{\ell', m'}}{\partial \mathbf{R}_s} \end{aligned} \quad (\text{F.21})$$

Using (F.14) and (F.10)

$$\frac{w_{\perp}}{k_{\perp}} J_1(\sqrt{2\mu B b}) = -\frac{w_{\perp}^2}{k_{\perp}^2} \frac{dJ_0}{d\mu B} = \sum_{\ell'=0} (\psi_{\ell'} + \psi_{\ell'-1}) \mathcal{J}_{\ell'-1}(b) \quad (\text{F.22})$$

Using (F.14), (F.10), and (F.8)

$$\frac{w_{\perp}^3}{2k_{\perp}} J_1(\sqrt{2\mu B b}) = \sum_{\ell'=0} ((\ell' + 1)\psi_{\ell'+1} + (3\ell' + 1)\psi_{\ell'} + (3\ell' - 1)\psi_{\ell'-1} + (\ell' - 1)\psi_{\ell'-2}) \mathcal{J}_{\ell'-1} \quad (\text{F.23})$$

Using (F.6), (F.8) and (F.12)

$$\begin{aligned}
-\mu \nabla_{\parallel} B \frac{\partial h}{\partial w_{\parallel}} &= \sqrt{m'+1} \frac{\nabla_{\parallel} B}{B} \sum_{\ell', m'} \mu B \psi^{\ell'} \phi^{m'+1} H_{\ell', m'} \\
&= \sqrt{m'+1} \frac{\nabla_{\parallel} B}{B} \sum_{\ell', m'} \left[(\ell'+1) \psi^{\ell'+1} + (2\ell'+1) \psi^{\ell'} + \ell' \psi^{\ell'-1} \right] \phi^{m'+1} H_{\ell', m'}
\end{aligned} \tag{F.24}$$

Using (F.3), (F.4), (F.5), (F.14) and (F.22)

$$\begin{aligned}
\mathcal{L}_{\ell} \mathcal{H}_m \left[J_{0s} (\varphi_k - v_{ts} w_{\parallel} A_{\parallel, k}) + \frac{\tau_s}{Z_s} \frac{2\mu B}{\alpha_s} J_{1s} \delta B_{\parallel} \right] \frac{e^{-(w_{\parallel}^2/2 + \mu B)}}{(2\pi)^{3/2}} \\
= \mathcal{J}_{\ell}^s (\varphi_k \delta_{m0} - v_{ts} \delta_{m1} A_{\parallel, k}) + \frac{\tau_s}{Z_s} (\mathcal{J}_{\ell-1}^s + \mathcal{J}_{\ell}^s) \delta_{m0} \frac{\delta B_{\parallel}}{B}
\end{aligned} \tag{F.25}$$

where all the quantities are normalized, $\alpha_s = \sqrt{(2\mu B) b_s}$ and $b_s = (k_{\perp} v_{th, s} / \Omega_s)^2$

F.2.3 Individual terms in the gyrokinetic model

In this section, we apply a Hermite-Laguerre transform to the gyrokinetic model and transform the model term by term. To do this, we use the identities and derived relationships from the previous sections.

The Hermite-Laguerre (HL) transform commutes with a time derivative. Therefore, applying (F.7) to a time derivative, we can write

$$\mathcal{L}_{\ell} \mathcal{H}_m \frac{\partial g_{s, k}}{\partial t} = \frac{\partial \mathcal{L}_{\ell} \mathcal{H}_m g_{s, k}}{\partial t} = \frac{\partial G_{\ell, m}}{\partial t}. \tag{F.26}$$

The HL transform also commutes with a spatial derivative. Using (F.3), (F.4), (F.5), (F.11) and

the component of (F.21) along the magnetic field

$$\begin{aligned} \mathcal{L}_\ell \mathcal{H}_m v_{ts} w_{\parallel} \mathbf{b} \cdot \nabla h_{s,k} &= -v_{ts} \nabla_{\parallel} (\log(B)) \left(\ell \sqrt{m} H_{\ell-1,m-1} + \ell \sqrt{m+1} H_{\ell-1,m+1} + \right. \\ &\quad \left. (\ell+1) \sqrt{m} H_{\ell,m-1} + (\ell+1) \sqrt{m+1} H_{\ell,m+1} \right) + \\ &\quad v_{ts} \nabla_{\parallel} (\sqrt{m} H_{\ell,m-1} + \sqrt{m+1} H_{\ell,m+1}) \end{aligned} \quad (\text{F.27})$$

Taking the HL transform of the drift frequency term and using (F.4), (F.2), (F.11) and (F.8)

$$\begin{aligned} \mathcal{L}_\ell \mathcal{H}_m i \tilde{k}_y (\mu B \omega_d^{\nabla B} + v_{\parallel}^2 \omega_d^{\kappa}) h_{s,k} &= i \tilde{k}_y \omega_d^{\nabla B} [\ell H_{\ell-1,m} + (2\ell+1) H_{\ell,m} + (\ell+1) H_{\ell+1,m}] \\ &\quad + i \tilde{k}_y \omega_d^{\kappa} \left[\sqrt{(m+1)(m+2)} H_{\ell,m+2} + (2m+1) H_{\ell,m} + \sqrt{m(m-1)} H_{\ell,m-2} \right] \end{aligned} \quad (\text{F.28})$$

Taking the HL transform of (F.23) and using (F.4), (F.5) and (F.24)

$$\begin{aligned} -\mathcal{L}_\ell \mathcal{H}_m v_{ts} \mu \nabla_{\parallel} B \frac{\partial h}{\partial w_{\parallel}} &= v_{ts} \nabla_{\parallel} (\log(B)) \sqrt{m} [\ell H_{\ell-1,m-1} + (2\ell+1) H_{\ell,m-1} \\ &\quad + (\ell+1) H_{\ell+1,m-1}] \end{aligned} \quad (\text{F.29})$$

The relations (F.26)-(F.29) completely define all the terms on the left side of the gyrokinetic equation. Next, we simplify the driving terms on the right side of the gyrokinetic equation. We start with the HL transform of the following term and use (F.4), (F.5), (F.8), (F.14) and (F.19)

$$\begin{aligned} \mathcal{L}_\ell \mathcal{H}_m \left[\frac{a_N}{L_{\text{ns}}} + \frac{a_N}{L_{\text{Ts}}} \left(\frac{w_{\parallel}^2 + w_{\perp}^2}{2} - \frac{3}{2} \right) \right] J_{0s} \frac{e^{-(w_{\parallel}^2/2 + \mu B)}}{(2\pi)^{3/2}} \\ = \left\{ \frac{a_N}{L_{\text{ns}}} \mathcal{J}_\ell^s \delta_{m0} + \frac{a_N}{L_{\text{Ts}}} \left[\frac{1}{\sqrt{2}} \mathcal{J}_\ell^s \delta_{m2} + (\ell \mathcal{J}_{\ell-1}^s + 2\ell \mathcal{J}_\ell^s + (\ell+1) \mathcal{J}_{\ell+1}^s) \delta_{m0} \right] \right\} \end{aligned} \quad (\text{F.30})$$

Next, we obtain the HL transform for the term that lies in front of the $A_{\parallel,k}$ in the GK equation

using (F.4), (F.5), (F.8), (F.14) and (F.20)

$$\begin{aligned} & \mathcal{L}_\ell \mathcal{H}_m \left\{ w_\parallel \left[\frac{a_N}{L_{\text{ns}}} + \frac{a_N}{L_{\text{Ts}}} \left(\frac{w_\parallel^2 + w_\perp^2}{2} - \frac{3}{2} \right) \right] \right\} J_{0s} \frac{e^{-(w_\parallel^2/2 + \mu B)}}{(2\pi)^{3/2}} \\ &= \left\{ \frac{a_N}{L_{\text{ns}}} \mathcal{J}_\ell^s \delta_{m1} + \frac{a_N}{L_{\text{Ts}}} \left[\sqrt{\frac{3}{2}} \mathcal{J}_\ell^s \delta_{m3} + (\ell \mathcal{J}_{\ell-1}^s + (2\ell + 1) \mathcal{J}_\ell^s + (\ell + 1) \mathcal{J}_{\ell+1}^s) \delta_{m1} \right] \right\} \end{aligned} \quad (\text{F.31})$$

Finally, we calculate the term in front of the compressive magnetic fluctuation δB_\parallel

$$\begin{aligned} & \mathcal{L}_\ell \mathcal{H}_m \left[\frac{a_N}{L_{\text{ns}}} + \frac{a_N}{L_{\text{Ts}}} \left(\frac{w_\parallel^2 + w_\perp^2}{2} - \frac{3}{2} \right) \right] \frac{2\mu B}{\alpha_s} J_{1s} \frac{\delta B_{\parallel,k}}{B} \frac{e^{-(w_\parallel^2/2 + \mu B)}}{(2\pi)^{3/2}} \\ &= \frac{a_N}{L_{\text{ns}}} (\mathcal{J}_\ell^s + \mathcal{J}_{\ell-1}^s) \delta_{m0} + \frac{a_N}{L_{\text{Ts}}} \left[\frac{1}{\sqrt{2}} (\mathcal{J}_\ell^s + \mathcal{J}_{\ell-1}^s) \delta_{m2} \right. \\ & \quad \left. + (\ell \mathcal{J}_{\ell-2}^s + 3\ell \mathcal{J}_{\ell-1}^s + (3\ell + 1) \mathcal{J}_\ell^s + (\ell + 1) \mathcal{J}_{\ell+1}^s) \delta_{m0} \right] \end{aligned} \quad (\text{F.32})$$

Now we have transformed each term of the gyrokinetic equation. These results will be directly used in §F.3.3.

F.3 Linear, collisionless gyrokinetic model in Fourier-Hermite-Laguerre space

In this section, we will obtain the gyrokinetic equations to a Fourier-Hermite-Laguerre space. In §F.3.1, we will rewrite the gyrokinetic model in Fourier space by imposing periodicity of the distribution and fields perpendicular to the field line. In the following section, we define and normalize the gyrokinetic model. Finally, in §F.3.3 we will use the identities obtained in §F.2.1 to finally transform all equations into their Hermite-Laguerre versions.

F.3.1 Gyrokinetic equation

We start with the gyrokinetic model described in chapter 3 in equations (3.18)-(3.21) and redefine the gyrokinetic distribution function

$$g_s = h_s - \frac{q_s F_{0s}}{T_s} \left\langle \varphi - \frac{\mathbf{w} \cdot \delta \mathbf{A}}{c} \right\rangle_{\mathbf{R}_s}, \quad (\text{F.33})$$

simplify and rewrite (3.18)

$$\frac{\partial g_s}{\partial t} + (w_{\parallel} \mathbf{b} + \mathbf{v}_{Ds}) \cdot \frac{\partial h_s}{\partial \mathbf{R}_s} = -\langle \mathbf{V}_E \rangle_{\mathbf{R}_s} \cdot \nabla F_{0s}. \quad (\text{F.34})$$

Next, we transform the gyrokinetic equation from (E, μ) space to (w_{\parallel}, μ) space using the relation

$$\frac{\partial h}{\partial \mathbf{R}_s} \Big|_{E, \mu, t} = \frac{\partial h}{\partial \mathbf{R}_s} \Big|_{w_{\parallel}, \mu, t} - \frac{\mu}{m w_{\parallel}} \frac{\partial h}{\partial w_{\parallel}} \Big|_{\mathbf{R}_s, \mu, t} \frac{\partial B}{\partial \mathbf{R}_s} \Big|_{E, \mu, t} \quad (\text{F.35})$$

and rewrite the convective derivative in the guiding-centre coordinate $(\mathbf{R}_s, w_{\parallel}, \mu, t)$

$$\frac{\partial g_s}{\partial t} + (w_{\parallel} \mathbf{b} + \mathbf{v}_{Ds}) \cdot \frac{\partial h_s}{\partial \mathbf{R}_s} - (\mathbf{b} \cdot \nabla B) \frac{\mu}{m} \frac{\partial h_s}{\partial w_{\parallel}} = -\langle \mathbf{V}_E \rangle_{\mathbf{R}_s} \cdot \nabla F_{0s}. \quad (\text{F.36})$$

We have now obtained the gyrokinetic equation in the new guiding-centre coordinates $(\mathbf{R}_s, w_{\parallel}, \mu, t)$.

Note that the field equations (3.19)-(3.21) remain unchanged. Next, we use the following ansatz

$$\begin{aligned}
h_s &= \sum_k h_{k_{\perp},s}(\theta, w_{\parallel}, \mu, t) \exp(i\mathbf{k}_{\perp} \cdot \mathbf{R}_s), \\
\varphi &= \sum_k \varphi_{k_{\perp}}(\theta, t) \exp(i\mathbf{k}_{\perp} \cdot \mathbf{r}), \\
\delta A_{\parallel} &= \sum_k \delta A_{\parallel,k_{\perp}}(\theta, t) \exp(i\mathbf{k}_{\perp} \cdot \mathbf{r}), \\
\delta B_{\parallel} &= \sum_k \delta B_{\parallel,k_{\perp}}(\theta, t) \exp(i\mathbf{k}_{\perp} \cdot \mathbf{r}),
\end{aligned} \tag{F.37}$$

and (F.15)-(F.18), to obtain the Fourier-transformed version of (F.36)

$$\begin{aligned}
&\frac{\partial g_{k_{\perp},s}}{\partial t} + w_{\parallel} \mathbf{b} \cdot \nabla h_{k_{\perp},s} + i\mathbf{k}_{\perp} \cdot \mathbf{v}_{Ds} h_{k_{\perp},s} - (\mathbf{b} \cdot \nabla B) \frac{\mu}{m} \frac{\partial h_{k_{\perp},s}}{\partial w_{\parallel}} = \\
&-i\omega_{*,s} \left[1 + \eta_s \left(\frac{E_s}{T_s} - \frac{3}{2} \right) \right] \left[J_0 \left(\frac{k_{\perp} w_{\perp}}{\Omega_s} \right) \left(\varphi_{k_{\perp}} - \frac{w_{\parallel} \delta A_{\parallel}}{c} \right) + J_1 \left(\frac{k_{\perp} w_{\perp}}{\Omega_s} \right) \frac{w_{\perp}}{k_{\perp}} \frac{\delta B_{\parallel}}{c} \right] F_{0s},
\end{aligned} \tag{F.38}$$

where

$$g_{k_{\perp},s} = h_{k_{\perp},s} - \frac{q_s F_{0s}}{T_s} \left[J_0 \left(\frac{k_{\perp} w_{\perp}}{\Omega_s} \right) \left(\varphi_{k_{\perp}} - \frac{w_{\parallel} \delta A_{\parallel}}{c} \right) + J_1 \left(\frac{k_{\perp} w_{\perp}}{\Omega_s} \right) \frac{w_{\perp}}{k_{\perp}} \frac{\delta B_{\parallel}}{c} \right] \tag{F.39}$$

and

$$\omega_{*,s} = \frac{c}{B} [(\mathbf{b} \times \mathbf{k}_{\perp}) \cdot \nabla \log n_s] = \frac{c}{L_{n,s} B_N} \tag{F.40}$$

is the diamagnetic frequency. Similarly, applying the Fourier ansatz to the the field equations gives

$$\sum_s \frac{q_s^2 N_s \varphi_{k_\perp}}{T_s} = \sum_s q_s \int d^3 \mathbf{v} J_{0s} h_{s,k_\perp}, \quad (\text{F.41})$$

$$k_\perp^2 \delta A_{\parallel,k_\perp} = \sum_s \frac{4\pi q_s}{c} \int d^3 \mathbf{v} w_\parallel J_{0s} h_{s,k_\perp}, \quad (\text{F.42})$$

$$\frac{B}{4\pi} \delta B_{\parallel,k_\perp} = - \sum_s \int d^3 \mathbf{v} w_\perp^2 \frac{M_s J_{1s} \Omega_s}{k_\perp w_\perp} h_{s,k_\perp}. \quad (\text{F.43})$$

This gives us the field equations. In the next section, we will take all the equations of the Fourier transformed gyrokinetic model and normalize them.

F.3.2 Normalized gyrokinetic model

Using these normalizing length a_N , magnetic field B_N and defining the thermal velocity¹ $v_{ts} = \sqrt{T_s/m_s}$ and replacing the subscript k_\perp with k for simplicity, the normalized gyrokinetic model becomes

$$\begin{aligned} \frac{\partial g_{s,k}}{\partial t} + v_{ts} w_\parallel \mathbf{b} \cdot \nabla h_{s,k} + \frac{\tau_s}{Z_s} i \omega_{Ds} h_{s,k} - v_{ts} (\mathbf{b} \cdot \nabla B) \mu \frac{\partial h_{s,k}}{\partial w_\parallel} = \\ i \omega_{*,s} \left[\frac{a_N}{L_{ns}} + \frac{a_N}{L_{Ts}} \left(\frac{w_\parallel^2 + w_\perp^2}{2} - \frac{3}{2} \right) \right] \left[J_{0s} (\varphi_k - v_{ts} w_\parallel \delta A_\parallel) + \frac{2\mu B}{\alpha_s} J_{1s} \delta B_\parallel \right] \end{aligned} \quad (\text{F.44})$$

$$\sum_s \frac{Z_s^2 n_s \varphi_k}{\tau_s} = \sum_s Z_s n_s \int d^3 \mathbf{v} J_{0s} h_s \quad (\text{F.45})$$

$$\tilde{k}_\perp^2 \delta A_{\parallel,k} = \frac{\beta_{\text{ref}}}{2} \sum_s Z_s n_s v_{ts} \int d^3 \mathbf{v} w_\parallel J_{0s} h_{s,k} \quad (\text{F.46})$$

¹The definition of $v_{ts} = \sqrt{T_s/m_s}$ in GX whereas $v_{\text{th},i} = \sqrt{2T_s/m_s}$ in GS2. One must be aware of this factor when comparing the results across different codes.

$$\delta B_{\parallel,k} = -\frac{\beta_{\text{ref}}}{2} \frac{1}{B} \sum_s n_s \tau_s \int d^3 \mathbf{v} \frac{w_{\perp}^2}{k_{\perp} w_{\perp}} J_{1s} h_{s,k}. \quad (\text{F.47})$$

In (F.44)

$$g_{s,k} = h_{s,k} - \frac{Z_s J_{0s}}{\tau_s} (\varphi - v_{ts} w_{\parallel} \delta A_{\parallel}) + 2\mu B \frac{J_{1s}}{\alpha_s} \delta B_{\parallel}, \quad (\text{F.48})$$

$$i\omega_{D_s} = \mu B \omega_{\text{d}}^{\nabla B} + w_{\parallel}^2 \omega_{\text{d}}^{\kappa} \quad (\text{F.49})$$

where $\omega_{*,s} = \tilde{k}_y$, $\alpha_s = \sqrt{(2\mu B)b_s}$ is the argument of the Bessel functions, $b_s = (k_{\perp} v_{\text{th},s}/\Omega_s)^2$, $\omega_{\text{d}}^{\nabla B} = i\tilde{k}_y(\mathbf{b} \times \nabla B) \cdot \nabla y$ and $\omega_{\text{d}}^{\kappa} = i\tilde{k}_y(\mathbf{b} \times (\mathbf{b} \cdot \nabla \mathbf{b})) \cdot \nabla y$. The quantity

$$\beta_{\text{ref}} = \frac{8\pi n_{\text{ref}} T_{\text{ref}}}{B_{\text{N}}^2} \quad (\text{F.50})$$

is the normalized reference plasma pressure. The four boxed equations (F.44)-(F.47) form a closed set of equations that completely define the δf gyrokinetic model. Note that the terms containing the wavenumber with a superscript $\sim \tilde{k}_{\perp}$ in (F.46), \tilde{k}_y in (F.49) differ from the other instances of k_{\perp} in that they do not have a factor of B in the denominator.

F.3.3 Transforming to Hermite-Laguerre space

In this section, we will apply the Hermite-Laguerre (HL) transform to (F.44)-(F.47). The definition of a HL transform is given in (F.7). Each term of the gyrokinetic equation after a Hermite-Laguerre transform is given in §F.2.3. We use relations (F.26)-(F.32) to transform the

gyrokinetic equation (F.44)

$$\begin{aligned}
& \frac{\partial G_{\ell,m}^s}{\partial t} + v_{ts} \nabla_{\parallel} \left(\sqrt{m+1} H_{\ell,m+1}^s + \sqrt{m} H_{\ell,m-1}^s \right) \\
& + v_{ts} \left[-(\ell+1) \sqrt{m+1} H_{\ell,m+1}^s - \ell \sqrt{m+1} H_{\ell-1,m+1}^s \right. \\
& \quad \left. + \ell \sqrt{m} H_{\ell,m-1}^s + (\ell+1) \sqrt{m} H_{\ell+1,m-1}^s \right] \nabla_{\parallel} \log(B) \\
& + i \frac{\tau_s}{Z_s} \omega_d^{\kappa} \left[\sqrt{(m+1)(m+2)} H_{\ell,m+2}^s + (2m+1) H_{\ell,m}^s + \sqrt{m(m-1)} H_{\ell,m-2}^s \right] \\
& + i \frac{\tau_s}{Z_s} \omega_d^{\nabla B} \left[(\ell+1) H_{\ell+1,m}^s + (2\ell+1) H_{\ell,m}^s + \ell H_{\ell-1,m}^s \right] \\
& = \mathcal{D}_{\ell,m}^s.
\end{aligned} \tag{F.51}$$

where

$$G_{\ell,m}^s = H_{\ell,m}^s - \frac{Z_s}{\tau_s} J_{\ell}^s (\varphi_k \delta_{m0} - v_{ts} \delta_{m1} \delta A_{\parallel,k}) + (J_{\ell-1}^s + J_{\ell}^s) \delta_{m0} \frac{\delta B_{\parallel,k}}{B}, \tag{F.52}$$

and

$$\begin{aligned}
\mathcal{D}_{\ell,m=0}^s &= i\omega_* \left[\frac{a_N}{L_{ns}} \ell^s + \frac{a_N}{L_{Ts}} [\ell \mathcal{J}_{\ell-1}^s + 2\ell \mathcal{J}_{\ell}^s + (\ell+1) \mathcal{J}_{\ell+1}^s] \right] \varphi, \\
& + \frac{\tau_s}{Z_s} i\omega_* \left[\frac{a_N}{L_{ns}} [\mathcal{J}_{\ell}^s + \mathcal{J}_{\ell-1}^s] + \frac{a_N}{L_{Ts}} [\ell \mathcal{J}_{\ell-2}^s + 3\ell \mathcal{J}_{\ell-1}^s + (3\ell+1) \mathcal{J}_{\ell}^s + (\ell+1) \mathcal{J}_{\ell+1}^s] \right] \frac{\delta B_{\parallel}}{B}, \\
\mathcal{D}_{\ell,m=1}^s &= -v_{ts} i\omega_* \left[\frac{a_N}{L_{ns}} \mathcal{J}_{\ell}^s + \frac{a_N}{L_{Ts}} [\ell \mathcal{J}_{\ell-1}^s + (2\ell+1) \mathcal{J}_{\ell}^s + (\ell+1) \mathcal{J}_{\ell+1}^s] \right] \delta A_{\parallel}, \\
\mathcal{D}_{\ell,m=2}^s &= \frac{1}{\sqrt{2}} i\omega_* \frac{a_N}{L_{Ts}} \mathcal{J}_{\ell}^s \varphi + \frac{\tau_s}{Z_s} \frac{1}{\sqrt{2}} i\omega_* \frac{a_N}{L_{Ts}} [\mathcal{J}_{\ell}^s + \mathcal{J}_{\ell-1}^s] \frac{\delta B_{\parallel}}{B}, \\
\mathcal{D}_{\ell,m=3}^s &= -v_{ts} \sqrt{\frac{3}{2}} i\omega_* \frac{a_N}{L_{Ts}} \mathcal{J}_{\ell}^s \delta A_{\parallel}, \\
\mathcal{D}_{\ell,m>3}^s &= 0.
\end{aligned} \tag{F.53}$$

To convert the quasineutrality equation (F.45), we use (F.4), (F.5), (F.14)

$$\sum_s \frac{Z_s^2 n_s}{\tau_s} \varphi = \sum_s Z_s n_s \sum_{\ell=0} \mathcal{J}_\ell^s H_{\ell,0}^s. \quad (\text{F.54})$$

Similarly, to convert the parallel Ampere's law (F.46), we use (F.3), (F.4), (F.5), (F.14)

$$\tilde{k}_\perp^2 \delta A_\parallel = \frac{\beta_{\text{ref}}}{2} \sum_s Z_s n_s v_{ts} \sum_{\ell=0} \mathcal{J}_\ell^s H_{\ell,1}^s, \quad (\text{F.55})$$

Finally, for perpendicular Ampere's law, we use (F.4), (F.5), (F.22).

$$\frac{\delta B_\parallel}{B} = -\frac{\beta_{\text{ref}}}{2} \frac{1}{B^2} \sum_s n_s \tau_s \sum_{\ell=0} (\mathcal{J}_\ell^s + \mathcal{J}_{\ell-1}^s) H_{\ell,0}^s. \quad (\text{F.56})$$

This completes the transformation of the δf gyrokinetic model from real space to Fourier-Hermite-Laguerre space. Note that we have ignored collisions and non-linear effects for simplicity. Before running GX non-linearly, we perform some linear electromagnetic tests with realistic equilibria. Some of the results are presented in the next section.

F.4 Linear tests

In this section, we will compare growth rates by solving the linear gyrokinetic equation using both GS2 and GX. We choose the case analyzed in figure 3.16(e).

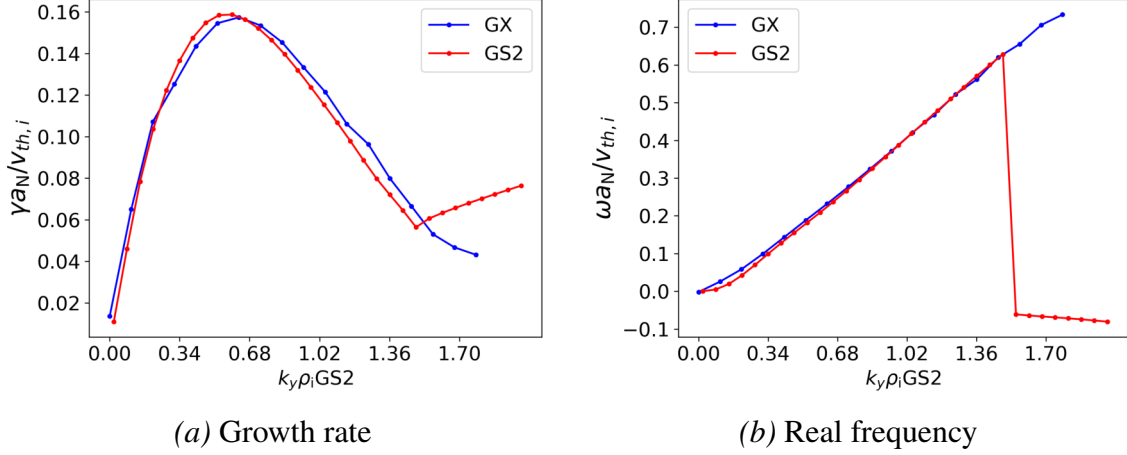


Figure F.1: This figure shows a comparison between the growth rates and real frequencies obtained from GS2 and GX for a realistic tokamak equilibrium. We have used the GS2 normalization for $v_{th,i}$. Note that with the given resolution, GX can capture the KBM but cannot capture the electron-driven mode around $k_y \rho_i = 1.5$. This should not affect our optimization results as we are only optimizing against the KBM.

Note that we have used a small electron-electron collisionality in GS2 for these linear tests to compensate for the hypercollisionality used in GX. This reduces the stabilizing effect of the trapped electrons, causing the growth rates to increase slightly. Hence, the growth rate values in figure F.1 are slightly larger than the ones in figure 3.16(e).

Bibliography

- [1] J. P. Freidberg. *Ideal MHD*. Cambridge University Press, 2014.
- [2] T. M. Antonsen Jr., J. F. Drake, P. N. Guzdar, A. B. Hassam, Y. T. Lau, C. S. Liu, and S. V. Novakovskii. Physical mechanism of enhanced stability from negative shear in tokamaks: Implications for edge transport and the L-H transition. *Physics of Plasmas*, 3:2221, 1996.
- [3] S. C. Hsu, M. Artun, and S. C. Cowley. Calculation and interpretation of analytic high-beta poloidal equilibria in finite aspect ratio tokamaks. *Physics of Plasmas*, 3:266, 1996.
- [4] S. Baalrud, N. Ferraro, L. Garrison, N. Howard, C. Kuranz, J. Sarff, E. Scime, and W. Solomon. A community plan for fusion energy and discovery plasma sciences. Report of the 2019–2020 American Physical Society Division of Plasma Physics Community Planning Process, 2020.
- [5] Medicine National Academies of Sciences, Engineering et al. *Bringing fusion to the U.S. grid*. 2021.
- [6] M. Shimada, D. J. Campbell, V. Mukhovatov, M. Fujiwara, N. Kirneva, K. Lackner, M. Nagami, V. D. Pustovitov, N. Uckan, and J. Wesley. Progress in the ITER physics basis chapter 1: Overview and summary. *Nucl. Fusion*, 47:S1, 2007.
- [7] Elena Bonner. Sakharov is tokamak’s originator. *Physics Today*, 58(12):15–15, 2005.
- [8] L. Spitzer Jr. The stellarator concept. *The Physics of Fluids*, 1(4):253–264, 1958.
- [9] V. P. Smirnov. Tokamak foundation in USSR/Russia 1950–1990. *Nuclear fusion*, 50(1):014003, 2009.
- [10] D. A. Garren and A. H. Boozer. Magnetic field strength of toroidal plasma equilibria. *Physics of Fluids B: Plasma Physics*, 3:2805–2821, 1991.
- [11] A. H. Boozer. Transport and isomorphic equilibria. *The Physics of Fluids*, 26:496–499, 1983.
- [12] Y. Xu. A general comparison between tokamak and stellarator plasmas. *Matter and Radiation at Extremes*, 1(4):192–200, 2016.
- [13] A. Cho. Energy department pulls plug on overbudget fusion experiment, 2008.
- [14] I. B. Bernstein, E. A. Frieman, M. D. Kruskal, and R. M. Kulsrud. An energy principle for hydromagnetic stability problems. *Proc. R. Soc. A*, 244:17, 1958.

- [15] J. W. Connor, R. J. Hastie, and J. B. Taylor. Shear, periodicity, and plasma ballooning modes. *Phys. Rev. Lett.*, 40:396, 1978.
- [16] R. L. Dewar and A. H. Glasser. Ballooning mode spectrum in general toroidal systems. *Phys. Fluids*, 26:3038, 1983.
- [17] A. E. White, N. T. Howard, M. Greenwald, M. L. Reinke, C. Sung, S. Baek, M. Barnes, J. Candy, A. Dominguez, D. Ernst, et al. Multi-channel transport experiments at Alcator C-Mod and comparison with gyrokinetic simulations. *Physics of Plasmas*, 20:056106, 2013.
- [18] A. J. Creely, N. T. Howard, P. Rodriguez-Fernandez, N. Cao, A. E. Hubbard, J. W. Hughes, J. E. Rice, A. E. White, J. Candy, G. M. Staebler, et al. Validation of nonlinear gyrokinetic simulations of L- and I-mode plasmas on Alcator C-Mod. *Physics of Plasmas*, 24:056104, 2017.
- [19] Boris Borisovich Kadomtsev. Plasma turbulence. *New York: Academic Press*, 1965.
- [20] GT Roberg-Clark, P Xanthopoulos, and GG Plunk. Reduction of electrostatic turbulence in a quasi-helically symmetric stellarator via critical gradient optimization. *arXiv preprint arXiv:2210.16030*, 2022.
- [21] GT Roberg-Clark, GG Plunk, and P Xanthopoulos. Coarse-grained gyrokinetics for the critical ion temperature gradient in stellarators. *Physical Review Research*, 4(3):L032028, 2022.
- [22] R Jorge, W Dorland, P Kim, M Landreman, NR Mandell, G Merlo, and T Qian. Direct microstability optimization of stellarator devices. *arXiv preprint arXiv:2301.09356*, 2023.
- [23] W. D. D’haeseleer, W. N. G. Hitchon, J. D. Callen, and J. L. Shohet. *Flux coordinates and magnetic field structure: a guide to a fundamental tool of plasma theory*. Springer Science & Business Media, 2012.
- [24] RAYC GRIMM, JOHN M GREENE, and JOHN L JOHNSON. Computation of the magnetohydrodynamic spectrum in axisymmetric toroidal confinement systems. *Methods in Computational Physics*, 16:253, 2012.
- [25] H. Grad and H. Rubin. Proceedings of the Second United Nations International Conference on the Peaceful uses of Atomic Energy. page 400, Geneva : 1958, 1958. UN.
- [26] V. D. Shafranov. On equilibrium magnetohydrodynamic configurations. *Zh. Eksp. Teor. Fiz.*, 33:710, 1957.
- [27] S. P. Hirshman and J. C. Whitson. Steepest-descent moment method for three-dimensional magnetohydrodynamic equilibria. *The Physics of fluids*, 26:3553, 1983.
- [28] M. D. Kruskal and R. M. Kulsrud. Equilibrium of a magnetically confined plasma in a toroid. *Phys. Fluids*, 1:265, 1958.

- [29] A. Marinoni, M. E. Austin, A. W. Hyatt, M. L. Walker, J. Candy, C. Chrystal, C. J. Lasnier, G. R. McKee, T. Odstrčil, C. C. Petty, et al. H-mode grade confinement in L-mode edge plasmas at negative triangularity on DIII-D. *Phys. Plasmas*, 26:042515, 2019.
- [30] G. Y. Fu, M. Isaev, L. Ku, M. Mikhailov, M. H. Redi, R. Sanchez, A. Subbotin, W. A. Cooper, S. P. Hirshman, D. A. Monticello, et al. Ideal magnetohydrodynamic stability of the ncsx. *Fusion science and technology*, 51:218–231, 2007.
- [31] S. A. Henneberg, M. Drevlak, C. Nührenberg, C. D. Beidler, Y. Turkin, J. Loizu, and P. Helander. Properties of a new quasi-axisymmetric configuration. *Nucl. Fusion*, 59:026014, 2019.
- [32] R. Gaur, I. G. Abel, D. Dickinson, and W. Dorland. Microstability of $\beta \sim 1$ tokamak equilibria. *arXiv preprint arXiv:2208.05435*, 2022.
- [33] M. C. Zarnstorff, L. A. Berry, A. Brooks, E. Fredrickson, G. Y. Fu, S. Hirshman, S. Hudson, L. P. Ku, E. Lazarus, D. Mikkelsen, et al. Physics of the compact advanced stellarator NCSX. *Plasma Physics and Controlled Fusion*, 43:A237, 2001.
- [34] RS Pease. Summary on alternate magnetic systems-experimental results. In *Plasma physics and controlled nuclear fusion research 1984*. 1985.
- [35] Per Helander and Dieter J Sigmar. *Collisional transport in magnetized plasmas*, volume 4. Cambridge university press, 2005.
- [36] H. P. Furth, J. Killeen, M. N. Rosenbluth, and B. Coppi. Plasma physics and controlled nuclear fusion research vol 1 IAEA. 1966.
- [37] D. V. Anderson, W. A. Cooper, R. Gruber, S. Merazzi, and U. Schwenn. TERPSICHORE: A three-dimensional ideal magnetohydrodynamic stability program. *Scientific Computing on Supercomputers II*, pages 159–174, 1990.
- [38] C. Schwab. Ideal magnetohydrodynamics: Global mode analysis of three-dimensional plasma configurations. *Physics of Fluids B: Plasma Physics*, 5:3195–3206, 1993.
- [39] L. C. Bernard, F. J. Helton, and R. W. Moore. GATO: an MHD stability code for axisymmetric plasmas with internal separatrices. *Computer Physics Communications*, 24(3-4):377–380, 1981.
- [40] P. B. Snyder, H. R. Wilson, J. R. Ferron, L. L. Lao, A. W. Leonard, T. H. Osborne, A. D. Turnbull, D. Mossessian, M. Murakami, and X. Q. Xu. Edge localized modes and the pedestal: A model based on coupled peeling–ballooning modes. *Physics of Plasmas*, 9:2037–2043, 2002.
- [41] J. W. Connor, R. J. Hastie, and J. B. Taylor. High mode number stability of an axisymmetric toroidal plasma. *Proc. R. Soc. London, Ser. A*, 365:1, 1979.
- [42] R. Sanchez, S. P. Hirshman, J. C. Whitson, and A. S. Ware. COBRA: An optimized code for fast analysis of ideal ballooning stability of three-dimensional magnetic equilibria. *Journal of Computational Physics*, 161:576, 2000.

- [43] A. S. Lewis and M. L. Overton. Eigenvalue optimization. *Acta numerica*, 5, 1996.
- [44] M. Landreman, B. Medasani, F. Wechsung, A. Giuliani, R. Jorge, and C. Zhu. Simsopt: A flexible framework for stellarator optimization. *Journal of Open Source Software*, 6:3525, 2021.
- [45] R. Davies, D. Dickinson, and H. R. Wilson. Kinetic ballooning modes as a constraint on plasma triangularity in commercial spherical tokamaks. *Plasma Physics and Controlled Fusion*, 2022.
- [46] A. O. Nelson, C. Paz-Soldan, and S. Saarelma. Prospects for H-mode inhibition in negative triangularity tokamak reactor plasmas. *Nuclear Fusion*, 62:096020, 2022.
- [47] Alan Glasser. DCON for stellarators. *Bulletin of the American Physical Society*, 63, 2018.
- [48] A. H. Glasser. The direct criterion of newcomb for the ideal mhd stability of an axisymmetric toroidal plasma. *Physics of Plasmas*, 23:072505, 2016.
- [49] W. M. Tang, J. W. Connor, and R. J. Hastie. Kinetic-ballooning-mode theory in general geometry. *Nuclear Fusion*, 20:1439, 1980.
- [50] AE White, L Schmitz, GR McKee, C Holland, WA Peebles, TA Carter, MW Shafer, ME Austin, KH Burrell, J Candy, et al. Measurements of core electron temperature and density fluctuations in diii-d and comparison to nonlinear gyrokinetic simulations. *Physics of Plasmas*, 15(5):056116, 2008.
- [51] P. J. Catto and K. T. Tsang. Linearized gyrokinetic equation with collisions. *Phys. Fluids*, 20:396, 1977.
- [52] T. M. Antonsen Jr. and B. Lane. Kinetic equations for low frequency instabilities in inhomogeneous plasmas. *The Physics of Fluids*, 23:1205, 1980.
- [53] E. A. Frieman and L. Chen. Nonlinear gyrokinetic equations for low-frequency electromagnetic waves in general plasma equilibria. *Phys. Fluids*, 25:502, 1982.
- [54] I. G. Abel, G. G. Plunk, E. Wang, M. Barnes, S. C. Cowley, W. Dorland, and A. A. Schekochihin. Multiscale gyrokinetics for rotating tokamak plasmas: fluctuations, transport and energy flows. *Reports on Progress in Physics*, 76:116201, 2013.
- [55] I. G. Abel, M. Barnes, S. C. Cowley, W. Dorland, and A. A. Schekochihin. Linearized model Fokker–Planck collision operators for gyrokinetic simulations. I. Theory. *Phys. Plasmas*, 15:122509, 2008.
- [56] M. A. Beer, S. C. Cowley, and G. W. Hammett. Field-aligned coordinates for nonlinear simulations of tokamak turbulence. *Phys. Plasmas*, 2:2687, 1995.
- [57] M. Kotschenreuther, G. W. Rewoldt, and W. M. Tang. Comparison of initial value and eigenvalue codes for kinetic toroidal plasma instabilities. *Comp. Phys. Comm.*, 88:128, 1995.

- [58] W. Dorland, F. Jenko, M. Kotschenreuther, and B. N. Rogers. Electron temperature gradient turbulence. *Phys. Rev. Lett.*, 85:5579, 2000.
- [59] F. Jenko and W. Dorland. Nonlinear electromagnetic gyrokinetic simulations of tokamak plasmas. *Plasma Phys. Control. Fusion*, 43:A141, 2001.
- [60] E. G. Highcock. *The Zero Turbulence Manifold in Fusion Plasmas*. PhD thesis, Oxford University, 2012.
- [61] M. Kotschenreuther, X. Liu, D. R. Hatch, S. Mahajan, L. Zheng, A. Diallo, R. Groebner, J. C. Hillesheim, C. F. Maggi, C. Giroud, et al. Gyrokinetic analysis and simulation of pedestals to identify the culprits for energy losses using ‘fingerprints’. *Nuclear Fusion*, 59:096001, 2019.
- [62] J. M. Greene and M. S. Chance. The second region of stability against ballooning modes. *Nucl. Fusion*, 21:453, 1981.
- [63] R. L. Miller, M. S. Chu, J. M. Greene, Y. R. Lin-Liu, and R. E. Waltz. Noncircular, finite aspect ratio, local equilibrium model. *Phys. Plasmas*, 5:973, 1998.
- [64] C. M. Bishop. Construction of local axisymmetric MHD equilibria. Technical report, UKAEA Culham Lab., 1985.
- [65] J. E. Menard, B. A. Grierson, T. G. Brown, C. Rana, Y. Zhai, F. M. Poli, R. Maingi, W. Guttenfelder, and P. B. Snyder. Fusion pilot plant performance and the role of a sustained high power density tokamak. *Nuclear Fusion*, 2022.
- [66] D. A. Gates and NSTX national research team. High- β , long-pulse, bootstrap-sustained scenarios on the National Spherical Torus Experiment (NSTX). *Physics of Plasmas*, 10:1659, 2003.
- [67] A. Sykes, R. J. Akers, L. C. Appel, P. G. Carolan, J. W. Connor, N. J. Conway, G. F. Counsell, A. Dnestrovskij, Yu N. Dnestrovskij, M. Gryaznevich, et al. H-mode operation in the START spherical tokamak. *Physical Review Letters*, 84:495, 2000.
- [68] O. A. Hurricane, B. D. G. Chandran, and S. C. Cowley. Internal kink stability of large aspect ratio high- β tokamaks. *Physics of Plasmas*, 7:4043, 2000.
- [69] M. S. Chance, S. C. Jardin, C. Kessel, J. Manickam, D. Monticello, Y. K. M. Peng, J. A. Holmes, D. J. Strickler, J. C. Whitson, A. H. Glasser, et al. Ideal MHD stability of very high beta tokamaks. Technical report, Princeton Univ., NJ (USA). Plasma Physics Lab., 1990.
- [70] H. R. Wilson, J. W. Ahn, R. J. Akers, D. Applegate, R. A. Cairns, J. P. Christiansen, J. W. Connor, G. Counsell, A. Dnestrovskij, W. Dorland, et al. Integrated plasma physics modelling for the culham steady state spherical tokamak fusion power plant. *Nuclear fusion*, 44(8):917, 2004.

- [71] S. C. Cowley, R. M. Kulsrud, and R. Sudan. Considerations of ion-temperature-gradient-driven turbulence. *Phys. Fluids B*, 3:2767, 1991.
- [72] B. Zhu, M. Francisquez, B. N. Rogers, and X.-Q. Xu. Generalized slab universal instability and its appearance in pair plasma. *Physics of Plasmas*, 27:102104, 2020.
- [73] A. Hirose. On finite β stabilization of the toroidal ion temperature gradient mode. *Physics of Plasmas*, 7:433, 2000.
- [74] A. Jarmén, P. Malinov, and H. Nordman. ITG modes with finite- β effects and the upper η_i stability regime. *Plasma physics and controlled fusion*, 40:2041, 1998.
- [75] M. Uchida, S. Sen, A. Fukuyama, and D. R. McCarthy. Stability of the ion-temperature-gradient-driven mode with negative magnetic shear. *Physics of Plasmas*, 10:4758, 2003.
- [76] J. Candy and R. E. Waltz. An Eulerian gyrokinetic-Maxwell solver. *J. Comp. Phys.*, 186:545, 2003.
- [77] J. C. Adam, W. M. Tang, and P. H. Rutherford. Destabilization of the trapped-electron mode by magnetic curvature drift resonances. *The Physics of Fluids*, 19:561, 1976.
- [78] J. W. Connor, R. J. Hastie, and T. J. Martin. Effect of pressure gradients on the bounce-averaged particle drifts in a tokamak. *Nuclear fusion*, 23:1702, 1983.
- [79] C. M. Roach, J. W. Connor, and S. Janjua. Trapped particle precession in advanced tokamaks. *Plasma physics and controlled fusion*, 37(6):679, 1995.
- [80] M. Landreman, T. M. Antonsen Jr., and W. Dorland. Universal instability for wavelengths below the ion larmor scale. *Physical review letters*, 114:095003, 2015.
- [81] E. A. Belli and J. Candy. Fully electromagnetic gyrokinetic eigenmode analysis of high-beta shaped plasmas. *Physics of Plasmas*, 17(11):112314, 2010.
- [82] J. Candy and R. E. Waltz. An Eulerian gyrokinetic-Maxwell solver. *J. Comp. Phys.*, 186:545, 2003.
- [83] M. Kotschenreuther, W. Dorland, M. A. Beer, and G. W. Hammett. Quantitative predictions of tokamak energy confinement from first-principles simulations with kinetic effects. *Phys. Plasmas*, 2:2381, 1995.
- [84] W. Guttenfelder, J. Candy, S. M. Kaye, W. M. Nevins, E. Wang, R. E. Bell, G. W. Hammett, B. P. LeBlanc, D. R. Mikkelsen, and H. Yuh. Electromagnetic transport from microtearing mode turbulence. *Physical review letters*, 106:155004, 2011.
- [85] D. Dickinson, C. M. Roach, F. J. Casson, A. Kirk, S. Saarelma, and R. Scannell. Microtearing modes and the pedestal. In *40th EPS Conference on Plasma Physics*. European Physical Society, 2013.
- [86] J. Y. Kim and W. Horton. Electromagnetic effect on the toroidal electron temperature gradient mode. *Physics of Fluids B: Plasma Physics*, 3:3194–3197, 1991.

- [87] N. Joiner and A. Hirose. Effects of magnetosonic perturbations on electron temperature gradient driven modes and the stability of skin depth sized electron ballooning modes. *Physics of Plasmas*, 14:112111, 2007.
- [88] D. J. Applegate, C. M. Roach, J. W. Connor, S. C. Cowley, W. Dorland, R. J. Hastie, and N. Joiner. Micro-tearing modes in the Mega Ampere Spherical Tokamak. *Plasma Physics and Controlled Fusion*, 49:1113, 2007.
- [89] B. S. Patel, D. Dickinson, C. M. Roach, and H. R. Wilson. Linear gyrokinetic stability of a high β non-inductive spherical tokamak. *Nuclear Fusion*, 62:016009, 2021.
- [90] M. Landreman, S. Buller, and M. Drevlak. Optimization of quasi-symmetric stellarators with self-consistent bootstrap current and energetic particle confinement. *Physics of Plasmas*, 29(8):082501, 2022.
- [91] C. C. Hegna. Local three-dimensional magnetostatic equilibria. *Physics of Plasmas*, 7(10):3921–3928, 2000.
- [92] F. Parra, I. Calvo, W. Sengupta, J. M. Garcia-Regana, and A. Gonzalez-Jerez. Linear equations for stellarator local MHD equilibria around irrational and rational flux surfaces. *Bulletin of the American Physical Society*, 2022.
- [93] K. Aleynikova, A. Zocco, P. Xanthopoulos, P. Helander, and C. Nührenberg. Kinetic ballooning modes in tokamaks and stellarators. *Journal of Plasma Physics*, 84, 2018.
- [94] W. A. Newcomb. Hydromagnetic stability of a diffuse linear pinch. *Ann. Phys.*, 10:232, 1960.
- [95] B Coppi, A Ferreira, JW-K Mark, and JJ Ramos. Ideal-mhd stability of finite-beta plasmas. *Nuclear Fusion*, 19(6):715, 1979.
- [96] N. R. Mandell, W. Dorland, and M. Landreman. Laguerre–Hermite pseudo-spectral velocity formulation of gyrokinetics. *Journal of Plasma Physics*, 84(1):905840108, 2018.
- [97] N. R. Mandell, W. Dorland, I. Abel, R. Gaur, P. Kim, M. Martin, and T. Qian. GX: a GPU-native gyrokinetic turbulence code for tokamak and stellarator design. *arXiv preprint arXiv:2209.06731*, 2022.
- [98] Per Helander. Available energy and ground states of collisionless plasmas. *Journal of Plasma Physics*, 83(4):715830401, 2017.
- [99] Michael Alexander Barnes. *Trinity: A unified treatment of turbulence, transport, and heating in magnetized plasmas*. University of Maryland, College Park, 2009.
- [100] Tony Qian, Braden Buck, Rahul Gaur, Noah Mandell, Patrick Kim, and William Dorland. Stellarator profile predictions using trinity3d and gx. *Bulletin of the American Physical Society*, 2022.
- [101] D. W. Dudt and E. Kolemen. DESC: A stellarator equilibrium solver. *Physics of Plasmas*, 27:102513, 2020.

- [102] Rory Conlin, Daniel W Dudt, Dario Panici, and Egemen Kolemen. The desc stellarator code suite part ii: perturbation and continuation methods. *arXiv preprint arXiv:2203.15927*, 2022.
- [103] Dario Panici, Rory Conlin, Daniel W Dudt, and Egemen Kolemen. The desc stellarator code suite part i: quick and accurate equilibria computations. *arXiv preprint arXiv:2203.17173*, 2022.
- [104] H. Hellmann. Zur rolle der kinetischen elektronenenergie für die zwischenatomaren kräfte. *Zeitschrift für Physik*, 85(3), 1933.
- [105] R. P. Feynman. Forces in molecules. *Physical review*, 56:340, 1939.
- [106] L. L. Lao, H. St. John, R. D. Stambaugh, A. G. Kellman, and W. Pfeiffer. Reconstruction of current profile parameters and plasma shapes in tokamaks. *Nuclear fusion*, 25(11):1611, 1985.
- [107] S. Liao. *Homotopy analysis method in nonlinear differential equations*. Springer, 2012.
- [108] S. S. Motsa, P. Sibanda, and S. Shateyi. A new spectral-homotopy analysis method for solving a nonlinear second order BVP. *Communications in Nonlinear Science and Numerical Simulation*, 15(9):2293–2302, 2010.
- [109] C. Mercier and H. Luc. Lectures in plasma physics. Technical report, Commission of the European Communities, Brussels, 1974.
- [110] Michael Barnes, Felix I Parra, and Matt Landreman. stella: An operator-split, implicit–explicit δf -gyrokinetic code for general magnetic field configurations. *Journal of Computational Physics*, 391:365–380, 2019.
- [111] M. Abramowitz, I. A. Stegun, and R. H. Romer. Handbook of mathematical functions with formulas, graphs, and mathematical tables, 1988.